Calibration free LIBS using multivariate hybrid chemometrics: An approach for precise quantitative elemental analysis of solid samples

BY

Owolabi Taoreed Olakunle

A Dissertation Presented to the

DEANSHIP OF GRADUATE STUDIES

KING FAHD UNIVERSITY OF PETROLEUM & MINERALS

DHAHRAN, SAUDI ARABIA

In Partial Fulfillment of the
Requirements for the Degree of

DOCTOR OF PHILOSOPHY

In

PHYSICS

May 2018

KING FAHD UNIVERSITY OF PETROLEUM & MINERALS

DHAHRAN- 31261, SAUDI ARABIA

DEANSHIP OF GRADUATE STUDIES

This thesis, written by Owolabi Taoreed Olakunle under the direction of his thesis advisor and approved by his thesis committee, has been presented and accepted by the Dean of Graduate Studies, in partial fulfillment of the requirements for the degree of **DOCTOR OF PHILOSOPHY IN PHYSICS.**

M. a. Gondal

Dr. Mohammed Ashraf Gondal
(Advisor)

Dr. Abdullah A. Al-Sunaidi
Department Chairman

13/5/2018

Dr. Ibraheem Nasser
(Member)

Dr. Salam A. Zummo
Dean of Graduate Studies

18 / 7 / 2018
Date

عمادة الدراسات العليا
DEANSHIP OF GRADUATE STUDIES

Dr. Watheq Al-Basheer
(Member)

Dr. Akthar Abass Naqvi
(Member)

Dr. Chanbasha Basheer
(Member)

This work is dedicated to Almighty Allah

ACKNOWLEDGMENTS

I acknowledge the support of my advisor, Distinguished Professor Mohammed Gondal who has been financially and morally supportive during the course of this research work. I appreciate his persistent teaching and encouragement in solving many challenges encountered during this research work. He combined a fatherly and advisory role during the time I spent with him. My special appreciation goes to my committee members which include Professor Ibraheem Nassir, Professor Watheq Al-Basheer, Professor Akthar Abass Naqvi and Professor Chanbasha Basheer for their support throughout the course of this research work. Theoretical background gained from the classes I attended with Professor Ibraheem Nasser at MS and PhD level cannot be left unacknowledged.

I would like to thank KFUPM institution for the scholarship granted to me to embark on my third degree program. I would also like to extend my gratefulness to the erudite faculty members of physics Department of the University for the rigorous and appealing training in the discipline to complement my physics background. My appreciation goes to formal chairman of the Department (Professor Abdul-Aziz Al-Jalal) and the present chairman (Professor Abdullah A. Al-Sunaidi) for the knowledge they impacted on me while taking statistical physics courses with them. The support of other departmental staffs such as Mr Arsha Qasi and Mr. Abdul Wahab Hussain among others are appreciated.

The contribution of my family cannot be left out in my pages of acknowledgement. I appreciate my first wife for her patience and words of encouragement. My acknowledgment goes to my parents Alahji Owolabi Tajudeen and Mrs Aina Owolabi for their supports. The supports of other wives of my father are acknowledged. The contributions of my sisters especially, Mrs Dasola Olarere are acknowledged.

Further, I wish to thank my colleagues in physics Department as well as Nigeria community (NCUPM) at large for their supports. The Supports of Professor S. Olatunji (Aadam), Akande kabiru, BashirYusuf and Dr. Sulaiman Muhammad are strongly appreciated.

TABLE OF CONTENTS

LIST OF TABLES

LIST OF FIGURES

LIST OF ABBREVIATIONS

SVR: Support Vector Regression chemometric

HSVR: Homogenously hybridized Support Vector Regression chemometric

ELM: Extreme Learning Machine chemometric

HELM : Homogenously hybridized Extreme Learning Machine chemometric

SVR-ELM : Hybrid fusion of Support Vector Regression and Extreme Learning Machine chemometric

ELM-SVR : Hybrid fusion of Extreme Learning Machine and Support Vector Regression chemometric

GSA : Gravitational Search Algorithm

IRP: Internal Reference Preprocessing method

WIRP : Without Internal Reference Preprocessing method

ABSTRACT

Full Name : [Owolabi Taoreed Olakunle]

Thesis Title : Calibration free LIBS using multivariate hybrid chemometrics: An approach for precise quantitative elemental analysis of solid samples

Major Field : [Physics]

Date of Degree : [May 2018]

Performance enhancement techniques for the improvement of chemometrics that are employed for quantitative analysis of LIBS spectra have been comprehensively studied in this work using spectral from different matrices which include solid samples such as standard bronze samples, semi-fluid samples such as grapes and biocompatible samples such as fish. Three novel techniques for performance enhancement are proposed and developed for hybrid support vector regression (SVR) based chemometrics as well as hybrid extreme learning machine (ELM) based chemometrics which are used for quantitative analysis of LIBS spectra. Specifically, the proposed techniques are internal reference preprocessing (IRP), homogenous hybridization and hybrid fusion. Prior to the implementation of the proposed techniques, sufficiency of single emission line for quantitative analysis of LIBS spectra using the developed chemometrics was investigated by comparing the elemental concentrations obtained from the developed sensitivity based linear learning method (SBLLM) based chemometrics using single, double and three emission lines. Experimental validation of the proposed techniques was carried out using seven standard bronze samples and excellent results are obtained. In addition, hybrid

support vector regression and hybrid extreme learning machine chemometrics are also developed and implemented for quantitative analysis of crayfish and grape samples. The obtained results from the two chemometric models were verified and compared with the result obtained from standard analytical technique such as inductively coupled plasma mass spectrometry (ICP-MS). Implementation of the developed performance enhancement techniques for the investigated chemometrics tools employed for quantitative analysis of LIBS spectra would definitely enhance the precision of quantitative analysis of LIBS spectra, especially for in situ applications, and ultimately widen the applicability of the technique

ملخص الرسالة

الاسم الكامل: توريد أولاكونلي أولابي

عنوان الرسالة: مطياف التكسير المستحث بالليزر الخالي من المعايرة باستخدام مقاييس كيميائية هجينة متعددة المتغيرات: منهج للتحليل الكمي الدقيق للعناصر الكيميائية في العينات الصلبة

التخصص: : فيزياء

تاريخ الدرجة العلمية: مايو 2018

هدف هذا العمل لدراسة وتحسين اداء الطرق المستخدمة في التحليل الكمي لطيف التكسير المستحث بالليزر بواسطة طيف من المصفوفات المختلفة والتي تشمل عينات صلبة مثل العينات البرونزية القياسية وعينات شبه السوائل مثل العنب وعينات متوافقة حيويا مثل السمك. تم اقتراح وتطوير ثلاث تقنيات جديدة لتحسين اداء الطرق المستخدمة للتحليل الكمي لطيف التكسير المستحث بالليزر. التحقق التجريبي للتقنيات المقترحة أظهر نتائج ممتازة لمجموعة من العينات المختلفة. زيادة دقة التحليل الكمي للعناصر الكيميائية في العينات الصلبة بواسطة مطياف التكسير المستحث بالليزر سوف يسهل استخدام المطياف للعمل الميداني وقابلية تطبيقه في نطاق أوسع

CHAPTER 1

INTRODUCTION

Laser induced breakdown spectroscopy (LIBS) is an analytical technique that uses laser pulse of high energy for material ablation [1]. The ablation generates laser induced plasma when the focused laser beam results into optical breakdown of the test samples [2]. Among the merits of this technique, as compared to other spectroscopic techniques include its rapid and real time analysis as well as small sample requirement [3]–[7]. In principle, any physical state of matter can be analyzed qualitatively and quantitatively using LIBS technique. The qualitative analysis premises on the emitted characteristic frequency of the plasma constituents when excited to high temperature while the quantitative analysis of the LIBS spectra can be carried out through calibration curve and calibration free approaches [8] [1], [9]–[12] [1], [2], [13]–[17]. Chemometric tools are techniques which relate the features (also called descriptors) to the desired quantity (also called output or target) in a given data set [18]. These techniques have gained a significant interest because of their simplicity and ability to effectively model non-linear interactions taking place in the laser induced plasma [8]–[11], [13], [15], [16], [19]. Chemometric technique that have been extensively employed in spectroscopic analysis include principal component analysis, parallel factor analysis, linear discriminate analysis, window factor analysis, orthogonal projection analysis and support vector regression [12],

[18], [20]–[22]. This present work develops extreme learning machine (ELM) based chemometric for quantitative analysis of LIBS spectra for the first time. The proposed chemometrics show good generalization performance as measured on the basis of root mean square error, mean absolute error and correlation coefficient when implemented on standard bronze samples. The performance of the proposed chemometrics is enhanced using internal reference preprocessing method (which minimizes self-absorption of the emission spectra), homogenous hybridization and hybrid fusion. The inherent ability of extreme learning machine to approximate non-linear function to a linear one distinguishes it from other computational intelligence based chemometrics [23]. ELM trains single-hidden layer feed-forward neural networks using a novel learning algorithm different from the popular gradient-based learning algorithms such as Levenberg-Marquardt and back-propagation which are known to be slow and sometimes converge to local minimum [24], [25]. ELM algorithm randomly selects input weights and hidden biases and determines the output weights analytically with the aid of Moore-Penrose generalized inverse matrix. The input weights relate the input layer to the hidden layer while the output weights link the hidden layer to output layer. The learning scheme adopted by ELM results into a fast learning rate, excellent generalization performance and non-convergence to local minimum. In order to fully capture the non-linear interactions in laser induced plasma, two ELM algorithms are hybridized thereby forming homogeneously hybridized extreme learning machine (HELM). This proposed HELM has many merits as compared with ordinary ELM as it allows utilization of multiple activation functions as well as generalization of error bound. Since ELM determines the input

weights as well as hidden biases in a random manner, hybridization of ELM optimization algorithm would definitely enhance the performance of the technique. In this work, ELM is hybridized with gravitational search algorithm (GSA) for number of hidden neuron optimization. GSA is a novel search algorithm that is based on Newtonian mechanics and mass interaction [26]. It treats the number of hidden neurons to be optimized as masses in gravitational pull in which heavy mass attracts lighter ones and move slowly until convergence to global minimum is attained. The performances of the resulted hybrid models were further improved using internal reference preprocessing method in which emission line intensities are normalized using the emission intensity which is characterized with highest upper level excitation energy and lowest transition probability. The effect of self-absorption on the emission intensity is minimized and more accurate quantitative results are obtained.

The plasma generated due to laser ablation is often optically thick and results into self-absorption since the plasma is spatially inhomogeneous and its evolution is temporal [8]. An optically thick plasma results into uneven plasma cooling in which one part of the plasma cools faster than the remaining part. Consequently, the photons emitted from the cooler part are reabsorbed by atoms of the same species in the hotter part of the plasma and ultimately leads to emission of reduced intensity. The emitted species with least transition probability (which is the probability per unit time of an atom in upper energy level making a transition to lower energy level) would have lowest possibility of being reabsorbed since the transition to the lowest energy state might be slower than the cooling time lag between different parts of the cooling plasma. Hence, normalization of the spectra intensity with the intensity that is rarely

affected by self-absorption reduces the effect of self-absorption in the entire spectra [13], [27]. The proposed methods of performance enhancement are also implemented on support vector regression chemometrics and improved performance was obtained. The results of the present modeling and simulations show the proposed chemometrics and performance enhancement methods are efficient and can ensure precise quantitative analysis of LIBS spectra.

1.1 Description of LIBS instrumentation

Laser induced breakdown spectroscopy (LIBS) is an atomic emission spectroscopic method that has been extensively utilized for elemental compositional analysis of a wide varieties of samples across the states of mater such as solid, liquid and gas [28]. Among the uniqueness of LIBS which dichotomizes it from other established spectroscopic techniques includes presence of little of no sample treatment or preparation before spectroscopic analysis, ability to detect both neutral and ion spectral features of all species present in the sample in a single measurement, quasi-nondestructive nature of the measurement as well as easy accessibility of potable and compact LIBS system [29]–[34]. As a result of the aforementioned unique features of LIBS, practical application and implementation of the technique has enjoyed a wider utilization, therefore various experimental configurations have been developed and designed to meet the requirements of the desired and specific applications. The operational measurement in LIBS involves focusing a short laser pulse onto the sample to be analyzed while high electron density and temperature plasma is formed due to the transference of a fraction of the impinging energy to the irradiated portion of the sample. This phenomenon is known as breakdown.

The ignition process of LIBS plasma can be influenced by the physical characteristics of the excitation pulse (this includes duration, wavelength, repetition among others) as well as the chemico-physical characteristics of the irradiated material. Plasma is formed when the vaporized portion of the material expands at supersonic velocity in a direction normal to the surface of the target. The electromagnetic radiation is emitted by the plasma and can be detected as well as analyzed spectrally, purposely to retrieve the elemental constituents of the target. Analyzing the elemental composition of the plasma in lieu of the target sample is only possible for stoichiometric ablation. The temporal delay to record the emitted spectrum is of significance since broad emission lines which can be attributed to stark effect superimposed on intense background (continuous) characterize the initial stage of spectrum acquisition [32], [35], [36]. The observed continuous background can be attributed to both free to bound electron recombination as well as free-free electron transitions known as Bremsstrahlung emission. The intensity of the continuous background decays rapidly after few hundreds of nanoseconds when ions capture the free electrons and the emission lines emanated from bound to bound electronic transitions become weaker and narrower. Meanwhile, the atomic lines suffer a slow decay as emission lines appear coming from molecules. For thermodynamic equilibrium condition which is bedrock for any quantitative analysis, the acquisition period should constitute a small fraction of the whole plasma emission time. Typically, LIBS apparatus contains the following basic components.

- A laser source through which light pulses are generated for plasma ignition
- Optical system that directs and focuses the laser pulse on the target.

- ❖ Light collection system employed in collection and transportation of the emitted light (from the plasma) to the detection system.
- ❖ A spectrometer for analyzing the spectral emitted from the plasma
- ❖ Detector for collection and recoding of the spectrum
- ❖ Electronic device as well as computer for controlling the experimental apparatus.

1.1.1 Laser source

For the purpose of plasma generation from any kind of sample involved in LIBS experiment, pulsed lasers of high energy are frequently used [37]. Varieties of coherent sources with such high energy are available in the market with different technical specifications. Physical parameters of laser pulse such as wavelength, pulse energy, pulse duration and beam quality among others, control the radiation to matter interaction and consequently influence the plasma formation as well as the quality of LIBS measurement. Therefore, the nature of the task to be performed determines the selection of the laser source suitable for the job accomplishment. The main features of a laser source include intensity, directionality, coherence and monochromaticity. Laser intensity is the ratio of the peak power of the laser and cross section of the output beam. The laser intensity is also called power density or simply irradiance [38]. Very large intensities around trillion of watts can be achieved per unit area since a short duration of order of femtoseconds and nanoseconds pulses can be generated. However, power per unit area impinging on the sample under investigation is mostly significant in LIBS experiment and this also depends on the optical systems for delivering the beam onto the target. The divergence angle of laser describes its directionality. The directionality property of laser beam allows

deliverance of high irradiance to the target since radiation can be easily focused to a very small spot size [39]. Spatial coherence enhances high irradiance in laser beam since is related to low divergence of the beam. Similarly, laser monochromaticity is of lesser significance since plasma formation as well as behavior depends strongly on laser intensity and weakly influenced by the frequency spread of the incident radiation. The beam quality factor measures the deviation of the energy density distribution in laser beam from the ideal Gaussian distribution. In LIBS experiment, the beam quality factor of most frequently used sources ranges from 2 to 10 where the ideal Gaussian distribution is assigned beam quality factor of 1. Despite the existence of wide varieties of laser sources in LIBS experiment, Nd:YAG solid state laser source with active Q-switching has enjoyed a wider utilization. Q-switching is an optical technique through which an intense and narrow laser pulses could be obtained. Implementation of Q-switching involves positioning of variable attenuator inside the optical resonator. This arrangement allows accumulation and increase in the stored energy in the active medium while depletion of upper energy level is prevented. Hence, intense and short pulse of light is released [40].

Similarly, high power pulsed fiber lasers has enjoyed a lot of applications in industries where LIBS plays a crucial role. Fiber laser is a class of standard solid state laser in which the usually used rod is replaced with optical fiber and results into longer interaction length and consequently improves the photon conversion efficiency. The structure of a typical dual-core fiber laser consists of un-doped outer core for pump light collection as well as guiding the light along the fiber while the generation of stimulated emission takes place in the inner doped core. Fiber laser are usually pumped by diode

lasers or other fiber lasers and both side and end mechanisms of pumping are used. The main difference the two mechanisms of pumping is that side pumping allows light to be coupled onto the outer core using fiber coupler while end pumping configuration directly fires light from pump laser into the end of fiber [41]. Similarly, mode-locking and Q-switching techniques are used in fiber laser for obtaining very narrow and short pulses. A very short pulse of like 50 femtosecond can be attained using mode-locking method while pulse duration obtained using Q-switch is in a range of nanosecond to microsecond. Decisively, the interest in fiber laser has increased significantly nowadays due to its uniqueness as compared to other available laser source which include excellent energy per pulse, compactness as well as beam quality factor which is very close to one.

1.1.2 Impact of laser source wavelength on laser mater interaction during LIBS experiment

The amount of energy that a laser photon is carrying (which is related to laser wavelength) has a significant influence on the plasma formation during LIBS experiment [42]. Of course, wavelength of the radiation causing excitement influences the two basic mechanisms (multi-photon absorption and collision-induced ionization) through which electrons are generated. Generally, multi-photon absorption dominates in electron generation when short wavelength laser causes excitement while collision-induced ionization takes preference in a case long wavelength laser source is used. Collision-induced ionization occurs when laser radiation electric field accelerates the free electrons present in the ablated materials which bring about interaction between the accelerated electrons and neutral atoms of the material and consequently leads to increase in electron energy. This phenomenon is called inverse-bremsstrahlung. Energy gained by electrons

causes further ionization of atoms and leads to exponential growth of electron density [43]. Other mechanism of electron generation, that is, multi-photon absorption occurs when an atom of molecule absorbs a certain number photons simultaneously and leads to atomic ionization. The density of electrons due to this ionization increases linearly with time. Hence, this mechanism has insignificant contribution to electron growth. However, multi-photon absorption at least, generates initial electrons before further ionization by other mechanism. As previously mentioned that laser wavelength has serious effect on the energy coupling between the laser and the material to be ablated, different research studies have attributed high ablation efficiency, lower background emission (continuum) and higher reproducibility to UV lasers. Particularly, reflectivity coefficient (R) of metallic surfaces reduces from 0.976 to 0.336 as the wavelength of laser decreases from 1064nm to 266nm. Since the impinging energy (1-R) is a fraction of reflectivity coefficient, UV laser has demonstrated a high impinging energy using metallic surfaces as the target [44]. High spatial resolution characterizes LIBS measurement where UV lasers are used since focusing the laser down to a lower spot diameter is not an issue on a sample surface. The influence of laser pulse duration on plasma formation cannot be left out. The full width at half maximum of pulse profile measures the pulse duration and determines the observed spectroscopic quantities. During laser-mater interaction, the initial impingement of laser beam on sample causes evaporation of part of target material while subsequent impingement leads to heat and ionization which ultimately enhances plasma formation. For picosecond laser source, thermal diffusion causes pulse energy lost more significantly as compared to nanosecond laser source and additionally, lower matter to radiation interaction time and higher delivered irradiation are observed in

picosecond laser as compared to nano-second pulsed laser. Decrease in plasma shielding effect as well as the duration of pulse laser contributes to high ablation rate often observed. In a case of femtosecond exciting laser, multi-photon ionization dominates plasma formation processes since pulse duration small compared to matter thermal coupling time constant. In summary, femtosecond coherent laser sources have higher irradiance than nanosecond laser sources because energy is delivered to the matter in a very short period of time [45]. Therefore, femtosecond lasers have higher efficiency, lower plasma temperature and precise removal of material.

2 CHAPTER 2

LITERATURE REVIEW

This section reviews the summary of the methods adopted so far for quantitative analysis of LIBS spectra. It presents the problems that affect the accuracy of quantitative analysis in LIBS measurements and the approaches employed in the literature to improve the accuracy of quantitative analysis. Furthermore, the backgrounds of hybrid chemometrics proposed in this research work are introduced. The proposed methods of enhancing the accuracy of the proposed chemometrics are also presented.

2.1 General introduction to the challenges of quantitative analysis of LIBS spectra, existing solutions and their limitations

Laser induced breakdown spectroscopy (LIBS) is an atomic spectroscopic technique in which a highly focused laser, fired at a sample creates plasma plume consisting of excited ions and atoms. Cooling down of atoms in the plume (a process called plasma cooling) results into emission of characteristic wavelength of light (which are the fingerprints of the elemental constituents of the sample) that is collected and dispersed using spectrometer. The characteristic emission spectrum of each of the elements present in the sample and the intensity of the characteristic peaks is directly proportional to the number of emitting atoms of the respective elements. Thus, elemental identification and quantification of samples can be conducted using LIBS technique. Quantitative analysis of its spectra has been a major challenge due to self-absorption of the emitted radiation during plasma cooling and inadequate description of non-linear complex interactions

taking place in the laser induced plasma. Matrix effect also remains a significant problem to elemental quantification of LIBS spectra. Matrix effect strongly reduces the accuracy of the quantitative analysis of LIBS spectra. It measures the influence of emission line intensities of other elements present in the sample on the element of interest. Samples of different matrix result into different electron plasma density consequent upon different laser plasma interaction. As a result, different ionization levels and excitation of plasma species are achieved [46]. Conventional calibration curves often suffer from matrix effect problem [47]. Among the reasons for the occurrence of matrix effect in LIBS measurement include spectral matrix, different chemical composition as well as physical feature difference. Spectral matrix effect happens when there is interference between the strong lines of matrix element and analyte element. This kind of matrix effect can be circumvented or overcome by either peak fitting or careful peak selection. The most challenging matrix effects correction are the one due to difference in physical properties of the samples or as a result of difference in chemical composition. Matrix effect is described as physical matrix effect if the physical properties of samples change the ablation parameters during LIBS measurement and ultimately alter the emission intensities of element of interest present in two or more samples of the same composition. When difference in chemical compositions of two or more samples result into different emission line intensities of element of interest of the same concentration in these samples, the matrix effect in this case is called chemical matrix effect [48]. Physical properties include thermal conductivity, heat of vaporization, water content and absorption coefficient. This constitutes a significant problem since it impedes the transport of ablated mass into plasma. Although calibration curves can be easily applied to matrix

matched samples, practical limitations for in-situ applications where unknown samples of complex matrices are to be measured using LIBS, is still a big challenge [49]. Each sample needs its own calibration and it is extremely difficult to achieve a universal calibration curve [50]. In fact merely doping samples of similar matrix with different elements result into chemical matrix effect that might not be accurately handled using calibration curve drawn from one sample [47], [51]. Finding matrix-matched standard for eliminating matrix effect problem for in –situ application in LIBS remains a challenge [46], [49], [52]. Multivariate chemometrics have been proposed as a viable means of circumventing self-absorption and matrix effect and ultimately lead to accurate means of quantitative analysis of LIBS spectra.

Chemometrics tools that effectively handle non-linear features of spectra have recently gained wider applicability especially for quantitative analysis. Chemometric technique that have been extensively employed in spectroscopic analysis include multivariate calibration method, principal component analysis, parallel factor analysis, linear discriminate analysis and window factor analysis orthogonal projection analysis [18]. Recently, support vector regression has received special interest due to its unique features such as non-convergence to local minimal, generalization of error bounds and utilization of kernel trick [53] . Bilal Malik et.al quantified near-infrared spectra of a mixture (urea, triacetin and glucose) with the aid of support vector regression based chemometrics and reasonable accuracy was achieved [20]. Among other areas where support vector regression based chemometrics has been applied include the quantification of animal fat biodiesel in soybean biodiesel [54] , blood glucose [55], herbal medicine [21] and rock samples [5], [11]. Based on our knowledge, the hybrid technique has not

been applied for quantification of LIBS spectra. This work proposes hybrid advanced chemometrics for quantification of LIBS spectra for the first time. The mathematical formulations of the conventional CF-LIBS as well as the hybrid techniques to be developed and implemented in this work are described in subsequent sections of this chapter.

2.2 Fundamental principles of CF-LIBS for analysis of measured LIBS spectra

The hypothetical background of calibration free algorithm as proposed by A. Ciucci and his group rely heavily on the plasma conditions as well as the experimental method of operation [56] . Apart from the assumption that the composition of the plasma truly represents that of the material to be ablated prior to the ablation, the plasma should also be in a condition of local thermodynamic equilibrium. The optical thinness of the radiation source is also significant and should be maintained for successful execution of the algorithm. Generally, normal LIBS operating conditions uphold optically thin plasma condition for trace element while self-absorption correction needs to be incorporated in the calibration free algorithm to enhance minor element quantification. Consider an atomic species (s) (neutral or singly ionized species), the transition between two energy levels E_i and E_j which gives raise to the observed integral line intensity I_λ^{ij} (measured in photon/s cm^3) is defined by equation (2.1).

$$I_\lambda^{ij} = N_s A_{ij} \frac{g_i \exp\left(-E_i / K_B T\right)}{U_s(T)} \qquad (2.1)$$

Where :

λ = transition wavelength

g_i = degeneracy of the ith level

N_s = emitting atomic number density (particle/cm^3) for each species

A_{ij} = transition probability of the given line intensity

$U_s(T)$ = partition function of s species at plasma temperature T

K_B =Boltzmann constant

T = plasma temperature

In the actual experimental set-up, the efficiency of the collecting system is factored as a scaling parameter for the measured intensity. Equation (2.1) can be modified as presented in equation (2.2).

$$I_{\lambda}^{ij*} = FC_s A_{ij} \frac{g_i \exp\left(-E_i / K_B T\right)}{U_s(T)} \quad (2.2)$$

Where I_{λ}^{ij*}, F and C_s respectively represent the measured integral intensity, the experimental parameter (it accounts for plasma volume, density and the optical collection efficiency of the data acquisition system) and the emitting atomic species concentration. It should be noted that changing in experimental conditions such as laser energy focusing and so on can affect the parameter F and care should be taken while collecting signal for several shots of laser or while repeating the experiment.

For the algorithm implementation, the parameters g_i, A_{ij} and E_i are to be extracted from NIST data base while F T and C_s are to be obtained from the experimental data. From the logarithm of equation (22.), a straight line equation presented in equation (2.3) can be obtained.

$$y = mx + Q \quad (2.3)$$

Where $y = In\frac{I_{\lambda}^{ij*}}{A_{ij}g_i}$, $x = E_i$, $m = -\frac{1}{K_B T}$ and $Q_s = In\frac{C_s F}{U_s(T)}$

A two dimensional space that defined in equation (2.3) is called Boltzmann plane and each species in the plasma has a specific Boltzmann plane. Therefore, each LIBS line can be well represented in Boltzmann plane. The concentration of each of the species can be easily determined from the Boltzmann plot intercept after which the plasma temperature has been determined. In order to avert uncertainty in the measurement and further improve the accuracy of the algorithm, several lines can be used for determining the concentration of a particular species while experimental parameter F is factored in this case. Equation (2.4) and (2.5) respectively details how the experimental factor and the concentration of atomic species are determined.

$$\sum_s C_s = \frac{1}{F}\sum_s U_s(T)\exp(Q_s) \quad (2.4)$$

$$C_s = \frac{U_s(T)\exp(Q_s)}{F} \quad (2.5)$$

The total concentration of a given element in the plasma is presented in equation (6)

$$C_{tot}^{element} = C_I + C_{II} \quad (2.6)$$

Where C_I and C_{II} are the concentrations of singly ionized and neutral species, respectively.

Another method of determining the concentration of one species of a given element after the concentration of the second species is known is to use Saha-Boltzmann equation presented in equation (2.7). Also, the electron density (N_e) can be determined using the concentration of element with known species concentration.

$$\frac{N_e N_c(II)}{N_c(I)} = 6X10^{21} \frac{g_{II}}{g_I} \exp(\frac{-E_c(I)}{T}) \quad (2.7)$$

Where $N_c(II)$ and $N_c(I)$ represents the population of the ground state of the singly ionized and neutral species respectively while g_{II} and g_I respectively represent their degeneracy. The ionization potential of the singly ionized species in the ground state and the plasma temperature are respectively represented in the equation as $E_c(I)$ and T .

2.3 Methods of improving the accuracy of calibration free laser induced breakdown spectroscopy

The recently proposed calibration free laser induced breakdown spectroscopy aims at circumventing the challenges of quantitative analysis of LIBS spectra [56]. This approach is promising and has been applied to several samples [8], [16], [57]–[59]. However, the problem of self-absorption still remains an obstacle that makes the results of calibration free laser induced breakdown spectroscopy far from the certified values [13], [27]. In an effort to correct self-absorption in classical calibration free laser induced breakdown

spectroscopy, Bulajic et al developed a software package (LIPS++) which minimizes the effect of self-absorption by computing curve of growth for all the emission lines [60]. Similarly, Sun et al. proposed a method of self-absorption correction through accurate determination of plasma temperature [27]. The accuracy of this method was further improved using genetic algorithm [13]. Another method of accurate plasma temperature determination for ensuring precise quantitative analysis in LIBS is an inverse method proposed lately where set of equations in the classical calibration free algorithm are reversed [61]. Furthermore, the work of Pershin et al attributes the disproportionality between the spectral line intensities and the element stoichiometry for selective evaporation of elemental components which occur during heating-melting-evaporation stage of ablation and thereby developed a model which accounts for Prokhorov–Bunkin melt transparency wave [62]. On the other hand, De Giacomo et al [63] extended the classical calibration free algorithm to a wide range of experimental conditions by relaxing the condition of local thermodynamic equilibrium in the algorithm and assumed neutral species to be of significant abundance as compared to other species. The internal normalization of the computed species densities was achieved using a black-body model of the plasma continuum spectrum. Aguilera et al [64] presents a calibration free approach in which Saha-Boltzmann plot was used for elemental relative number densities determination in addition to plasma temperature estimation from the plot. The density of ionic species was calculated using Saha equilibrium equation while the intercept of Saha-Boltzmann plot was adopted in the calculation of neutral species densities. This method improves the accuracy of the classical calibration free algorithm since a regression of larger number of spectral data was used for intercept evaluation. Also, the result of the

classical calibration free algorithm was corrected by Burakov et al [65] using known concentration of one of the components. The accuracy of CF-LIBS technique still remains a challenge. A comprehensive review on calibration free methods in LIBS has been presented in the work of Tognoni et al [8].

2.4 General introduction to multivariate chemometrics tools

The Multivariate regression constructs calibration model using spectra and compositional information to establish a correlation between the spectral intensity and the elemental composition. Practical implementation of multivariate regression involves utilization of spectra datasets of samples of known concentration for building the training dataset base. The determination of the concentration of unknown samples can be carried out using the acquired pattern in the developed model during the training phase. Multivariate calibration methods assume that both physical and chemical matrix effects are expressed in the intensities of the spectra and construct a statistical model that takes all these into account. While fulfillment of plasma conditions is the backbone of the conventional CF-LIBS, multivariate regression models can construct calibration models without prior assumption of plasma conditions [47]. Guang yang et. al applied forest regression (FR) for determining the basicity of sintered ore in 2017. The emission characteristic lines of the major components of the ore obtained from LIB measurement are used for building the model while the model parameters such as the number of decision trees as well as the number of random variables are optimized using out-of-bag error estimation method [66]. The authors further compared the results of their model with that of partial least square regression chemometric model and forest regression and a better performance was obtained in terms of model generalization and future prediction. The standard sintered ore

samples utilized in the experiment was supplied by Shyang Jingcheng Equipment Development and manufacturing Co., Ltd. Regression forest is a chemometric tool developed by prof.Leo in 2001 and is capable of both regression and classification task. Qi Shi et.al present support vector regression based LIBS method of quantitative and qualitative analysis of sedimentary rock samples and the concentration of five main elements were quantified [11]. Spectral lines obtained from LIBS measurement are used as descriptors to their model. The outcomes of their developed SVR based model are compared with that of partial least square method and SVR model demonstrated a superior performance. Both developmental and validation stages of their models were carried out using certified samples presented in table 1 of their paper. Classification and quantitative analysis of slag samples were presented by Tianlong Zhang et. al in 2015 using SVR based LIBS using characteristic emission lines of the elements as descriptors to the model [67]. A comparison between their SVR based chemometric and partial least square based chemometric was made and they showed that SVR based chemometrics performed better than its counterpart. The certified concentration used for building their models are presented in table 1 of their manuscript while the wavelengths of their descriptors are shown in table 2 of their published work[67] . Jiao Wei et. al presented wavelet neural network based LIBS for quantitative analysis of coal ash [68]. The inputs to their model are the spectra preprocessed using wavelet threshold de-noising and kalman filtering [68]. Similarly, their proposed model was developed using certified samples. Jianhong Yang et.al developed relevance vector machine regression based chemometric for quantitative analysis of 23 certified standard high alloy steel samples [69]. The training and testing of their developed models were carried out using the

intensities of the analytical lines obtained from LIBS measurement. The results of their proposed model demonstrated superior performance over the conventional partial least square regression. Narahara Chari et.al [70] incorporated support vector machines algorithm in LIBS toolbox for easy and precise quantification as well as classification of LIBS spectra. The robustness of their model was demonstrated by comparing the outcome of support vector machines chemometric with other conventional chemometrics using certified pharmaceutical samples [70]. Kernel based learning machine was introduced recently for quantitative analysis of sulfur content in coal samples using LIBS [71]. Their model was developed and validated using standard certified samples with 5-fold cross validation. The performance of their model was compared with other chemometrics tools such as least square support vector regression, back propagation based neural network among others. Classification of blood samples for the purpose of lymphoma discrimination was presented by Xue Chen et al [72] using classification coupled LIBS [72]. Another classification based chemometric model was presented by Gibaek Kim et. al for discriminating pesticide-contaminated samples using LIBS [73]. Comparative study between the performance of support vector regression chemometrics and partial least square model are presented in the work of Ye Tian et al using geological cutting samples. The intensities of the elemental constituents of the samples obtained after LIBS measurement were correlated and classified based on the developed models [74]. Leave out one cross validation approach was adopted for the model parameters optimization. Thomas F.B et al compares the performance of eight chemometrics for analysis of rock samples. The compared chemometrics include principal component regression , least absolute shrinkage and selection operator, linear support vector

regression, kernel principal component regression , polynomial kernel support vector regression , elastic net, partial least square and k-nearest neighbor regression [75]. The training and testing stages of each of the model were carried out using the emission line spectra obtained after LIBS measurement. Xiongwei et al [76] improves the measurement accuracy of carbon content of coal using dominant factor based partial least square method coupled with LIBS system. Twenty-four bituminous samples were used for the modeling and simulations. The performance of their developed models was characterized using correlation coefficient, root mean square error and average relative error [76]. M. Darby Dyar et. al compares the prediction capacity as well as accuracy of models developed using the entire spectra information and those based on specific spectra region containing element of interest using univariate and multivariate coupled LIBS [77]. Their study was implemented on 1356 spectra coined from 452 geologically-diverse samples which represent the largest LIBS rock spectra ever assembled. Other applications [78] of chemometrics to certified samples are detailed in [79]–[84].

2.5 Description of the hybrid chemometrics tools proposed in this work

The hybrid chemometrics proposed in this work include hybridization of support vector regression with gravitational search algorithm (SVR-GSA), hybridization of extreme learning machine with gravitational search algorithm (ELM-GSA) and hybridization of sensitivity based linear learning method with gravitational search algorithm (SBLLM-GSA). Performance enhancing methods proposed include homogenous hybridization of support vector regression (HSVR), homogenous hybridization of extreme learning machine (HELM), hybrid fusion of support vector regression and extreme learning

machine (SVR-ELM and Elm-SVR) and internal reference preprocessing method (IRP). The backgrounds of each of these methods are presented in this section.

2.5.1 Background of support vector regression multivariate chemometric

Support vector regression is a chemometric based technique that relates input descriptors to output data through pattern acquisitions. It generates a function $f(x)$ that gives outputs with maximum deviations of epsilon (ε) for all training dataset $(x_1, y_1), ...(x_s, y_s) \subset Px\,\mathbb{R}$ where P stands for input pattern space. Effectiveness of SVR algorithm is due to its unique ability for mapping input descriptors to a feature space of high dimensionality using suitable kernel function. The entire SVR algorithm can be divided into two while dealing with non-linear problems. The first stage is the preprocessing stage while all training input data is mapped $K : x \to \Gamma$ to feature space using kernel mapping function. The second stage involves the development of linear regression at the feature space. The linear regression in the high dimensional space is described by equation (2.8).

$$f(x) = \langle \omega, x \rangle + b, w \in P, b \in \mathbb{R} \quad (2.8)$$

where $\langle .,. \rangle$ represents the dot product in the input pattern space P

The algorithm determines ω and b so that the maximum tolerable deviation of the estimated target from the experimental values does not exceed ε . In determining ω, among the objectives of SVR algorithm is to ensure that the vector ω is as small as possible. In other word, a flat function is desired. Flat function requirement enhances the

estimates to be less sensitive to fluctuations or perturbations in the descriptors. Hence, SVR based model would be less sensitive to experimental error or error due to descriptors measurement. Euclidean norm $\|w\|^2$ minimization remains the key to flatness requirement and problem is transformed to convex optimization problem as depicted in equation (2.9)

$$\begin{aligned} &\text{minimize} \quad \frac{\|w\|^2}{2} \\ &\text{subject to} \begin{cases} f_s - \langle w, x_s \rangle - b \le \varepsilon \\ \langle w, x_s \rangle + b - f_s \le \varepsilon \end{cases} \end{aligned} \tag{2.9}$$

Equation (9) indicates the existence of a function f_s that relates descriptors with targets in such a way that the error emanated from the approximation does not exceed the threshold. Concisely, convex optimization problem is said to be feasible. However, some real life problems may impose infeasibility to the optimization problem and equation (9) does not hold. In order to extend the versatility and robustness of equation (9), non-zero variables called slack variables are introduced into the problem and the convex optimization problem is written as presented in equation(2.10).

$$\begin{aligned} &\text{minimize} \quad \frac{\|w\|^2}{2} + C\sum_{s=1}^{S}\left(\xi_s + \xi_s^*\right) \\ &\text{subject to} \begin{cases} f_s - \langle w, x_s \rangle - b \le \varepsilon + \xi_s \\ \langle w, x_s \rangle + b - f_s \le \varepsilon + \xi_s^* \\ \xi_s, \xi_s^* \ge 0 \end{cases} \end{aligned} \tag{2.10}$$

Where C represents a penalty factor

The penalty factor (also called regularization factor) trades-off the minimization of the Euclidean norm and maximum allowable deviation of the estimates from the targets. The

solution to the optimization problem presented in equation (2.10) could be easily obtained using Standard dual formalism. This formalism also enhances SVR algorithm to effectively solve non-linear functions using kernel trick. Dual set of variables are introduced in order to develop a Lagrange function using the objective function and the constraints. It should be noted that in SVR algorithm, the flatness and loss function are combined as a single objective. The formulated Lagrange function L is presented in equation (2.11) while the positivity constraint that must be satisfied by the function is shown in equation (2.12).

$$L = \frac{\|w\|^2}{2} + C\sum_{s=1}^{S}\left(\xi_s + \xi_s^*\right) - \sum_{s=1}^{S}\left(\alpha_s\xi_s + \alpha_s^*\xi_s^*\right) - \sum_{s=1}^{S}\eta_s\left(\varepsilon + \xi_s + \langle w, x_s\rangle + b - f_s\right) - \sum_{s=1}^{S}\eta_s^*\left(\varepsilon + \xi_s^* - \langle w, x_s\rangle - b + f_s\right) \quad (2.11)$$

$$\alpha_s^*, \eta_s^* \geq 0 \quad (2.12)$$

Where $\alpha_s, \alpha_s^*, \eta_s$ and η_s^* are Lagrange multipliers

The Lagrange function has a saddle point with respect to dual variables and the objective function at solution. The condition of the saddle point requires that the derivatives of the Lagrange function with respect to the variables $\left(w, b, \xi_s^* \text{ and } \xi_s\right)$ contained objective function have to be zero. The derivatives go thus:

$$\frac{\partial L}{\partial w} = w - \sum_{s=1}^{S}\left(\eta_s - \eta_s^*\right)x_s = 0 \quad (2.13)$$

$$\frac{\partial L}{\partial b} = \sum_{s=1}^{S}\left(\eta_s^* - \eta_s\right) = 0 \quad (2.14)$$

$$\frac{\partial L}{\partial \xi_s^*} = C - \eta_s^* - \alpha_s^* = 0 = \frac{\partial L}{\partial \xi_s} \quad (2.15)$$

By substituting equations (2.13), (2.14) and (2.15) in equation (2.11), dual optimization problem to be maximized is obtained as presented in equation (2.16).

$$L = -\frac{1}{2}\sum_{s,r=1}^{S}\left(\eta_s - \eta_s^*\right)\left(\eta_r - \eta_r^*\right)\langle x_s, x_r\rangle - \varepsilon\sum_{s=1}^{S}\left(\eta_s + \eta_s^*\right) + \sum_{s=1}^{S} f_s\left(\eta_s - \eta_s^*\right)$$
$$\textit{subjected to } \sum_{s=1}^{S}\left(\eta_s - \eta_s^*\right) = 0 \text{ and } \eta_s, \eta_s^* \in [0, C] \quad (2.16)$$

Substituting w obtained from equation (2.16) into equation (2.9) gives equation (2.17).

$$f(x) = \sum_{s=1}^{S}\left(\eta_s - \eta_s^*\right)\langle x_s, x\rangle + b \quad (2.17)$$

The biasing parameter b is obtained through Karush-Kuhn-Tucker theorem which states that the product of the constraints and the dual variables becomes zero at the point of the solution. Computation of biasing parameter b has been extensively treated elsewhere [85]–[87]

2.5.2 Brief description of extreme learning machine based chemometrics

Extreme learning machine (ELM) is a multivariate chemometric technique that is based on pattern acquisition and effectively relates input descriptors to the output layer [23], [88]. Consider a single-hidden layer feed-forward neural network which is to be trained with Z number of hidden neurons and $f(x)$ activation function using k number of

test samples $(\mathbf{x}_k, \mathbf{t}_k)$ in which $\mathbf{x}_k = [x_{k\,1}, ..., x_{k\,z}]^T \in \mathbf{R}^z$ and $t_k = [t_{k\,1}, ..., t_{k\,n}]^T \in \mathbf{R}^n$ (where n and z are the number of data-points for input and output layer, respectively) . ELM transforms non-linear system to a linear one using the transformation equation presented in equation (18).

$$\mathbf{H\beta} = \mathbf{T} \quad (2.18)$$

where $\mathbf{H} = \{h_{kl}\}(k = 1, ..., i \text{ and } l = 1, ..., Z)$

$h_{kl} = f(\mathbf{w}_l.\mathbf{x}_k + b_l)$, that is, lth hidden neuron output with respect to $\mathbf{x}_k$

$\mathbf{w}_l = [w_{j\,1}, ..., w_{j\,z}]^T$ =weight vector, it links lth hidden neuron to input neurons

b_l =bias of the lth hidden neuron

$\boldsymbol{\beta} = [\beta_1, ..., \beta_Z]^T$, output weight matrix

$\boldsymbol{\beta}_l = [\beta_{l1}, ..., \beta_{j\,n}]^T (l = 1, ..., Z)$, weight vector linking lth hidden neuron to the output neurons

$\mathbf{T} = [t_1, ..., t_Z]^T$, matrix containing elemental concentration of test samples

After the linearization of the system as described by equation (2.18), the elemental concentrations of standard bronze samples constituents are obtained through least-square with minimum norm given by equation (2.19).

$$\hat{\boldsymbol{\beta}} = \mathbf{H}^{\dagger}\mathbf{T} \quad (2.19)$$

where $\mathbf{H}^{\dagger}$ = Moore-Penrose generalized inverse of matrix $\mathbf{H}$

The proposed homogeneously hybridized extreme learning machine (HELM) based chemometric goes a further step beyond ordinary ELM. HELM further linearizes the function obtained from ordinary ELM and thereby results into more accurate model. In the implementation of HELM based chemometric, the input descriptors (in this case, they are emission line intensity of the desired element whose concentration is to be determined, its transition probability, degeneracy, upper level transition energy and transition wavelength of the emission line) are mapped to the output (elemental concentration of ablated test samples) through a function which is approximated using equation (18). The output of ordinary ELM is fed into another ELM algorithm which subsequently approximates the function until linear function with high degree of correlation coefficient is obtained. This kind of homogenous hybridization was first proposed and implemented using support vector regression based chemometric for fatty acid melting points estimation and enhanced performance was obtained [89]. This work extends it to extreme learning machine.

2.5.3 Sensitivity based linear learning method chemometrics

In one- layer neural network of N number of neurons, equation (20) relates the input descriptors to the desired target.

$$y_{nm} = f_n\left(\sum_{r=0}^{R} w_{nr} x_{rm}\right) \qquad n = 1,2.....N\ , m = 1,2,.....M \tag{2.20}$$

Where r = number of input descriptors

m = number of data-point

f_n = Activation function (non-linear)

The estimates obtained using equation (20) can be easily compared with the experimental value of the target through computation of some weights w_{nr} that link the descriptors with the target. Therefore, the sum of the squared error (E) is minimized using equation (21) as described in [90], [91].

$$E = \sum_{m=1}^{M}\sum_{n=1}^{N}\left(y_{nm} - f_n\left(\sum_{r=0}^{R} w_{nr} x_{rm}\right)\right)^2 \quad (2.21)$$

Another approach of determining the cost function C_f especially when invertible non-linear activation functions are involved is presented in equation (2.22)

$$C_f = \sum_{m=1}^{M}\sum_{n=1}^{N}\left(\sum_{r=0}^{R} w_{nr} x_{rm} - f_n^{-1}(y_{nm})\right)^2 \quad (2.22)$$

Equation (22) is minimized as presented in equations (2.23) and (2.24)

$$\frac{\partial C_f}{\partial w_{nk}} = 2\sum_{m=1}^{M}\left(\sum_{r=0}^{R} w_{nr} x_{rm} - f_n^{-1}(y_{nm})\right) x_{km} = 0, k = 1, 2.....R, \forall m \quad (2.23)$$

$$\sum_{m=1}^{M} f_n^{-1}(y_{nm}) x_{km} = \sum_{r=0}^{R} w_{nr} \sum_{m=1}^{M} x_{rm} x_{km}, k = 1, 2.....R, \forall m \quad (2.24)$$

Sensitivities of C_f with respect input descriptors and output data are computed using equations (25) and (26).

$$\frac{\partial C_f}{\partial y_{kq}} = -\frac{2\left(\sum_{r=0}^{R} w_{rk} x_{rq} - f_k^{-1}(y_{kq})\right)}{f_k^{'}(y_{kq})}, \forall q, k \quad (2.25)$$

$$\frac{\partial C_f}{\partial x_{kq}} = 2\sum_{m=1}^{M}\left(\sum_{r=0}^{R} w_{mr} x_{rq} - f_m^{-1}(y_{mq})\right) w_{mk}, \forall p, q \quad (2.26)$$

The obtained sensitivities relations presented in equations (2.25) and (2.26) can be extended to two-layer feedforward neural network of r number input, n number of output and q number of hidden unit. The cost functions of layer one and layer two are represented by $C_f^1(T)$ and $C_f^2(T)$ respectively where T represent the outputs of the intermediate layer which are assumed to be known.

$$C_f(T) = C_f^1(T) + C_f^2(T) \quad (2.27)$$

The cost function for the two-layer network is obtained in a similar manner as that presented in equation (22). Equation (28) presents the new cost function.

$$C_f(T) = \sum_{m=1}^{M}\left(\sum_{q=1}^{Q}\left(\sum_{r=0}^{R} w_{qr}^{(1)} x_{rm} - f_q^{(1)^{-1}}(T_{qm})\right)^2 + \sum_{n=1}^{N}\left(\sum_{q=0}^{Q} w_{nq}^{(1)} x_{qm} - f_n^{(2)^{-1}}(y_{nq})\right)^2\right) \quad (2.28)$$

Solutions obtained from equations (2.23) and (2.24) would be of immense significance while computing weights of the first ($w_{qr}^{(1)}$) and second layer ($w_{nq}^{(2)}$). Rate of change of the cost function with respect to T_{qm} (sensitivities) is determined using equations (2.29) and (30)

$$\frac{\partial C_f}{\partial T_{qm}} = \frac{\partial C_f^1}{\partial T_{qm}} + \frac{\partial C_f^2}{\partial T_{qm}} \quad (2.29)$$

$$\frac{\partial C_f}{\partial T_{qm}} = -\frac{2\left(\sum_{r=0}^{R} w_{qr}^{(1)} x_{rm} - f_q^{(q)^{-1}}(T_{qm})\right)}{f_q^{'(q)}} + 2\sum_{n=1}^{N}\left(\sum_{q=0}^{Q} w_{nq}^{(2)} x_{qn} - f_n^{(2)^{-1}}(y_{nq})\right) w_{nq}^{(2)} \quad (2.30)$$

where $T_{0m} = 1, \forall \mathrm{m}$

The Taylor expansion of presented in equation (2.31) results into an increment depicted by equation (2.21) where λ represents the relaxation factor.

$$\mathrm{C}_f(\mathrm{T}+\Delta T) = \mathrm{C}_f(\mathrm{T}) + \sum_{q=1}^{Q}\sum_{m=1}^{M}\frac{\partial C_f(T)}{\partial T_{qm}}\Delta T_{qm} \approx 0 \quad (2.31)$$

$$\Delta T = -\lambda \frac{C_f(T)}{\left\|\nabla C_f\right\|^2}\nabla C_f \quad (2.32)$$

Procedures for SBLLM implementation are summarized as follow

Step 1: Training data partitioning and threshold error specification: the dataset is divided into input descriptors and the output target. The thresholds for the expected error is specified as ξ and ξ^* while the value of the relaxation factor λ that measures the step size is also specified. This means that there are four inputs for model training which include the descriptors, corresponding desired target, threshold errors for controlling the convergence and the relaxation factor while the outputs remain the weights of each of the two layer as well as the sensitivities of the sum of the squared error with respect to input and output data sample.

Step 2: *Initialization.* Outputs are assigned to the intermediate layer using some random weight $w^{(1)}(0)$ and error ξ_{qm} (which is generated randomly). The assigned intermediate output is defined by equation (2.33).

$$T_{qm} = f_q^{(1)}\left(\sum_{r=0}^{R} w_{qr}^{(1)}(0)x_{rm}\right) + \xi_{qm} \quad (2.33)$$

Other parameters to be initialized include:

$C_f^{previous}$ = previous cost function (a large value is assumes initially)

$\delta_{previous}$ = Previous mean sum of square error (a large value is assumes initially as well).

δ measures the means of the sum of square error between the estimated output and the desired values.

Step 3: *weights and sensitivities computation.* Systems of equation are solved while the weights $\left(w^{(1)} \text{ and } w^{(2)}\right)$ and the associated sensitivities are obtained. Equation (34) governs the computation.

$$\sum_{m=1}^{M} f_n^{-1}(y_{nm})x_{km} = \sum_{r=0}^{R} w_{nr} \sum_{m=1}^{M} x_{rm}x_{km}, k = 1,2.....R, \forall m \quad (2.34)$$

Step 4: *Evaluation of δ. Means sum of square error (δ)* is evaluated using equation (2.35).

$$C_f(T) = \sum_{m=1}^{M}\left(\sum_{q=1}^{Q}\left(\sum_{r=0}^{R} w_{qr}^{(1)}x_{rm} - f_q^{(1)^{-1}}(T_{qm})\right)^2 + \sum_{n=1}^{N}\left(\sum_{q=0}^{Q} w_{nq}^{(1)}x_{qm} - f_n^{(2)^{-1}}(y_{nq})\right)^2\right) \quad (2.35)$$

Step 5: *Convergence verification:*

$$\begin{cases} \left|C_f - C_f^{previous}\right| < \xi \text{ or} \left|\delta - \delta_{previous}\right| < \xi^* \text{ stop, return weights and sensitivities} \\ \text{Otherwise, proceed to the next step} \end{cases}$$

Step 6: Test for the improvement.

$$\begin{cases} C_f > C_f^{previous}, \text{ set } \lambda = \frac{\lambda}{2}, T = T_{previous}, C_f = C_f^{previous} \text{ and proceed to the next step} \\ \text{Otherwise, set } C_f^{previous} = C_f, T_{previous} = T, \delta = \delta_{previous} \text{ and obtain the sensitivities using equ.(30)} \end{cases}$$

Step 7: *Intermediate output update.* The intermediate output is update using equation (2.35) and return to **step 3.**

$$p = p - \alpha \frac{Q(p)}{\|\nabla Q\|^2} \nabla Q$$

Step VI: *Intermediate output update.* Update the intermediate output using

$T = T - \lambda \frac{C_f(T)}{\|\nabla C_f\|^2} \nabla C_f$ and return to **Step II.**

2.5.4 Physical description of gravitational search algorithm for hyper-parameters selection

Gravitational search algorithm (GSA) is a recently developed heuristic population based optimization technique that is principally governed by the Newtonian mechanics [26]. Its exploration and exploitation mechanisms are premised on the Newtonian gravitational attractive force between two objects in the same vicinity and Newton second law of motion. Virtually all the physical parameters that are employed in describing the motion

of objects under the influence of gravitational force are carried over to GSA terminologies except that the objects in Newtonian description are replaced by the term agents. The algorithm measures the performance of each of the agent using their masses and it is a known fact from gravitational influence that heavier masses move slowly as compared with lighter once. Therefore, the heaviest agent corresponds to the desired solution. Four parameters are used to characterize each of the agents involved in GSA [92]. The parameters include the inertial mass, position, active and passive gravitational mass. The solution of the optimization problems corresponds to the position of the agent whereas the inertial and gravitational masses are determined through a predefined fitness function and the algorithm is navigated by adjusting the inertial and gravitational masses after iteration [93]–[98]. In this implementation, number of hidden neurons is encoded in each agent of the population. The masses are updated subsequently until convergence is reached. The sequential steps involved in GSA implementation are summarized below.

Step I: *Initialization:* Consider a search space of $s-$ dimension and randomly initialized with N_p number of initial population of agents. The position of *pth* agent in *dth* dimension is represented in equation 2.36) by x_p^d .

$$X_p = \left(x_p^1, ...x_p^d, ..., x_p^s\right), p = 1, 2, ...N_p \quad (2.36)$$

Step II: *Fitness and inertial mass computation*: With the aid of the predefined fitness function(RMSE between the estimated elemental concentration and the certified values) coupled with initialized position of the agents in **step I**, the fitness of each of the agent is evaluated and the agents with best and worst fitness at *jth* iteration are identified as

$fitbest(j)$ and $fitworst(j)$ respectively. The inertial mass $M_p(j)$ of pth agent which measures its reluctance to change in the state of motion due to gravitational pull is computed using equation (2.37) and (2.38).

$$M_p(j) = \frac{m_p(j)}{\sum_{p=1}^{N_p} m_p(j)} \tag{2.37}$$

$$m_p(j) = \frac{fitn_p(j) - fitworst(j)}{fitbest(j) - fitworst(j)} \tag{2.38}$$

where $fitn_p(j)$ represents the fitness of pth agent

Step III: *Computation of the acceleration of the agents:* The acceleration at which each of the agents in the search space is computed using equations (2.39-2.44). The computations go thus:

$$G = G_0 \exp\left(-\alpha(j/t)\right) \tag{2.39}$$

$$r_{pq}(j) = \left\| X_p(j), X_q(j) \right\|_2 \tag{2.40}$$

$$F_{pq}^d(j) = G(j)\frac{M_p(j)M_q(j)}{r_{pq}(j)+\tau}\left(x_p^d(j) - x_q^d(j)\right) \tag{2.41}$$

$$F_p^d(j) = \sum_{q \in kbest, p \neq q}^{N_p} rand_p F_{pq}^d(j) \tag{2.42}$$

$$a_p^d(j) = \frac{F_p^d(j)}{M_p(j)} \quad (2.43)$$

Where $r_{pq}(j)$ =Euclidian distance between p and q agent

$M_p(j)$ =active gravitational mass of *pth* agent

τ =small constant value

$G(j)$ =gravitational constant

t =maximum number of iteration

$rand_p$ = random number spanning in $[0,1]$ range

Step IV: *Velocity and position of the agents.* Velocity $v_p^d(j)$ and position $x_p^d(j)$ of each of the agent are determined using equation (11) and (12) respectively.

$$v_p^d(j+1) = rand_p x \; v_p^d(j) + a_p^d(j) \quad (2.44)$$

$$x_p^d(j+1) = x_p^d(j) + v_p^d(j+1) \quad (2.45)$$

Step V: Repeat steps II to step IV until stopping criteria (that is, maximum iteration) is reached.

2.5.5 Homogeneously hybridized support vector regression chemometrics

Support vector regression (SVR) is a computational intelligence based chemometric that relates the spectral features with the concentrations through pattern acquisitions. It generates a function $f(x)$ that estimates the elemental concentration of the ablated samples with maximum deviations of epsilon (ε) for all training dataset $(x_1, y_1), ...(x_s, y_s) \subset Px\mathbb{R}$ in which P and $\mathbb{R}$ stand for input pattern space and real number, respectively while x_s and y_s respectively represent the descriptors and target for s number of data-points . Effectiveness of SVR algorithm is due to its unique ability for mapping input descriptors to a feature space of high dimensionality using suitable kernel option. The entire SVR algorithm can be divided into two stages while dealing with non-linear problems [99]. The first stage is the preprocessing stage where all training input data is mapped $K : x \to \Gamma$ to feature space using kernel mapping function. The second stage involves the development of linear regression in the feature space. The linear regression in the high dimensional space in it general form is described by equation (2.46).

$$f(x) = \langle \omega, x \rangle + b, w \in P, b \in \mathbb{R} \qquad (2.46)$$

where $\langle .,. \rangle$ represents the dot product in the input pattern space P and b is the biasing factor.

SVR has demonstrated good generalization and predictive performance for spectroscopic regression [20], [100]. However, the usual single kernel function contained in SVR

decision function is not capable of effectively mining the abundant information and patterns in the training dataset of LIBS spectral due to the complex nature of the laser induced plasma that governs LIBS quantitative analysis. Standard SVR performs poorly when used for complex non-linear spectroscopic regression containing both smooth and steep variations as standard SVR cannot simultaneously avoid the problem of both under-fitting and over-fitting [101], [102]. To improve the performance of SVR for LIBS quantitative analysis, this work proposes homogeneously hybridized support vector regression (HSVR) which combines two standard SVR algorithms in which the output of the first SVR algorithm serves as the input to the second SVR algorithm. The advantages of the proposed method include (i) the use of multiple kernel function which circumvents the inability of the standard SVR to simultaneously avoid both under-fitting and over-fitting and (ii) incorporation of multiple generalization of error bound which is achieved after multiple transformations of input data to high feature space until linear regression of high correlation coefficient is attained. Equation (2.47) and (2.48) respectively depicts the decision function for the first and second stage of the proposed hybrid model.

$$f(x) = y = \sum_{i=1}^{N} \left(\eta_i - \eta_i^*\right) \exp\left(-\frac{\left\|\overrightarrow{x_i} - \vec{x}\right\|}{\sigma}\right), 0 \le \eta_i^* < C, 0 \le \eta_i \le C \quad (2.47)$$

$$g(y) = \sum_{j=1}^{N} \left(\lambda_j - \lambda_j^*\right) (\overrightarrow{y_i} \cdot \overrightarrow{y_j} + 1)^d, 0 \le \lambda_j^* < C, 0 \le \lambda_j \le C \quad (2.48)$$

Where $\eta_i, \eta_i^*, \lambda_j$ and λ_j^* represent Langrage multipliers while σ, C and d respectively stands for Gaussian kernel option, regularization factor and polynomial kernel option.

2.5.6 Homogeneously hybridized extreme learning chemometrics

The proposed homogeneously hybridized extreme learning machine (HELM) based chemometric goes a further step beyond ordinary ELM. HELM further linearizes the function obtained from ordinary ELM and thereby results into more accurate model. In the implementation of HELM based chemometric, the input descriptors (in this case, they are emission line intensity of the desired element whose concentration is to be determined, its transition probability, degeneracy, upper level transition energy and transition wavelength of the emission line) are mapped to the output (elemental concentration of ablated test samples) through a function which is approximated using equation (1). The output of ordinary ELM is fed into another ELM algorithm which subsequently approximates the function until linear function with high degree of correlation coefficient is obtained. This kind of homogenous hybridization was first proposed and implemented using support vector regression based chemometric for fatty acid melting points estimation and enhanced performance was obtained [89]. This work extends it to extreme learning machine.

2.5.7 Hybrid fusion of support vector regression and extreme learning machine chemometrics

The significance of non-linear technique in chemometrics cannot be over-emphasized especially in LIBS where the chemical compositions of the materials are identified and quantified using mainly, emission line intensity [18]. The plasma generated due to laser ablation is often thick optically, which denotes complex interactions between the radiation and the constituent atoms/ions as well as the complexity due to further reabsorption of the emitted radiations. This complexity strengthens non-linearity in the

calibration function as the concentration progresses. Excluding this non-linearity and complexity of the plasma has profound effect on the quantitative analysis and the need for non-linear analytical modeling method becomes paramount for accuracy enhancement in LIBS spectra quantification. Extreme learning machine (ELM) is a non-linear chemometric method that is based on empirical risk minimization principle and has inherent characteristic of approximating many non-linear functions to linear ones [23]. ELM is a novel algorithm for training single hidden layer feedforward neural networks without iterative learning process. Its operating principle involves setting a number of nodes in the hidden layer prior to the training process and randomly assigns the input weights and hidden biases and determines the output weights analytically with the aid of Moore-Penrose generalized inverse matrix [24], [25], [88], [103], [104]. The input weights relate the input layer to the hidden layer while the output weights link the hidden layer to output layer. ELM uniquely generates optimal solution without iteration and translates to fast learning speed. Since the ELM obtains its optimal solution through computation of generalized inverse of the hidden output matrix, over-fitting sets in when the number of nodes in the hidden layer becomes large or high order hidden output matrix is obtained. Over-fitted ELM based model describes random error instead of the actual relationship governing the input and outputs. It interacts with minor fluctuation in the training data excessively and leads to poor performance of the model. Support vector regression (SVR) on the other hand, is a non-linear modeling tool that has attracted attention in chemometrics due to its characteristics which include generalization of error bound, high stability, convergence to global minimum and its sound mathematical foundation [20], [22], [54], [55], [101]. SVR algorithm does not fully capture the non-

linear interactions in laser induced plasma. However, it effectively handles over-fitting problem especially when its hyper-parameters are well tuned. Hyper-parameter tuning of the proposed hybrid models was carried out using a novel gravitational search algorithm (GSA) recently proposed [26]. Therefore, hybrid fusion of the two algorithms results into robust model with excellent generalization performance. The novelties of the proposed hybrid fusion include (i) incorporation of structural risk minimization principle into empirical risk minimization principle and vice versa for over-fitting correction (ii) multiple minimization of generalized error bound as the output of ELM flows into SVR (and vice versa) (iii) improved generalization and predictive performance.

2.5.8 Internal reference preprocessing method of enhancing the performance of chemometrics

The plasma generated due to laser ablation in LIBS is often optically thick and results into self-absorption since the plasma is spatially inhomogeneous and its evolution is temporal [8]. An optically thick plasma results into uneven plasma cooling in which one part of the plasma cools faster than the remaining part. Consequently, the photons emitted from the cooler part are reabsorbed by atoms of the same species in the hotter part of the plasma and ultimately leads to emission of reduced intensity. The emitted species with least transition probability (which is the probability per unit time of an atom in upper energy level making a transition to lower energy level) would have lowest possibility of being reabsorbed since the transition to the lowest energy state might be slower than the cooling time lag between different parts of the cooling plasma. Hence, normalization of the spectra intensity with the intensity that is rarely affected by self-absorption reduces the effect of self-absorption in the entire spectra [13], [27]. In order to apply this

principle to quantitative analysis of LIBS spectra, the emission line intensity with least transition probability is selected to normalize the remaining emission line intensities correspond to a particular element identified as the constituent of the test samples. This process was carried out for each of the elements present in each of the seven standard bronze samples used for the present modeling and simulation.

2.5.9 Broadening for plasma diagnosis

The electrons in the excited states in laser induced plasma frequently undergo relaxation which leads to the release (or emission) of radiation with a characteristic wavelength (or frequency) that signifies the presence of a particular element in the analyzed sample. Spectral lines characterized with finite widths are acquired and obtained after the atomic emission which may be attributed to different broadening mechanisms [105]. This leads to spectral distribution of photons around the central wavelength. Different line broadening mechanisms result into different line profiles while the significance of any broadening mechanism is measured by the full width at half maximum [106]. Although, the information regarding the wing of the lines does not necessarily contained in full width at half maximum. The significance of spectral line profile cannot be overemphasized in quantitative analysis of LIBS spectral as the attainment of local thermodynamic equilibrium can be inferred from the stark spectral line profile. Two basic mechanisms are responsible for the observed finite spectral width and these include emission of photons with a range of frequencies from an energy level (since energy levels are not totally sharp) and the frequency difference between the observed photons and the emitted photons (a phenomenon known as Doppler effect). Different broadening mechanisms observed in laser induced plasma and discussed in this research work

include natural broadening, Doppler (and thermal Doppler) broadening, pressure (or collisional) broadening and stark broadening.

2.5.10 Natural broadening

Supposing an excited state is of energy E above the ground state and electrons in an excited state stays for at the state for an average period of Δt before decaying to the ground state. The uncertainty principle relation between the uncertainty in the energy (ΔE) of a level and Δt can be written as presented in equation (2.49).

$$\Delta E \, \Delta t \approx \frac{h}{2\pi} \quad (2.49)$$

The width of the spectral line as obtained from equation (2.49) is presented in equation (2.50) using the relation $E = hf$, $\Delta E = h\Delta f$.

$$\Delta f \approx \frac{1}{2\pi \Delta t} \quad (2.50)$$

The broadening resulted from this phenomenon is called natural broadening

2.5.11 Doppler (and thermal Doppler) broadening

The concept of the Doppler broadening experienced by spectral lines obtained from LIBS measurement is derived from the usual Doppler effect which measures a wavelength shift whenever there is a relative motion between a source and an observer. Generally, a blue shift (decrease in wavelength) is attained when a source moves towards an observer while a red shift is recorded when a source moves away from an observer [106]. The intensity distribution of a Doppler broadened spectral line is usually Gaussian profile while the Maxwell's law governs the statistical distribution of velocities if the motion is in thermal

equilibrium. The full width at half maximum of a Doppler broadened spectral line can be derived as follows

The Doppler shift in frequency attributed to non-relativistic thermal velocities of particles is given by equation (2.51)

$$\nu = \nu_0 \left(1 + \frac{v}{c}\right) \quad (2.51)$$

ν, ν_0 c_0 and c respectively represent the observed frequency, the rest frequency, the velocity of the emitter towards the observer and the speed of light

Since the speed is distributed in both directions (towards and away from the observer) for a radiating body, the overall effect is the broadening of the observed spectral line. Assuming the fraction of particles with characteristic velocity component between c_0 and $c_0 + dc_0$ along a line of sight is $P_{c_0}(c_0)dc_0$, the frequency distribution correspond to this is given by equation (2.52)

$$P_\nu(\nu)d\nu = P_{c_0}(c_0^*)\frac{dc_0}{d\nu}d\nu \quad (2.52)$$

where $c_0^* = c\left(\frac{\nu}{\nu_0} - 1\right)$ represents the velocity towards the observer corresponds to the shift between ν_0 and ν. Therefore, equation (2.52) becomes

$$P_\nu(\nu)d\nu = \frac{c}{\nu_0}P_{c_0}\left(c\left(\frac{\nu}{\nu_0} - 1\right)\right)d\nu \quad (2.53)$$

The broadening can be expressed in term of wavelength using non-relativistic limit $\frac{\lambda-\lambda_0}{\lambda_0} \approx \frac{\nu-\nu_0}{\nu_0}$ as

$$P_\lambda(\lambda)d\lambda = \frac{c}{\lambda_0} P_{c_0}\left(c\left(1-\frac{\lambda}{\lambda_0}\right)\right)d\lambda \quad (2.54)$$

In case of thermal Doppler broadening, Maxwell distribution governs the distribution of the velocity. Therefore,

$$P_{c_0}(c_0)dc_0 = \sqrt{\frac{m}{2\pi kT}} \exp(\frac{-mc_0^{\,2}}{2kT})dc_0 \quad (2.55)$$

Where m , k and T respectively represent the mass of the emitting particle, Boltzmann constant and temperature. Equation (2.55) can be simplified further to equation (2.56)

$$P_\nu(\nu)d\nu = \frac{c}{\nu_0}\sqrt{\frac{m}{2\pi kT}} \exp(\frac{-m\left(c\left(\frac{\nu}{\nu_0}-1\right)\right)^2}{2kT})d\nu \quad (2.56)$$

This can be simplified as equation (2.57)

$$P_\nu(\nu)d\nu = \sqrt{\frac{mc^2}{2\pi k\nu_0^{\,2}T}} \exp(\frac{-mc^2(\nu-\nu_0)^2}{2k\nu_0^{\,2}T})d\nu \quad (2.57)$$

This is a Gaussian profile with standard deviation of $\sigma = \sqrt{\frac{kT}{mc^2}}\nu_0$ and full width at half maximum (FWHM) $\Delta\nu_{FWHM} = \sqrt{\frac{8kTIn2}{mc^2}}\nu_0$

2.5.12 Pressure (or collisional) broadening

The emission process that occurs during the relaxation process in laser induced plasma might be interrupted by colliding particles which leads to a broadening called impact pressure or collisional broadening [106]. The uncertainty in the emitted energy rises when the characteristic time is shortened in accordance to uncertainty principle. In a dense plasma, plasma constituents collide frequently and ultimately reduces the lifetime of states to a value below the one stipulated by the quantum mechanical lifetime. If the frequency of collision of plasma constituent is $f_{collision}$, the broadening due to this effect can be estimated as $f_{collision} \approx f_{broadening}$. Since frequency of collision rises with density, it is expected that high density plasma (that is, plasma of high electron number density) is largely affected by collisional broadening. In the case of laser plume at local thermodynamic equilibrium condition in which optically thin plasma is assumed, the effect of this broadening is inconsequential.

2.5.13 Stark broadening and electron density determination

Shapes of spectral lines are well established diagnostic measures for plasma characterization and in determining plasma electron number density [107], [108]. The shape of hydrogen spectral line was first implemented for plasma diagnostic applications [109]. However, the quest for further extension to non-hydrogenic line shapes became imperative since the possibility of hydrogen lines to be present in every plasma is not realistic, especially in the laser plume of laser induced breakdown spectroscopic technique which is aimed at enjoining wider applications to varieties of samples [107], [110]–[114]. As a result, large volumes of experimental and theoretical data have been

reposted in literature for non-hydrogenic line shapes. Generally, two sets of theoretical data in conjunction with experimental results are often used while determining the electron plasma density from the shape of non-hydrogenic line. Both set of theoretical data, presented by Griem et al. (henceforth referred as Griem) and Dimitrijevic Sahal-Brechot (henceforth referred as DSB) et al., are culled from semi-classical calculations [115], [116]. It worth mentioning that the results presented by both of the authors show differences as well as overlapping for the same plasma conditions. However, the observed differences can be traced to different approximations employed for data evaluation as well as the incorporation of improved set of energy level data by DSB which are not available during the period of Griem's calculation. Additionally, lack of ion broadening parameters corresponding to electron impact width reported by DSB further widens the differences between the two sets of theoretical stark broadening data for neutral atomic lines [108]. The impact approximation used for both perturbing ions and electrons results into a line shape having symmetric Lorentz profile which is correct when plasma is of low electron density. This approximation is invalid for high electron density plasma such as the laser plume in LIBS measurement with asymmetric line shape such as the one presented for Mg I line in [108]. The equation that depicts the broadening of emission line (expressed in full width at half maximum) due to stark effect as presented by Griem [116] and extensively used in the literature [112], [117]–[122] for laser induced plasma diagnosis is presented in equation (2.58)

$$\Delta\lambda = 2\omega\left(\frac{n_e}{10^{16}}\right) + 3.5A\left(\frac{n_e}{10^{16}}\right)^{1/4}\left[1 - BN_D^{-1/3}\right]\omega\left(\frac{n_e}{10^{16}}\right) \quad (2.58)$$

where ω, n_e, A, B and N_D respectively represent the electron impact parameter, electron density, ion broadening parameter, a constant(which can be 1.2 or 0.75 for ionic and neutral line respectively) and number of particles in Debye sphere

The first term of equation (2.58) is the contribution of electrons to broadening while the second term is the contribution due to ions. For typical LIBS condition, the ionic contribution of the equation (2.58) is negligible [112], [121], [122]. Thus, equation (2.58) is reduced to equation (2.59).

$$\Delta\lambda = 2\omega\left(\frac{n_e}{10^{16}}\right) \qquad (2.59)$$

Equation (2.59) is implemented for electron density calculation in this work since stark broadening is the only dominant broadening in typical laser induced plasma due to strong electric field generated by the electrons and ions in the plasma.

3 CHAPTER 3

EXPERIMENTAL SETUP AND COMPUTATIONAL DETAILS

3.1 Experimental set-up and computational methodology

This chapter presents the description of the experimental set-up as well as the adopted computational methodology in modeling the hybrid chemometrics implemented on the samples. The standard bronze samples employed in this research work were purchased from metal online store (see the appendix for the details of the standard bronze samples)[123]. The proposed hybrid chemometrics are initially developed using single, double and three emission lines of elemental compositions of the standard samples purposely to ascertain the optimum number of emission lines needed for determining the elemental concentrations. After that, methods to enhance the performance of the chemometrics are implemented. The proposed hybrid chemometrics are also developed for quantitative analysis of real life food samples which include four crayfish samples and two different brands of grape (black and green grapes). The results of the developed hybrid chemometrics for both crayfish samples and grape samples are validated using ICP-OES analytical method. Prior to LIBS measurement conducted on all the investigated samples, optimum operating conditions of the LIBS system was ensured purposely to achieve best limit of detection as well as minimum possible signal to noise

ratio. This section presents the implemented operating conditions of the LIBS system and methods adopted for samples preparation for both LIBS system and ICP system used for results validation. Details of each of the components of the LIBS system are also presented.

3.1.1 Experimental set-up of laser induced breakdown spectroscopy

Figure 3.1 presents the main components of LIBS system which consists of a pulsed laser of high energy focused on a test sample. The light energy results into sample vaporization and ultimately induces the plasma. The spectrometer diffracts the collected light using inbuilt diffraction grating as an optical system in the spectrometer that acquires and diffracts light into different beams travelling in different directions. Subsequently, intensified charged coupled device (ICCD) detects, amplifies and resolves the light into different specific wavelengths that is a direct signature of the sample constituents. Other photon detective devices such as photodiode array (PDA) and photomultiplier tube (PMT) serve similar purposes. The LIBS spectral acquired is transmitted to a computer system for adequate spectroscopic analysis. Definitely, improving spectral emission lines as well as acquiring high quality spectral involves adequate time control mechanisms of LIBS measurement so as to avoid some plasma stage that might deteriorate the spectral quality. The components of LIBS system that need adequate monitoring and optimization include Nd:YAG pulsed laser, light focusing system which include lens and mirror, optical fiber for transmitting the radiation, target holder to enhance proper focusing of pulsed laser on the desired target, spectrometer for spectral detection and diffraction as well as the computer system for data collection.

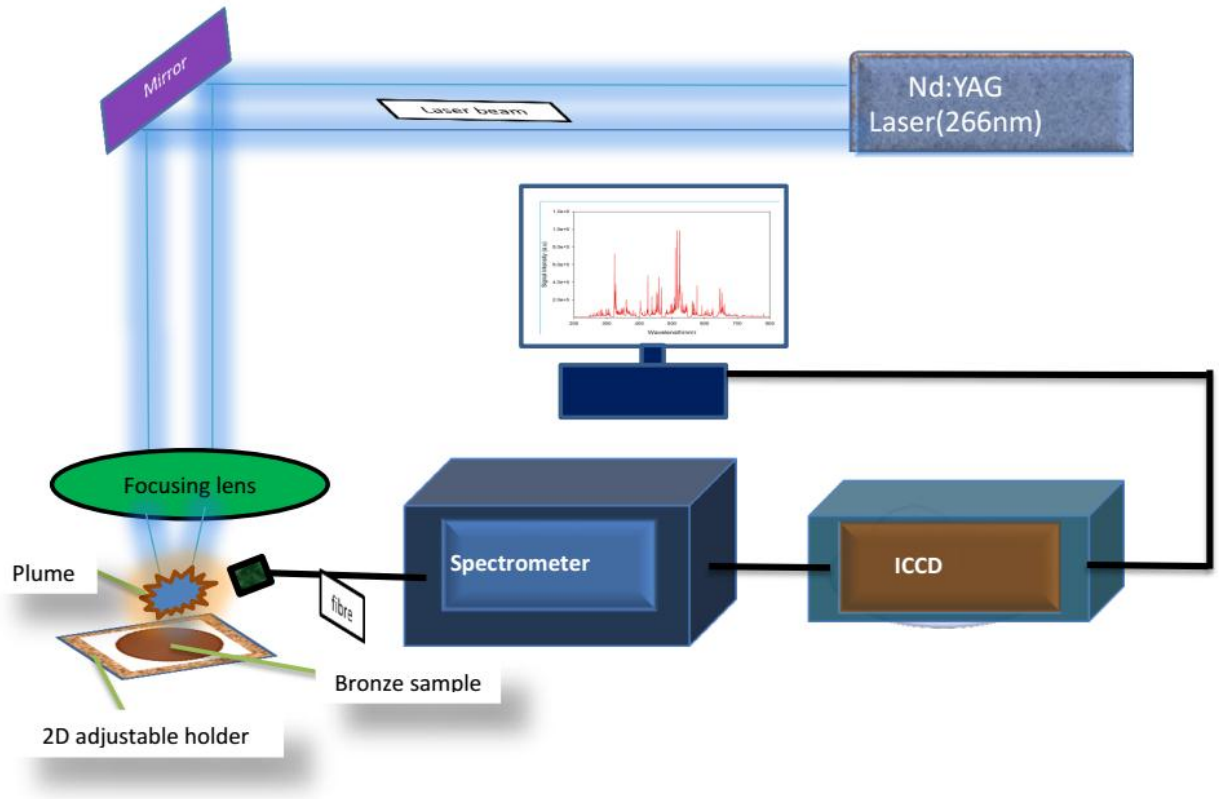

Figure 3.1: Experimental set up for standard bronze sample spectrum acquisition

3.1.2 Configuration of laser in LIBS system

For the purpose of plasma generation from any kind of sample involved in LIBS experiment, pulsed lasers of high energy are frequently used [37]. Varieties of coherent sources with such high energy are available in the market with different technical specifications. Physical parameters of laser pulse such as wavelength, pulse energy, pulse duration and beam quality among others, control the radiation to matter interaction and consequently influence the plasma formation as well as the quality of LIBS measurement. Therefore, the nature of the task to be performed determines the selection of the laser source suitable for the job accomplishment. The main features of a laser source include

intensity, directionality, coherence and monochromaticity. Laser intensity is the ratio of the peak power of the laser and cross section of the output beam. The laser intensity is also called power density or simply irradiance [38]. Very large intensities can be achieved per unit area in our LIBS system since a short duration of order of nanoseconds pulses can be generated. However, power per unit area impinging on the sample under investigation is mostly significant in LIBS experiment and this also depends on the optical systems for delivering the beam onto the target. The divergence angle of laser describes its directionality. The directionality property of laser beam allows deliverance of high irradiance to the target since radiation can be easily focused to a very small spot size [39]. Spatial coherence enhances high irradiance in laser beam since is related to low divergence of the beam. It worth mentioning that laser coherence is of limited significance in LIBS measurements in as much the irradiance is not altered. The plasma behavior remains unchanged for coherent and not coherent radiation of similar irradiance. Similarly, laser monochromaticity is of lesser significance since plasma formation as well as behavior depends strongly on laser intensity and weakly influenced by the frequency spread of the incident radiation [124]. Despite the existence of wide varieties of laser sources in LIBS experiment, Nd:YAG solid state laser source with active Q-switching has enjoyed a wider utilization. Q-switching is an optical technique through which an intense and narrow laser pulses could be obtained. Implementation of Q-switching involves positioning of variable attenuator inside the optical resonator. This arrangement allows accumulation and increase in the stored energy in the active medium while depletion of upper energy level is prevented. Hence, intense and short pulse of light is

released [40]. Nd:YAG solid state laser source is employed for all LIBS measurement conducted on all our test samples.

3.1.3 The light collecting system

The light collecting system refers to an optical device employed in LIBS measurement for collection and transmission of the emitted radiation from the plasma to spectral detection unit. For all the LIBS measurement conducted in this research work, the collection and transmission of plasma emitted radiation was carried out using optical fiber. In order to prevent unnecessary broadening of emission lines and ensure formation of high quality plasma, the optical plasma is positioned few millimeters (very close to the plasma plume) to the laser plume. The fiber supported with a small miniature lens (of 30mm focal length) positioned at an angle 45^0 for efficient collection of the created plasma spark on the surface of the test samples. The radiation collecting efficiency of the fiber is also enhanced by mounting it on 3-D translator for three movement along x,y and z-axis.

3.1.4 LIBS spectrometer

The spectral composition of the emitted plasma radiation in LIBS measurement is obtained using spectrometer. It identifies the wavelength fingerprint of each of the atomic species present in the test sample. There are requirements and prerequisites to be satisfied by an ideal spectrometer in LIBS measurement due to broad spectrum range capacity of the LIBS measurement ranging from vacuum ultraviolet to near infra-red. These basic requirements include: (i) Excellent capacity for spectral resolution(ability to resolve spectral lines that are very close to each other and see them as distinct lines) (ii) large

dynamic range and high quantum efficiency (iii) short data-acquisition and readout time. The spectrometer employed in this research work satisfies the aforementioned requirements. A 500mm spectrograph having a grating groove density of 1200 lines/mm was utilized in this study. It offers maximum resolution between 200nm to 900nm wavelength range.

3.1.5 Optics for beam focusing

Optical systems (which can be cylindrical or spherical lens) are very useful for delivering laser radiation of high fluence to the matter under investigation. It focuses the laser beam down to a very narrow spot and enhances plasma formation processes [125]. Assuming an ideal laser beam with Gaussian intensity profile, beam waist radius (w_o) presented in equation (3.1) can be easily achieved using an aberration free lens.

$$w_o = \frac{\lambda f}{\pi D} \qquad (3.1)$$

Where f , λ and D respectively represent the focal length of the lens, laser radiation wavelength and the diameter of unfocused beam impinged on the lens.

From the equation, a shorter focal length coupled with large unfocused beam results into higher power densities (lower, beam waist radius). Highly localized sparks are also generated for spatially resolved measurements using lens of shorter focal length while lens of longer focal length are often used when the optical system cannot be brought close to the sample [126]. The consequence of longer focal length lens is that higher laser energy source would be required for plasma excitement since larger focal volume would be generated. It should be noted that the focusing configuration plays a big role in LIBS measurement since lens-to-surface distance (LTSD) remains a very critical parameter. It

has been noted that small change in beam waist radius leads to significant variations in the irradiance delivered to the sample [124]. Rayleigh range helps to control the measurement variation that is due to LTSD. The distance between the beam waist and the position along propagation direction where cross section doubles (or beam waist radius raises by a factor of $\sqrt{2}$) is called the Rayleigh range. Rayleigh range is expressed in equation (3.2)

$$R = \frac{\pi w_o^2}{\lambda} \qquad (3.2)$$

3.1.6 Target holder

Target holder constitutes a vital component of LIBS system because it holds the test sample at appropriate position where irradiance of the laser interacts with the sample. The sample holder for our LIBS measurement is a 2-dimensional holder that allows manual movement of the sample along x and y plane. Another important feature of the sample holder used for our LIBS measurement is the nature of the material (eye protective polymer) used to make the holder that provides a clear view of the sample. The advantage of the 2-dimentional rotational feature of the holder is that it prevents creation of crater on the test sample. Formation of crater significantly deteriorates the quality of the collected radiation as the optical fiber used for radiation collection might not effectively collect the signal from the laser plasma plume due to the presence of crater. Movement of the test sample during LIBS measurement becomes significant for ensuring collection of high quality radiation. Another merit of the two dimensional movement of the sample is that it always provide fresh surface for every shot of laser and ultimately improves the quality of the plasma formation.

3.1.7 Operating principle of inductively coupled plasma mass spectroscopy (ICP-MS)

Inductively coupled plasma mass spectrometry (ICP-MS) is one of the famous analytical tools employed in determination of elemental compositions of various kinds of samples. The instrumental parts of ICP-MS include a nebulizer, spray chamber, plasma touch, interface and detector. The technique utilizes the spontaneous emission of photons from ions and atoms in radio frequency discharge. Analysis of the samples is carried out in liquid or gaseous phase while digestion or extraction processes using an acidic solution has to be carried out on solid samples before ICP-MS can be applied on the sample. The operational principle of the technique involves formation of aerosol and vaporization afterwards. Quick vaporization of aerosol is made possible due to the operating temperature of the technique which is around 10,000K. The inflow of argon gas at 1L/min aids the conversion liquid sample pumped into nebulizer into fine aerosol from which fine droplet (of about 5 μm in diameter) is separated form large droplet of the sample. The injector directs the separated fine droplets into plasma torch from the spray chamber. The function of plasma touch is to generate charged ions (which are positively charged) and direct them to spectrometer through an interface with vacuum pressure of one to two torr. The ions then migrate to the main vacuum chamber and then to the ion optics from the interface region. The ion optics (also called electrostatic lenses) leads the ion beam toward mass separation device and prevents the photons, neutral species and particulates from entering the detector. The ions are then converted to electrical signal through ion detector while the data handling systems process the information into readable analyte concentrations.

3.2 Preparation of standard bronze samples in the LIBS set up details

Seven different standard bronze samples purchased from online metal stores with trade names C510, C642, C655, C863, C954, C932 and C673 are cut into small disc shape sizes purposely to easy LIBS measurement and acquisition of LIBS spectra. The disc shaped samples were further polished using methanol and tissues and placed inside oven for 20 minutes while the oven temperature was maintained at 70 ^{0}C to remove and vaporize any debris and contaminants that might have accumulated on the samples. Fig.3.2 and Fig.3.3 respectively shows the standard bronze samples before being cut and after being cut and polished. Table 3.1 shows the certified elemental composition of each of the standard sample. It should be noted that the concentration of silver is considered negligible in sample C642. The LIBS spectra of each of the seven standard bronze samples were acquired using quadrupled Q-switch Nd:YAG (QUV-266-5 model with wavelength of 266 nm) laser source of repetition rate of 20 Hz, pulse generation of 8 ns and maximum energy output of 30 mJ/pulse. The laser pulse emanated from the source was collimated with the aid of plane mirror and subsequently focused on the test samples using an ultraviolent convex lens of focal length 30mm. Throughout the experimental stage, the test samples were allowed to move along x and y plane using 2D sample holder. The two dimensional movement of the samples helps in preventing formation of craters on the samples. The laser induced plasma generated after laser ablation was collected using optical fibre positioned at about 45^0 with respect to the normal to the samples, purposely to ensure optimum acquisition of the plasma. The fibre was then coupled with 500mm spectrograph (Andor SR 500i-A) having grating groove density of 1200lines/mm. Optimum delay time was maintained between the laser pulse and opening

of the shutter intensified charged coupled device (ICCD, model iStar 320T,690x255 pixels) for minimizing the background. The emision spectrum captured by ICCD was integrated into computer using USB cable for acquisition. The procedures were repeated for seven different standard bronze samples and the emission line intensities of all the elements present in the samples were extracted.The experiment was repeated two times Fig.3.1 presents the stages of each of the aforementioned processes of LIBS spectra acquisition.

Figure 3.2: Standard bronze samples as bought

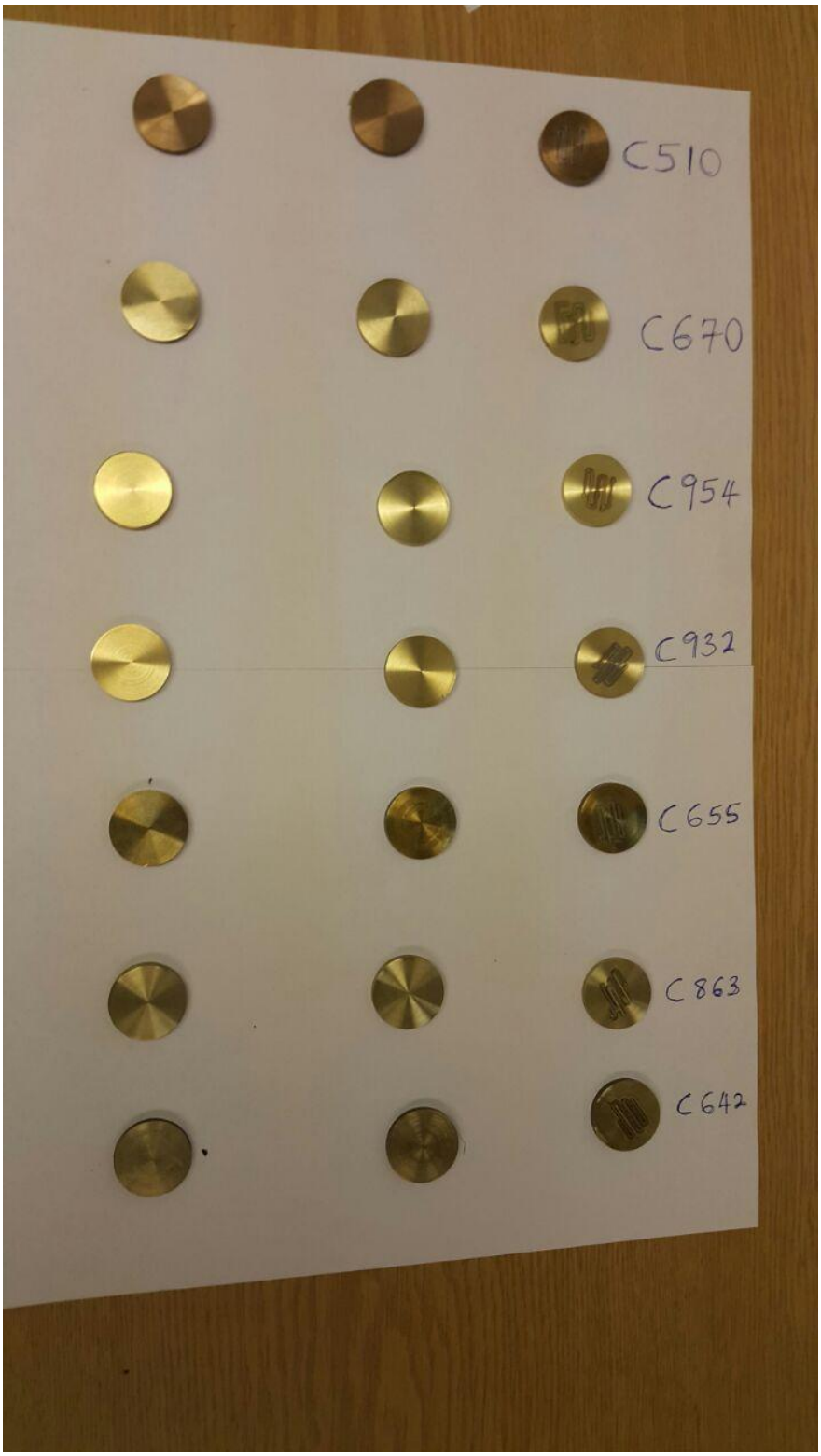

Figure 3.3 : Standard Bronze sample before and after LIBS measurement

Table 3.1 Elemental concentrations (in wt %) of each of the standard bronze samples as provided by the manufacturer

Trade name	Cu	Pb	Fe	Sn	Zn	Al	Mn	Ni	P	Si	Sb	Co	Others
C510	94.9900	----	---	4.6600	---	---	---	---	---	---	---	---	0.3500
C642	90.8500	----	0.1800	0.0100	0.0400	6.8200	0.0200	0.1500	---	1.78	---	0.15	0.0000
C655	60.3030	0.0133	0.0159	0.8145	38.8533	---	---	---	---	---	---	---	
C863	62.9000	0.0100	2.4300	0.0200	26.4100	5.2100	2.9090	---	---	---	---	---	0.1100
C954	85.8150	----	3.4640	---	---	10.433	0.2360	0.0520	---	---	---	---	0.0000
C932	81.2192	7.6680	0.1250	6.4670	3.780			0.4030	0.041	---	0.253	---	0.0438
C673	59.4	1.76	0.06	0.05	35.17		2.5	0.06	---	0.97	---	---	0.0300

3.2.1 Preparation of crayfish samples for LIBS measurement

Crayfish samples purchaced from four different markets in south west Nigeria (most populated countary in west africa) were prepared purposely to identify and quantify the elemental compositions. Fig.3.4 shows the crayfish in its dried form. The dried crayfish samples were further air-dried to remove any moisture content in the samples. The samples were also pulverized into powder using blender in order to ensure homogeneity of the samples. One gram of each of the samples was weighed using analytical weighing balance of 5digits accuracy and pelleted using hydraulic pelleting machine for LIBS measurement. Fig.3.4 shows the preparation stages of the samples including the grinding machine (Fig.3.4b) and hydraulic press (Fig.3.4a) for making pellets. The experimental set up through which LIBS spectral for pelleted crayfish samples were aqcuired consists of quadrupled Q-switch Nd:YAG (QUV-266-5 model with wavelength of 266 nm) laser source of 20Hz repeatition rate and 8ns pulses genreation. The samples were allowed to move along x- y plane using 2D adjustable holder so as to prevent the occurrence of

craters on the samples. The laser beam emanated from the source was collimated with the aid of a plane mirror and further focused on the crayfish samples using the ultraviolet convex focusing lens of 30mm focal length. The generated plasma plume after the ablation was collected using optical fibre. In order to ensure maximum signal collection, the fibre was positioned 45^0 with respect to a normal to the samples. The fibre was then coupled with 500mm spectrograph (Andor SR 500i-A) having grating groove density of 1200lines/mm. Optimum delay time was mantained between the laser pulse and opening of the shutter intensified charged coupled device (ICCD, model iStar 320T,690x255 pixels) to minimize the emergence of continum spectrum. The maximum resolution of the presented LIBS system ranges from 200nm to 800nm. The emision spectrum captured by ICCD was integrated into computer using USB cable for acquization. 20 number of accumulation was used during LIBS measurement. The delay time as well as laser energy were optimized and optimum values of 100ns and 30mJ were respectively used for the LIBS measurement.

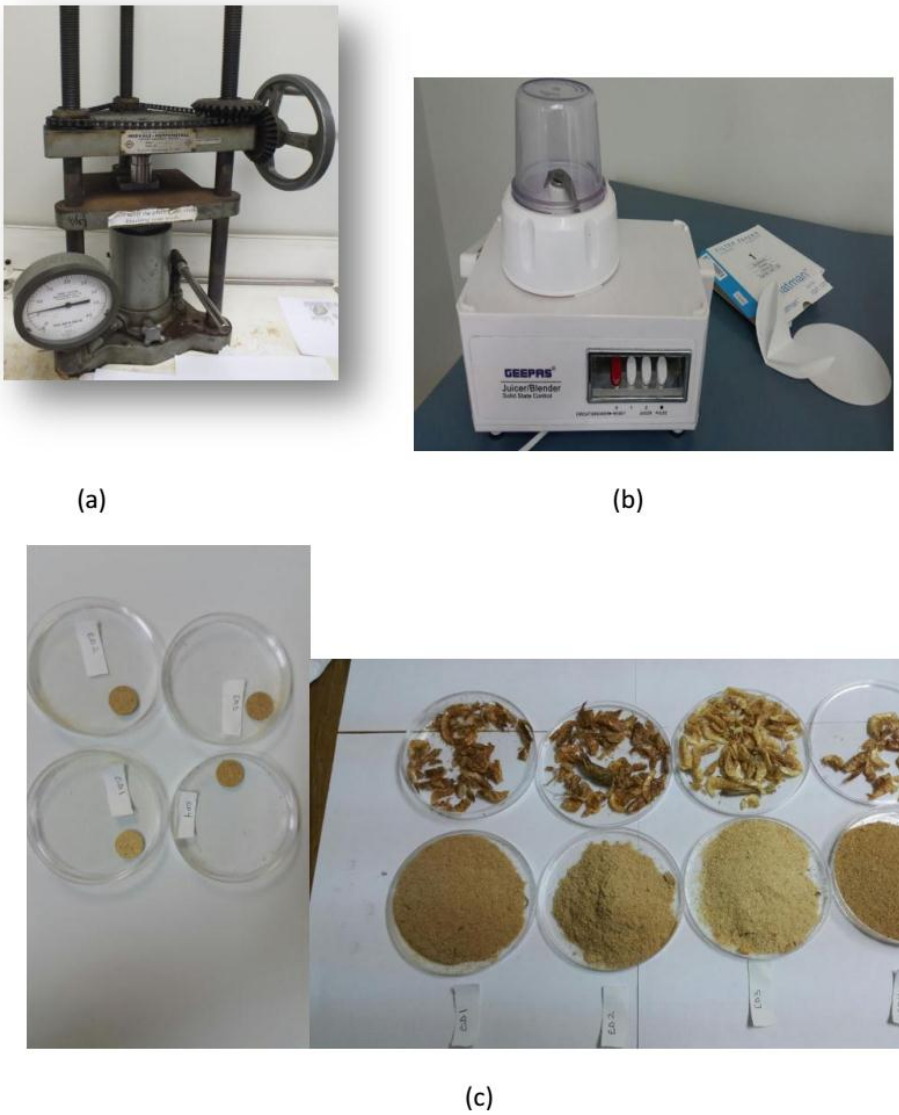

Figure 3.4 : Instrument employed for crayfish sample preparation; (a) hydraulic machine for making pellet (b) grinding machine and (c) the crayfish samples in different forms

3.2.2 Preparation of grape samples for LIBS measurement

Two brands of grape used for this experiment was purchased in Alkhobar (eastern part of Saudi Arabia) market. The grapes were sliced into pieces, dried continuously for four days using home heater (operated at a constant temperature of 40 ^{0}C) before being air-dried for additional two days and subsequently pulverized using grinding machine shown

in Fig.3.4b. The significance of pulverization is that it ensures homogenous sample and any part of the sample used for analysis is assumed to be the actual and true representative of the entire sample. 0.5g of each of the brands of grape was weighed using analytical weighing balance of 5digts accuracy and pelleted into disc like samples. The processing stages of the grape samples are shown in Fig. 3.5. The LIBS measurement was carried out on the samples using similar procedures described in section 3.2.2 for crayfish spectrum acquisition.

Figure 3.5 : Processing stages of the two brands of grape

3.2.3 Preparation of crayfish and grapes samples for ICP-OES measurement

The grape and crayfish samples employed in this research work were air-dried to remove the moisture content and pulverized into powder to ensure homogeneity. 0.5g of each of the sample was mixed with 10ml of concentrated nitric acid (HNO_3) inside sample vessels. The sample vessels were left inside the fume cupboard for 15minutes before being capped tightly, assembled and placed inside microwave digestion machine shown

in Fig.3.5. The essence of leaving the samples open for 15minutes is to prevent accumulation of pressure inside the vessel which can lead to a significant difficulty while opening the vessels after being removed from the digester. Then, a preset method for food digestion was selected from the instrument with temperature and pressure variations depicted in Fig.3.6. The microwave digester heats the samples from room temperature to 200^0C at 12^0C/minute and holds the sample at 200 ^{0}C for additional 15minutes before the sample cools downs to room temperature. The pressure variation of the samples is also depicted in the figure. The samples were transferred from the microwave digester to fume cupboard where the sample lids were removed to prevent the release of toxic gas into laboratory. The samples were then poured into 50ml plastic centrifuge bottle inside the fume cupboard and left for additional 15minutes before being capped for further analysis.

The digested solution was filtered and made up to 50ml. The samples were diluted two times with deionized water and analyzed using optima 8300 ICP-OES (optical emission spectroscopy) spectrometer (by perkin elmer). All these aforementioned sample preparation procedures were conducted in Center of Integrative Petroleum Research, KFUPM.

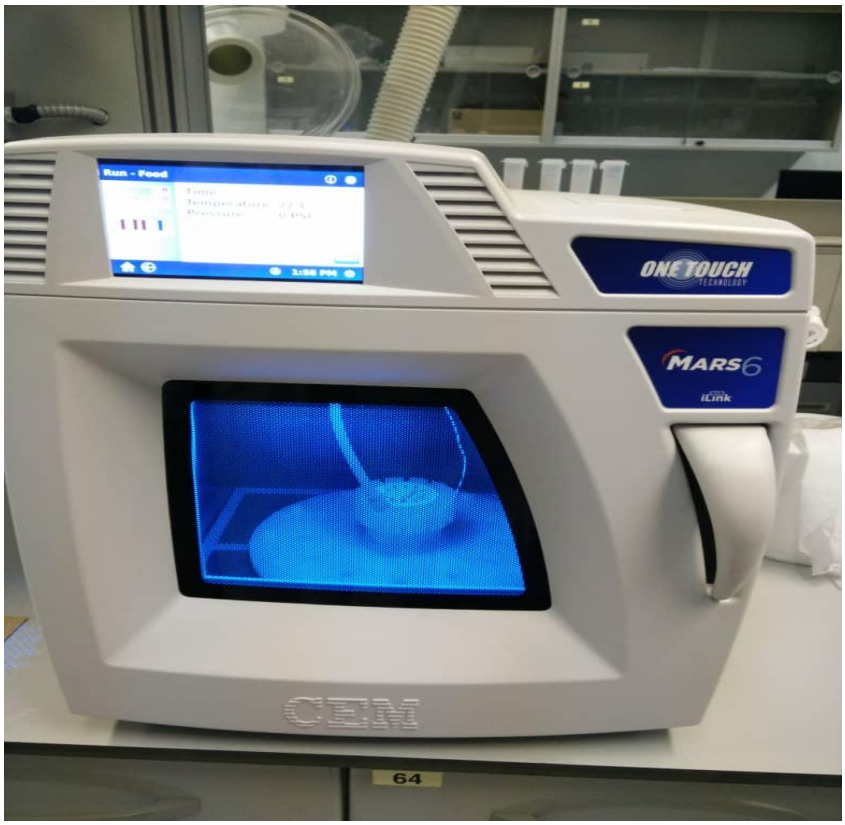

Figure 3.6 : Microwave digestion machine

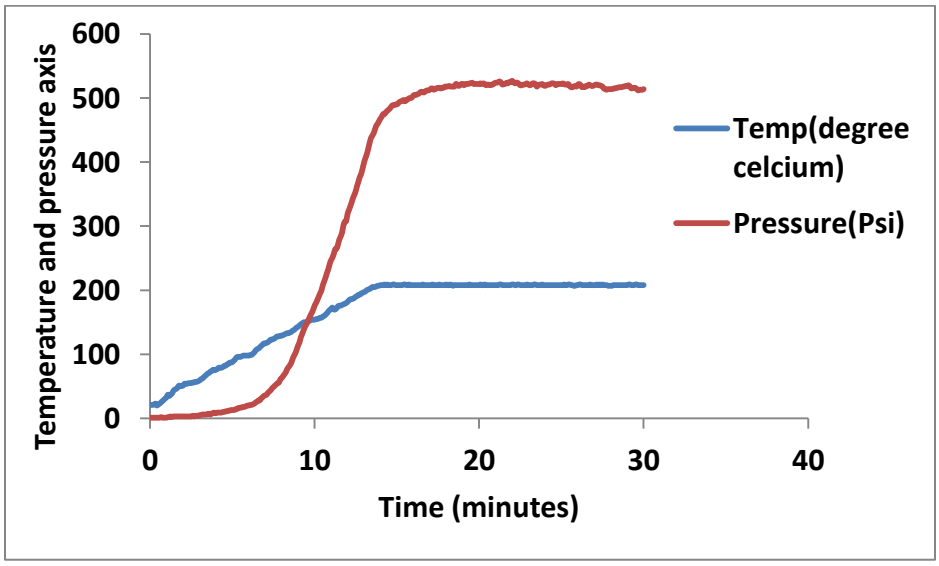

Figure 3.7 : Variation of temperature and pressure of microwave digestion machine with time while digesting grape and crayfish samples

3.3 Computational methodology on standard bronze samples

LIBS measurement was conducted over standard bronze samples and the obtained spectra was quantitatively analyzed using three chemometric techniques coupled with internal reference preprocessing method (IRP) for self-absorption correction. The chemometrics techniques developed and implemented include sensitivity based linear learning chemometric method (SBLLM), support vector regression (SVR) and extreme learning machine (ELM) chemometric .In each of the chemometric technique, gravitational search algorithm (GSA) was used for hyper-parameters optimization. The physical principle behind the internal reference preprocessing method can be well understood from the nature of LIBS plasma which is often optically thick and results into self-absorption since the plasma is spatially inhomogeneous and its evolution is temporal [8]. An optically thick plasma results into uneven plasma cooling in which one part of the plasma cools faster than the remaining part. Consequently, the photons emitted from the cooler part are reabsorbed by atoms of the same species in the hotter part of the plasma and ultimately leads to emission of reduced intensity. The emitted species with least transition probability (which is the probability per unit time of an atom in upper energy level making a transition to lower energy level) would have lowest possibility of being reabsorbed since the transition to the lowest energy state might be slower than the cooling time lag between different parts of the cooling plasma. Hence, normalization of the spectra intensity with the intensity that is rarely affected by self-absorption reduces the effect of self-absorption in the entire spectra [13], [27]. The robustness of the proposed performance enhancement methods was investigated by using three different methods of data extraction from the intensity wavelength spectrum obtained from our LIBS

instrument. The methods include (i) using line intensities of each of the elements at a wavelengths obtained from our spectrometer. Chemometrics developed using this data begin with a letter ***A*** as a nomenclature and (ii) using the integrated line intensity around the standard wavelength contained in the NIST data base. Chemometrics developed using this data begin with a letter ***I*** as a nomenclature.

3.3.1 Computational development of the proposed hybrid SVR-GSA chemometric and implementation of internal reference preprocessing method (IRP)

The proposed methods of enhancing the generalization and predictive capacity of SVR for LIBS spectra quantitative analysis are implemented within MATLAB computing environment. The data-points used for modeling are the elemental constituents of seven bronze standard samples purchased from online metal store [123]. The descriptors for the proposed SVR based chemometric include the emision line intensity obtained from LIBS measurement, transition probability, degeneracy, upper level transition energy and transition wavelength. The choice of other spectra variables such as transition probability, degeneracy, upper level transition energy and transition wavelength is due to their contributions in influencing the concentration of species in laser induced plasma as these variables are well captured by plasma Boltzmann distribution. Furthermore, incorporating these descriptors in the proposed model makes the models independent of the experimental conditions of spectra acquisition as the model can be a standalone chemometric model. The dataset was divided into seven different folds where elemental constituents of each of the standard bronze samples correspond to the data content of each fold. Therefore, the experiment was performed M-times (where M=7, number of

folds, also number of standard bronze samples) using M-1 data set for training and the remaining for testing in each experiment and computing the average root mean square error (RMSE) , mean absolute error (MAE) and correlation coefficients (CC) across all M-trials. This method of validation is called leave-one -out cross validation. The details of the computational procedures are illustrated as follow:

Step I: Divide the data set into M number of folds. Each fold contains elemental constituents of each of the standard bronze samples.

Step II: Train SVR algorithm with M-1 number of dataset and conduct the testing procedures using the remaining dataset which is not included in the training phase. The hyper-parameters of SVR are optimized using GSA. Compute the values of performance evaluation parameters which include RMSE, MAE and CC.

Step III: With optimum values of SVR hyper-parameters obtained from **Step II**, perform M-1 number of experiment (that is, training and testing SVR algorithm using the specified dataset) in which testing fold is replaced after each experiment until every fold is involved in testing stage of the simulation. Compute the values of performance evaluation parameters after each experiment and evaluate the average of these values. Also, compute the average of the model estimates over all the folds. The model that is trained and tested using normalized emission line intensities is referred to as SVR-GSA-IRP model while the model which is trained and tested using un-normalized emission line intensities is called SVR-GSA-WIRP model.

Step IV: Train another SVR algorithm with GSA for hyper-parameters optimization using the outputs of **Step III** and validate the models using leave-one -out cross

validation method as described in **Step III**. The model that is trained and tested using the outputs of SVR-GSA-IRP is referred to as HSVR-GSA-IRP while the model which is trained and tested using the outputs of SVR-GSA-WIRP is called HSVR-GSA-WIRP model. The computational flow chart of the proposed SVR-based chemometric is presented in Fig.3.2.

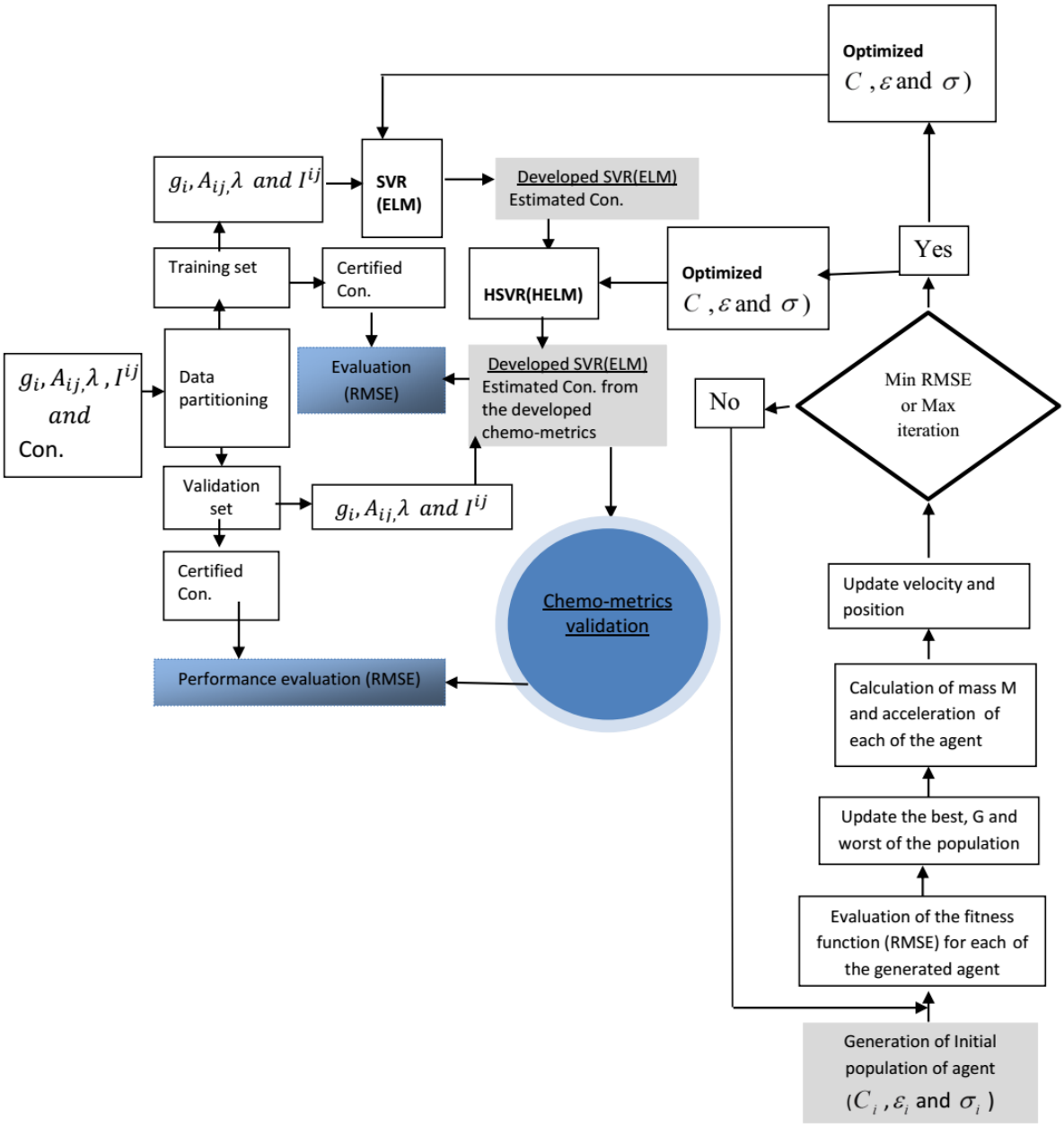

Figure 3.8: Computational flow chart of the developed ELM and SVR chemometric

3.3.2 Procedures for computational development and implementation of ELM-GSA and HELM-GSA based chemometric

Step I: *Initialization:* for a number of iteration $j = 0$, randomly initialize N_p number of agent within a search space bounded by [1,1000]. Each agent encodes the number of hidden neurons for a selected activation function.

Step II: *Inertial mass calculation:* compute the inertial mass of each of the agents in the defined search space using their fitness. The fitness of each of the agent is determined using root mean square error (RMSE) between the certified and estimated elemental concentrations. The fitness is determined in the following ways: (a) divide the data set into M-folds (seven different folds in this case where each fold contains the data set for a standard bronze sample), (b) for a given mass of the agent; determine the input weights $\mathbf{w}_l$ and the hidden layer biases b_l randomly on uniform distribution function using the data set of M-1 folds while the remaining one fold is kept for validation purpose, (c) Select an activation function and set hidden nodes, (d) compute the hidden layer output matrix $\mathbf{H}$, (e) compute the output weights $\hat{\boldsymbol{\beta}}$, (f) Determine the elemental concentration of the laser induced plasma constituents (since ablation is stoichiometric) using Moore-Penrose generalized inverse matrix , (g) compare the estimated concentration with the certified values and compute the RMSE-tr for the training data set (that is, data set for M-1 folds). (i) For the chosen activation function, use the obtained weights during the training stage and number of hidden neuron to assess the generalization capacity of the trained model using the data set that was not included in the training phase. (j)

Determine the RMSE-ts on the testing data set (that is, a fold that was not included in the training phase) and keep the minimum RMSE of the iteration.

Step III: *Gravitational pull and acceleration computation:* gravitational pull and mass of each of the agents in the search space computed using equation (9) and (10), respectively

Step IV: *Velocity and position:* The velocity and position of each of the agents are updated in accordance to equation (11) and (12) respectively.

Step V: Steps I to **Step IV** are repeated (while the minimum RMSE-ts of each iteration is saved) until the 100 iteration is reached or fifty consecutive iterations give equal RMSE

Step VI: Using optimum value of number of hidden neurons and activation function, perform the experiment M-times using M-1 data set for training and the remaining for testing in each experiment and compute average RMSE, mean absolute error (MAE) and correlation coefficients (CC) across all M-trials. This method of validation is called leave-one -out cross validation.

The aforementioned procedures (that is, **Step I** to **Step VI**) were repeated using data set containing normalized emission intensity (this gives rise to GSA-ELM-IRP model) as well as data set containing raw emission line intensity (this gives rise to GSA-ELM-WIRP model). Development of GSA-HELM based chemometrics has two stages. The first stage implements the developmental procedures for GSA-ELM based chemometrics while the second stage takes the output of the first stage as its input and repeat the procedures contain in **Step I** to **Step VI** described above. The first stage of GSA-HELM

based chemometrics can be viewed as feature extraction stage where all needed patterns, connections and intricacies contained in the previous descriptors are centralized and aggregated in a single parameter and ultimately translates to a better predictive and generalization ability [127], [128]. The adopted stopping criteria improve the stability of ELM algorithm since more than fifty iterations convergence to a single RMSE

3.3.3 Procedures for computational development and implementation of hybrid fusion based chemometric

In the fusion of SVR and ELM models, two hybrid models which include SVR-ELM and ELM-SVR were developed and the hyper-parameters of both models were optimized using GSA. The computational development of SVR-ELM model is similar to ordinary ELM model except that the input to SVR-ELM model is the final output of SVR model. Similarly, ELM-SVR and SVR models share the same computational details except the input to ELM-SVR model is the final output of ELM-based model. This proposed hybrid models translate to improved performance and excellent generalization capacity.

CHAPTER 4

Results and discussion: Sufficiency of single persistent lines for chemometrics

This chapter presents the results of the developed hybrid SBLLM-GSA and ELM-GSA chemometrics. Both SBLLM-GSA and ELM-GSA chemometrics are developed using one, two and three persistent lines of the standard bronze samples. In order to ascertain the minimum number of persistent emission lines needed for effective modeling of the relationship between spectral intensity and the elemental concentration, the results of both of the developed chemometrics are compared for single, double and three emission lines. The complexity of the chemometrics as the number of emission lines increase is also investigated and analyzed. Prior to the commencement of the modeling and simulation, the persistent emission lines of the standard bronze samples to be used for the modeling are identified using NIST database [129].

4.1 Identification of persistent emission lines of the elements recorded in our LIBS set-up in the standard bronze samples

The standard bronze samples employed include C510, C655, C673, C863, C932, C954 and C642 which are purchased from online metal store [123]. The elemental compositions of each of the standard bronze samples are presented in table 4.1.

Table 4.1: Elemental certified compositions of the standard bronze samples as provided by the manufacturer

Material	Elemental composition	Concentration (wt%)
C510	Cu	94.960
	Sn	4.660
	Other	0.380
C655	Cu	60.303
	Zn	38.853
	other	0.844
C673	Cu	59.400
	Mn	2.500
	Pb	1.760
	Zn	35.170
	other	1.170
C863	Cu	62.900
	Fe	2.430
	Al	5.210
	Mn	2.909
	Zn	26.410
	other	0.141
C932	Cu	81.219
	Sn	6.467
	Zn	3.780
	Pb	7.668
	other	0.866

C954	Cu	85.815
	Fe	3.464
	Al	10.433
	other	0.288
C642	Al	6.820
	Cu	90.830
	other	2.350

Fig.4.1 and Fig.4.2 show the elemental compositions of C510 standard samples for copper and tin, respectively. The three persistent emission lines of copper are identified at wavelengths of 510.55nm, 515.32nm and 521.82nm. Similarly, persistent lines used in modeling tin concentrations are identified at 270.65nm, 283.99nm and 286.33nm wavelengths.

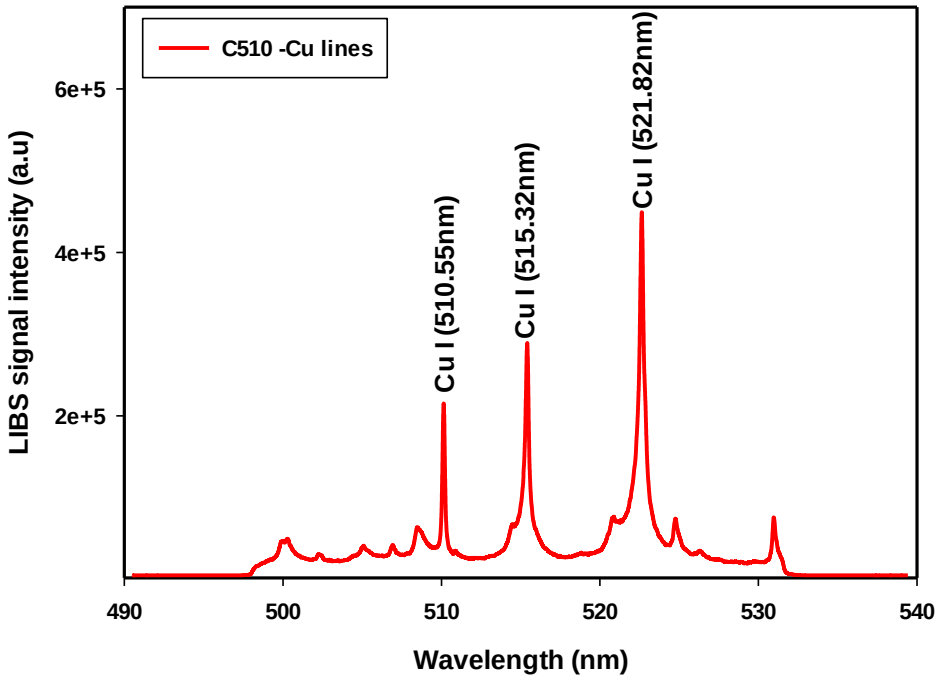

Figure 4.1: A typical LIBS spectrum recorded in 490-540nm region indicating copper persistent emission lines for C510 standard bronze sample

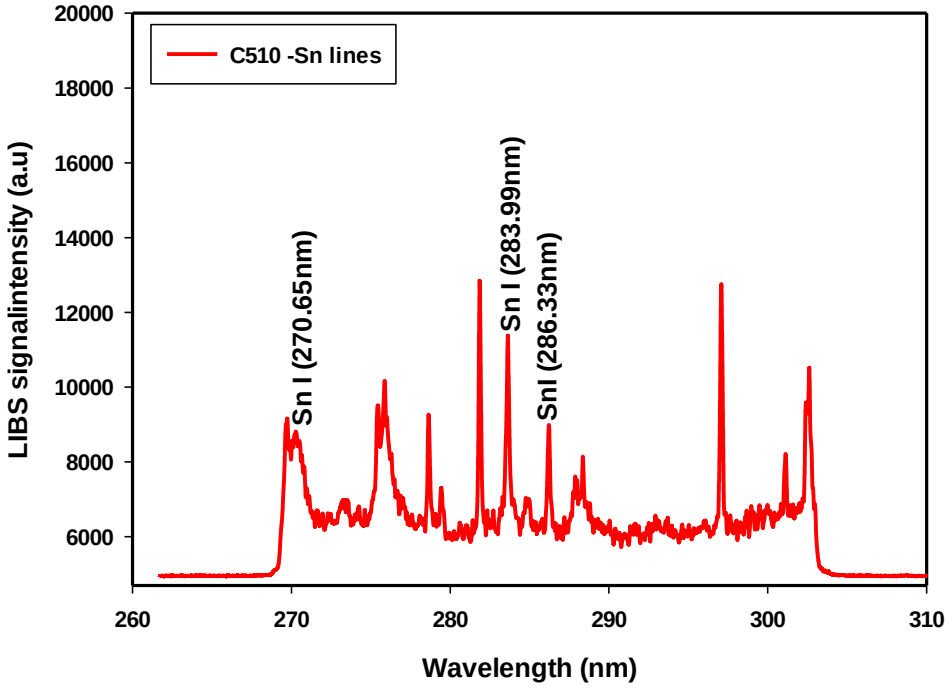

Figure 4.2 : A typical LIBS spectrum recorded in 260-310nm region indicating tin persistent emission lines for C510 standard bronze sample

For standard sample C655, the major elements include copper and zinc. The persistent emission lines for copper and zinc for this sample are respectively presented in Fig.4.3 and Fig.4.4. In order not to bias the chemometrics, the persistent emission lines of copper are identified at wavelengths of 510.55nm, 515.32nm and 521.82nm similar to sample C510 while zinc lines are identified at 328.23nm, 330.29nm and 334.50nm wavelengths.

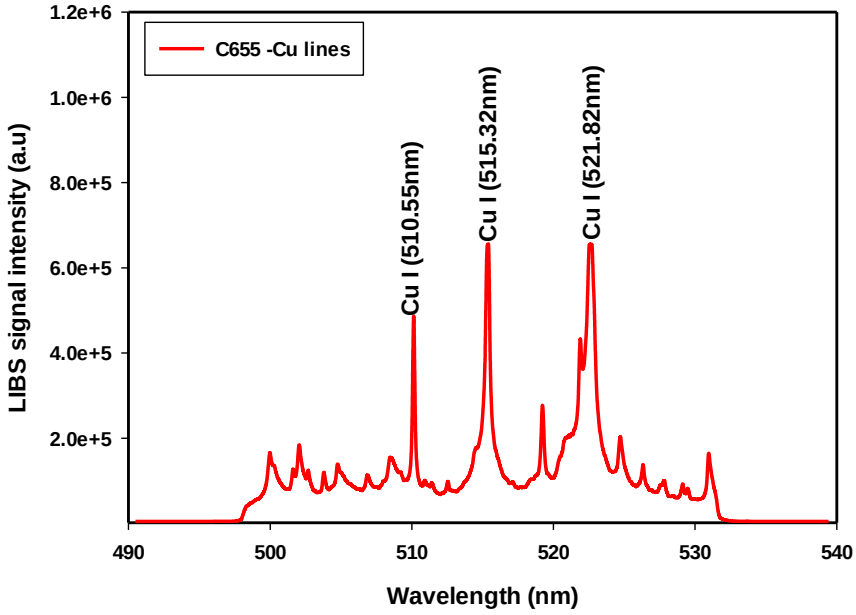

Figure 4.3: A typical LIBS spectrum recorded in 490-540nm region indicating persistent emission lines of copper for C655 standard bronze sample

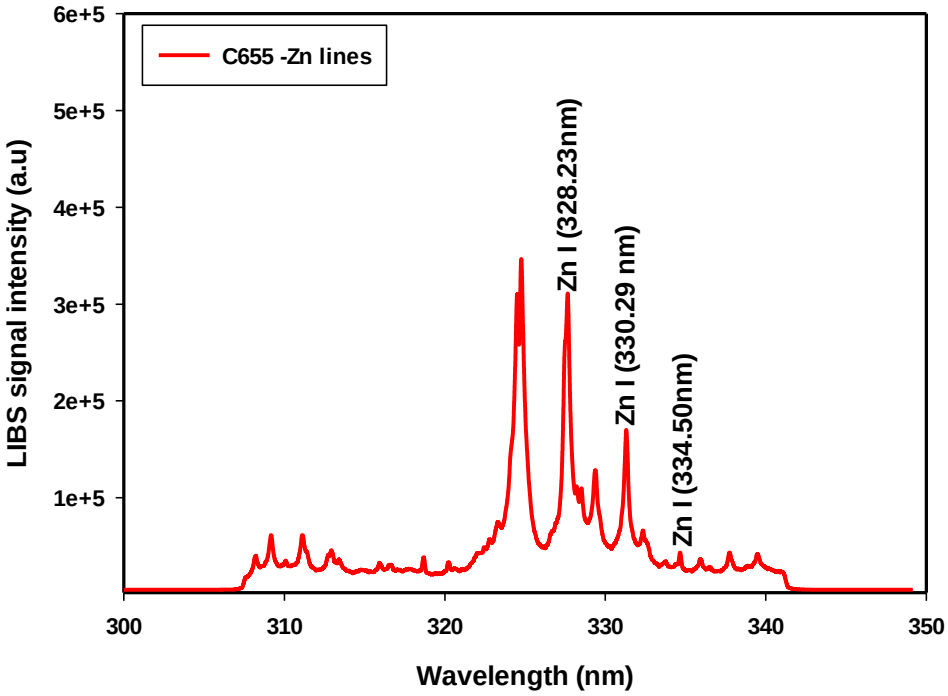

Figure 4.4: A typical LIBS spectrum recorded in 300-350nm region indicating persistent emission lines of zinc for C655 standard bronze sample

For standard sample C670, copper (Cu) manganese (Mn) lead (Pb) and zinc (Zn) lines are identified. Similar to other samples, copper and zinc emission lines are identified at 510.55nm, 515.32nm, 521.82nm and 328.23nm, 330.29nm, 334.50nm wavelengths, respectively. Manganese emission lines are identified at 403.08nm, 403.31 nm 404.14nm wavelengths in accordance to NIST database while lead lines are identified at 363.96nm, 368.35nm and 373.99nm wavelengths. Fig.4.5, Fig.4.6, Fig.4.7 and Fig.4.8 respectively present the emission lines for copper, manganese, lead and zinc.

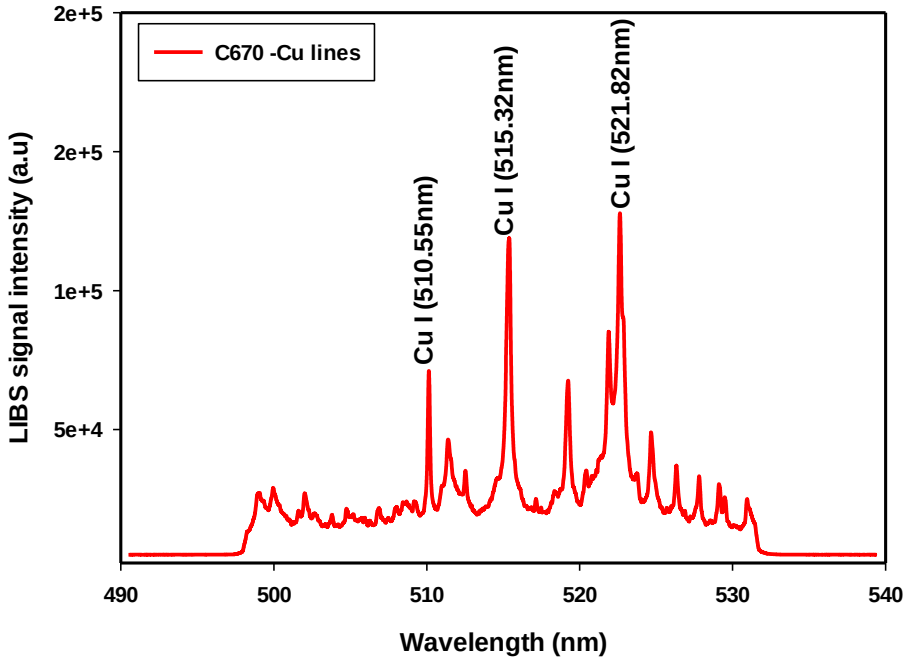

Figure 4.5 : A typical LIBS spectrum recorded in 490-540nm region indicating persistent emission lines of copper for C670 standard bronze sample

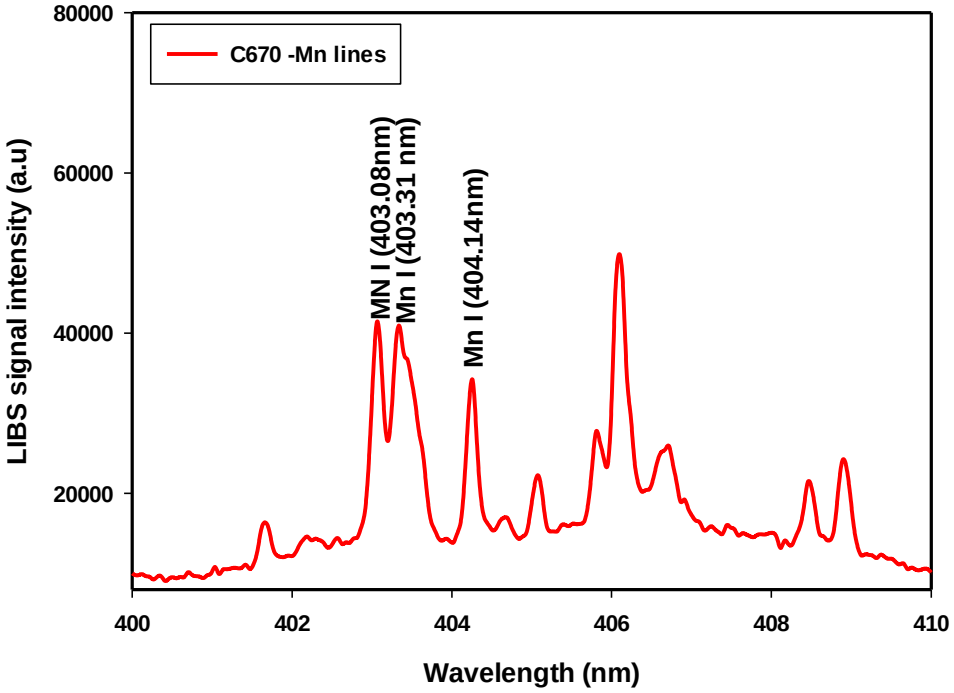

Figure 4.6: A typical LIBS spectrum recorded in 400-410nm region indicating persistent emission lines of manganese for C670 standard bronze sample

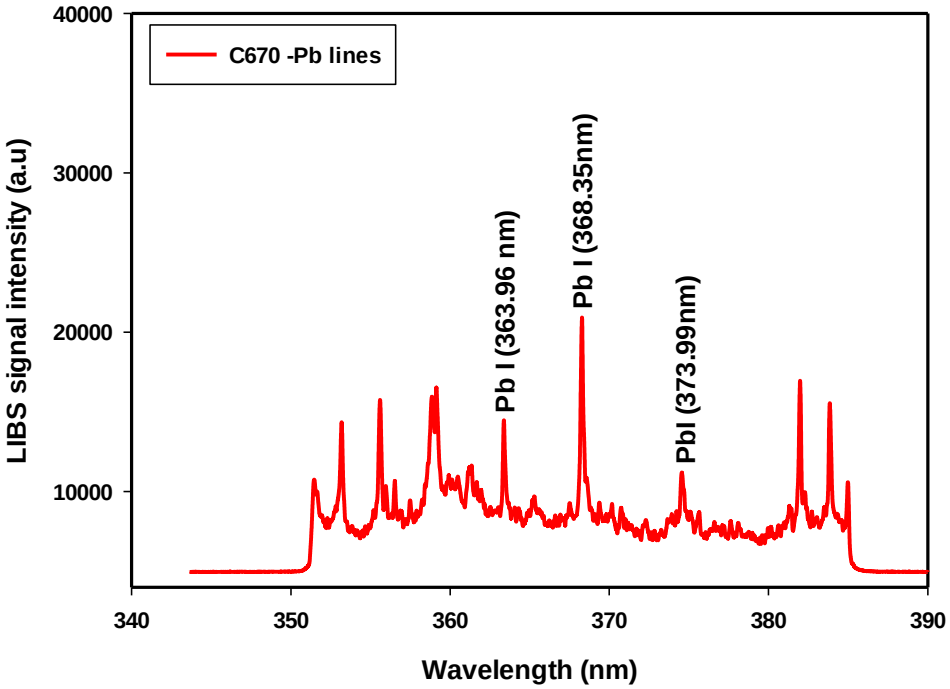

Figure 4.7: A typical LIBS spectrum recorded in 340-390nm region indicating persistent emission lines of lead for C670 standard bronze sample

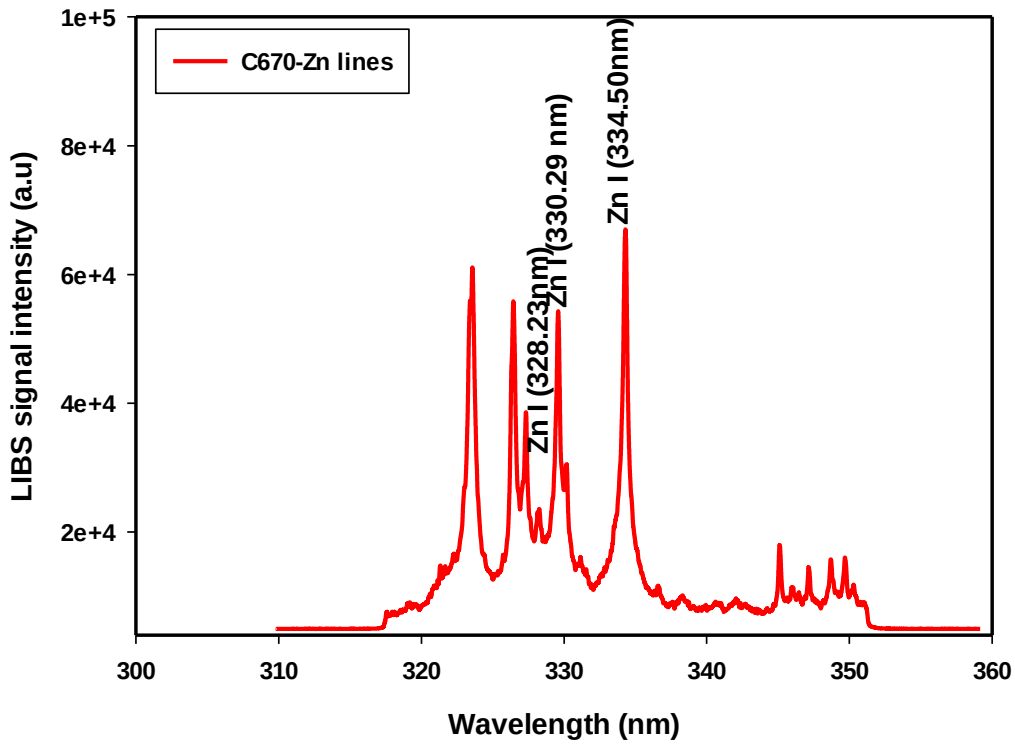

Figure 4.8: A typical LIBS spectrum recorded in 300-360nm region indicating persistent emission lines of zinc for C670 standard bronze sample

Persistent emission lines identified and implemented in chemometrics building for elemental compositions of sample C863 are shown in Fig. 4.9, Fig.4.10, Fig.4.11, Fig.4.12: and Fig.4.13 for aluminum, copper, iron and zinc . Aluminum lines at 308.21nm 309.27nm and 394.40nm wavelengths while copper lines are identified at 510.55nm, 515.32nm and 521.82nm. Iron and zinc lines are identified at 358.12nm, 371.99nm, 373.71 nm and 328.23nm, 330.29nm , 334.50nm respectively.

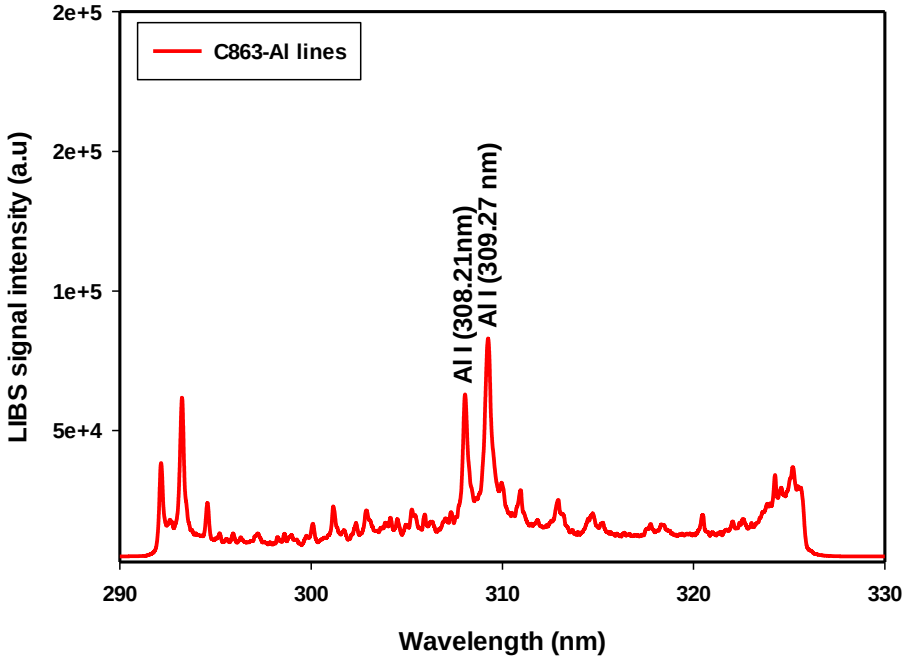

Figure 4.9: A typical LIBS spectrum recorded in 290-330nm region indicating persistent emission lines of aluminum for 863 standard bronze sample

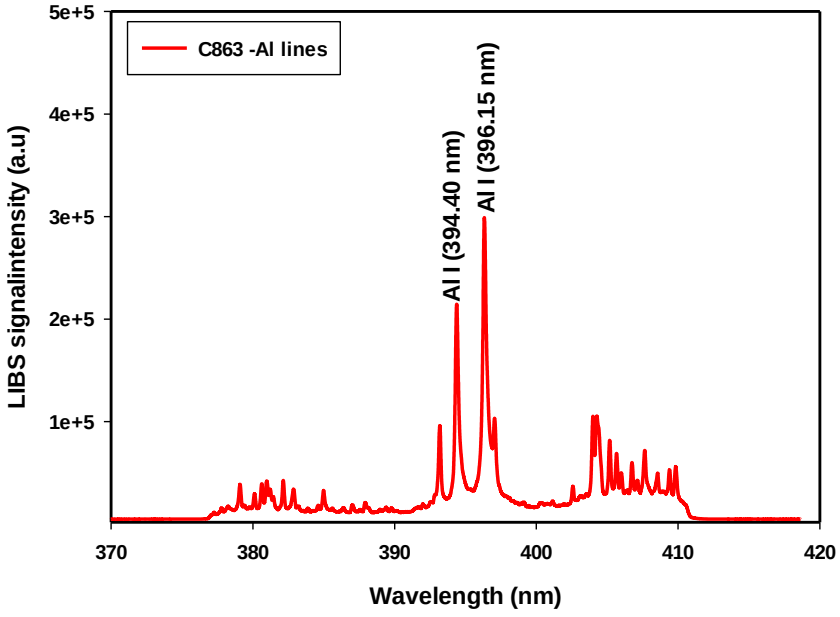

Figure 4.10: A typical LIBS spectrum recorded in 370-420nm region indicating persistent emission lines of aluminum (only wavelength 394.40nm is used) for 863 standard bronze sample

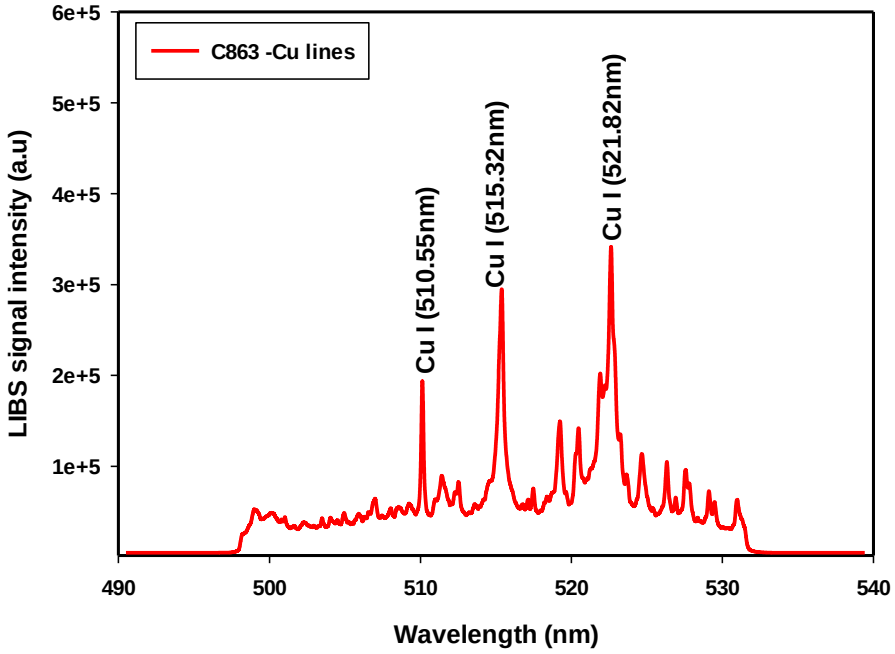

Figure 4.11: A typical LIBS spectrum recorded in 490-540nm region indicating persistent emission lines of copper for 863 standard bronze sample

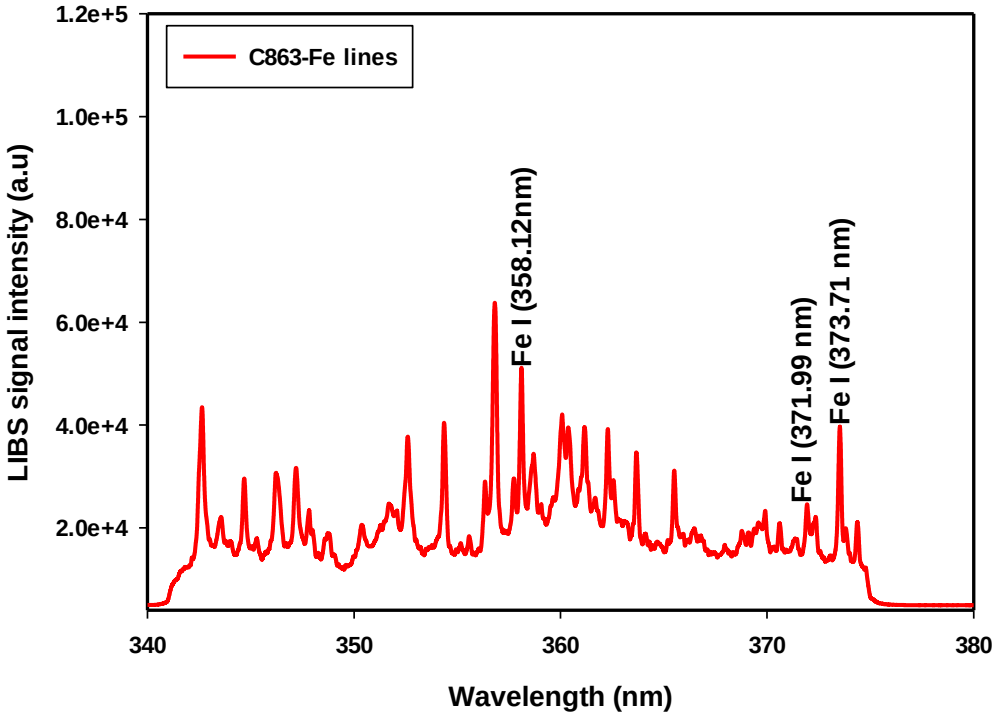

Figure 4.12: A typical LIBS spectrum recorded in 340-380nm region indicating persistent emission lines of iron for 863 standard bronze sample

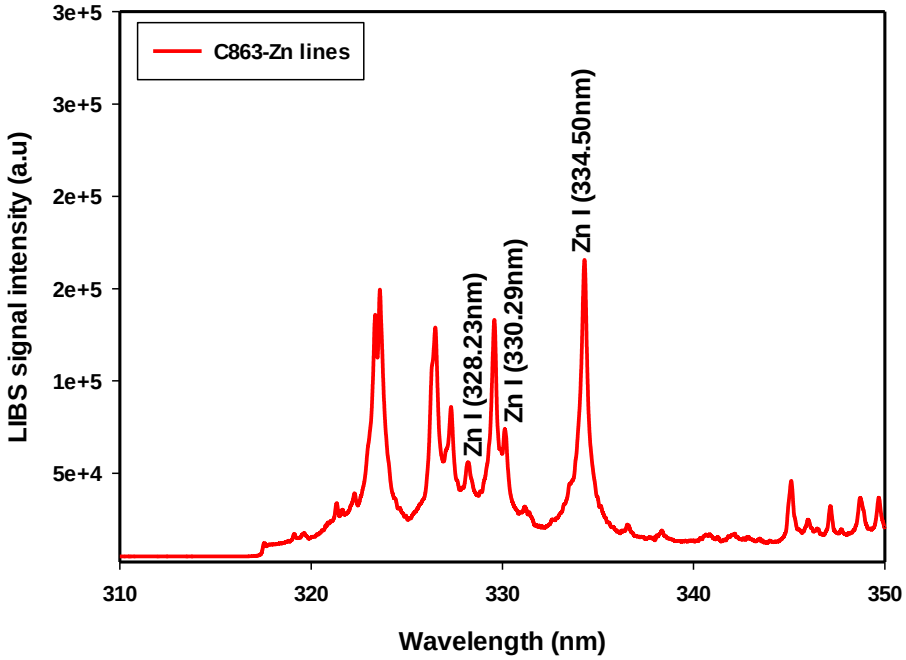

Figure 4.13: A typical LIBS spectrum recorded in 310-350nm region indicating persistent emission lines of zinc for 863 standard bronze sample

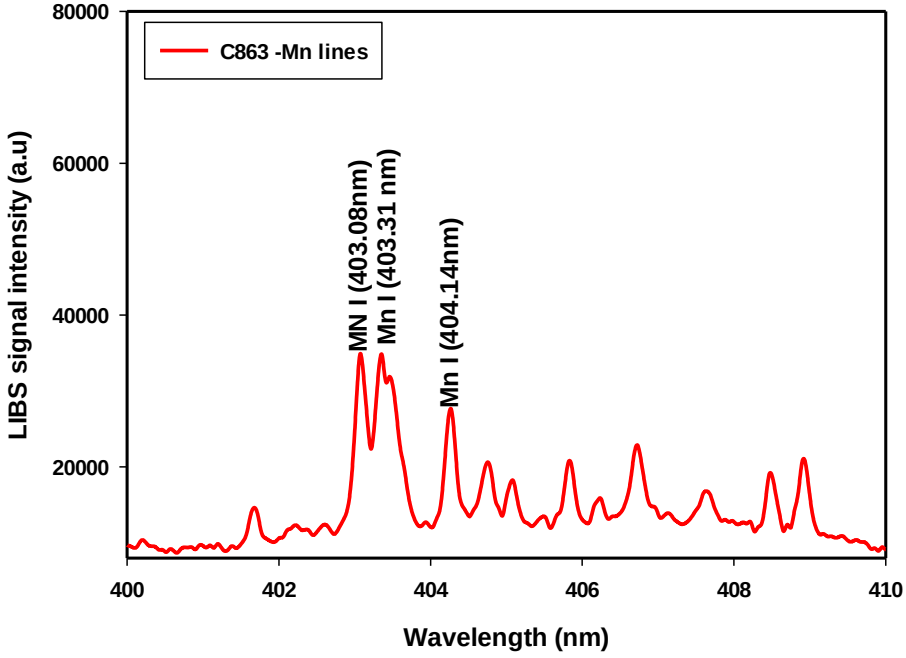

Figure 4.14: A typical LIBS spectrum recorded in 400-410nm region indicating persistent emission lines of manganese for 863 standard bronze sample

The elements identified in sample C932 include copper, tin and zinc. These elements are identified at the same wavelengths as aforementioned in other standard samples

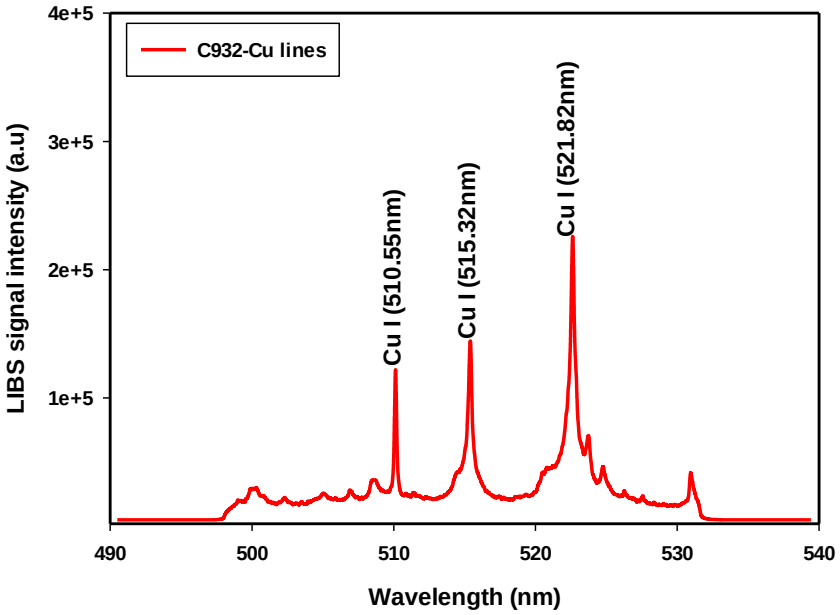

Figure 4.15: A typical LIBS spectrum recorded in 490-540nm region indicating persistent emission lines of copper for C932 standard bronze sample

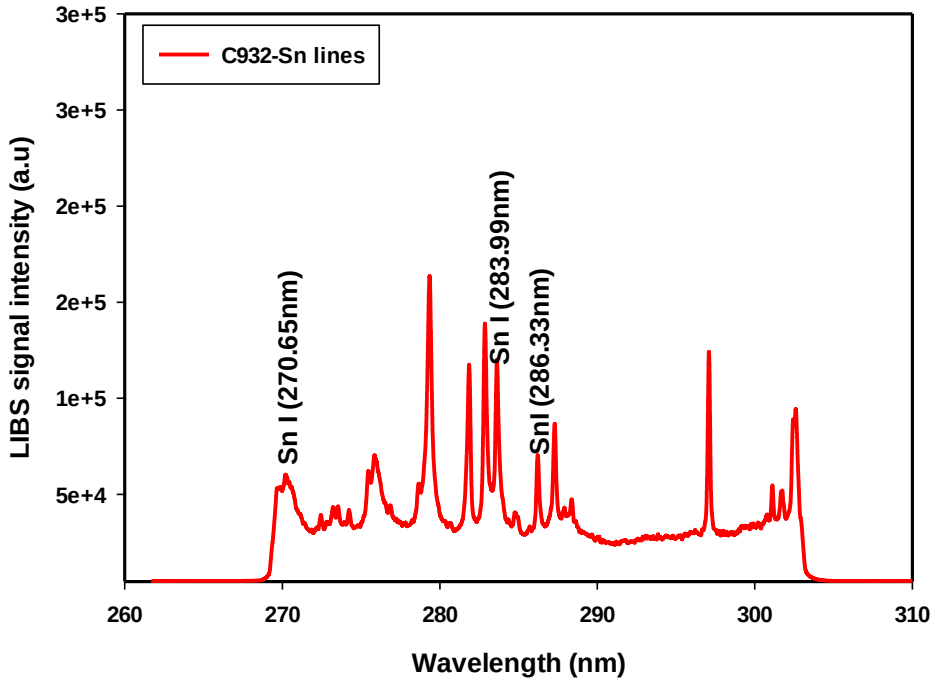

Figure 4.16: A typical LIBS spectrum recorded in 260-310nm region indicating persistent emission lines of tin for C932 standard bronze sample

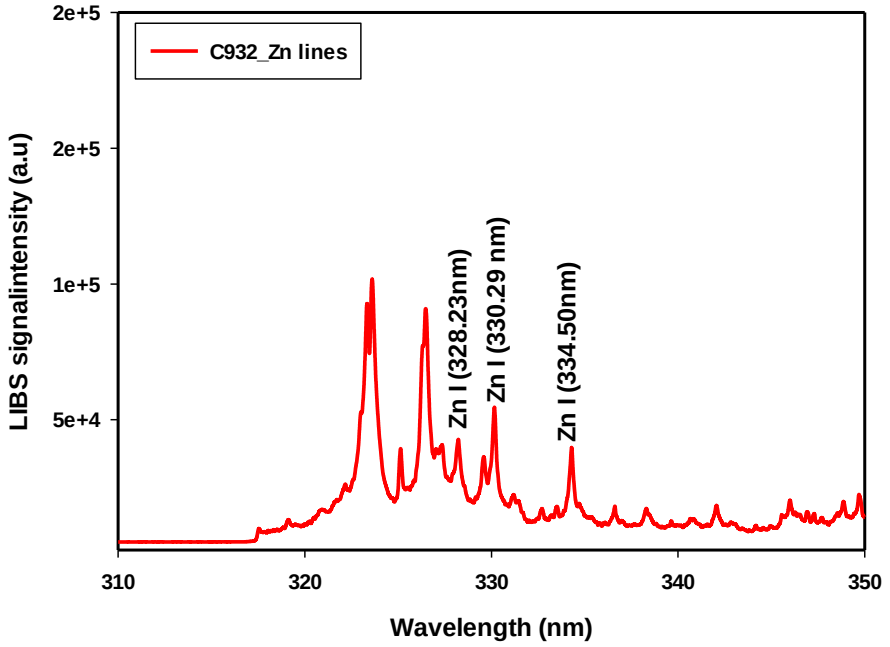

Figure 4.17: A typical LIBS spectrum recorded in 310-350nm region indicating persistent emission lines of zinc for C932 standard bronze sample

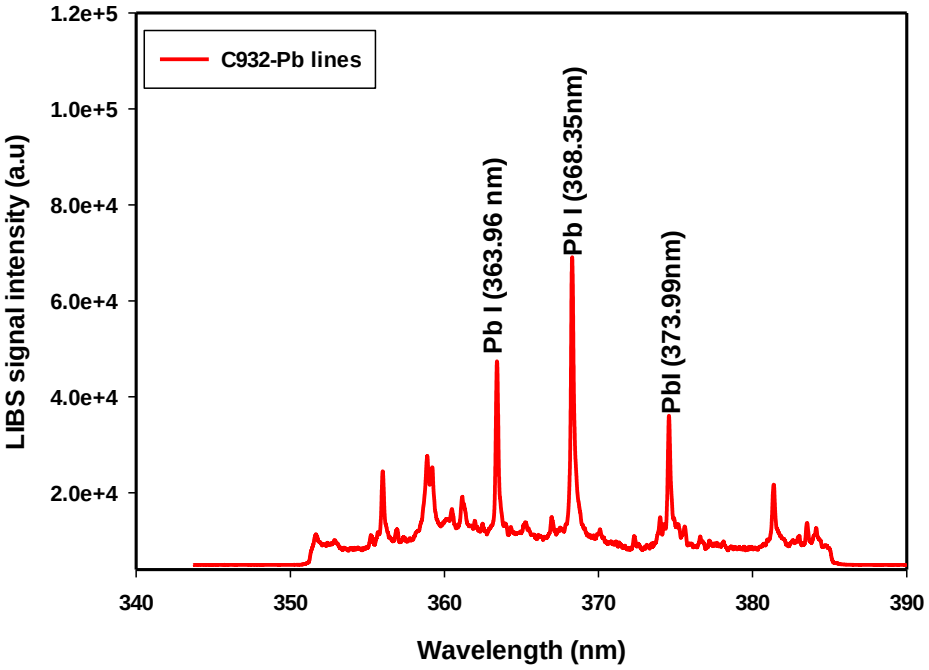

Figure 4.18: A typical LIBS spectrum recorded in 340-390nm region indicating persistent emission lines of lead for C932 standard bronze sample

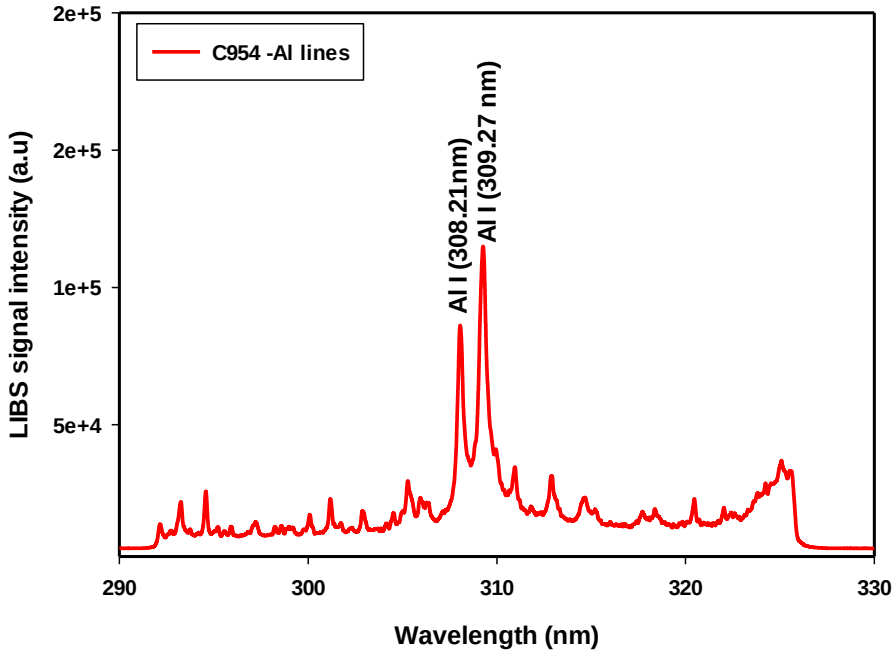

Figure 4.19: A typical LIBS spectrum recorded in 290-330nm region indicating persistent emission lines of aluminum for C954 standard bronze sample

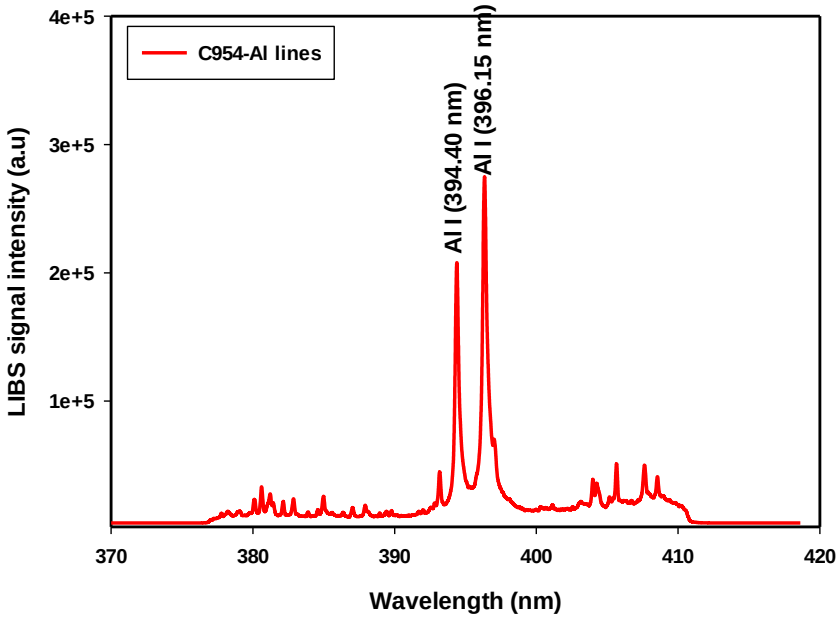

Figure 4.20: A typical LIBS spectrum recorded in 370-420nm region indicating persistent emission lines of aluminum (only line 394.40nm is used) for C954 standard bronze sample

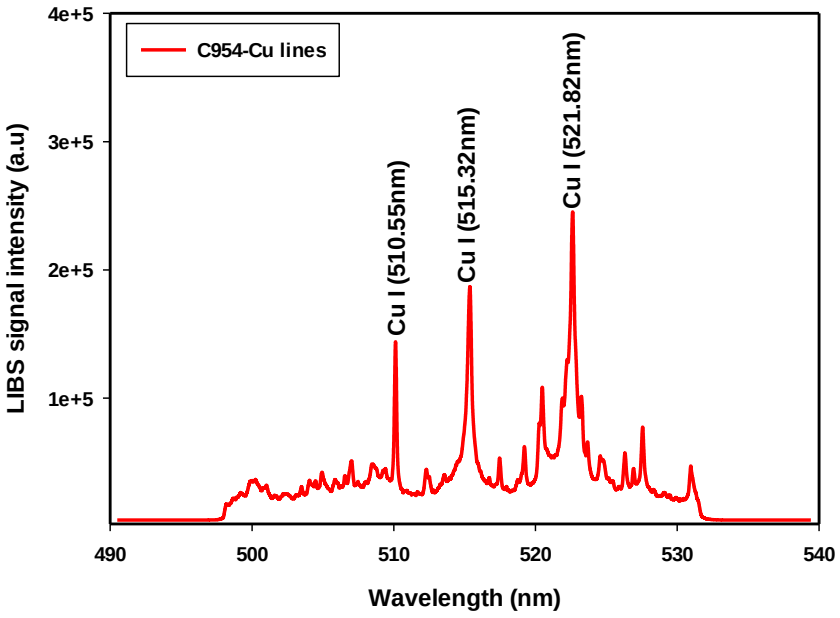

Figure 4.21: A typical LIBS spectrum recorded in 490-540nm region indicating persistent emission lines of copper for C954 standard bronze sample

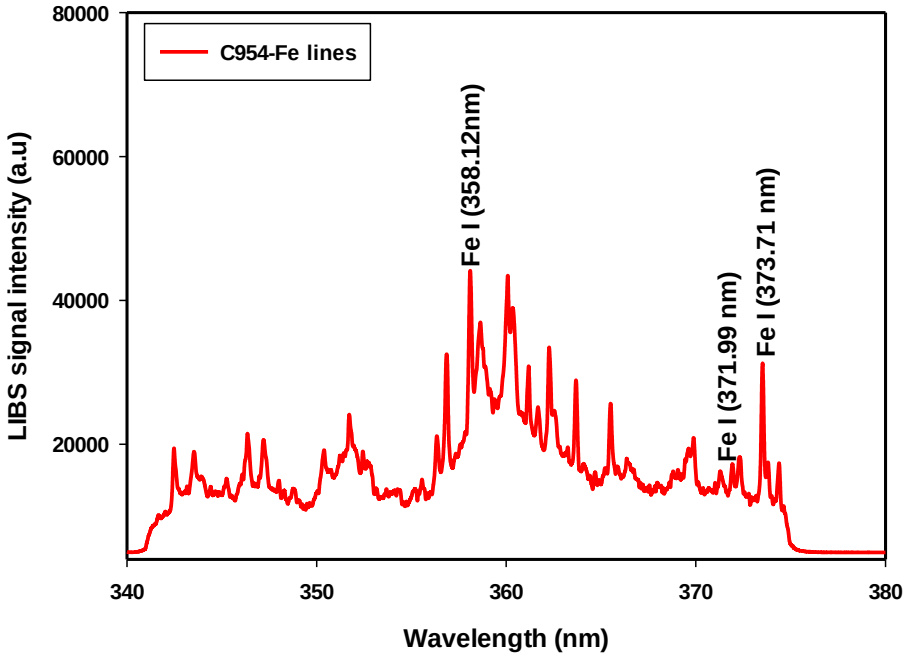

Figure 4.22: A typical LIBS spectrum recorded in 340-380nm region indicating persistent emission lines of iron for C954 standard bronze sample

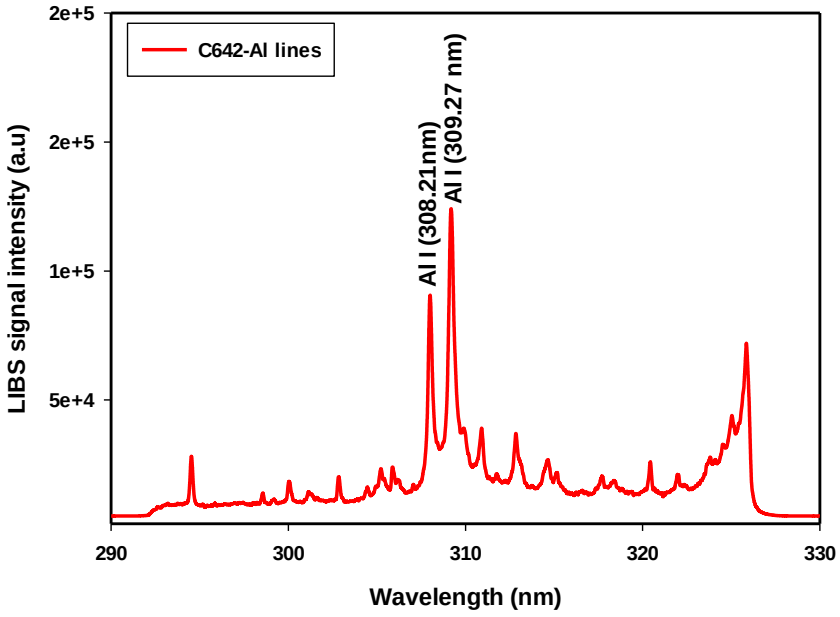

Figure 4.23: A typical LIBS spectrum recorded in 290-330nm region indicating persistent emission lines of aluminum for C642 standard bronze sample

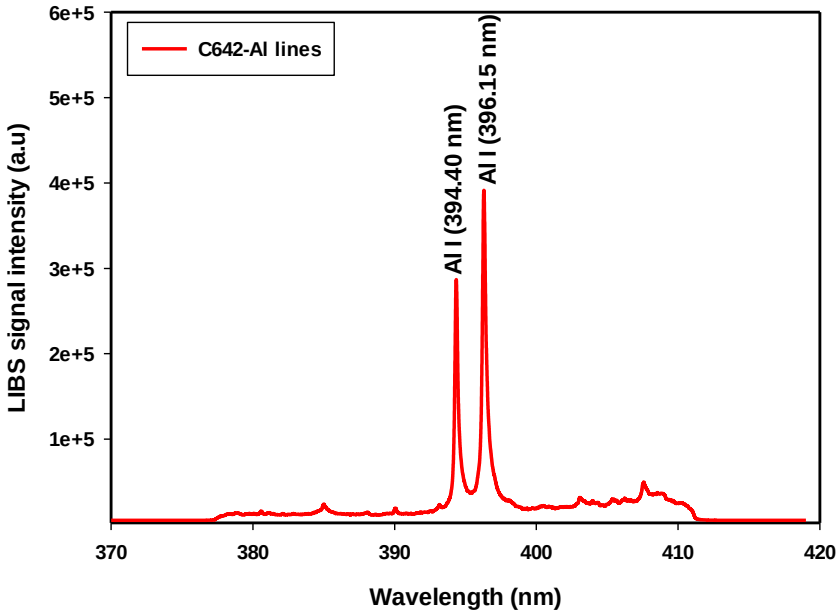

Figure 4.24: A typical LIBS spectrum recorded in 370-420nm region indicating persistent emission lines of aluminum (only line 394.40nm is used) for C642 standard bronze sample

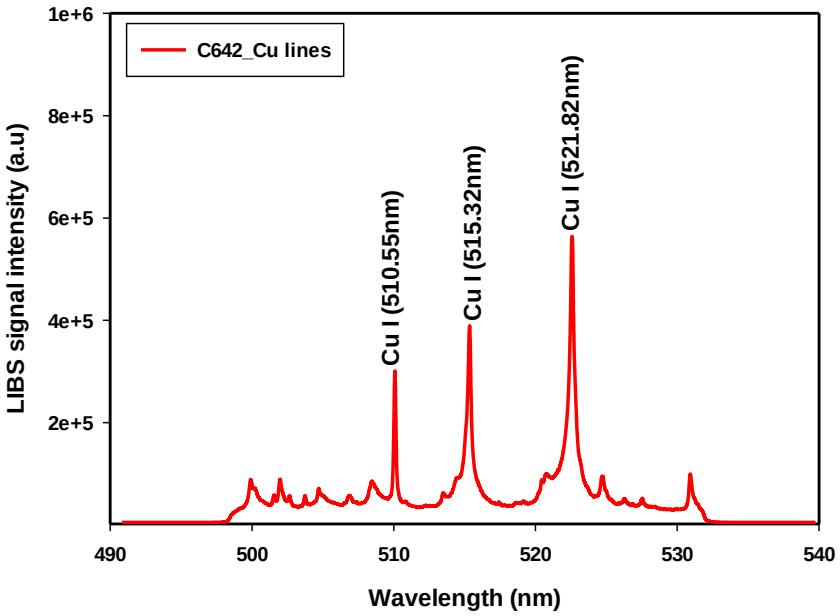

Figure 4.25: A typical LIBS spectrum recorded in 490-540nm region indicating persistent emission lines of copper for C642 standard bronze sample

4.2 Investigating the exploration and exploitation capacity of GSA to the number of agent

In order to maintain a balance between the exploitation and exploration ability of gravitational search algorithm for optimizing model parameters such as the number of epoch and hidden neuron in the developed SBLLM chemometric algorithm, number hidden neuron in the developed ELM algorithm as well as the regularization factor, epsilon and kernel option in SVR chemometric, the number of initial population of agents are varied from ten to thirty using three persistent emission lines in SBLLM chemometric algorithm.

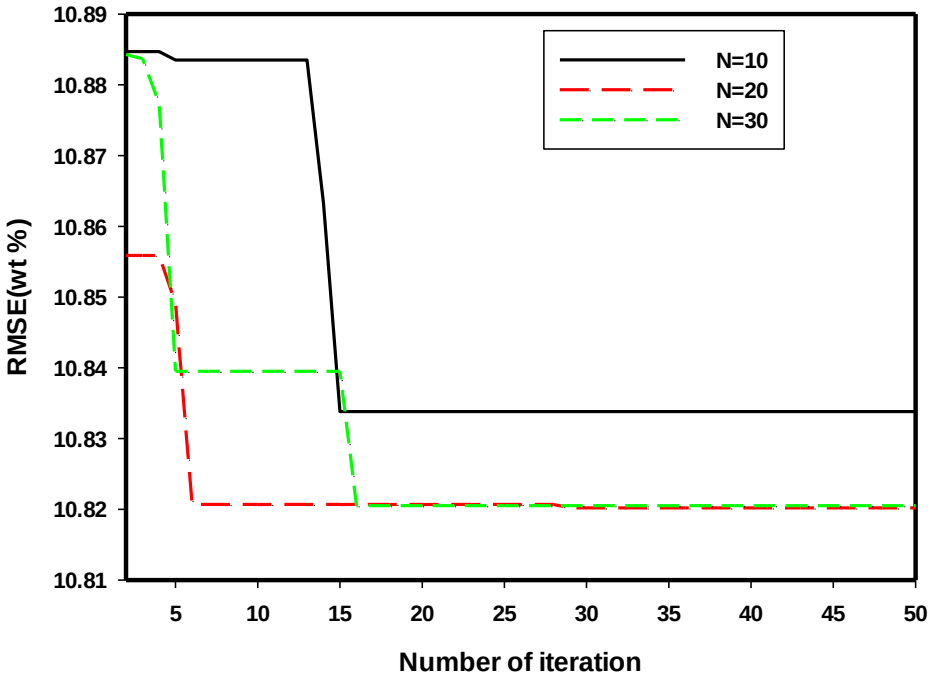

Figure 4.26: A graph of RMSE against the number of iteration for sensitivity of ELM chemometric to the initial population of agents (Single emission line)

At a small number of agents (say N=10 in Fig.4.30), the exploration capacity of the model becomes poor as the search space will be insufficiently explored as can be observed in Fig.4.26. Similarly, when large number of agent are assessing a given search space (say N=30 in Fig.4.26), complexity might set in. The optimum number of agents that maintains excellent exploration and exploitation capacity with special consideration to computational time complexity is obtained in Fig.4:26 as twenty. Although, thirty also shows an optimum value but twenty numbers of agents was used in all the remaining modeling and simulation because of lower computational time.

4.3 Convergence of SBLLM-GSA chemometric for single, double and three emission lines based model

While setting the number of agents to twenty, single emission line of each of the element presented in section 4.1 are input to the developed SBLLM-GSA chemometric to obtain an estimated concentration of each of the element. Another two SBLLM-GSA models were developed using double and three persistent emission lines and the results are compared in Fig.4.27. Molar mass and the wavelength of each of the elements are included into modeling and simulation so as to enhance the accuracy of the model. From Fig.4.27, SBLLM-GSA chemometric developed based on three emission lines has highest root mean square error (RMSE) followed the chemometric based double emission lines while the chemometric developed based on single emission line has the least value of RMSE. Since single emission line based chemometric is less computationally complex (this will be shown in next section), then single emission line is sufficient for effectively quantifying the elemental concentration using the developed SBLLM-GSA chemometric.

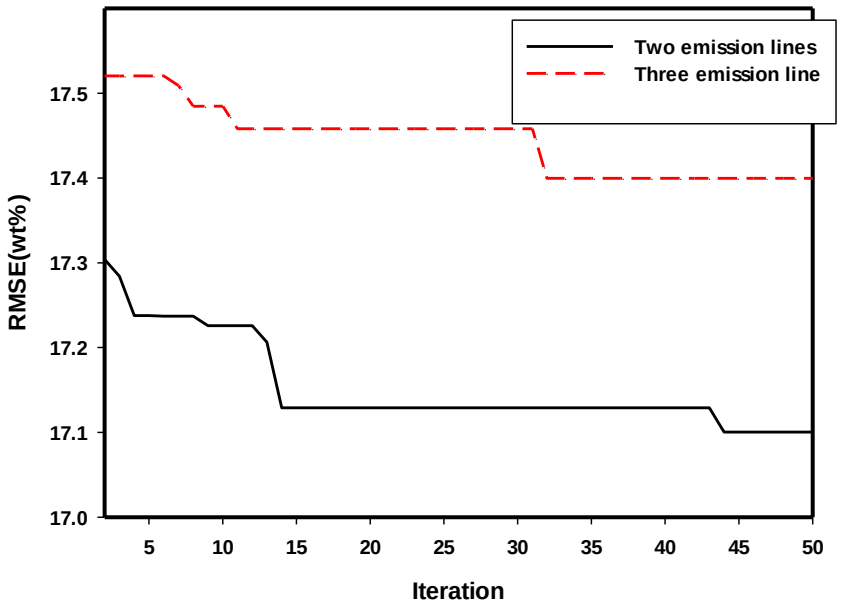

(a)

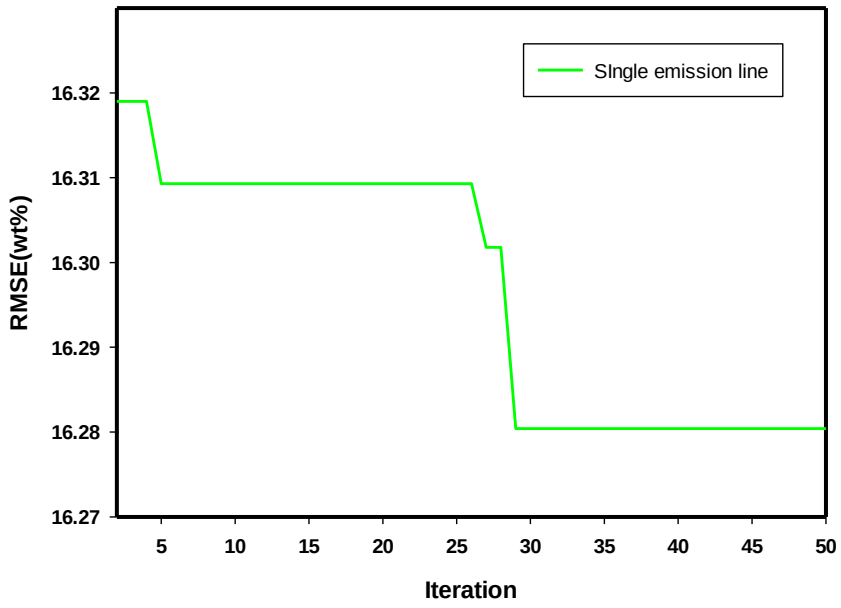

(b)

Figure 4.27: A graph of RMSE against the number of iteration for comparison between the convergence of single, double and three emission lines SBLLM-GSA chemometrics

4.4 Convergence of ELM-GSA chemometric for single, double and three emission lines based model

The significance of non-linear technique in chemometrics cannot be over-emphasized especially in LIBS where the chemical compositions of the materials are identified and quantified using mainly, emission line intensity [18]. The plasma generated due to laser ablation is often thick optically, which denotes complex interactions between the radiation and the constituent atoms/ions. This complexity strengthens non-linearity in the calibration function as the concentration progresses. Excluding this non-linearity and complexity of the plasma has profound effect on the quantitative analysis and the need for non-linear analytical modeling method becomes paramount for accuracy enhancement in LIBS spectra quantification. Extreme learning machine (ELM) is a non-linear chemometric method that is based on empirical risk minimization principle and has inherent characteristic of approximating many non-linear functions to linear ones [23] and has been proposed in this study for relating the elemental intensities with the compositions.

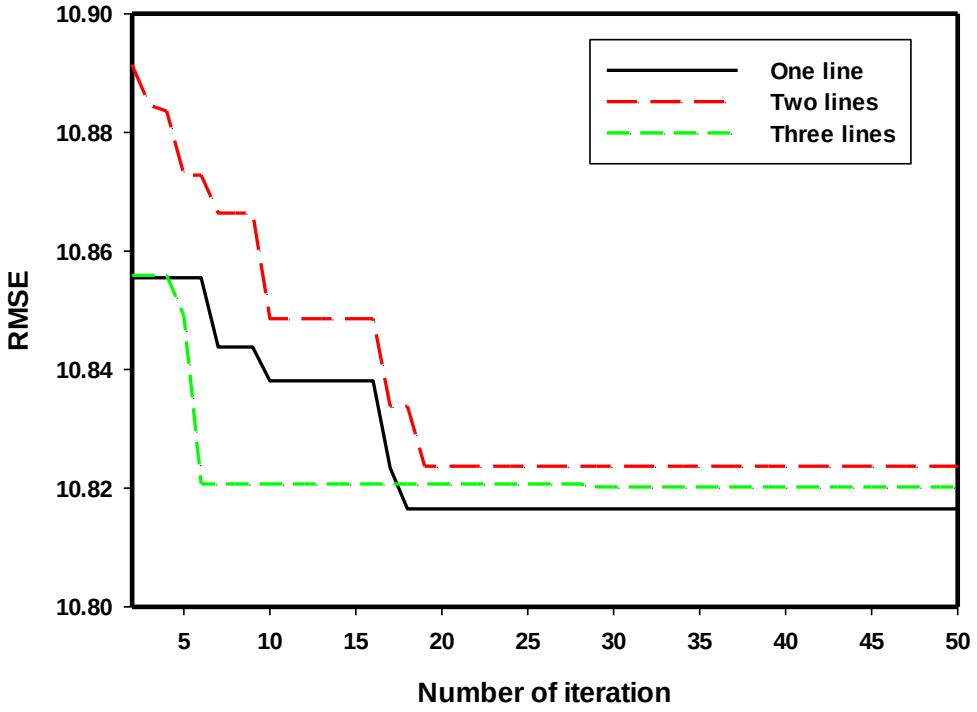

Figure 4.28: A graph of RMSE against the number of iteration for comparison between the convergence of single, double and three emission lines ELM-GSA chemometrics

The comparison between the convergences of three models based on ELM-GSA is presented in Fig.4.28. ELM-GSA model developed using single persistent emission lines converges at lowest RMSE while ELM-GSA developed using double and three emission lines show similar convergence with values higher than that of single emission line based model.

It can be easily deduced from the results of SBLLM-GSA and ELM-GSA chemometrics that single emission line is sufficient to build the developed chemometrics with reasonable degrees of accuracy. The computational complexity perspective of preferring single emission lines to multiple is detailed in next section of this chapter.

4.5 Performance comparison between SBLLM-GSA and ELM-GSA chemometrics

Performance comparison between the developed hybrid SBLLM-GSA and ELM-GSA chemometrics is presented in Fig.4.29. The comparison shows that ELM-GSA chemometric outperform SBLLM-GSA chemometric with performance improvement of 33.54%.

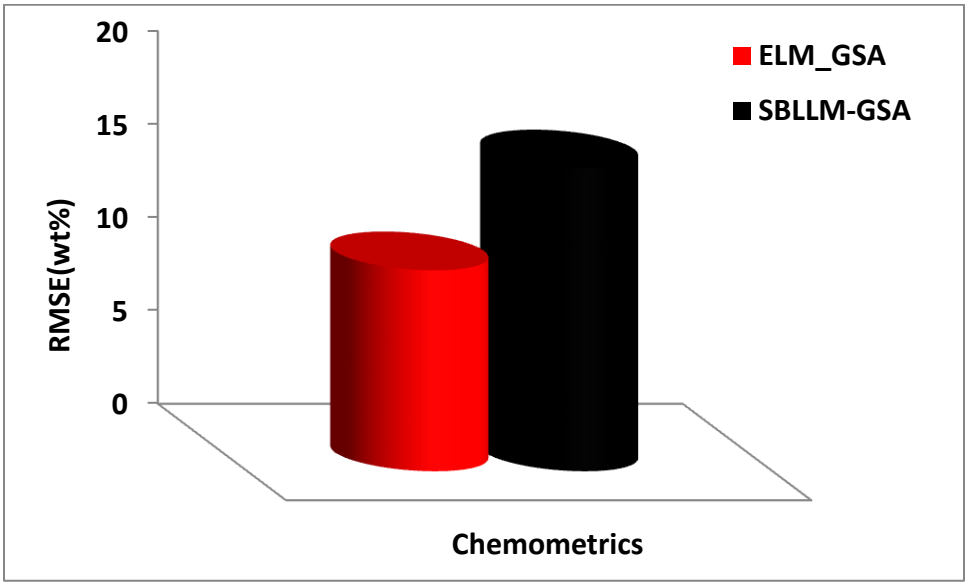

Figure 4.29: A graph of RMSE against the developed chemometric models for performance comparison between the developed chemometrics

The inherent ability of extreme learning machine to approximate non-linear function to a linear one distinguishes it from other computational intelligence based chemometrics. Hence, only performance of ELM based chemometrics would be improved in the next chapter of this report.

4.6 Comparison of the computational complexity of the developed chemometrics with respect to the number of emission lines employed in model development

The comparison between the computational complexities of the developed chemometrics as the number of input emission line increases is depicted in Fig.4.30.

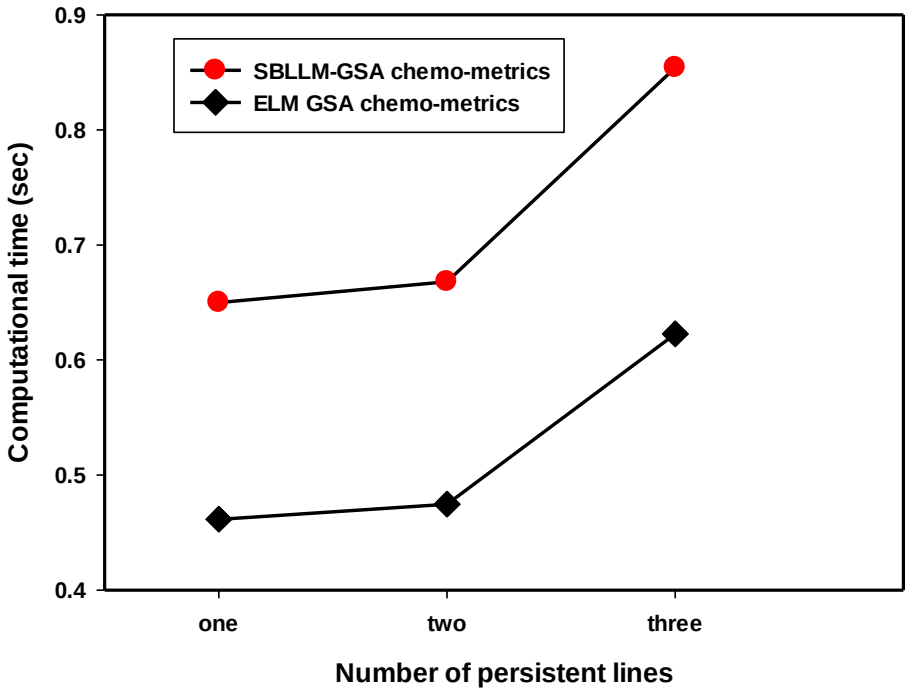

Figure 4.30: A graph of computational time against the number of persistent lines for comparison of the computational complexities of the developed chemometrics with respect to the number of input emission lines

The simulation and modeling was conducted using Samsung personal computer with Processor: Intel(R) Core™ i5-2450M CPU @ 2.50 GHz and RAM of 8GB. Comparison between the SBLLM-GSA model that employs single emission line with double emission line and three emission lines shows that SBLLM-GSA chemometrics with single emission line is 2.79% and 31.41% , respectively faster. Similarly for ELM-GSA based

chemometrics, Single emission line based ELM-GSA chemometric is 6% and 40.17% faster than double and three emission lines based chemometrics, respectively.

4.7 Comparison of the computational complexity of SBLM-GSA and ELM-GSA chemometrics

Fig.4.31 presents the comparison between the computational complexity of SBLLM-GSA and ELM-GSA based chemometrics. ELM-GSA chemometric is 46.36% faster than SBLLM-GSA chemometric. This can be attributed to the fact that ELM-GSA chemometric trains single-hidden layer feed-forward neural networks using a novel learning algorithm different from the popular gradient-based learning algorithms such as Levenberg-Marquardt and back-propagation which are known to be slow and sometimes converge to local minimum [24], [25]. ELM algorithm randomly selects input weights and hidden biases and determines the output weights analytically with the aid of Moore-Penrose generalized inverse matrix. The input weights relate the input layer to the hidden layer while the output weights link the hidden layer to output layer. The learning scheme adopted by ELM results into a fast learning rate, excellent generalization performance and non-convergence to local minimum.

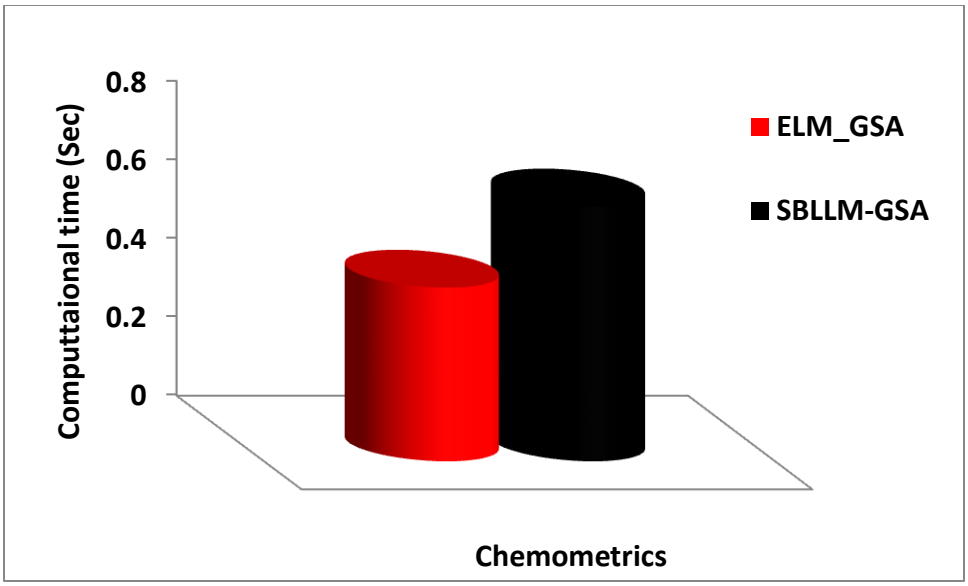

Figure 4.31: A graph of computational time against the developed chemometric models for comparison between the computational complexity of SBLLM-GSA and ELM-GSA chemometrics

The results of the modeling and simulation presented in this chapter show that single emission line is sufficient for elemental quantification using the developed hybrid chemometrics. Chemometrics developed using single emission lines are faster than the chemometrics developed using multiple emission line while the accuracy is preserved in single emission line chemometrics. Furthermore, the developed ELM-GSA chemometrics are more accurate and faster than SBLLM-GSA chemometrics.

5 CHAPTER 5

Results and discussion: standard bronze sample

5.1 Results of the methods of enhancing the performance of the developed chemometrics

This chapter presents the results of the proposed methods of enhancing the performance of the developed chemometrics and the comparison between the developed chemometrics (hybrid ELM-GSA) and the existing one (SVR). The proposed methods of performance enhancement include internal reference preprocessing method and homogenous hybridization. All the modeling and simulations presented in this chapter were carried out using single emission line since we have found from the results presented in chapter 4 that single emission line is sufficient for the developed chemometrics tools in term of accuracy and computational complexity. Identification of emission lines obtained after LIBS measurement on all standard samples is presented here over a wide range of wavelength since the entire (indicated by the manufacturer) major and minor elements of each of the standard samples are quantified. Before applying the chemometric tools for quantitative analysis, the existence of plasma in local thermodynamic equilibrium was ascertained through satisfaction of McWhirter criterion as well as electron energy distribution function (EEDF). The significance of the proposed three novel methods of chemometric performance enhancement was demonstrated using SVR and ELM

chemometrics. Finally, the results of the chemometrics with inclusion of the proposed methods of performance enhancement were compared with chemometric tools in which the proposed methods were not implemented.

5.2 Emission line identification of standard bronze samples

The LIBS spectra obtained for the seven standard bronze samples are presented in this section. Emission lines of each of the elements indicated by the manufacturer are well identified. Similarly, spectrum that shows the emission line used for modeling (highlighted in blue) and normalization (highlighted in red) are also presented. The spectrum of C640 standard bronze sample shown in Fig.5.1 presents the persistent emission lines of neutral copper (Cu) at wavelength of 510.63nm, 515.00nm and 521.39nm while the emission line of neutral iron at (Fe) wavelength of 388.42nm and 438.80nm are identified. Similarly emission lines of neutral nickel (Ni) are also identified at different specific wavelengths. The presence of neutral manganese is also identified at wavelength of 403.76nm. The spectral indicating the intensities used for modeling and normalization (while implementing IRP) for sample C640 is shown in Fig.5.2

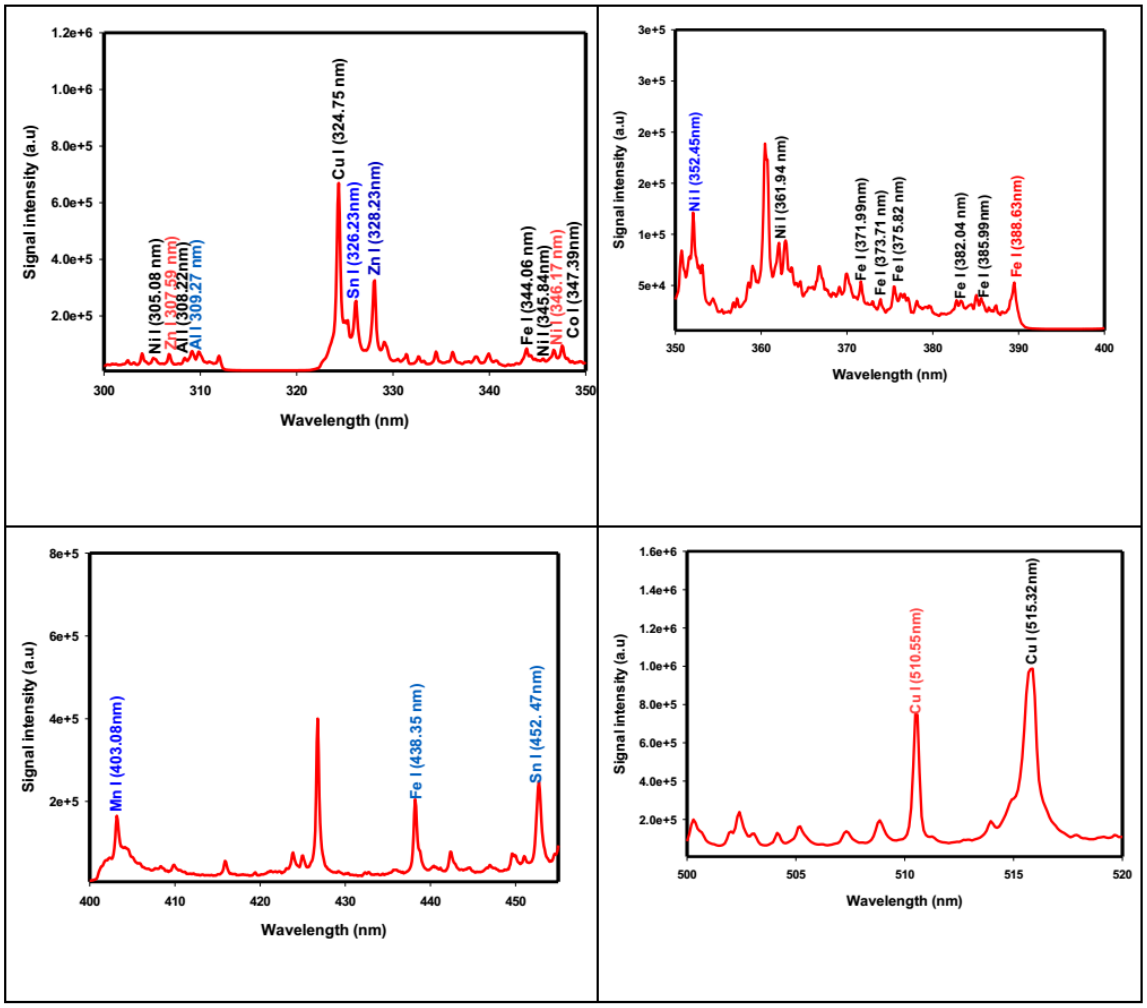

Figure 5.1 A typical LIBS spectrum recorded for C640 standard bronze indicating the intensity (highlighted in blue) used for chemometrics modeling and intensity (highlighted in red) used for IRP normalization

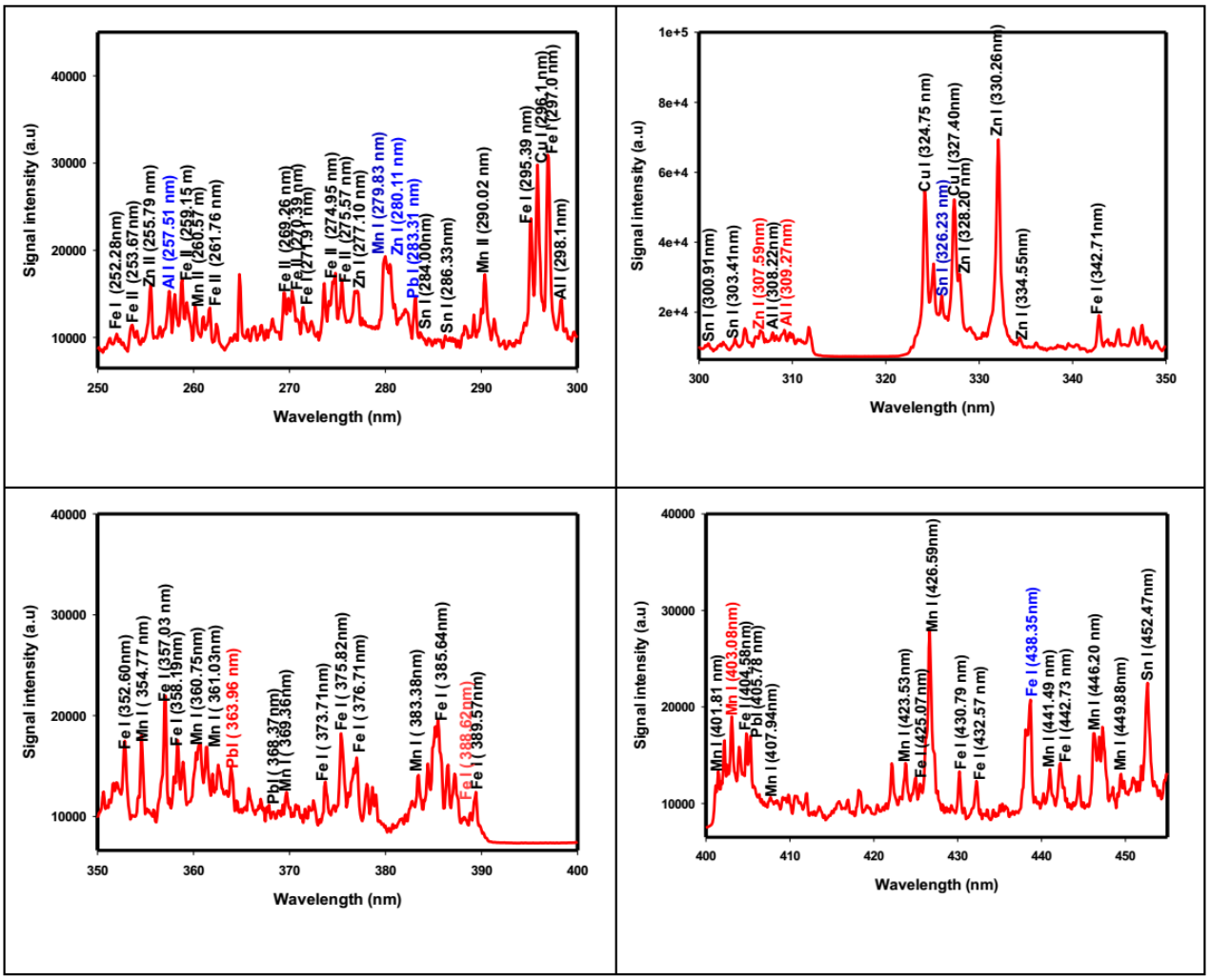

Figure 5.2: A typical LIBS spectrum recorded for C863 standard bronze indicating the intensity (highlighted in blue) used for chemometrics modeling and intensity (highlighted in red) used for IRP normalization

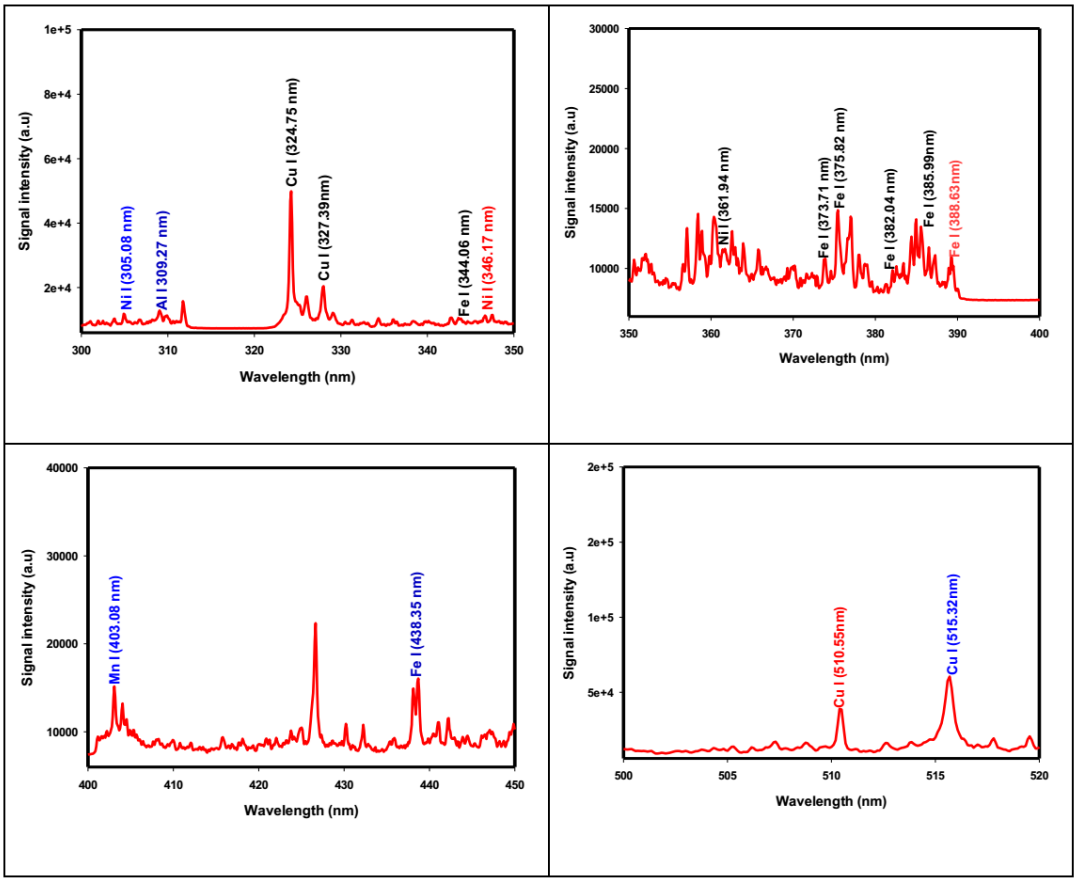

Figure 5.3: A typical LIBS spectrum recorded for C954 standard bronze indicating the intensity (highlighted in blue) used for chemometrics modeling and intensity (highlighted in red) used for IRP normalization

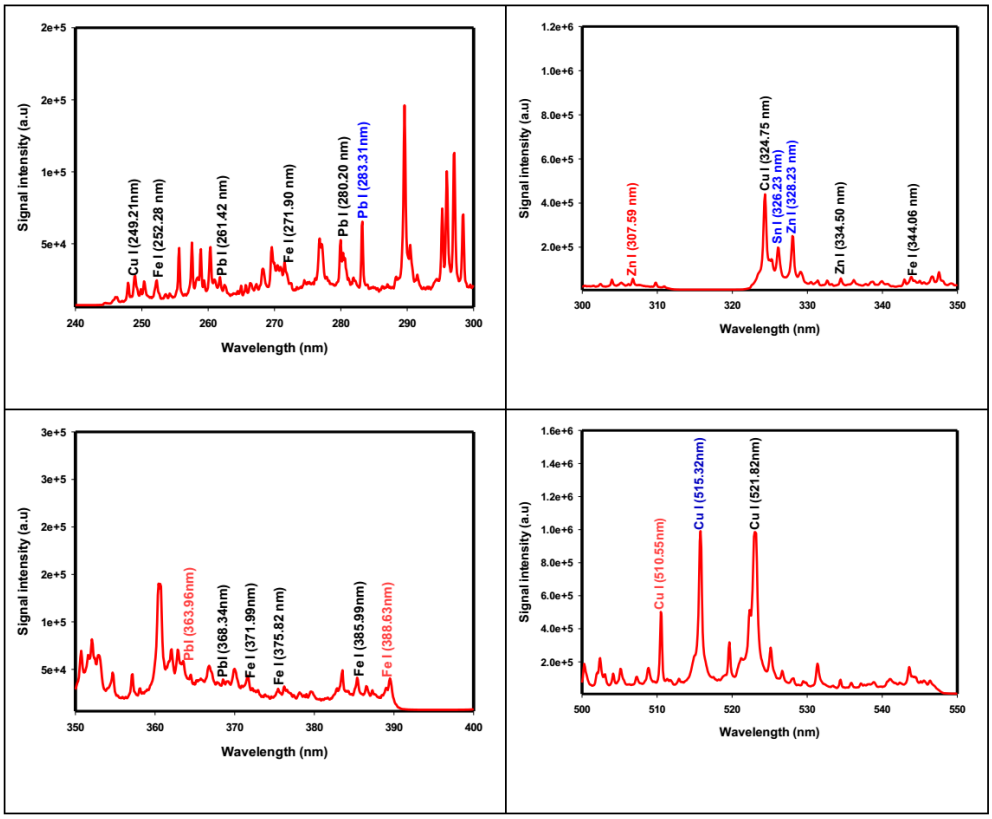

Figure 5.4: A typical LIBS spectrum recorded for C655 standard bronze indicating the intensity (highlighted in blue) used for chemometrics modeling and intensity (highlighted in red) used for IRP normalization

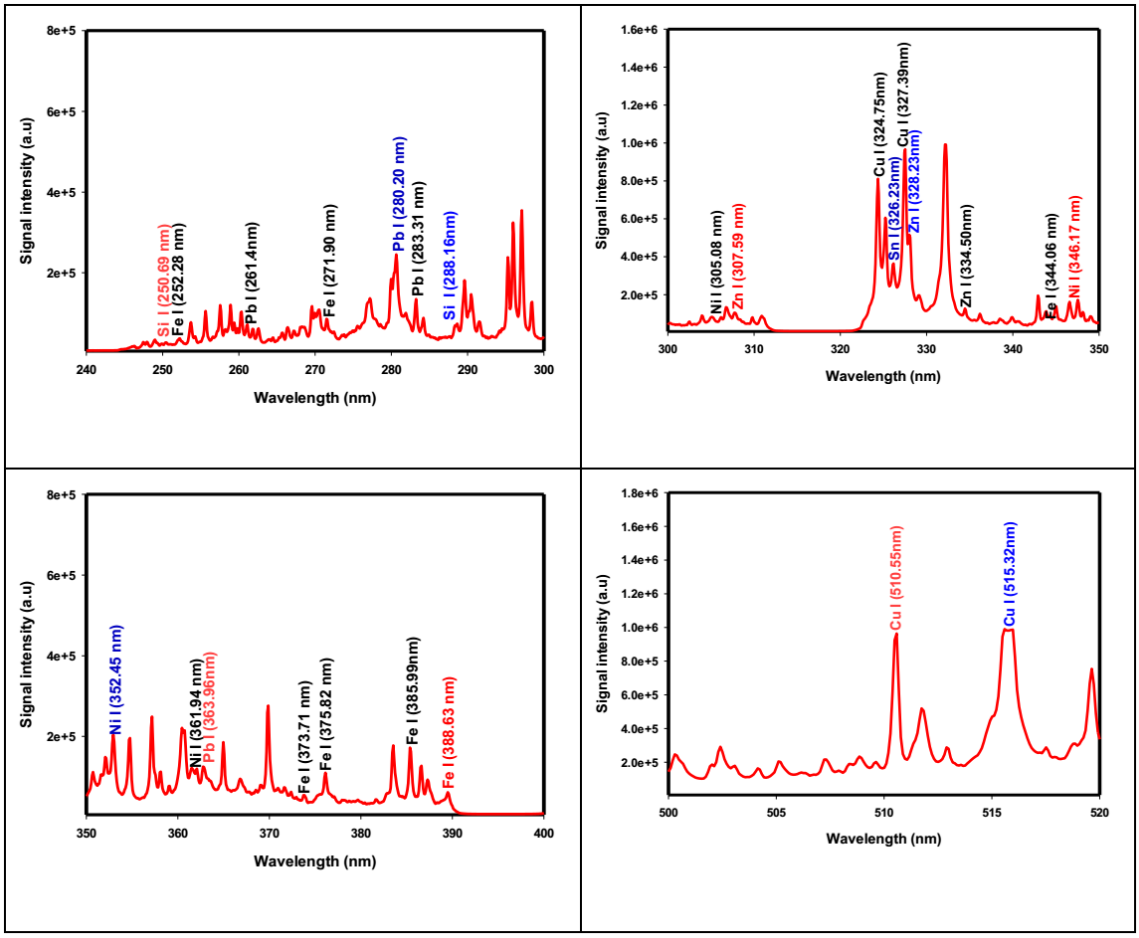

Figure 5.5: A typical LIBS spectrum recorded for C673 standard bronze indicating the intensity (highlighted in blue) used for chemometrics modeling and intensity (highlighted in red) used for IRP normalization

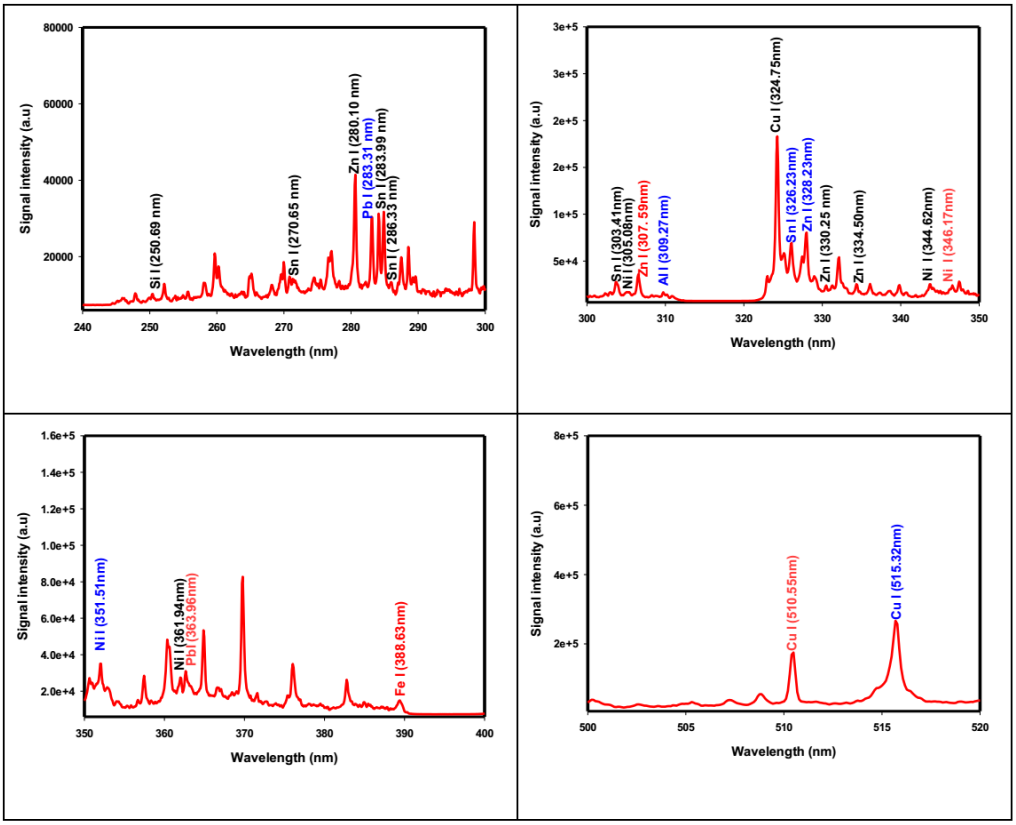

Figure 5.6: A typical LIBS spectrum recorded for C932 standard bronze indicating the intensity (highlighted in blue) used for chemometrics modeling and intensity (highlighted in red) used for IRP normalization

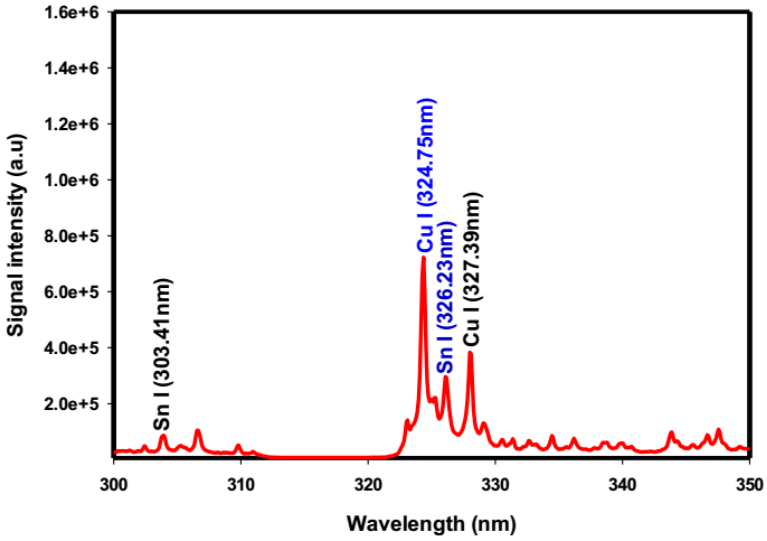

(a)

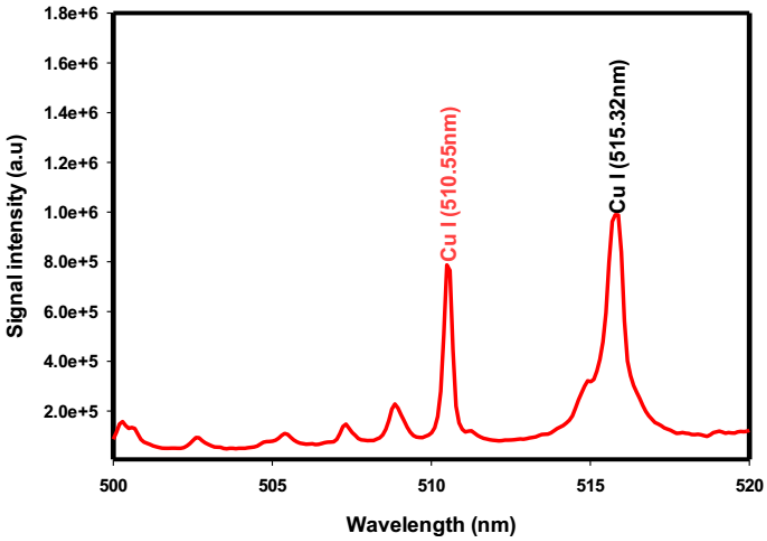

(b)

Figure 5.7: A typical LIBS spectrum recorded for C510 standard bronze indicating the intensity (highlighted in blue) used for chemometrics modeling and intensity (highlighted in red) used for IRP normalization

Similarly, Fig.5.3 shows the results of LIBS measurement performed on C863 standard bronze sample. The finger print of elements identified include aluminum (Al), lead (Pb), zinc (Zn), iron (Fe) and copper (Cu). Like Fig.5.1, the persistent emission lines of neutral copper (Cu) were identified at wavelength of 510.63nm, 515.00nm and 521.39nm while singly ionized aluminum emission lines are identified at 257.62nm, 298.1 nm and 466.85 nm. Other elements identified in this sample include tin at a wavelength of 452.38nm and

neutral zinc at wavelengths of 328.2 nm and 330.70 nm. The spectral indicating the intensities used for modeling and normalization (while implementing IRP) for sample C863 is shown in Fig.5.4 .Fig.5.5 presents the spectrum of standard bronze sample with trade name of C954. Similarly, copper, iron and other elements specified by the manufacturer are identified at their unique wavelengths. The details of the elemental constituents of each of the standard bronze samples can be found in table 3.1.

5.3 quantitative analysis results performed on the standard bronze sample

Since the operational physical principles of LIBS include formation of high temperature plasma when laser pulse ablates the material of interest, emission of specific light during plasma cooling and dispersion of the emitted light in accordance to their wavelengths, the probability of transitions as well as the degeneracy of the states in which transitions occur influence the state population and concentrations of the constituent species in accordance to Boltzmann distribution. All these parameters together with the energy of transition are incorporated into the present model in order to enhance its robustness and precision. It should be noted that the models developed in this work presume that the plasma is in local thermodynamic equilibrium and the ablation is stoichiometry (high power density on the target ensures this criteria) while the optical thinness is difficulty to be achieved in

real plasma especially for most intense lines such as resonance line. Therefore, before the implementation of the proposed models, local thermodynamic equilibrium was ensured through electron energy distribution function and McWhirter criterion fulfillment

5.3.1 Validation of local thermodynamic equilibrium criteria for standard bronze sample plasma

A situation where the distributions of all plasma components (atoms, electrons, radiation and ions) are characterized by distinct value of temperature is refereed as local thermodynamic equilibrium (LTE). Achieving LTE state is practically impossible since it requires full equilibrium state between the plasma components and the plasma must therefore by optically thin so as to prevent loss of photons [8]. However, with the assumption that the energy lost due to escaping photons is small compared to the total energy of the plasma, then attaining LTE is possible and the distribution of atoms, electrons and ions could be modeled using Saha-Boltzmann and Maxwell equations. Ensuring LTE is very significant in deriving the global population distribution of electronics levels of elemental species using the upper level population of the observed transitions [130], [131]. The outcome of calibration free approach of elemental quantification in LIBS becomes unreliable without quantitatively verifying the LTE conditions. The McWhirter criterion that for stationary and homogenous plasmas, the collision rate dominates radiative processes in LTE is often used in LIBS analysis [132]. Although, McWhirter LTE validity condition is necessary for laser-induced plasmas but rather insufficient since the plasmas are inhomogeneous and evolve in time [133]. Another condition that compliments McWhirter criterion for the validity of LTE is the assumption that the attainment of ionization –excitation equilibrium requires a large time

scale as compared to the rate of variation of thermodynamic parameters such as electron density and plasma temperature. In other word, thermodynamic parameters do not change towards the attainment of equilibrium state [8]. In this study, the LTE condition of the plasma was ensured and verified using electron energy distribution function (EEDF) and McWhirter criterion. EEDF holds when $N_e > 10^{16} cm^{-3}$ (where N_e is the electron density) and $k_B T < 5\ eV$ (where k_B and T respectively represent the Boltzmann constant and plasma temperature) while McWhirter criterion is contained in equation (5.1) as described in [132].

$$\begin{cases} N_e \geq F(T,E), in\ LTE \\ N_e < F(T,E),\ \text{not in LTE} \\ F(T,E) = 1.6X10^{12} T^{1/2} (\Delta E)^3 \end{cases} \qquad (5.1)$$

where ΔE represents energy difference between upper and lower levels for the transition

Plasma temperature was determined from the slope of Boltzmann plot for Cu I at wavelengths of 324.75nm, 510.54nm, 515.32nm and 521.82nm while ΔE and other parameters were extracted from NIST database. Boltzmann plot is a plot of $In\frac{I_\lambda^{ij}}{A_{ij} g_i}$ against upper level energy (E_i) as formulated from equation (5.2).

$$I_\lambda^{ij} = N_s A_{ij} \frac{g_i \exp\left(-E_i / k_B T\right)}{U_s(T)} \qquad (5.2)$$

Where λ = transition wavelength, g_i = degeneracy of the *ith* level, N_s = emitting atomic number density (particle/cm^3) for each species, A_{ij} = transition probability of the Cu I line intensity, $U_s(T)$ = partition function of s species at plasma temperature.

Boltzmann plot through which the plasma temperature for standard sample C932 was determined are presented in Fig. 5.8, while Fig.5.9 shows the Boltzmann plot for sample C510. Plasma temperature of standard bronze sample C863 was determined from the plot presented in Fig.5.10 while Fig. 5.11 shows the Boltzmann plot for sample C673.

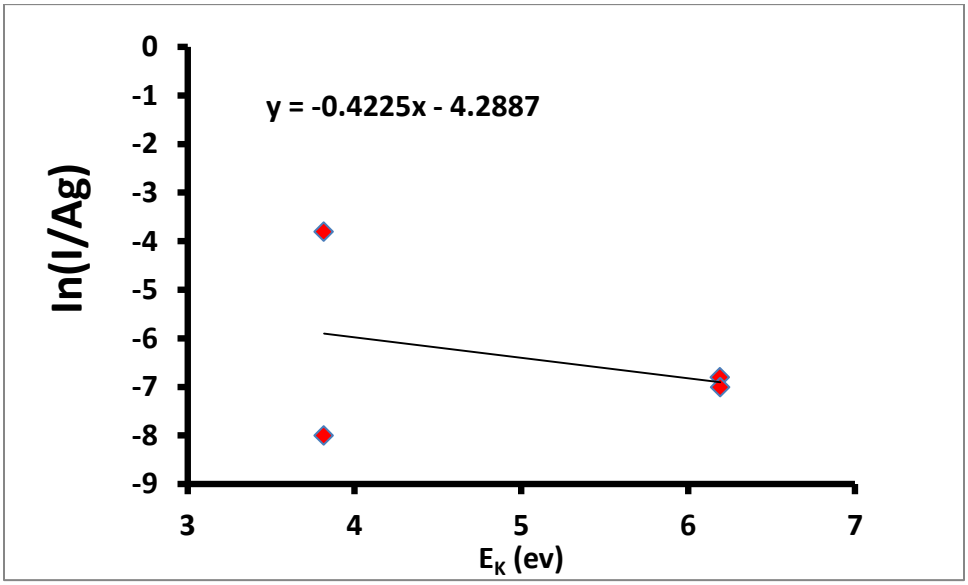

Figure 5.8: Boltzmann plot of sample C932 for plasma temperature determination

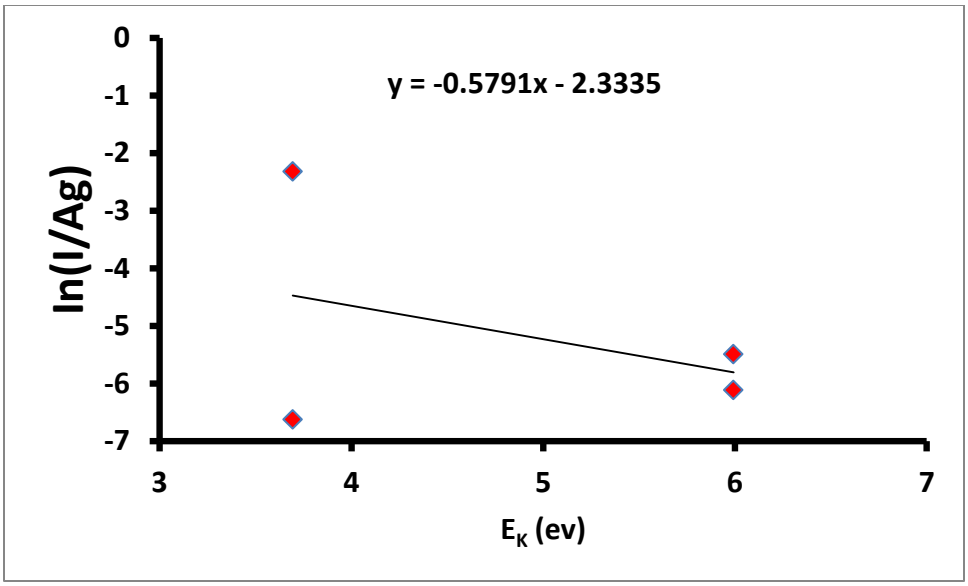

Figure 5.9: Boltzmann plot of sample C510 for plasma temperature determination

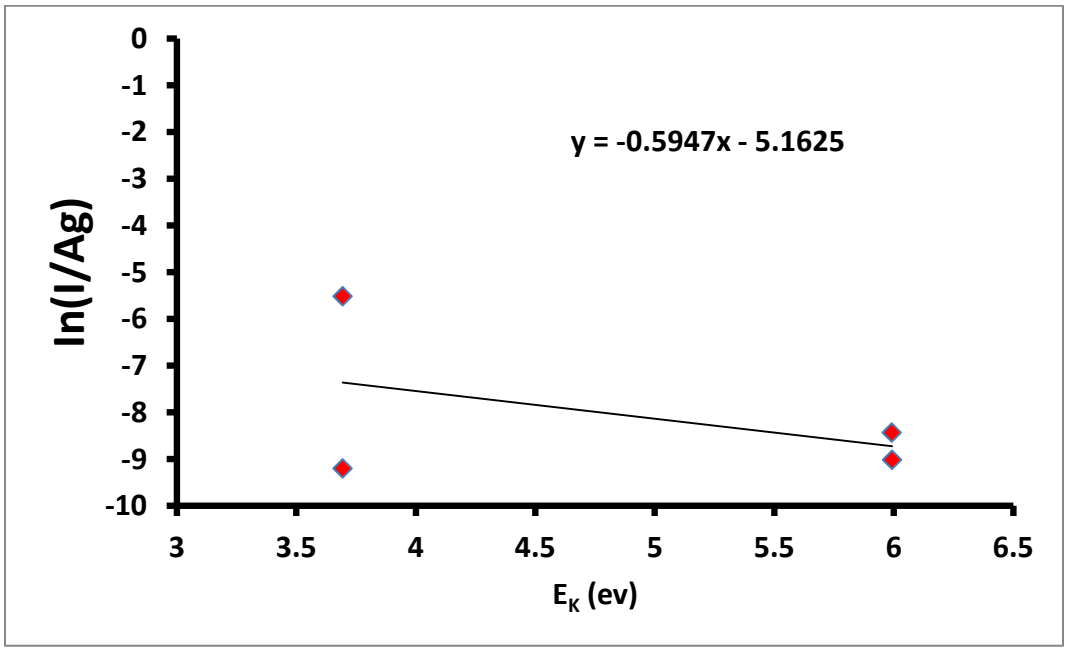

Figure 5.10: Boltzmann plot of sample C863 for plasma temperature determination

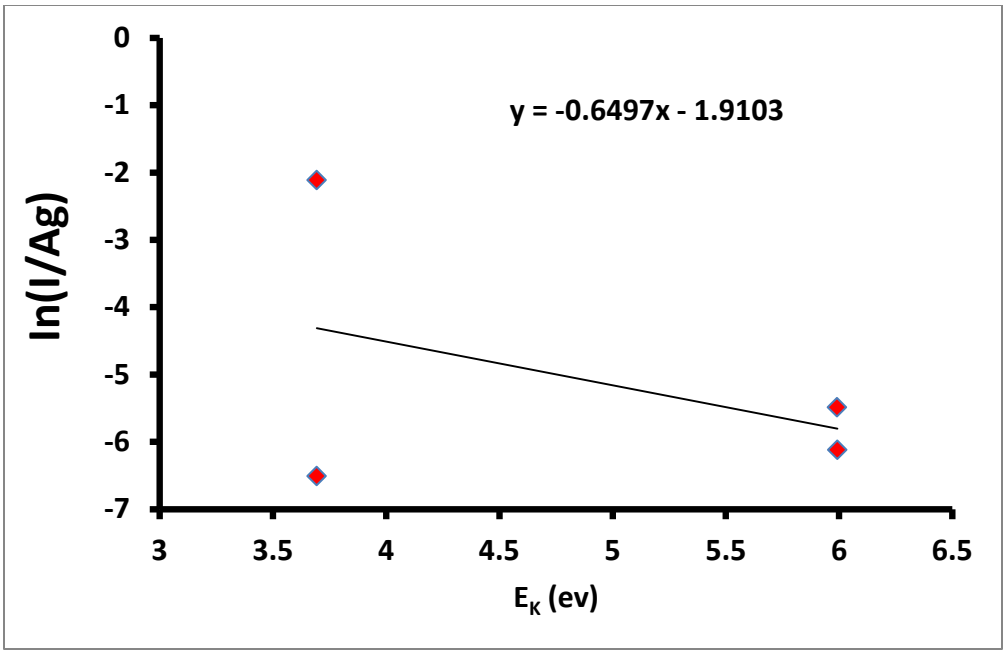

Figure 5.11: Boltzmann plot of sample C673 for plasma temperature determination

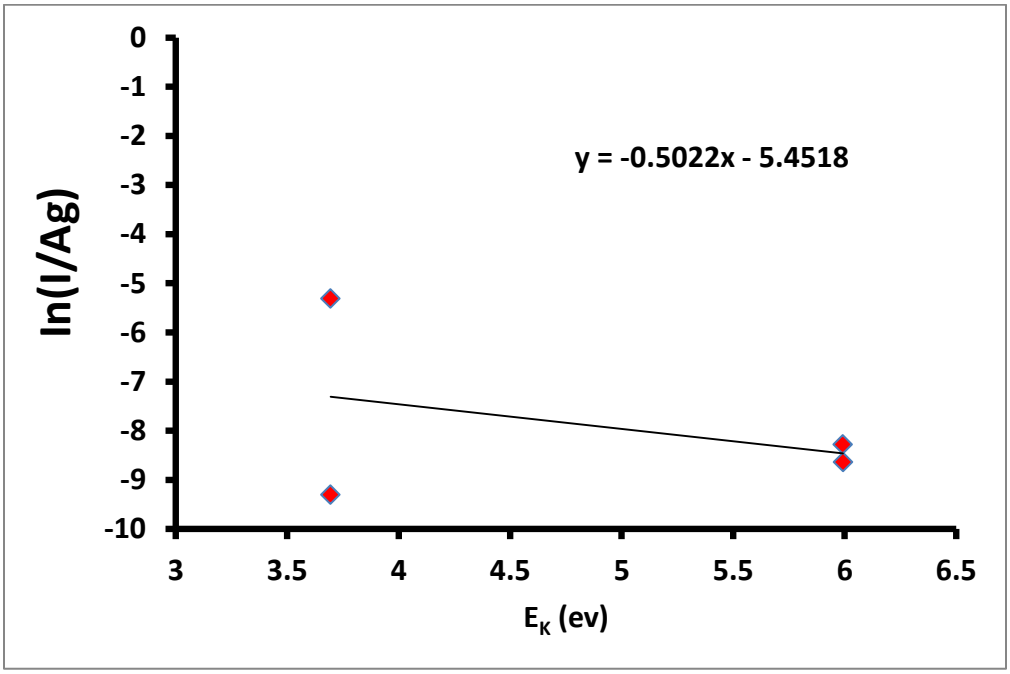

Figure 5.12: Boltzmann plot of sample C954 for plasma temperature determination

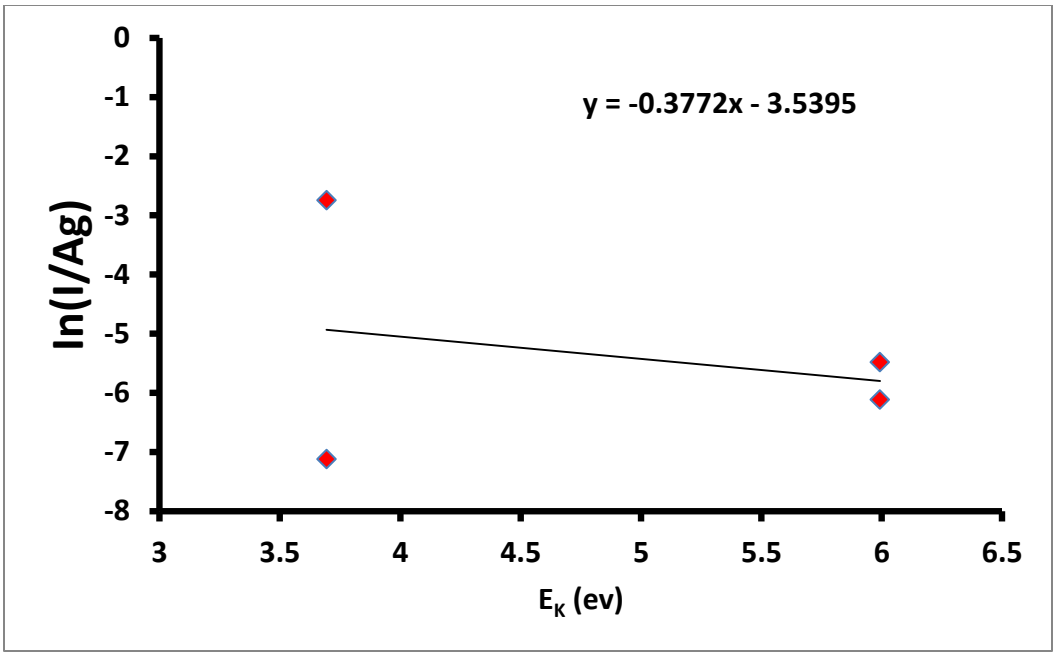

Figure 5.13 Boltzmann plot of sample C655 for plasma temperature determination

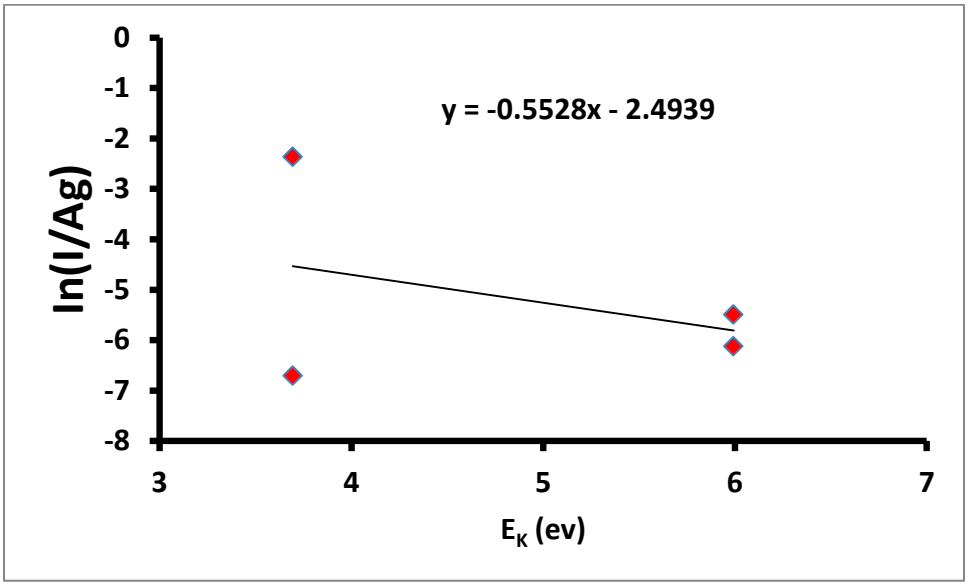

Figure 5.14 Boltzmann plot of sample C642 for plasma temperature determination

Fig.5.12 presents the graph through which plasma temperature of the sample C954 was determined while Fig.5.13 and Fig.5.14 show similar plots for standard bronze samples C655 and C642, respectively. Table 5.1 shows the values of the plasma temperature for each of the sample. Electron density for each of the samples was estimated from stark

broadened profile of Cu I at the value of wavelength of 510.55nm. Although, Doppler broadening (due to varying velocity of different atomic species and resulted into Doppler shift) as well as pressure broadening (emanating from frequency disturbance due to the interaction between the radiating atoms with their surrounding particles) are probable for major line broadening in LIBS spectrum, however, stark broadening (splitting of energy level as a result of plasma induced electric field) dominates [134]. The Lorentzian function that relates the wavelength ($\Delta\lambda_{1/2}$) for the full width at half maximum (FWHM) of the broadening profile with the electron density is presented in equation (5.3) while electron densities for Cu I emission line intensity are presented in table 1.

$$\Delta\lambda_{1/2} = 2W\frac{N_e}{10^{16}} \quad (5.3)$$

where W is the electron impact parameter in angstrom. The values of W used for this work were obtained from [135]

Table 5.1: Plasma Parameter for LTE verification using Cu I line (at 510.55nm) in each of the sample

Sample	Slope of Boltzmann plot	Plasma temperature (K)	K_BT(ev)	F(T,E) cm^{-3}	FWHM (nm)	Ne cm^{-3}
C932	-0.4225	27457	2.37	6.44E+14	0.39	4.47 E+16
C510	-0.5791	20032	1.73	5.45E+14	0.39	4.47 E+16
C673	-0.6497	17855	1.54	5.14E+14	0.39	4.48 E+16

C954	-0.5022	23100	1.99	5.85E+14	0.39	4.52 E+16
C655	-0.3772	30755	2.65	6.75E+14	0.29	3.36 E+16
C642	-0.5528	20986	1.81	5.58E+14	0.29	3.36 E+16
C863	-0.5947	19507	1.68	5.38E+14	0.29	3.36 E+16

From the results presented in table 5.1, it can be concluded that the plasma temperature of the plasmas generated when the standard samples were ablated are in LTE since each samples satisfy EEDF criteria and McWhirter criterion represented by equation (5.1).

5.4 Analytic figures of merit for the standard bronze samples

This section presents the measurement precision (that is, repeatability of the measurement) as the limit of detection for all the LIBS measurement performed on each of the standard samples.

5.4.1 Measurement precision

The closeness of the results of different measurements carried out on the same sample under similar experimental conditions is termed measurement precision or simply repeatability. Enhancement of LIBS measurement precision is of great significance in ensuring precise and accurate quantitative analysis of the ablated samples. In order to ensure precise quantitative analysis of the samples, the measurement was repeated five times on each of the seven standard bronze samples under similar experimental conditions and the precision of the measurements was assessed using the percentage relative standard deviation (RSD) presented in equation (5.4)

$$RSD = \frac{\text{Standard deviation of integrated spectral line intensity}}{\text{Mean of integrated spectral line intensity}} \qquad (5.4)$$

The percentage relative standard deviation was calculated for the internal reference preprocessed (IRP) spectral line intensities as well as the spectral line intensities without internal reference preprocessing method (WIRP). The results of RSD for each of the samples are presented in table 5.2. The significance of the proposed IRP method which translates to precise quantitative analysis can be easily inferred from the table as the integrated spectral line intensities (using trapezoidal approximation) that are preprocessed suffer little fluctuation as compared with intensities that are not subjected to IRP method. It should be noted that the proposed hybrid SVR-GSA based chemometric has excellent measurement precision as it gives the same results when executed over the same data-set and the same operating conditions.

Table 5.2: Measurement precision (repeatability) of the acquired LIBS spectra on the basis of relative standard deviation (RSD) integrated spectra line intensity(using Cu I at 515.32nm and Cu I at 510.55nm for spectral normalization)

Standard bronze sample	RSD of WIRP spectra	RSD of IRP spectra
C510	0.28	0.06
C642	0.21	0.13
C863	0.15	0.09
C932	0.22	0.11
C954	0.46	0.30
C655	0.28	0.04
C670	0.14	0.05

5.4.2 Limit of detection (LOD)

The minimum concentration of the sample constituents that can be readily detected by the LIBS system is referred to as the limit of detection (LOD). The limits of detection for all the elements present in the analyzed samples were estimated using equation (5.5) and the results are presented in table 5.3.

$$\text{LOD} = \frac{3\sigma}{s} \qquad (5.5)$$

where σ and s represent the standard deviation of the background of the averaged spectrum taken nearby the emission line and the ratio of the line intensity to the certified concentration, respectively.

Table 5.3: Limit of detection (LOD) of each of the elements present in the standard bronze samples

Element	LOD (wt%)
Cu	4.03
Sn	0.01
Al	0.69
Fe	0.02
Mn	0.002
Ni	0.02
Pb	0.003

Zn	0.77

5.5 Results of chemometric based models for quantitative analysis of standard bronze LIBS spectra

The results of the chemometric techniques developed using the exact intensities obtained from our LIBS instrument at different wavelengths very close to those contained in NIST data base are presented in this section. All the chemometric models presented in this section start with a letter A as a means of differentiating the models from other chemometrics developed using other set of data. The performance enhancement capacities of the proposed internal reference preprocessing method (IRP) , homogenous hybridization and hybrid fusion are also presented for both hybrid SVR and ELM based chemometrics.

5.5.1 Results of A-SVR based chemometrics for quantitative analysis of standard bronze spectra

Two techniques for enhancing the performance of SVR model in quantitative analysis of LIBS spectra are presented in this section. The proposed methods include the homogeneous hybridization and internal reference preprocessing method. The third method of performance improvement (hybrid fusion) is presented in the subsequent section. Four A-SVR based chemo-metrics are developed using these techniques and the results of these models are compared with one another. Before presenting the results of the model, the significance of the implemented optimization method (GSA) for hyper-parameters optimization is presented.

5.5.2 Optimization of A-SVR model parameters using GSA

The penalty factor, epsilon and kernel option of the selected kernel function are optimized using GSA. While implementing the gravitational search algorithm, the performance sensitivity of the number of initial population of the agents on the performance of the models was investigated. Fig.5.15 presents the variation of the number of agents with the number of iteration. The convergence of GSA-A-HSVR-IRP model is only presented to avoid repetition. Optimum value of the number of agents ensures a balance between the exploration and exploitation ability of the model.

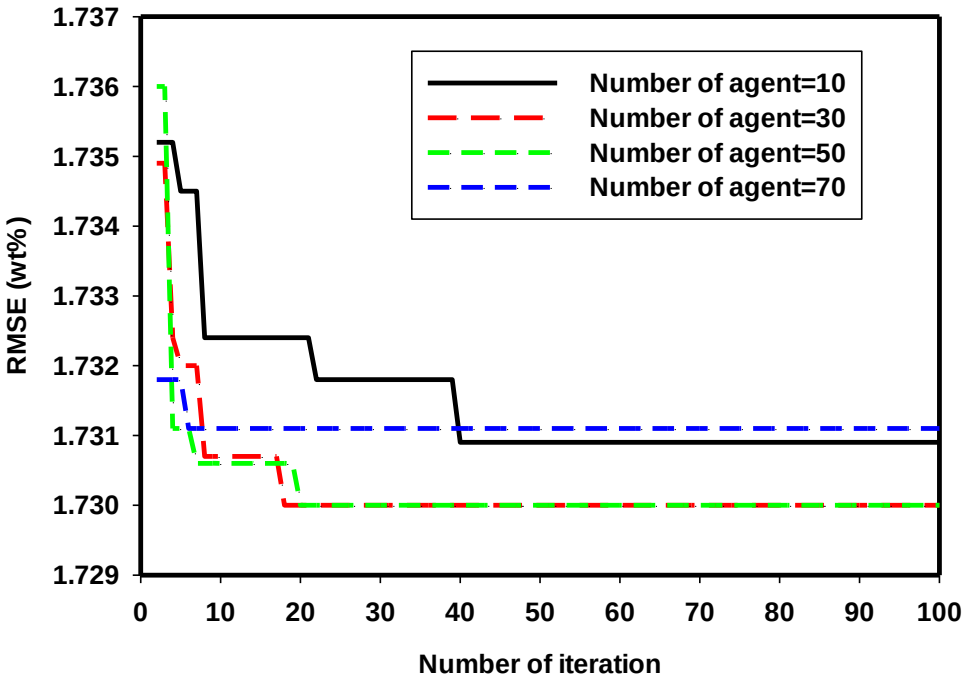

Figure 5.15: A graph of RMSE against the number of iteration for performance sensitivity of GSA-A- HSVR-IRP to the number of agents

In the graph presented in Fig.5.15, the model converges to local minimum when ten numbers of agents are involved in global minimum search. A global solution is attained

when the number of agents in the search space increased to thirty. Similar solution is obtained when the number of agents increases to fifty. After this point, the exploitation ability of the model became weaken and the model consequently converges to local minimum. The optimum number of agents in this case is thirty. Similar investigation was conducted for GSA-A-SVR-WIRP, GSA-A-HSVR-WIRP and GSA-A-SVR-IRP model. Table 5.4 shows the values of the parameters at which the proposed models display their optimum performances.

Table 5.4 : Optimum values of the A-SVR model parameters

	GSA-A-SVR-WIRP	GSA-A-HSVR-WIRP	GSA-A-SVR-IRP	GSA-A-HSVR-IRP
Penalty factor	44.5813	161.0286	554.7362	489.6015
Epsilon	0.8158	0.1942	0.9743	0.9983
Kernel option	0.405	0.6781	0.9809	0.4964
Kernel function	Gaussian	Polynomial	Gaussian	Polynomial
Hyper-parameter lambda	E-7	E-1	E-7	E-1
Agent population	10	10	30	30

5.5.3 Performance comparison of A-SVR based chemometric on the basis of root mean square error (RMSE), mean absolute error (MAE) and correlation coefficient (CC)

The performance of the developed models was evaluated using CC between the estimated elemental concentrations and the certified values, RMSE and MAE. Fig.5.16 shows the performance comparison based on the value of RMSE, Fig.5.17 compares the models

using the value of MAE while Fig.5.18 compares the developed models on the basis of CC.

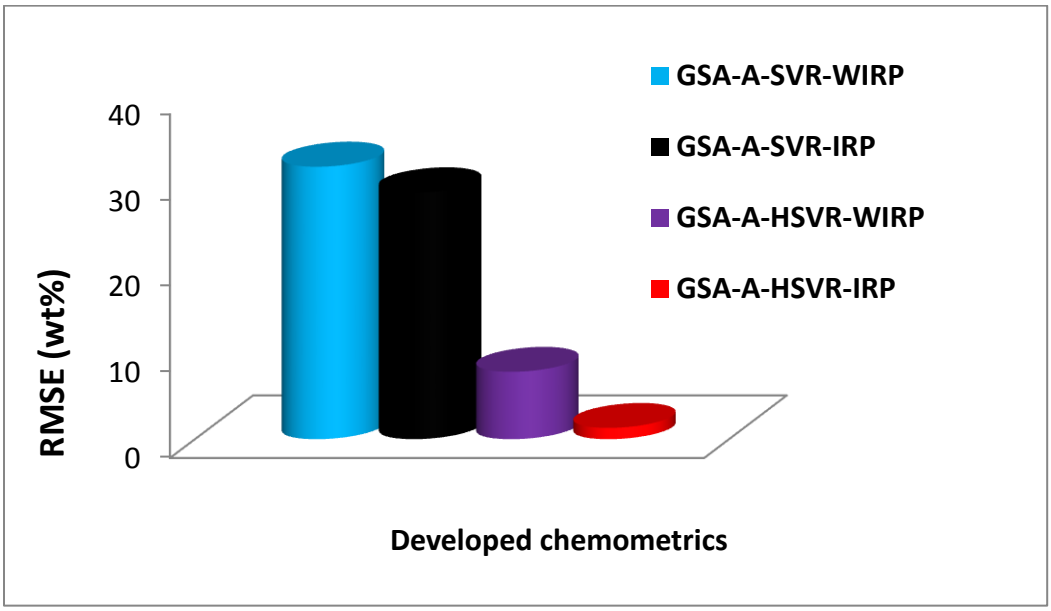

Figure 5.16: A graph of RMSE against the developed chemometric models for performance enhancement of A-SVR chemometrics on the basis of RMSE

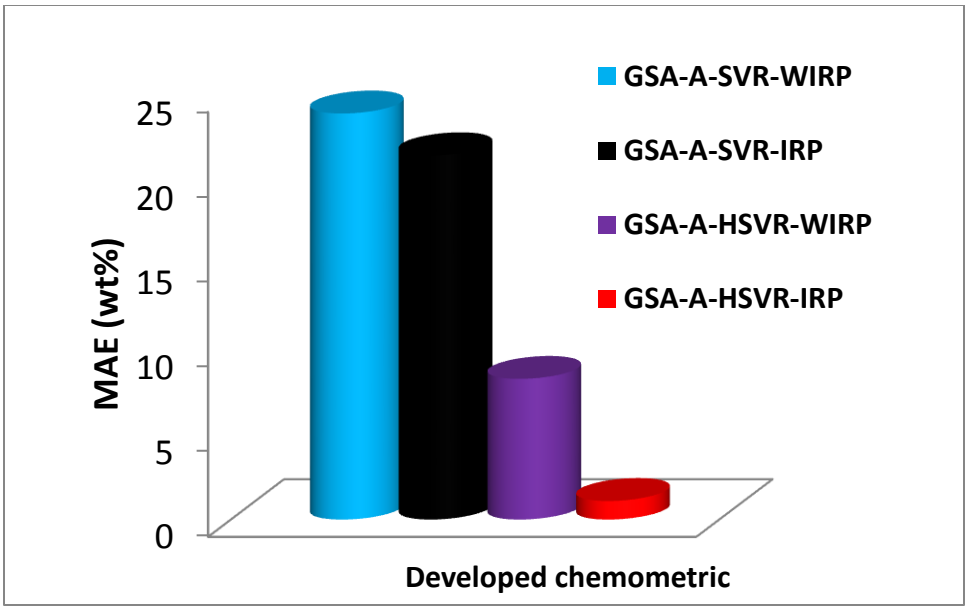

Figure 5.17: A graph of MAE against the developed chemometric models for performance enhancement of A-SVR chemometrics on the basis of MAE

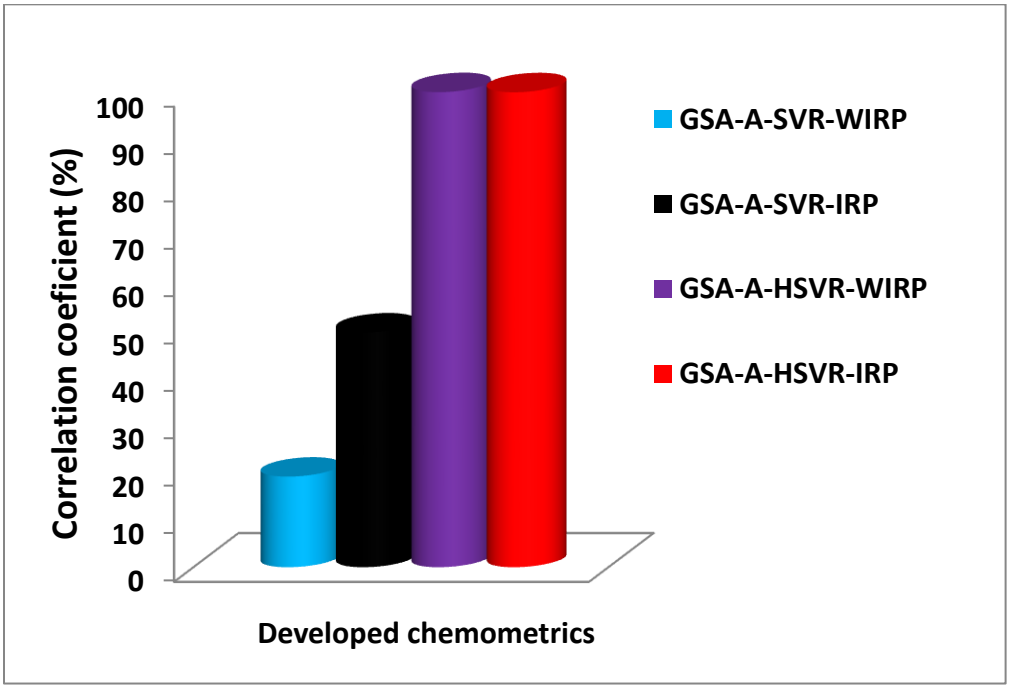

Figure 5.18: A graph of CC against the developed chemometric models for performance enhancement of A-SVR chemometrics on the basis of CC

The results of the modeling and simulation illustrated in Fig.5.18 shows that GSA-A-HSVR-WIRP model performs better than GSA-A-SVR-WIRP model with about 80.88% performance improvement. Better performance of GSA-A-HSVR-WIRP model is due to the inherent ability of the model to map input data to high dimensional space more than once using multiple kernel functions and thereby constructing linear regression with high correlation coefficient in the space. GSA-A-HSVR-WIRP model further circumvents the problem of ordinary SVR algorithm while dealing with non-linear problem that shows over-fitting and under-fitting simultaneously [102]. On the basis of RMSE, GSA-A-HSVR-WIRP performs better than GSA-SVR-WIRP model with 75.17% performance improvement and 65.40% performance improvement was attained on the basis of MAE as shown in Fig.5.17. However, the effect of self-absorption is not fully minimized in GSA-A-HSVR-WIRP model. Similarly, for the model with internal reference preprocessing, GSA-A-HSVR-IRP performs better than GSA-A-SVR-IRP with performance enhancement of about 50.53%, 95.41% and 94.92% on the basis of CC, RMSE and MAE, respectively. Because GSA-A-HSVR-IRP model constructs linear regression in high dimensional space after two successive transformations and minimizes self-absorption due to normalization of its emission line intensity with the intensity which is least affected by self-absorption, GSA-A-HSVR-IRP model generalizes better than other presented models. The performance comparison between the models are tabulated and presented in table 5.5.

Table 5.5 : Evaluation of the predictive capacity of the developed A-SVR based chemometrics

	GSA-SVR-WIRP	GSA-HSVR-WIRP	GSA-SVR-IRP	GSA-HSVR-IRP
CC (%)	19.11	99.93	49.43	99.91
RMSE (wt%)	31.73	7.88	28.75	1.32
MAE (wt%)	23.9	8.27	21.44	1.09

5.5.4 Comparison of the results of the developed A-SVR based chemometrics with the certified values

Comparison between the results of the developed A-SVR chemometrics and the certified concentrations are presented in table 5.6 and table 5.7. GSA-A-HSVR-IRP performs better than other presented model for C510 sample especially for major element Cu. Also for C642 test sample, GSA-A-HSVR-IRP model gives the most accurate result of 7.43 wt% for Al, 90.24 wt% for Cu, 0.46 wt% for Fe and 0.52 wt % for Ni while the result of GSA-A-HSVR-WIRP shows a better performance for only Mn. Generally, GSA-A-SVR-WIRP model demonstrates lowest performance as compared to the results of other models while GSA-A-HSVR-IRP shows better performance in comparison to the results of all the presented models. The poor performance of GSA-A-SVR-WIRP model could be attributed to inability of the chemo-metric tool to fully linearize the function linking the descriptors and the target and does not cater for self-absorption. GSA-A-HSVR-WIRP shows improved performance since it fully captures the non-linear relationship between the inputs and the output after successive transformation to high

dimensional space while is unable to minimize self-absorption. On the other hand, GSA-A-SVR-IRP shows a better performance but still far higher than the certified value. In other test samples presented in the table, the results of GSA-A-HSVR-IRP are closer to the certified values followed by that of GSA-A-HSVR-WIRP, then GSA-A-SVR-IRP and GSA-A-SVR-WIRP chemometrics.

Table 5.6 : Comparison between the results of the developed GSA-A-SVR-WIRP and GSA-A-HSVR-WIRP chemometrics including their standard deviations from the certified values

Sample	Element	Con. (wt%)	GSA-A-SVR-WIRP (wt%)	Standard deviation (wt%)	GSA-A-HSVR-WIRP (wt%)	Standard deviation (wt%)
C510	Cu	94.99	51.18	30.98	74.61	14.41
	Sn	4.66	6.69	1.43	5.40	0.52
	Others	0.35	42.13	29.55	19.99	13.89
C642	Al	6.82	8.59	1.25	8.35	1.08
	Cu	90.85	51.20	28.04	74.64	11.46
	Fe	0.18	2.89	1.92	0.50	0.23
	Mn	0.02	2.76	1.94	0.72	0.49
	Ni	0.15	2.87	1.92	0.54	0.28
Others		1.98	31.70	21.01	15.25	9.38

C655	Cu	60.30	51.18	6.45	74.61	10.12
	Fe	0.02	2.42	1.70	1.25	0.87
	Pb	0.01	2.41	1.70	1.25	0.87
	Zn	38.85	34.31	3.21	22.90	11.28
Others		0.81	9.68	6.27	0.00	0.58
C863	Cu	62.90	51.18	8.29	74.61	8.28
	Sn	0.02	2.53	1.77	1.07	0.74
	Pb	0.01	2.52	1.77	1.09	0.76
	Zn	26.41	23.75	1.88	15.25	7.89
	Fe	2.43	4.59	1.53	2.14	0.20
	Al	5.21	6.98	1.25	5.85	0.45
Others		3.02	8.45	3.84	0.00	2.14
C954	Cu	85.82	51.18	24.49	74.61	7.92
	Fe	3.46	5.47	1.42	3.50	0.03
	Ni	0.05	2.55	1.76	1.05	0.70
	Al	10.43	11.44	0.71	12.79	1.67
others		0.24	29.36	20.60	8.05	5.52

C932	Ni	0.40	3.10	1.91	0.18	0.16
	Sn	6.47	8.30	1.30	7.91	1.02
	Zn	3.78	6.00	1.57	4.32	0.38
	Cu	81.22	51.18	21.24	74.61	4.67
Others		8.13	31.42	16.47	12.98	3.43
C673	Cu	59.40	51.11	5.86	74.49	10.67
	Fe	0.06	2.60	1.80	0.96	0.64
	Pb	1.76	4.06	1.62	1.30	0.32
	Mn	2.50	4.69	1.55	2.29	0.15
	Ni	0.06	2.60	1.80	0.96	0.64
	Zn	35.17	31.30	2.74	19.99	10.74
Others		1.05	3.65	1.84	0.00	0.74

Table 5.7: Comparison between the results of the developed GSA-A-SVR-IRP and GSA-A-HSVR-IRP chemometrics including their standard deviations from the certified values

Sample	Element	Con. (wt%)	GSA-A-SVR-IRP (wt%)	Standard deviation (wt%)	GSA-A-HSVR-IRP (wt%)	Standard deviation (wt%)
C510	Cu	94.99	83.08	8.42	94.00	0.70
	Sn	4.66	7.59	2.07	5.99	0.94
	Others	0.35	9.34	6.35	0.01	0.24
C642	Al	6.82	8.76	1.37	7.43	0.43
	Cu	90.85	79.84	7.78	90.24	0.43
	Fe	0.18	1.87	1.20	0.46	0.20
	Mn	0.02	1.34	0.93	0.90	0.62
	Ni	0.15	1.80	1.16	0.52	0.26
Others		1.98	6.39	3.12	0.44	1.09
C655	Cu	60.30	53.45	4.85	59.49	0.58
	Fe	0.02	0.97	0.68	1.21	0.84
	Pb	0.01	3.44	2.42	1.23	0.86
	Zn	38.85	34.33	3.20	37.22	1.16

Others		0.81	7.81	4.95	0.86	0.03
C863	Cu	62.90	55.86	4.98	62.30	0.42
	Sn	0.02	2.38	1.67	0.08	0.04
	Pb	0.01	3.61	2.55	1.43	1.01
	Zn	26.41	24.57	1.30	25.85	0.40
	Fe	2.43	3.55	0.80	1.36	0.75
	Al	5.21	8.07	2.02	6.62	1.00
Others		3.02	1.95	0.76	2.35	0.48
C954	Cu	85.82	75.29	7.44	84.94	0.62
	Fe	3.46	3.58	0.08	1.39	1.46
	Ni	0.05	3.44	2.40	1.23	0.83
	Al	10.43	11.45	0.72	10.56	0.09
others		0.24	6.24	4.25	1.88	1.16
C932	Ni	0.40	0.61	0.14	1.51	0.78
	Sn	6.47	8.17	1.21	6.75	0.20
	Zn	3.78	7.85	2.88	6.37	1.83
	Cu	81.22	71.71	6.72	80.77	0.32

Others		8.13	11.65	2.49	4.60	2.49
C673	Cu	59.40	52.72	4.73	58.64	0.54
	Fe	0.06	0.57	0.36	1.54	1.05
	Pb	1.76	4.98	2.28	3.03	0.90
	Mn	2.50	1.76	0.52	0.55	1.38
	Ni	0.06	1.22	0.82	1.00	0.67
	Zn	35.17	31.51	2.59	33.93	0.88
Others		1.05	7.24	4.38	1.31	0.19

The absolute percentage deviations of the results of each of the developed A-SVR based chemometrics from the certified values are presented in Fig.5.19. Chemometrics without the proposed internal reference preprocessing method have large number of elements with percentage deviation above 20% while model with internal reference preprocessing have large number of elements with percentage deviation below 5%.

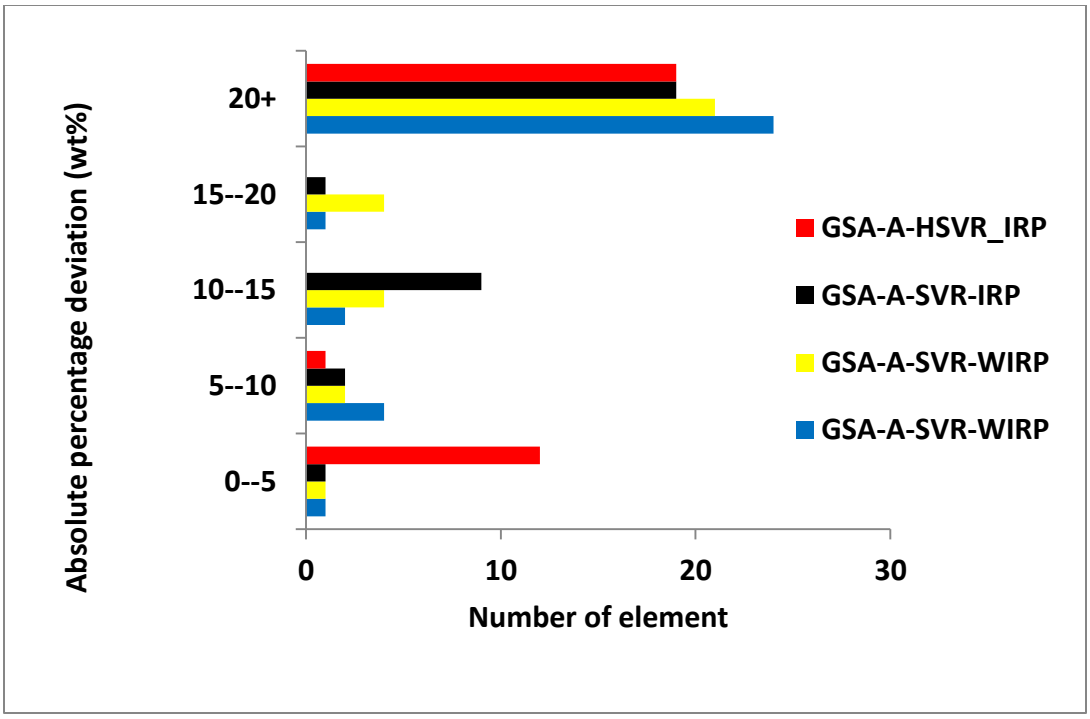

Figure 5.19: A graph of absolute percentage deviation against the number of element for each of the developed A-SVR based chemometrics

5.5.5 Results of A-ELM based chemometrics for quantitative analysis of standard bronze spectra

This section presents the results of extreme learning machine (ELM) and its hybrid HELM (homogenously hybridized ELM), for the first time in modeling the complex interactions of laser induced plasma and quantification of LIBS spectra. The result of internal reference preprocessing (IRP) method for enhancing the performance of ELM based chemometrics is also presented. Since the proposed chemo-metrics (ELM and HELM) determine their input weights as well as their hidden biases in a random manner,

ELM and HELM are respectively hybridized with gravitational search algorithm (GSA) for optimization of the number of hidden neurons.

5.5.6 Influence of the agent population on convergence of the A-ELM based chemometrics

Influence of the agent population on convergence of the proposed chemo-metrics **.**The dependence of the performance GSA-A-ELM-WIRP chemo-metric on the initial population of agents is presented in Fig.5.20. The gravitational pull between the agents become significant when large number of agents is exploiting a small portion of a search space for a global solution. Similarly, exploration ability of the model is weakened when few agents explore a wide search space. In order to strike a balance between exploration and exploitation capacity of the gravitational search algorithm based chemo-metric, the initial population of the agents is varied until the model demonstrates its optimum performance. The tuning of GSA parameters is not as tedious as tuning the number of hidden neurons in a case where optimization search algorithm is not employed. Apart from the fact that GSA improves the stability of ELM, it also ensures global solution and save valuable time as well as other resources. As depicted in Fig.5.20, GSA-A-ELM-WIRP converges to local minima when thirty, fifty and seventy number of agents was used for the simulation. Optimum performance was achieved when the number of agent reaches ninety and the exploitation ability of the model became weakened afterwards. Similar trend is obtained for GSA-A-HELM-WIRP based chemo-metric depicted in Fig.5.21. The optimum value of agent in this case is obtained as thirty.

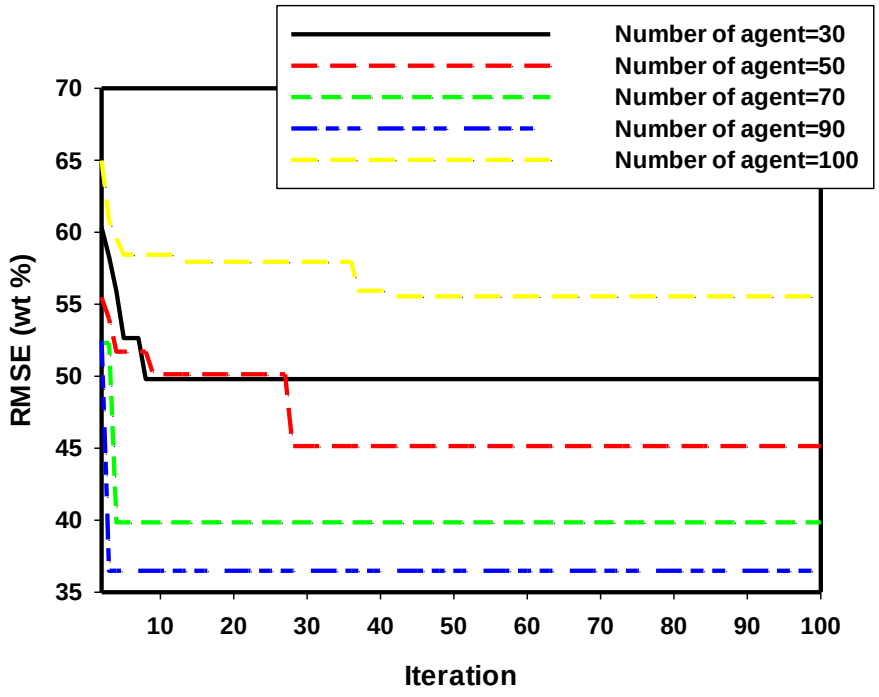

Figure 5.20: A graph of RMSE against the number of iteration for performance sensitivity of GSA-A- ELM-WIRP to the number of agents

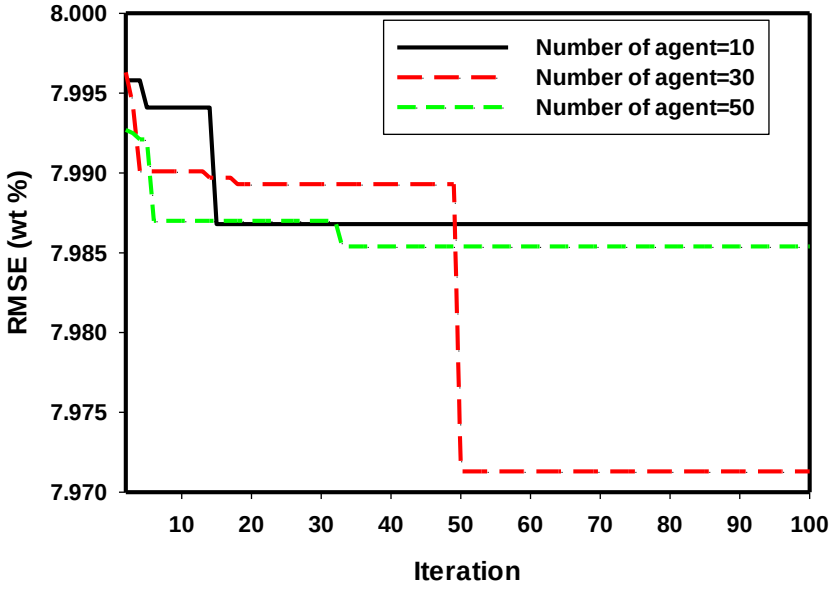

Figure 5.21: A graph of RMSE against the number of iteration for performance sensitivity of GSA-A- HELM-WIRP to the number of agents

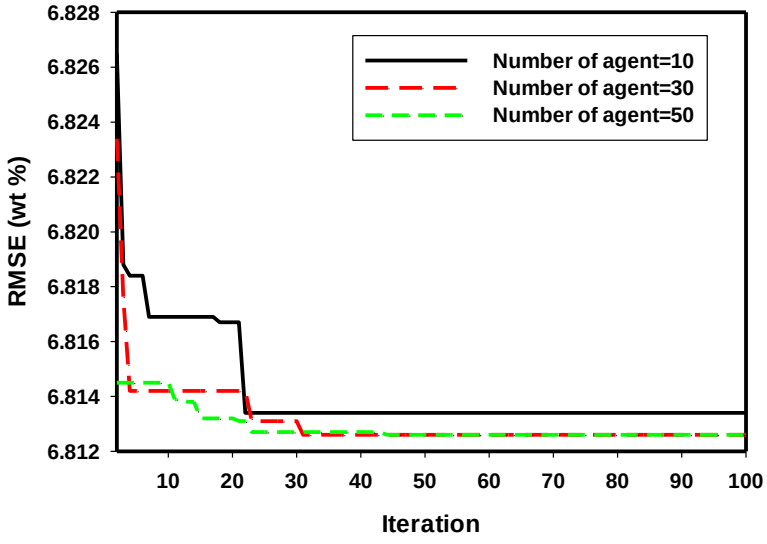

Figure 5.22: A graph of RMSE against the number of iteration for performance sensitivity of GSA-A- ELM-IRP to the number of agents

The performance sensitivity of GSA-A-ELM-IRP chemo-metric to the initial population of the agents is illustrated in Fig.5.22. Only ten number of agent converges to local minimum while the model converges to global minimum when the number of agents exceeds ten. The optimum number of agents was taken as thirty so as to reduce the computational complexity at high number of agent population

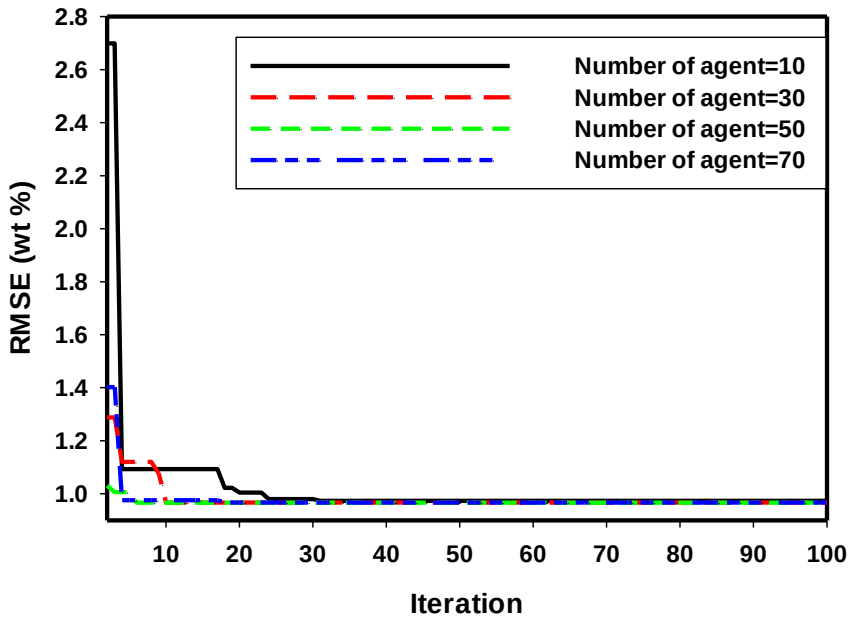

Figure 5.23: A graph of RMSE against the number of iteration for performance sensitivity of GSA-A- HELM-IRP to the number of agents

For the case of GSA-A-HELM-IRP chemo-metric depicted in Fig.5.23, the optimum value of agent population was obtained as fifty. Table 5.8 presents the activation function, number of hidden neurons and the number of agents that optimize the proposed extreme learning machine based chemo-metrics.

Table 5.8: Optimum values of A-ELM based chemometrics parameters

Extreme learning based chemo	Activation function	Number of hidden neurons	Number of agent
GSA-ELM-WIRP	Sine function	51	90
GSA-HELM-WIRP	Sigmoid function	194	30
GSA-ELM-IRP	Sine function	766	30
GSA-HELM-IRP	Sigmoid function	183	10

5.5.7 Performance comparison of A-ELM based chemometric on the basis of root mean square error (RMSE), mean absolute error (MAE) and correlation coefficient (CC)

The performance of each of the developed A-ELM based chemo-metrics was evaluated using correlation coefficient (CC) between the results of the model and certified values, root mean square error (RMSE) and mean absolute error (MAE). These generalization performance evaluation parameters were averaged over the seven folds. This poor generalization performance demonstrated by GSA-A-ELM-WIRP also manifests in the value of its RMSE and MAE as illustrated in Fig.5.24 and Fig.5.25, respectively. In the case of RMSE and MAE, the lower the value, the better the model.

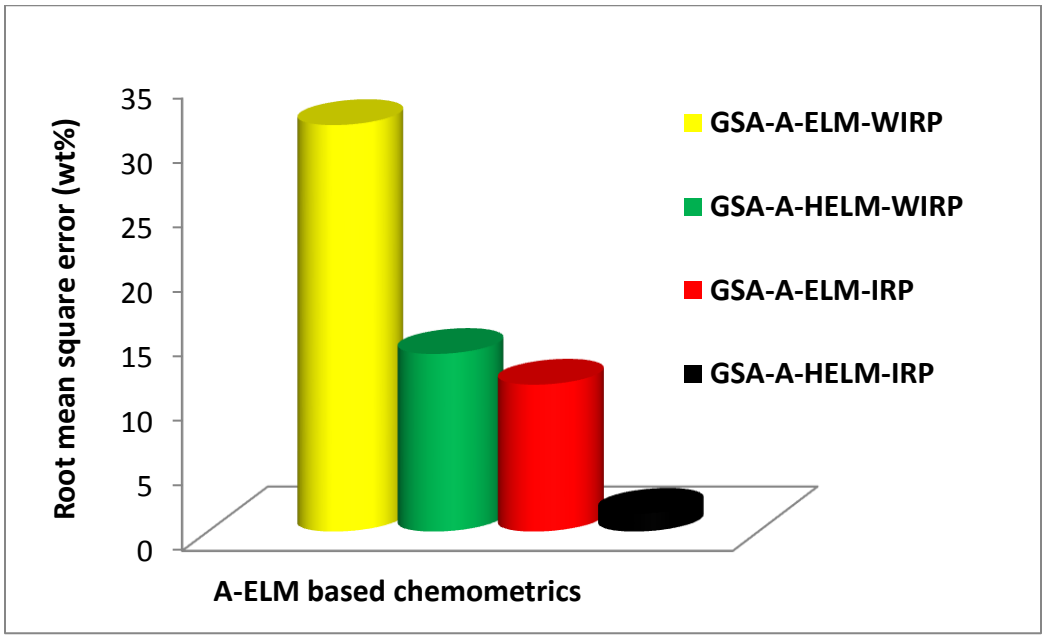

Figure 5.24: A graph of RMSE against the developed chemometric models for performance enhancement of A-ELM chemometrics on the basis of RMSE

GSA-A-HELM-WIRP shows a better performance as compared to GSA-A-ELM-WIP chemo-metric since the function approximated by GSA-ELM-WIP model was further approximated and linearized in GSA-A-HELM-WIP chemo-metric and ultimately results into more robust and accurate model. The deviations of the results of GSA-A-HELM-WIP from the certified values only occur in atomic species that are affected by self-absorption. Lower value of RMSE and MAE for GSA-A-HELM-WIP chemo-metric depicted by Fig. 5.24 and Fig.5.25, respectively further shows its better performance as compared to its counterpart.

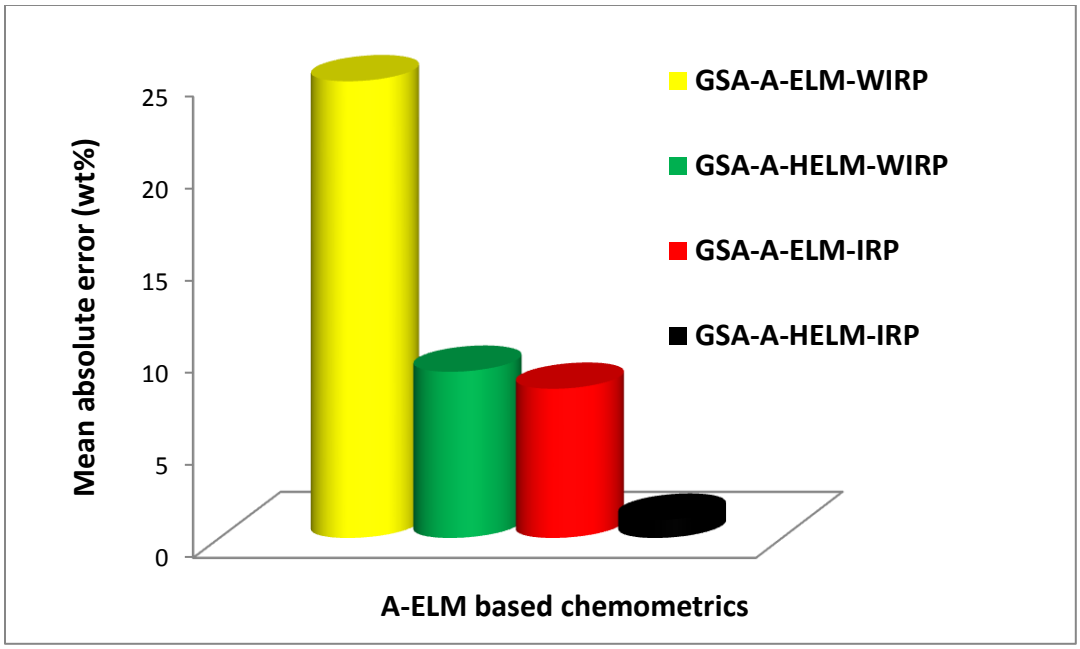

Figure 5.25: A graph of MAE against the developed chemometric models for performance enhancement of A-ELM chemometrics on the basis of MAE

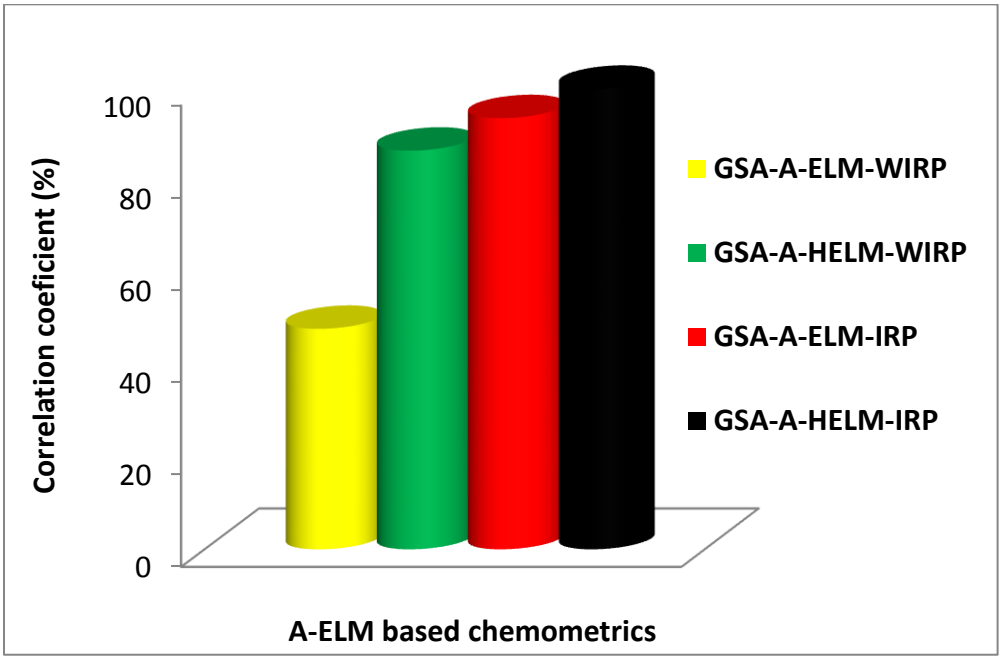

Figure 5.26: graph of CC against the developed chemometric models for performance enhancement of A-ELM chemometrics on the basis of CC

The performance comparison of GSA-A-ELM-IRP chemometric as compared to other models is also shown in Fig. 5.24, Fig.5.25 and Fig.5.26 for RMSE, MAE and CC

respectively. GSA-A-ELM-IRP performs better than GSA-A-ELM-WIRP and GSA-A-HELM-WIRP due to its self-absorption minimization capacity. The only inaccuracy attached to GSA-A-ELM-IRP model can be attributed to inability of the model to fully linearize the function linking the descriptors with the target. GSA-A-HELM-IRP shows a better generalization and predictive capacity due to its ability to linearize the acquired function more than once in addition to the reduction of self-absorption on some atomic species. Fig.5.26 shows the performance comparison of the proposed chemo-metrics on the basis of correlation coefficient. It should be noted that the higher the value of CC, the better the model. GSA-A-ELM-WIRP shows the lowest value of CC. This can be attributed to the extent of self-absorption in the spectra used in developing the model as well as inability of ordinary ELM to fully capture the non-linear relationship between the descriptors and the elemental concentrations. Table 5.9 shows the values of generalization performance evaluation parameters for all the developed chemo-metrics

Table 5.9: Measure of generalization performance of the proposed A-ELM based chemo-metrics (averaged over all the seven folds)

	GSA-ELM-WIRP	GSA-HELM-WIRP	GSA-ELM-IRP	GSA-HELM-IRP
CC (%)	47.97	86.45	93.47	99.81
RMSE (wt%)	31.45	13.8	11.43	1.4
MAE (wt%)	24.76	9.01	8.09	0.99

5.5.8 Comparison of the results of the developed A-ELM based chemometrics with the certified values

Comparison between the results of the developed models and the certified concentrations are presented in table 5.10 and table 5.11. For C640 test sample, GSA-A-HELM-IRP model gives the most accurate result of 7.02 wt% while other chemo-metrics give a value far above the certified values. GSA-A-ELM-WIRP model gives worst results 45.31 wt % for the copper which is the major element of the composition as shown in table 5.11. The poor performance of GSA-A-ELM-WIRP model could be attributed to inability of the chemo-metric tool to fully linearize the function linking the descriptors and the target without catering for self-absorption.

Table 5.10 : Comparison between the results of the developed GSA-A-ELM-IRP and GSA-A-HELM-IRP chemometrics including their standard deviations from the certified values

Element	Sample	Con (wt%)	GSA-A-ELM-IRP(wt%)	Standard deviation (wt%)	GSA-A-HELM-IRP (wt%)	Standard deviation (wt%)
Al	C642	6.82	8.40	1.12	7.02	0.14
Cu		90.85	87.79	2.17	90.54	0.22
Si		1.78	1.75	0.02	1.03	0.53
others		0.55	2.06	1.07	1.42	0.61
Cu	C655	60.30	68.72	5.95	61.34	0.73
Zn		38.85	21.88	12.00	36.15	1.91

others		0.84	9.39	6.04	2.51	1.18
Cu	C863	62.90	69.05	4.35	63.67	0.54
Zn		26.41	23.15	2.31	26.00	0.29
Al		5.21	5.35	0.10	5.22	0.01
others		5.48	2.45	2.14	5.11	0.26
Cu	C954	85.82	71.91	9.83	83.73	1.48
Fe		3.46	1.35	1.50	2.12	0.95
Al		10.43	8.85	1.12	10.96	0.37
Others		0.29	17.89	12.44	3.19	2.05
Cu	C510	95.00	97.57	1.82	95.21	0.15
Sn		5.00	2.43	1.82	4.78	0.15
Pb	C932	7.67	4.32	2.37	7.25	0.30
Sn		6.47	2.61	2.73	5.98	0.35
Zn		3.78	17.50	9.70	5.50	1.21
Cu		81.22	71.34	6.99	79.84	0.97
Others		0.87	4.23	2.38	1.43	0.40
Cu	C673	59.40	68.61	6.51	60.56	0.82

Pb	1.76	0.99	0.54	0.88	0.62
Mn	2.50	1.12	0.98	1.52	0.69
Zn	35.17	21.42	9.72	33.93	0.88
others	1.17	7.85	4.73	3.11	1.37

GSA-A-HELM-WIRP shows improved performance since it fully captures the non-linear relationship between the inputs and the output while is unable to minimize self-absorption. On the other hand, GSA-A-ELM-IRP shows a better performance but still far higher than the certified value. For C510 test sample, the results of GSA-A-HELM-IRP and GSA-HELM-WIRP are very close to the certified values. This might due to the assumption that the test sample has no trace element and not seriously affected by self-absorption. In other test samples presented in the table, the results of GSA-A-HELM-IRP are closer to the certified values followed by that of GSA-A-ELM-IRP, then GSA-AHELM-WIRP and GSA-A-ELM-WIRP chemo-metrics.

Table 5.11: Comparison between the results of the developed GSA-A-ELM-WIRP and GSA-A-HELM-WIRP chemometrics including their standard deviations from the certified values

Element	Sample	Con (wt%)	GSA-A-ELM-WIRP (wt%)	Standard deviation (wt%)	GSA-A-HELM-WIRP(wt%)	Standard deviation (wt%)
Al	C642	6.82	27.14	14.37	8.88	1.46
Cu		90.85	45.31	32.20	90.85	0.00

Si		1.78	27.55	18.22	0.27	1.07
others		0.55	0.00	0.39	0.00	0.39
Cu	C655	60.30	28.58	22.43	66.54	4.41
Zn		38.85	8.24	21.64	15.56	16.47
others		0.84	28.58	19.62	17.89	12.05
Cu	C863	62.90	38.39	17.33	66.54	2.57
Zn		26.41	11.62	10.46	26.41	0.00
Al		5.21	19.61	10.19	5.21	0.00
others		5.48	1.79	2.61	1.84	2.57
Cu	C954	85.82	28.58	40.47	66.54	13.63
Fe		3.46	11.62	5.77	1.02	1.73
Al		10.43	27.14	11.81	8.88	1.10
Others		0.29	32.65	22.88	23.57	16.46
Cu	C510	95.00	55.65	27.83	95.00	0.00
Sn		5.00	44.35	27.83	5.00	0.00
Pb	C932	7.67	26.38	13.23	4.75	2.06
Sn		6.47	1.89	3.23	2.29	2.95

Zn		3.78	8.24	3.16	15.56	8.33
Cu		81.22	28.58	37.22	66.54	10.38
Others		0.87	34.90	24.06	10.85	7.06
Cu	C673	59.40	28.58	21.79	66.54	5.05
Pb		1.76	10.96	6.50	0.59	0.83
Mn		2.50	0.48	1.43	0.77	1.22
Zn		35.17	8.24	19.04	15.56	13.86
others		1.17	51.74	35.76	16.53	10.86

Absolute percentage error analysis comparison between the developed A-ELM based models is presented in Fig.5.27. GSA-A-ELM-WIRP chemo-metric that was developed without internal reference preprocessing (WIRP) shows worst performance in all the seven investigated test standard bronze samples. The performance of the models can be ranked in the following order ranging from worst to best; GSA-A-ELM-WIRP<GSA-A-HELM-WIRP<GSA-A-ELM-IRP<GSA-A-HELM-IRP. Outstanding performance of GSA-A-HELM-IRP chemo-metric can be attributed to its ability to minimize the effect of self-absorption and multiple linearization of the acquired function relating the inputs to the output.

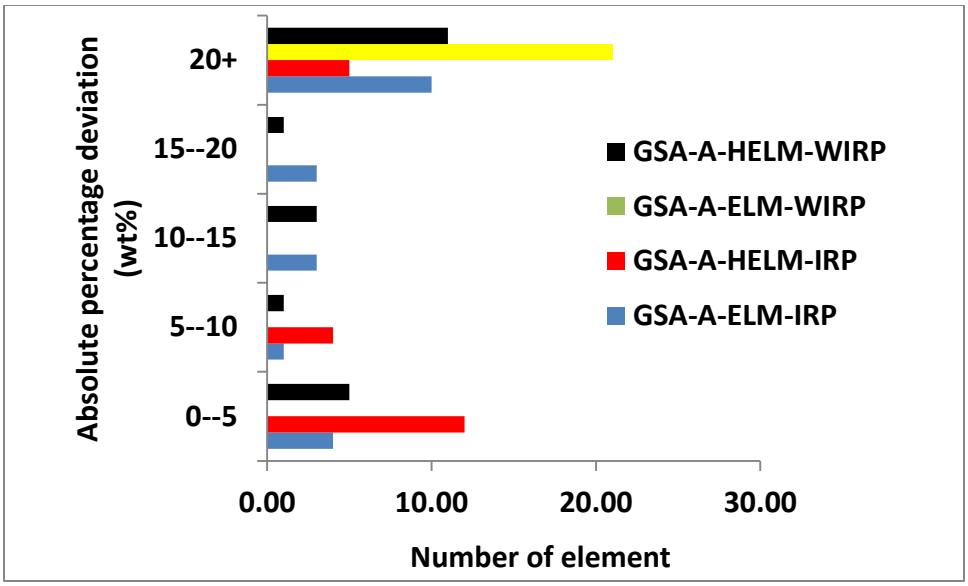

Figure 5.27: A graph of absolute percentage deviation against the number of element for each of the developed A-ELM based chemometrics

5.5.9 Results of hybrid fusion of SVR and ELM chemometrics for quantitative analysis of standard bronze spectra

The result of hybrid fusion of extreme learning machine (ELM) and support vector regression (SVR) with IRP method is presented in this section. Extreme learning machine (ELM) is a non-linear chemo-metric method that has inherent capacity to approximate any non-linear relation describing the laser induced plasma. However, ELM surfers from over-fitting which affects its accuracy for spectroscopic regression. On the other hand, SVR is a non-linear chemo-metric tool based on statistical learning theory and overcomes the problem of over-fitting by proper tuning of its hyper-parameters. The merits of both chemo-metrics are harnessed in this work and implemented for quantitative analysis of LIBS spectra of seven standard bronze samples.

5.6 Optimization of hybrid ELM-SVR hyper-parameters

Optimization of the parameters of the developed hybrid fusion models was carried out using GSA. In order to maintain a balance between the exploration and exploitation capacity of the model, the initial population of the agents was varied between five and fifty as shown in Fig.5.28 for A-ELM-SVR based model.

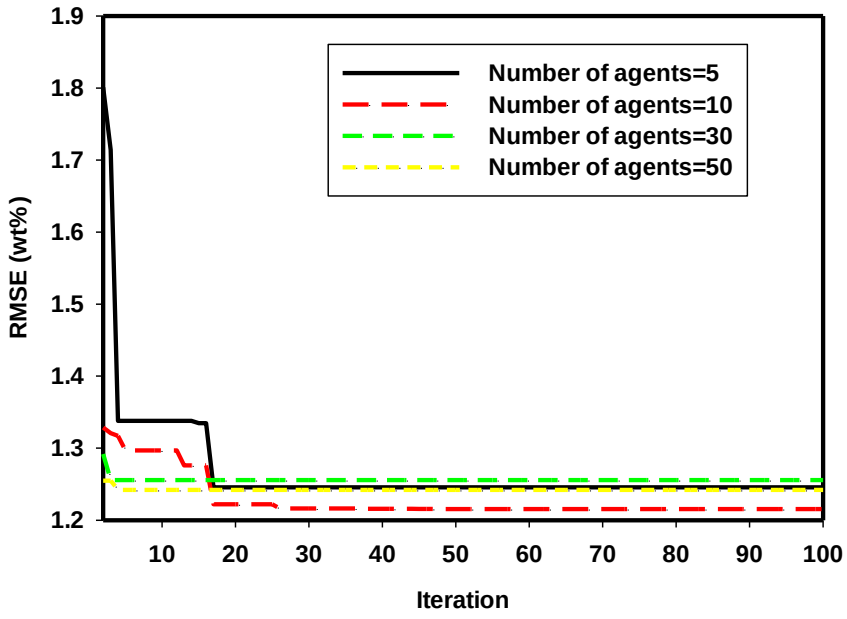

Figure 5.28: A graph of RMSE against the number of iteration for performance sensitivity of GSA-A- ELM-SVR to the number of agents

The exploitation ability of the model is more favored as compared to the exploration capacity when the number of agents exploring a search space is large while otherwise in case of small number of agents assessing similar search space. As can be deduced from Fig.5.28, when the number of initial population of agent is small (say five), the model converges to local minimum. The same premature convergence was also observed at high number of agent due to high complexity which reduces the model exploitation strength.

The optimum performance was observed when the initial population of agents was ten. The values of model hyper-parameters (which include the activation number and the number of hidden neuron for A-ELM and A-SVR-ELM models while the kernel option, penalty factor and epsilon are the model parameters for A-SVR and A-ELM-SVR based models) were recorded at optimum values of agent population. Table 5.12 shows the optimum values of the model parameters for all the developed models.

Table 5.12 : Optimum parameters for hybrid SVR and ELM model

Parameters	A-SVR	A-ELM	A-SVR-ELM	A-ELM-SVR
Number of agent	30	30	20.0000	10
Activation function	-------	Sine	Sigmoidal	-------
Hidden neuron	-------	766	15	-------
Penalty factor	554.7362	-------	-------	604.2271
Kernel function	Gaussian	-------	-------	Gaussian
Kernel option	0.9809	-------	-------	0.5073
Epsilon	0.9743	-------	-------	0.2386
Hyper-parameter lambda	E-7	-------	-------	E-7

5.6.1 Comparison of the performance of hybrid fusion based chemometrics on the basis of RMSE, MAE and CC

The performance comparison between the developed hybrid models and the individual models before hybridization is presented in Fig.5.36, Fig.5.37 and Fig.5.38 respectively on the basis of root mean square error (RMSE) , mean absolute error (MAE) and correlation coefficient (CC). Ordinary A-SVR model shows the least performance as indicated by the smallest value of CC in Fig.5.28 and highest value of RMSE in Fig.5.29 as well as highest value of MAE in Fig.5.30. The weak performance of A-SVR model can be attributed to the inability of the model to fully capture the inherent non-linearity characterizing the laser induced plasma generated after the ablation. On the other hand A-A-ELM model performs better than ordinary A-SVR since non-linear function can be approximated by A-ELM model with a reasonable degree of accuracy. While comparing the performance of A-SVR and A-ELM model on the basis of RMSE, MAE and CC, as depicted in Fig.5.29, Fig.5.30 and Fig.5.31 respectively, A-ELM performs better than A-SVR with performance improvement of 60.24% , 62.28% and 89.06% on the basis of RMSE,MAE and CC, respectively.

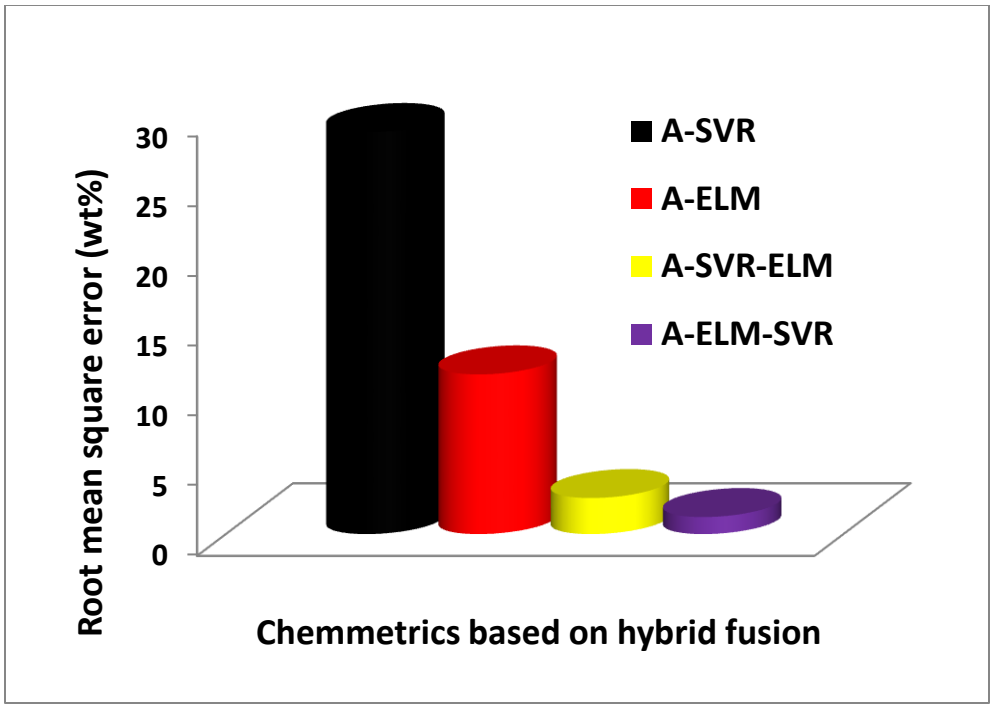

Figure 5.29: A graph of RMSE against the developed chemometric models for performance enhancement of hybrid fusion based chemometrics

Similarly, hybrid fusion of A-SVR model in A-ELM model results into A-SVR-ELM model with a better performance than individual A-SVR and A-ELM. A-SVR-ELM model takes the output of A-SVR as its input and further approximate the spectroscopic regression constructed by A-SVR algorithm in high dimensional feature space after transformation using Gaussian function. A-SVR-ELM model performs better than A-SVR model with performance improvement of 101.36%, 91.03% and 94.97% on the basis of CC, RMSE and MAE, respectively. In the same vein, A-SVR-ELM performs better than ordinary A-ELM with performance improvement of 77.43%, 86.65% and 6.50% on the basis of RMSE, MAE and CC as respectively shown in Fig.5.29, Fig.5.30 and Fig.5.31.

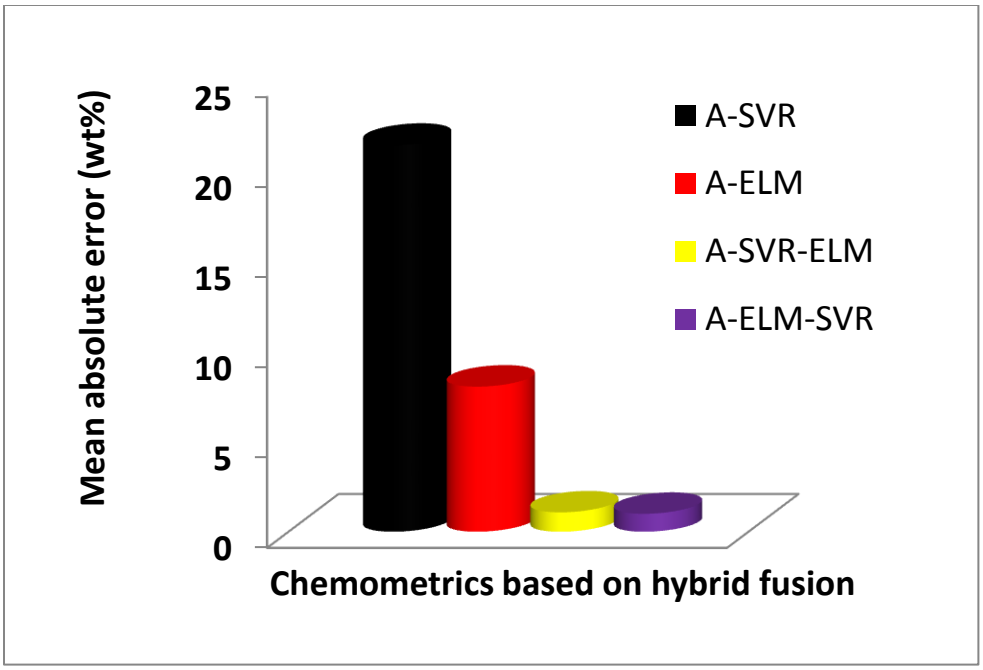

Figure 5.30: A graph of MAE against the developed chemometric models for performance enhancement of hybrid fusion based chemometrics

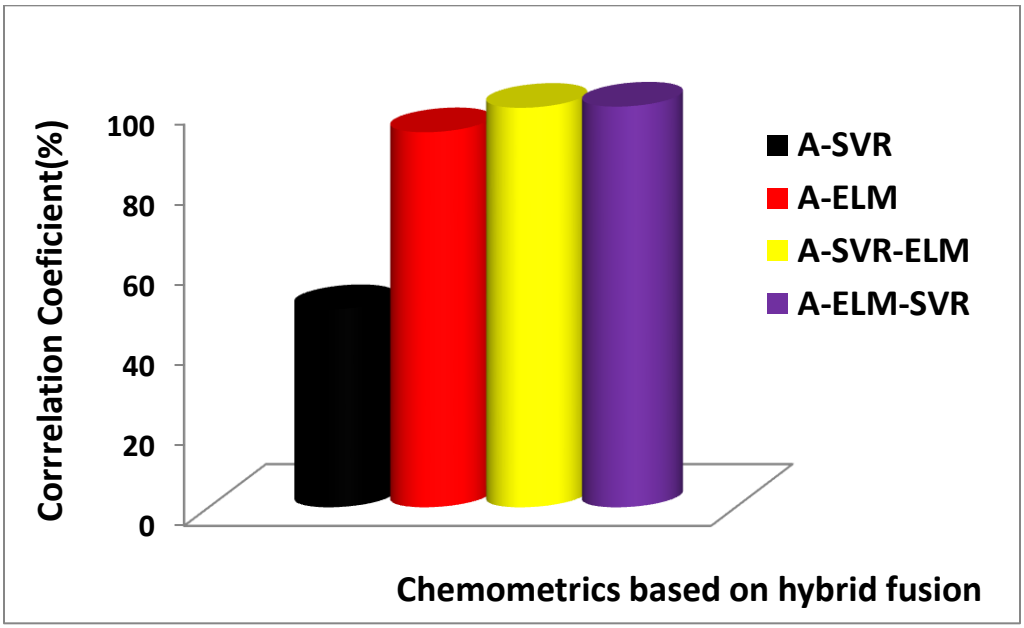

Figure 5.31: A graph of CC against the developed chemometric models for performance enhancement of hybrid fusion based chemometrics

Hybrid A-ELM-SVR model has shown the overall better performance as compared with other models presented in Fig.5.30. A-ELM-SVR model takes the final output of A-ELM model as its input. The better performance demonstrated by A-ELM-SVR model can be attributed to transformation of the approximated non-linear function governing the laser induced plasma to high dimensional feature space by A-SVR algorithm where linear spectroscopic regression of high degree of correlation coefficient is constructed. Table 5.13 shows the values of the parameters that measure the performance of each of the developed model.

Table 5.13 : comparison of the performance of the developed hybrid fusion based chemometrics

	A-SVR	A-ELM	A-SVR-ELM	A-ELM-SVR
CC (%)	49.44	93.47	99.55	99.85
RMSE (wt %)	28.75	11.43	2.58	1.22
MAE (wt%)	21.45	8.09	1.08	1

A-ELM-SVR model performs better than ordinary A-SVR with a performance improvement of 101.96%, 95.76% and 95.34% on the basis of CC, RMSE and MAE, respectively while it performs better than ordinary A-ELM with a performance improvement of 6.83%, 89.32% and 87.64%, respectively. A-ELM-SVR model also performs better than A-SVR-ELM model with a performance improvement of 0.3%, 52.71% and 7.4% on the basis of CC, RMSE and MAE, respectively. The overall

performance of the developed hybrid fusion based chemometrics can be arranged as A-ELM-SVR>A-SVR-ELM>A-ELM>A-SVR.

5.6.2 Comparison of the results of the chemometrics based on hybrid fusion with certified values

Table 5.14 and table 5.15 present the comparison between the results of the developed hybrid models and the certified concentration for seven standard bronze samples with inclusion of standard deviations. The results of the hybrid chemometrics are closer to the certified values for all the investigated standard samples.

Table 5.14 : Comparison between the results of the developed A-SVR and A-ELM chemometrics including their standard deviations from the certified values

Samples	Element	Con.(wt%)	A-SVR	Standard deviation (wt%)	A-ELM (wt%)	Standard deviation (wt%)
C510	Cu	94.99	83.08	8.42	91.75	2.29
	Sn	4.66	7.59	2.07	2.43	1.58
	others	0.35	9.34	6.35	5.82	3.87
C642	Al	6.82	8.76	1.37	8.40	1.12
	Co	0.15	3.77	2.56	0.59	0.31
	Cu	90.85	69.58	15.04	68.48	15.82
	Fe	0.18	1.87	1.20	0.94	0.54

	Mn	0.02	1.34	0.93	0.81	0.56
	Ni	0.15	1.80	1.16	0.20	0.03
	Si	1.78	5.17	2.40	1.75	0.02
	Sn	0.01	3.64	2.57	1.80	1.27
	Zn	0.04	4.07	2.85	17.03	12.02
C655	Cu	60.30	53.45	4.85	68.72	5.95
	Fe	0.02	0.97	0.68	0.92	0.64
	Pb	0.01	3.44	2.42	3.36	2.37
	Sn	0.81	2.92	1.49	1.90	0.77
	Zn	38.85	34.33	3.20	21.88	12.00
	others	0.00	4.89	3.46	3.21	2.27
C863	Cu	62.90	55.86	4.98	63.99	0.77
	Sn	0.02	2.38	1.67	1.81	1.26
	Pb	0.01	3.61	2.55	0.78	0.54
	Zn	26.41	24.57	1.30	23.15	2.31
	Fe	2.43	3.55	0.80	1.22	0.86
	Al	5.21	8.07	2.02	5.35	0.10

	Mn	2.91	1.95	0.68	3.72	0.57
	others	0.11	0.00	0.08	0.00	0.08
C954	Cu	85.82	75.29	7.44	71.91	9.83
	Fe	3.46	3.58	0.08	1.35	1.50
	Ni	0.05	3.44	2.40	0.74	0.49
	Al	10.43	11.45	0.72	8.85	1.12
	Mn	0.24	2.09	1.31	0.83	0.42
	others	0.00	4.15	2.93	16.31	11.53
C932	Fe	0.13	3.00	2.03	0.93	0.57
	Pb	7.67	10.34	1.89	4.32	2.37
	Ni	0.40	0.61	0.14	0.23	0.12
	P	0.04	3.80	2.66	0.10	0.04
	Sn	6.47	8.17	1.21	2.61	2.73
	Zn	3.78	7.85	2.88	17.50	9.70
	Sb	0.25	3.98	2.64	0.64	0.27
	Cu	81.22	58.48	16.08	71.34	6.99
	others	0.04	3.77	2.63	2.33	1.62

C673	Cu	59.40	52.72	4.73	68.61	6.51
	Fe	0.06	0.57	0.36	0.92	0.61
	Pb	1.76	4.98	2.28	0.99	0.54
	Mn	2.50	1.76	0.52	1.12	0.98
	Ni	0.06	1.22	0.82	0.19	0.09
	Si	0.97	2.87	1.34	0.55	0.30
	Sn	0.05	2.87	2.00	1.81	1.24
	Zn	35.17	31.51	2.59	21.42	9.72
	others	0.03	1.50	1.04	4.39	3.08

The results of A-ELM-SVR model which uses the output of A-ELM as its input is compared to that of A-SVR-ELM model which takes the output of A-SVR as its input and presented in table 5.15.

Table 5.15 : Comparison between the results of the developed A-SVR-ELM and A-ELM-SVR chemometrics including their standard deviations from the certified values

Sample	Element	Con. (wt%)	A-SVR-ELM(wt%)	Standard deviation (wt%)	A-ELM-SVR(wt%)	Standard deviation (wt%)
C510	Cu	94.99	94.06	0.66	94.76	0.16
	Sn	4.66	4.81	0.10	5.24	0.41

	others	0.35	1.13	0.55	0.00	0.25
C642	Al	6.82	6.27	0.39	7.06	0.17
	Co	0.15	0.60	0.32	0.10	0.03
	Cu	90.85	88.42	1.72	90.61	0.17
	Fe	0.18	0.68	0.36	0.35	0.12
	Mn	0.02	0.50	0.34	0.04	0.02
	Ni	0.15	0.78	0.44	0.16	0.01
	Si	1.78	1.58	0.14	1.31	0.33
	Sn	0.01	0.65	0.46	0.08	0.05
	Zn	0.04	0.51	0.33	0.28	0.17
C655	Cu	60.30	60.03	0.19	60.06	0.17
	Fe	0.02	0.25	0.16	0.25	0.17
	Pb	0.01	0.70	0.49	0.25	0.17
	Sn	0.81	0.47	0.24	0.58	0.17
	Zn	38.85	38.55	0.21	38.61	0.17
	others	0.00	0.00	0.00	0.24	0.17
C863	Cu	62.90	63.09	0.13	62.66	0.17

	Sn	0.02	0.16	0.10	0.03	0.01
	Pb	0.01	0.66	0.46	0.07	0.04
	Zn	26.41	25.15	0.89	26.65	0.17
	Fe	2.43	0.68	1.24	2.48	0.03
	Al	5.21	5.33	0.09	5.45	0.17
	Mn	2.91	3.25	0.24	2.67	0.17
	others	0.11	1.68	1.11	0.00	0.08
C954	Cu	85.82	86.33	0.37	85.58	0.17
	Fe	3.46	0.67	1.97	3.23	0.17
	Ni	0.05	0.70	0.46	0.07	0.01
	Al	10.43	9.17	0.90	10.67	0.17
	Mn	0.24	0.37	0.09	0.00	0.17
	others	0.00	2.76	1.95	0.46	0.32
C932	Fe	0.13	0.54	0.29	0.32	0.14
	Pb	7.67	8.44	0.55	7.91	0.17
	Ni	0.40	0.38	0.02	0.16	0.17
	P	0.04	0.59	0.39	0.28	0.17

	Sn	6.47	5.46	0.71	6.23	0.17
	Zn	3.78	5.08	0.92	4.02	0.17
	Sb	0.25	0.53	0.19	0.03	0.16
	Cu	81.22	78.38	2.01	80.98	0.17
	others	0.04	0.60	0.40	0.07	0.02
C673	Cu	59.40	59.11	0.20	56.98	1.71
	Fe	0.06	0.17	0.08	0.28	0.15
	Pb	1.76	1.25	0.36	0.68	0.77
	Mn	2.50	0.81	1.19	1.62	0.62
	Ni	0.06	0.20	0.10	0.17	0.08
	Si	0.97	0.43	0.38	0.15	0.58
	Sn	0.05	0.43	0.27	0.94	0.63
	Zn	35.17	34.99	0.13	36.76	1.12
	others	0.03	2.61	1.82	2.42	1.69

The absolute percentage deviation of each of the elements present in all the standard bronze samples are compared for each of the chemometrics developed based on hybrid

fusion and presented in Fig.5.32. A-ELM-SVR chemometric has highest number of elements with less than 5% deviation while A-SVR chemometric has the lowest.

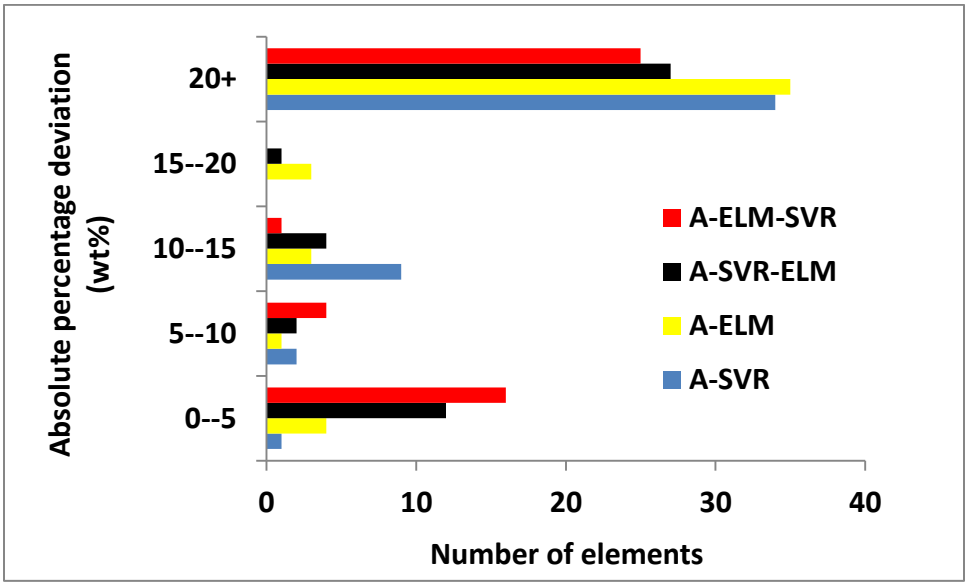

Figure 5.32: A graph of absolute percentage deviation against the number of element for each of the developed chemometrics developed based on hybrid fusion

The figure shows the deviation of the results of each of the chemometrics based on hybrid fusion. It can be deduced from the figure that the proposed hybrid fusion method improves the performance of ordinary A-SVR and A-ELM chemometrics

5.6.3 Results of I-SVR based chemometrics for quantitative analysis of standard bronze spectra

This section presents the results of three novel techniques by which the performance of SVR chemometric has been improved for the quantitative analysis of LIBS spectra using integrated line intensity. The hyper-parameters of the developed models are optimized using gravitational search algorithm (GSA).

5.6.4 Optimization of I-SVR based chemometrics parameters using GSA

Fig.5.33 shows how number of agents affects the convergence of the I-SVR based chemometric. The graph of RMSE against the number of iteration for I-SVR-GSA-IRP chemometric is only shown to avoid repetition.

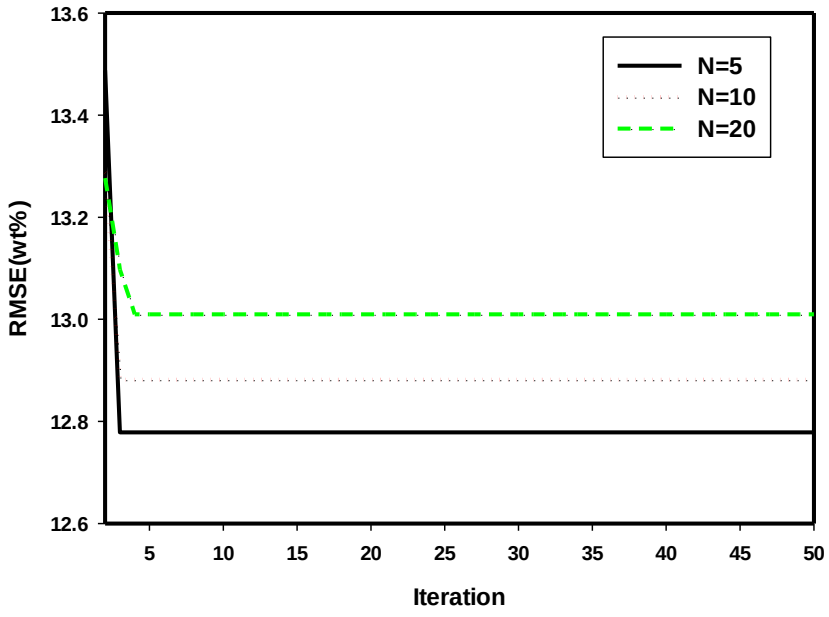

Figure 5.33: A graph of RMSE against the number of iteration for performance sensitivity of I-SVR-GSA-WIRP to the number of agents

In the graph presented in Fig.5.33, the model converges to local minimum when ten and twenty numbers of agents are involved in global minimum search. The small number of agents converges faster than large number of agents; the optimum number of agents in the presented figure is five. Similar investigation was conducted for other I-SVR based chemometric. Table 5.16 presents the values of the optimum parameters for each of the chemometrics.

Table 5.16 : Optimum values of the model parameters

	I-SVR-GSA-WIRP	I-HSVR-GSA-WIRP
Penalty factor	651.9521	41.9645
Epsilon	0.1122	0.9486
Kernel option	0.493	0.8458
Kernel function	Polynomial	Gaussian
Hyper-parameter lambda	10E-1	E-7
Agent population	10	5

5.6.5 Significance of the proposed homogenous hybridization to the performance of I-SVR chemometrics

The performance enhancement of the proposed homogenous hybridization is presented in Fig.5.34, Fig.5.35 and Fig.5.36 for chemometrics developed without using internal reference preprocessing method. The comparison between the chemometrics was made using three criteria in line with usual practices in chemometrics [136]. On the basis of RMSE as presented in Fig. 5.34, I-HSVR-GSA-WIRP outperforms I-SVR-GSA-WIRP with performance improvement of 50.53%

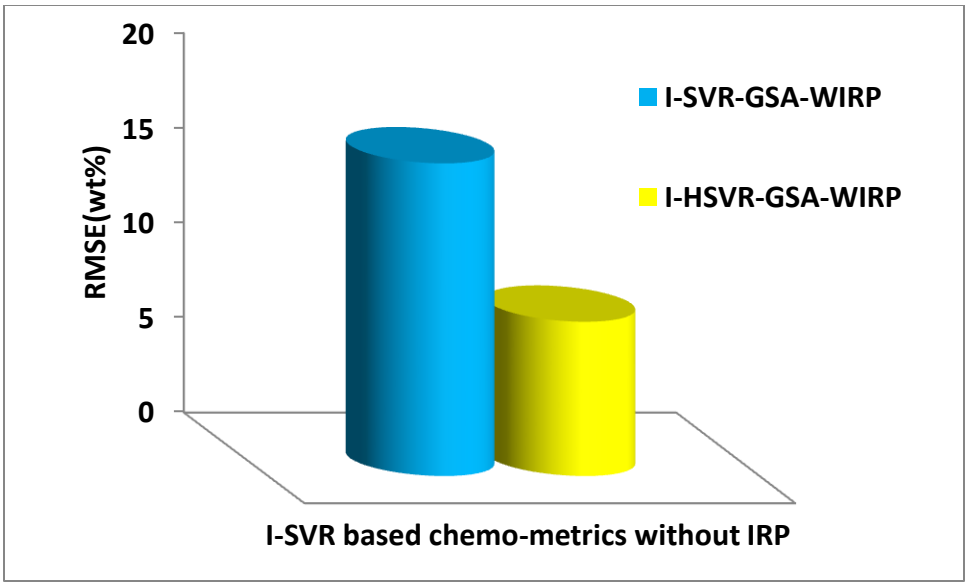

Figure 5.34: A graph of RMSE against the developed chemometric models for performance enhancement of SVR chemometrics without IRP on the basis of RMSE using homogenous hybridization

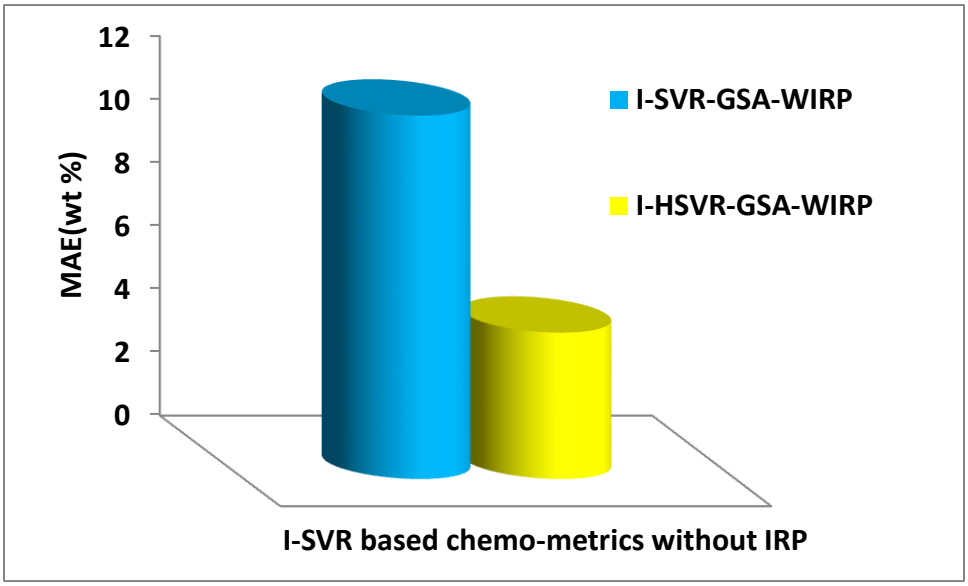

Figure 5.35: A graph of RMSE against the developed chemometric models for performance enhancement of SVR chemometrics without IRP on the basis of MAE using homogenous hybridization

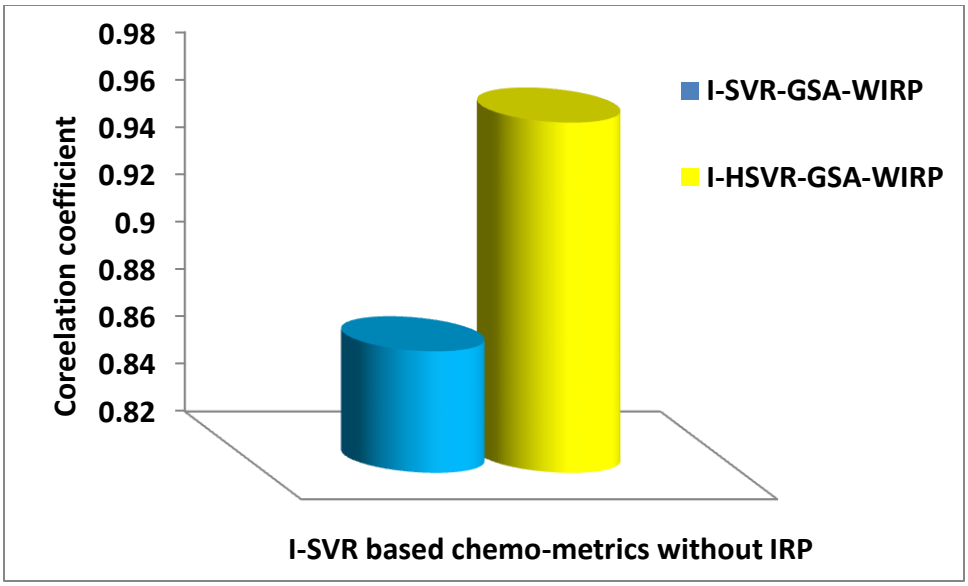

Figure 5.36: A graph of RMSE against the developed chemometric models for performance enhancement of SVR chemometrics without IRP on the basis of correlation coefficient using homogenous hybridization

Similarly, on the basis of MAE as presented in Fig.5.35, I-HSVR-GSA-WIRP outperforms I-SVR-GSA-WIRP with performance improvement of 59.61% while performance improvement of 11.06% was obtained when the models are compared on the basis of correlation coefficient as shown in Fig. 5.36. The performance comparison between the models are tabulated and presented in table 5.17.

Table 5.17 : Evaluation of the predictive and generalization ability of the proposed SVR based chemometrics

	GSA-SVR-WIRP	GSA-HSVR-WIRP
CC (%)	0.8715	0.9679
RMSE (wt%)	16.5009	8.1620
MAE (wt%)	11.5039	4.6470

5.6.6 Comparison of the results of the proposed I-SVR chemometrics with the certified values

The outputs of the developed I-SVR based chemometrics are presented in table 5.18 with inclusion of standard deviation of each of the results from the certified concentration. I-HSVR-GSA chemometric gives better results as its outputs are close to the certified concentration. The performance of I-HSVR-GSA over I-SVR-GSA chemometric can be attributed to the implementation of the proposed homogenous hybridization performance enhancement.

Table 5.18: Comparison between the results of the developed I-SVR based chemometric with certified values. The standard deviation of each of the point is also included

Element	Sample	Certified value (wt%)	I-SVR-GSA (wt%)	Standard deviation (wt%)	I-HSVR-GSA (wt%)	Standard deviation (wt%)
Cu	C510	94.99	58.76	25.62	85.17	6.95
Sn		4.66	4.18	0.34	4.10	0.40
Others		0.35	37.06	25.96	10.74	7.35
Al	C642	6.82	8.55	1.22	12.54	4.05
Cu		90.85	61.44	20.80	84.09	4.78
Fe		0.18	0.97	0.56	0.82	0.46
Ni		0.15	0.21	0.04	1.11	0.68

Sn		0.01	0.27	0.19	0.80	0.56
Others		1.99	28.56	18.79	0.62	0.97
Cu	C655	60.30	54.12	4.37	59.16	0.81
Fe		0.02	1.06	0.74	0.78	0.54
Sn		0.81	0.23	0.42	1.03	0.15
Zn		38.85	26.33	8.86	37.92	0.66
Others		0.01	18.27	12.91	1.11	0.77
Cu	C863	62.90	63.62	0.51	58.65	3.01
Sn		0.02	1.01	0.70	0.81	0.56
Pb		0.01	0.98	0.69	0.82	0.57
Zn		26.41	2.02	17.24	1.46	17.64
Fe		2.43	4.07	1.16	4.26	1.30
Al		5.21	4.13	0.76	4.18	0.73
Mn		2.91	4.79	1.33	3.33	0.30
Others		0.11	19.37	13.62	26.48	18.64
Cu	C954	85.82	65.65	14.26	77.89	5.60
Fe		3.46	5.00	1.08	4.48	0.72

Ni		0.05	1.11	0.75	0.75	0.49
Al		10.43	12.62	1.54	14.55	2.91
Mn		0.24	1.15	0.65	0.71	0.33
Others		0.00	14.48	10.24	1.63	1.15
Fe	C932	0.13	1.63	1.06	0.83	0.50
Pb		7.67	2.40	3.72	1.74	4.19
Ni		0.40	1.25	0.60	0.66	0.18
Sn		6.47	0.97	3.88	0.82	3.99
Zn		3.78	4.61	0.59	3.14	0.45
Al		0.00	1.71	1.21	0.93	0.65
Cu		81.22	61.44	13.99	84.09	2.03
Others		0.34	25.99	18.14	7.78	5.26
Cu	C673	59.40	53.86	3.92	58.52	0.62
Fe		0.06	1.05	0.70	0.78	0.51
Pb		1.76	2.91	0.82	1.51	0.18
Mn		2.50	4.47	1.39	3.36	0.61
Zn		35.17	37.20	1.44	35.33	0.11

Others	1.11	0.50	0.43	0.49	97.97

5.6.7 Results of I-ELM based chemometrics for quantitative analysis of standard bronze spectra

The results of the quantitative analysis performed on the seven standard bronze samples using the developed I-ELM based chemometrics are presented and discussed in this section. The optimization of I-ELM chemometrics parameters is also presented. The exploration and exploitation capacity of the chemometrics as a function of the number of objects searching for global solution is investigated using varying number of objects and observe how the convergence of the models behave under different number of objects

5.6.8 Influence of the agent population on the convergence of the proposed ELM based chemometrics

The dependence of the performance ELM based chemometric on the initial population of agents is presented in Fig.5.37 for HELM-GSA-WIRP. The gravitational pull between the agents become significant when large number of agents is exploiting a small portion of a search space for a global solution. Similarly, exploration ability of the model is weakened when few agents explore a wide search space. In order to strike a balance between exploration and exploitation capacity of the gravitational search algorithm based chemometric, the initial population of the agents is varied until the model demonstrates its optimum performance. As depicted in Fig.5.37, GSA-I-HELM-WIRP converges to global minima when five numbers of agents was used for the simulation. Similar search was conducted for other I-ELM based chemometrics developed.

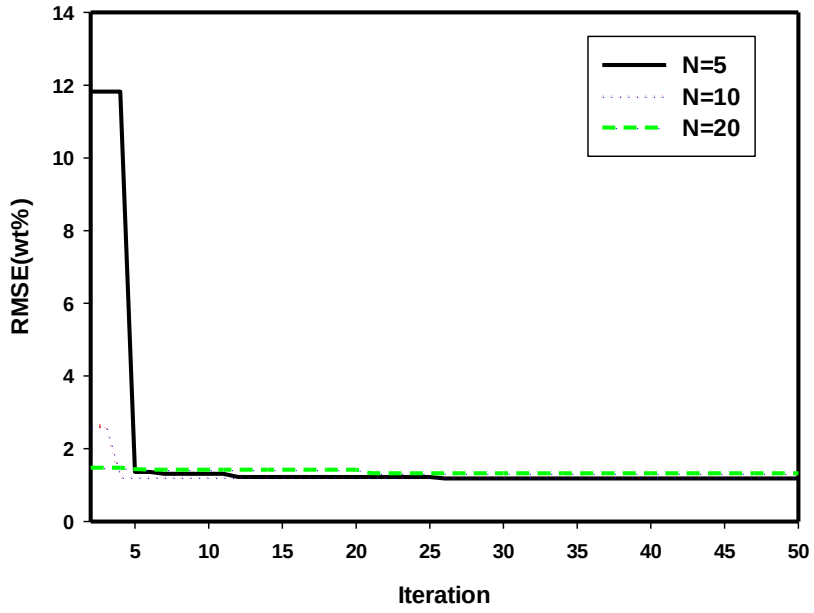

Figure 5.37 : A graph of RMSE against the number of iteration for performance sensitivity of HELM- GSA-WIRP chemometric to the population of agent

Table 5.19 shows the optimum values of hyper-parameters for the developed I-ELM based chemometrics.

Table 5.19 : Optimum values of extreme learning machine based chemometrics parameters

Extreme learning based chemo	Activation function	Number of hidden neurons	Number of agent
ELM- GSA-WIRP	Sine function	53	10
HELM- GSA-WIRP	Sigmoid function	14	5

5.6.9 Performance sensitivity of I-ELM chemometrics to the proposed homogenous hybridization method

The performance enhancing effect of the proposed homogeonus hybridization method to I-ELM based chemometrics is presented in Fig.5.38, Fig.5.39 and Fig.5.40 on the basis of RMSE, MAE and CC, respectively. I-HELM-GSA-WIRP outperforms I-ELM-GSA-WIRP with performance improvement of 58.33%, 58.41% and 0.6183% on the basis of RMSE, MAE and CC, respectively as presented in Fig.5.38, Fig.5.39 and Fig.5.40. It should be noted that the higher the value of CC, the better the model. GSA-I-ELM-WIRP shows the lowest value of CC. This can be attributed to the extent of self-absorption in the spectra used in developing the model as well as inability of ordinary ELM to fully capture the non-linear relationship between the descriptors and the elemental concentrations. This poor generalization performance demonstrated by GSA-I-ELM-WIRP also manifests in the value of its RMSE and MAE as illustrated in Fig.5.39 and Fig.5.40, respectively.

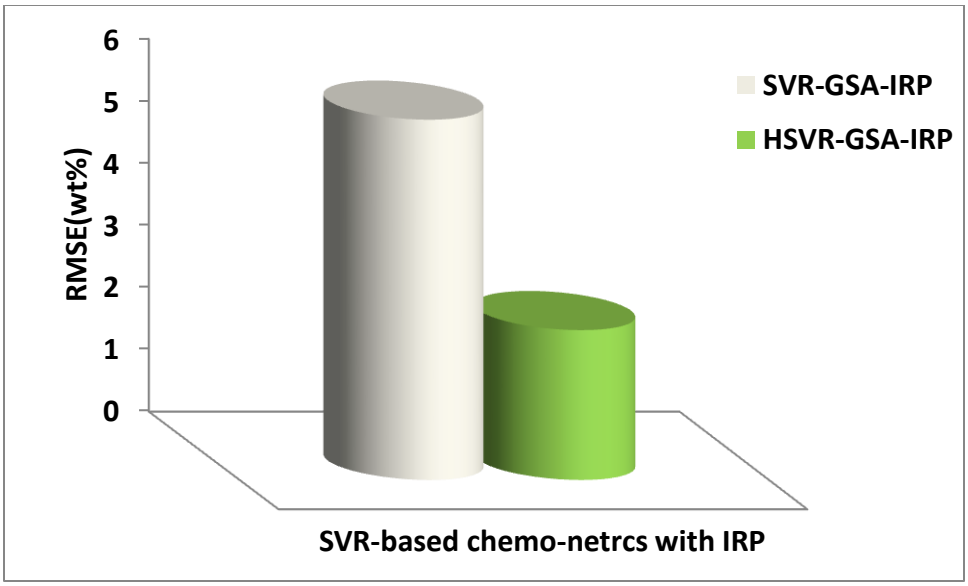

Figure 5.38: A graph of RMSE against the developed chemometric models for performance enhancement of ELM chemometrics without IRP on the basis of RMSE using homogenous hybridization

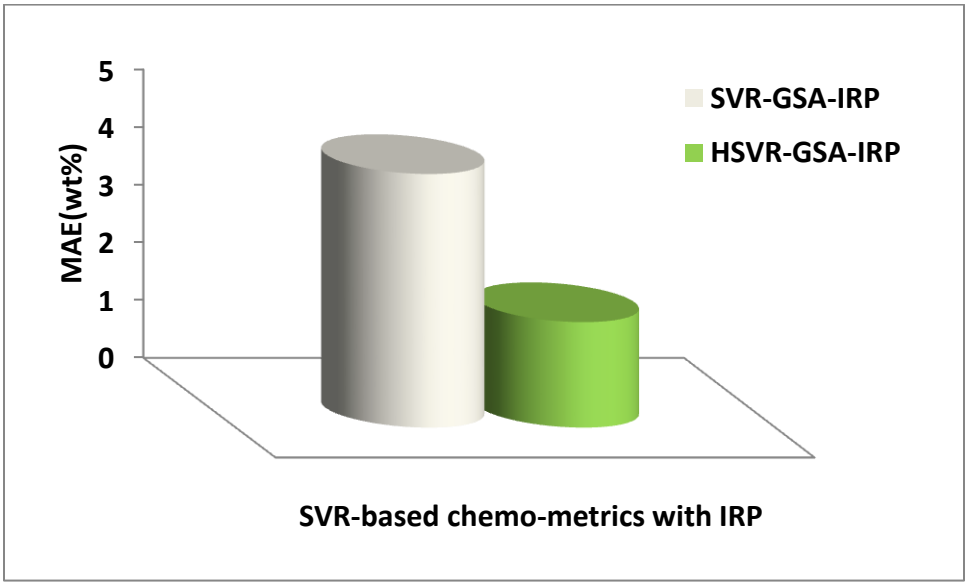

Figure 5.39: A graph of RMSE against the developed chemometric models for performance enhancement of ELM chemometrics without IRP on the basis of MAE using homogenous hybridization

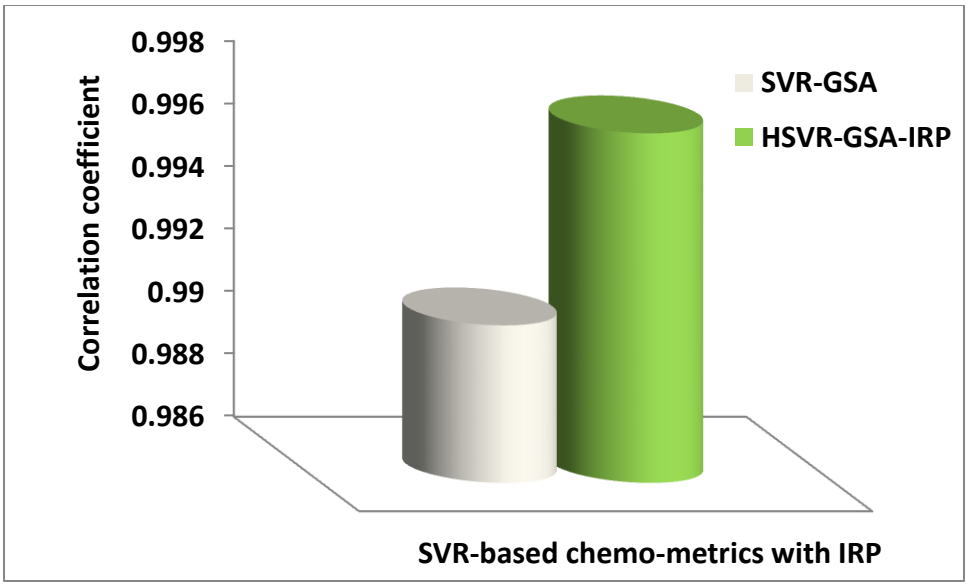

Figure 5.40: A graph of RMSE against the developed chemometric models for performance enhancement of ELM chemometrics without IRP on the basis of MAE using homogenous hybridization

In the case of RMSE and MAE, the lower the value, the better the model. GSA-HELM-WIRP shows a better performance as compared to GSA-ELM-WIP chemometric since the function approximated by GSA-ELM-WIP model was further approximated and linearized in GSA-HELM-WIP chemometric and ultimately results into more robust and accurate model. The performance measuring parameters for I-ELM chemometrics are presented in table 5.20.

Table 5.20 : Measure of generalization performance of the proposed extreme learning machine based chemometrics (average over all the seven folds)

	ELM-GSA-WIRP	HELM-GSA-WIRP
RMSE (wt%)	5.8061	2.4196
MAE (wt%)	4.3983	1.8292
CC (wt%)	0.9911	0.9972

5.7 Comparison of the results of the developed I-ELM based chemometrics with the certified values

Comparison between the results of the developed I-ELM based chemometrics and the certified concentrations are presented in table 5.21. For all samples, GSA-I-HELM chemometric gives a value closer the certified value and shows better performance as compared to GSA-I-ELM chemometric. GSA-I-HELM shows improved performance since it fully captures the non-linear relationship between the inputs and the output while and minimizes the effect of self-absorption.

Table 5.21: Comparison of the results of the developed I-ELM based chemometrics with certified values. Standard deviation of each of the results is also included

Samples	Composition	Certified value (wt%)	I-ELM-GSA (wt%)	Standard deviation (wt%)	I-HELM-GSA (wt%)	Standard deviation (wt%)
Cu	C510	94.99	93.86	0.80	96.28	0.91
Sn		4.66	4.66	0.00	3.30	0.96
others		0.35	1.48	0.80	0.43	0.06
Al	C642	6.82	6.12	0.50	4.84	1.40
Cu		90.85	78.59	8.67	87.00	2.72
Fe		0.18	1.55	0.97	0.11	0.05
Mn		0.02	2.24	1.57	0.21	0.13

Ni		0.15	1.10	0.67	0.35	0.14
Sn		0.01	1.98	1.40	0.16	0.11
Zn		0.04	7.13	5.01	3.61	2.52
others		1.93	1.29	0.46	3.72	1.27
Cu	C655	60.30	52.67	5.40	58.98	0.94
Fe		0.02	2.41	1.69	0.46	0.32
Zn		38.85	37.14	1.21	39.27	0.29
others		0.83	7.78	4.92	1.29	0.33
Cu	C863	62.90	58.79	2.91	66.89	2.82
Sn		0.02	0.45	0.31	0.26	0.17
Zn		26.41	23.98	1.72	26.47	0.04
Al		5.21	6.16	0.67	4.82	0.28
Mn		2.91	3.31	0.28	1.35	1.10
others		2.55	7.31	3.37	0.22	1.65
Cu	C954	85.82	76.53	6.57	85.37	0.32
Fe		3.46	7.97	3.18	2.32	0.81
Ni		0.05	1.07	0.72	0.35	0.21

Al		10.43	12.46	1.43	10.34	0.07
Mn		0.24	1.52	0.91	0.10	0.09
others		0.00	0.46	0.32	1.53	1.08
Fe	C932	0.13	2.99	2.02	1.17	0.74
Pb		7.67	6.62	0.74	4.37	2.33
Ni		0.40	0.36	0.03	0.58	0.12
Sn		6.47	5.72	0.53	4.87	1.13
Zn		3.78	3.36	0.30	1.38	1.70
Al		0.00	3.19	2.25	1.29	0.91
Cu		81.22	73.07	5.76	82.40	0.84
others		0.34	4.68	3.07	3.95	2.56
Cu	C673	59.40	51.97	5.25	58.06	0.95
Fe		0.06	1.30	0.88	0.28	0.15
Pb		1.76	8.56	4.81	1.75	0.00
Si		0.97	1.32	0.25	0.26	0.50
Sn		0.05	1.16	0.79	0.35	0.21
Zn		35.17	33.24	1.37	34.68	0.35

others	2.59	2.45	0.10	4.61	97.84

CHAPTER 6

Results of LIBS measurement on crayfish and grape samples

This chapter presents the results obtained when the proposed chemo-metric based techniques are applied to crayfish and grape samples. The significance of chemo-metrics based technique is investigated by comparing the obtained results with the results of quantitative analysis using the standard ICP-OES analytical method. The elemental compositions of each of the crayfish and grape samples are identified using finger print wavelengths of the element in accordance to NIST data base. Furthermore, local thermodynamic equilibrium condition of the plasma was investigated and ensured before quantitative analysis. The chemometric methods applied on these samples include SVR and ELM with the hyper-parameters of all the chemometrics optimized using GSA.

6.1 Elemental identification of crayfish and grape constituents using LIBS

The results of the LIBS measurement performed on crayfish and grape samples are presented in this section. The peaks observed in each of the spectrum was compared with the NIST data base, as a result, the finger print of all the elements present in the samples are identified.

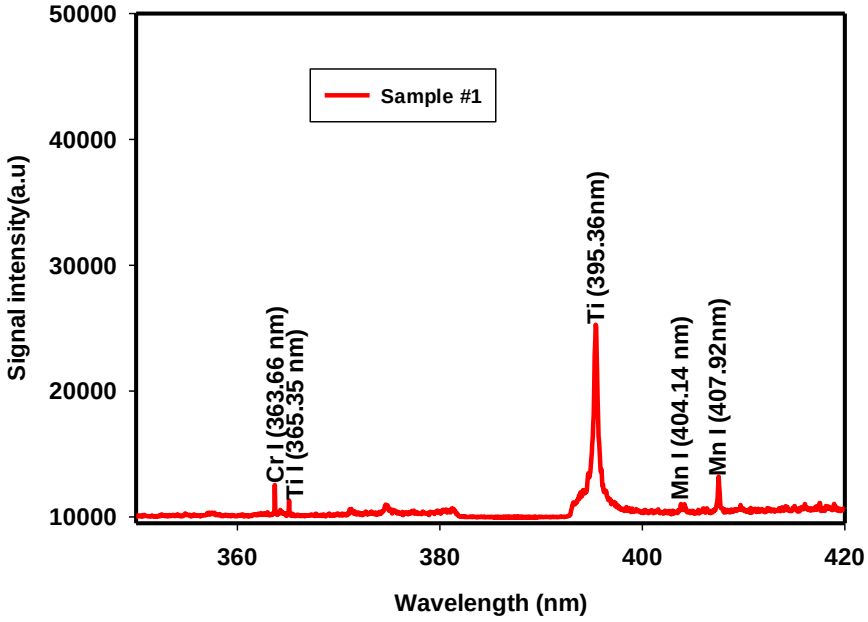

Figure 6.1: A typical LIBS spectrum recorded for crayfish (sample #1) at wavelength range of 350nm to 420nm

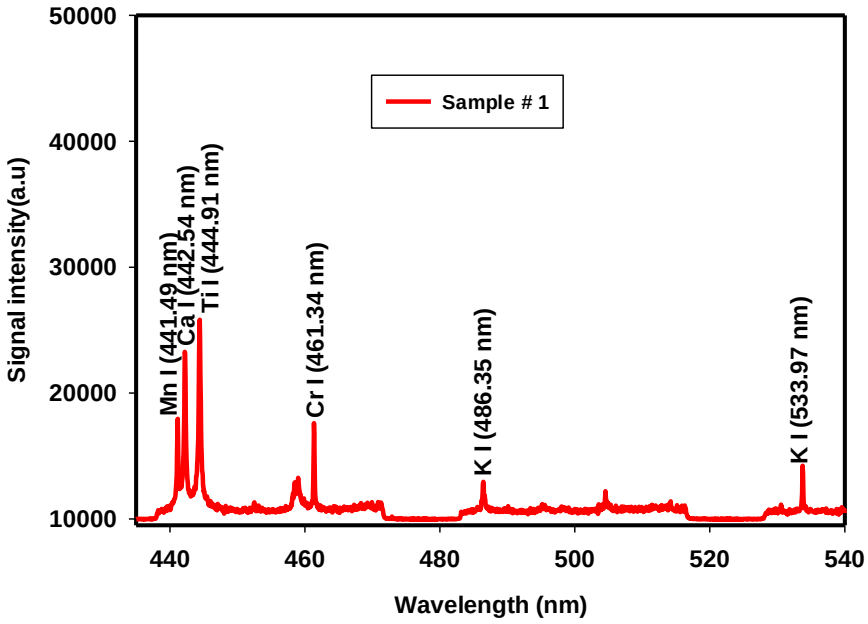

Figure 6.2: A typical LIBS spectrum recorded for crayfish (sample #1) at wavelength range of 420 nm to 540 nm

Fig. 6.1 shows a graph of LIBS intensity against wavelength for wavelength range of 360nm to 420nm, Fig.6.2 presents the same spectrum over a wavelength range of 440nm to 540nm, Fig.6.3 shows the spectrum for wavelength range of 520nm to 660nm while Fig.6.4 depicts the spectrum for sample 1 over a wavelength range of 720nm to 820nm. Elements that are identified include chromium, titanium, manganese, calcium, potassium, lead and sodium aluminum. Neutral chromium emission lines are observed at wavelength of 363.66nm and 461.34 nm in sample #1. Calcium and manganese lines of sample #1 are shown in Fig.6.5. The neutral species chromium is identified in LIBS emission line spectrum obtained from sample #2 at 428.97nm as shown in Fig.6.6 and at 534.83 nm wavelength as shown in Fig.6.7. Calcium emission line of sample #2 is shown in Fig.6.8. Similarly, in sample #3 chromium emission line is identified at 534.83nm while the chromium finger print is identified in sample #4 at 392.10nm and 534.83nm. In case of titanium, sample #1 contains titanium as identified in its spectrum presented at 365.35nm, 395.36nm and 444.91nm wavelengths. Similarly, titanium is present in other investigated crayfish samples. Neutral Titanium is identified in sample #2 at wavelengths of 428.6 nm, 586.82nm, and 595.32nm and 720.94, titanium appears in sample #3 spectrum at wavelength of 375.36nm, 441.73nm, 444.91nm as shown in Fig.6.9, 586.65nm as depicted in Fig.6.10 and 720.94nm as presented in Fig.6.11while the last sample (sample #4) spectrum shows titanium peak at 375.36nm as depicted in Fig.6.12, 441.73nm, 444.91 nm, 586.65nm as presented in Fig.6.13 and 720.94nm as shown in Fig.6.14. Another element identified in all the four samples is manganese which is identified at wavelength of 404.14 nm, 407.92 nm and 441.49nm in sample #1, 404.87nm, 408.36 nm and 428.11nm in sample #2. Sample #3 shows manganese peak at

404.87 nm and 408.36nm while sample #4 shows manganese peak at 404.87 nm and 408.36nm. Presence of calcium in all the four samples is shown in the presented spectrum. Calcium lines are identified in sample #1 at 442.54 nm, 644.98nm and 647.16nm while at 393.36 nm (singly ionized), 396.85nm (singly ionized), 443.02nm (neutral), 442.54nm (neutral), 443.39nm (neutral), 445.59nm (neutral), 610.27nm (neutral) and 714.81nm (neutral) for sample #2. The emission lines of calcium identified in sample #3 include 393.36nm (singly ionized), 396.85nm (singly ionized), 442.54nm (neutral), 616.21nm (neutral), 646.26nm (neutral), 714.81nm (neutral) and 820.17nm (singly ionized). In sample #4, calcium emission lines are identified at wavelength of 442.54 nm (neutral), 616.21nm (neutral), 646.28nm (neutral), 714.81nm (singly ionized), and 820.17nm (singly ionized). Strong and persistence emission lines of potassium are also identified in all the four samples at wavelength of 766.49nm and 769.90nm. The details about the wavelength of the identified peaks can be observed from presented spectral.

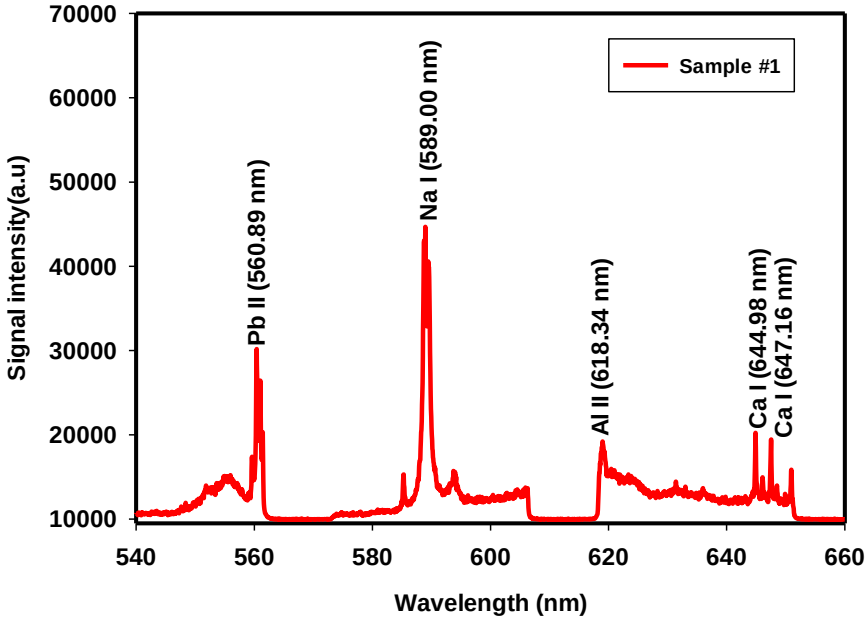

Figure 6.3: A typical LIBS spectrum recorded for crayfish (sample #1) at wavelength range of 540 nm to 660 nm

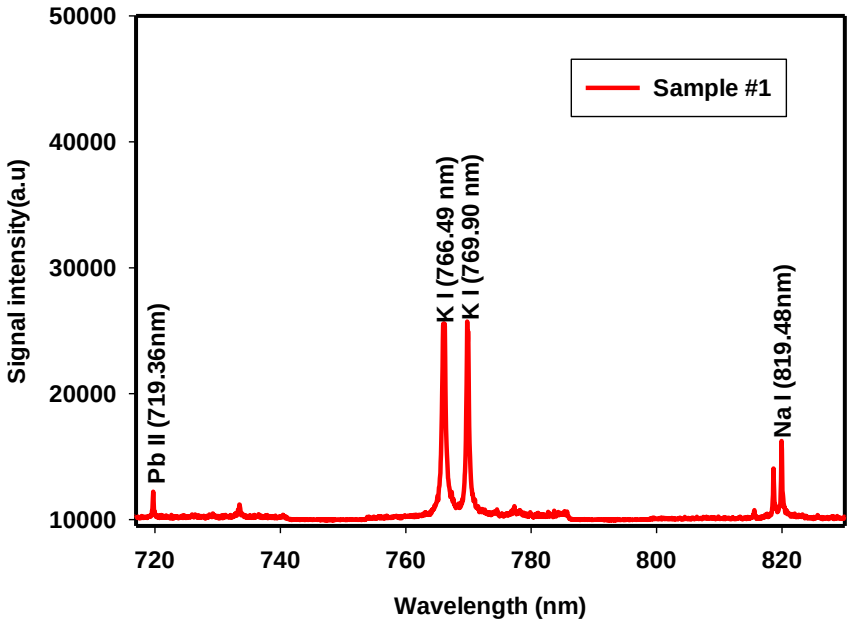

Figure 6.4: A typical LIBS spectrum recorded for crayfish (sample #1) at wavelength range of 720 nm to 820 nm

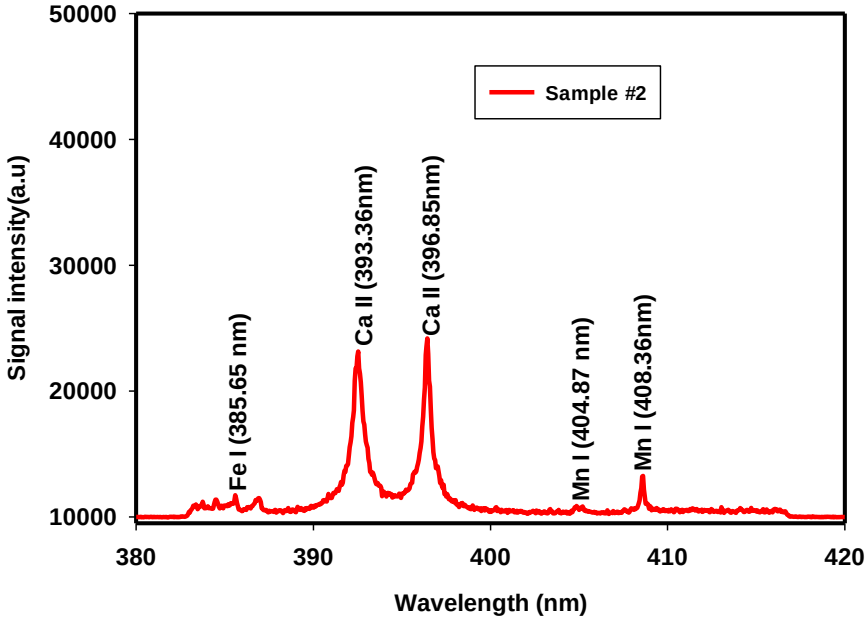

Figure 6.5: A typical LIBS spectrum recorded for crayfish (sample #2) at wavelength range of 380 nm to 420 nm

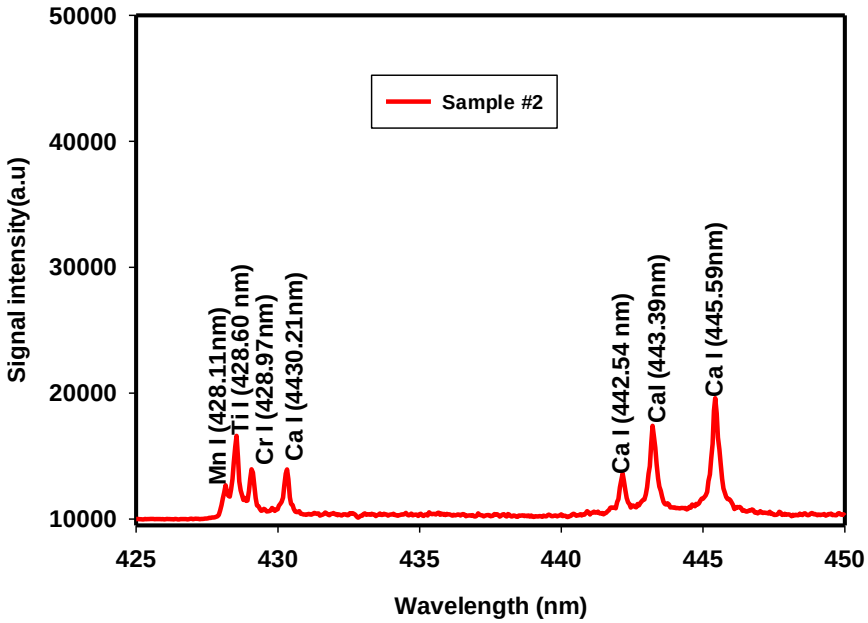

Figure 6.6: A typical LIBS spectrum recorded for crayfish (sample #2) at wavelength range of 425 nm to 450 nm

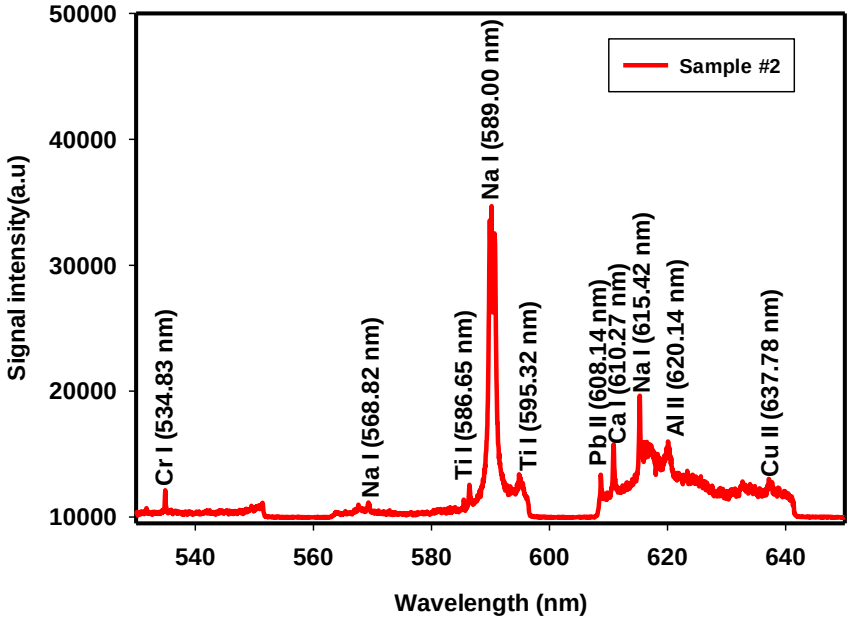

Figure 6.7 : A typical LIBS spectrum recorded for crayfish (sample #2) at wavelength range of 540 nm to 640 nm

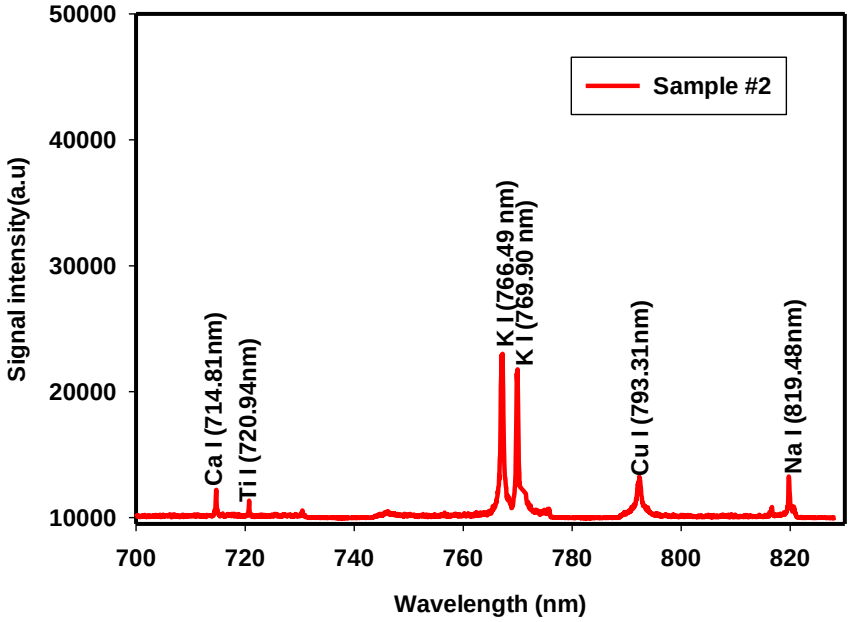

Figure 6.8: A typical LIBS spectrum recorded for crayfish (sample #2) at wavelength range of 700 nm to 820 nm

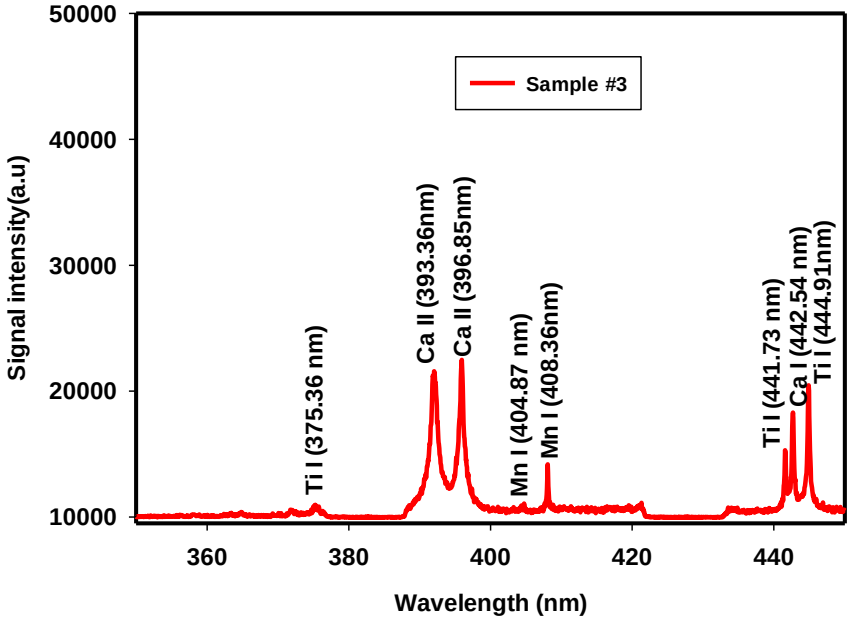

Figure 6.9 : A typical LIBS spectrum recorded for crayfish (sample #3) at wavelength range of 350 nm to 450 nm

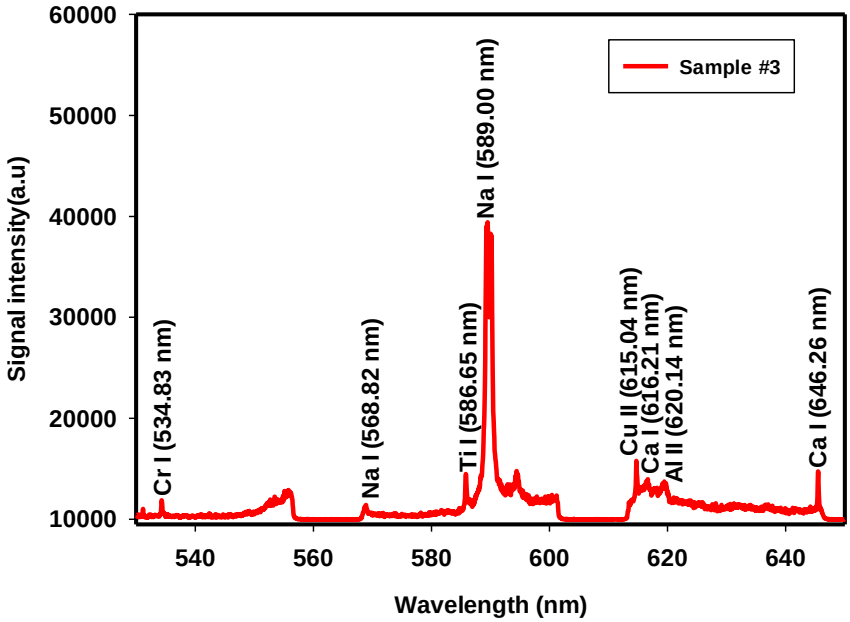

Figure 6.10: A typical LIBS spectrum recorded for crayfish (sample #3) at wavelength range of 530 nm to 650 nm

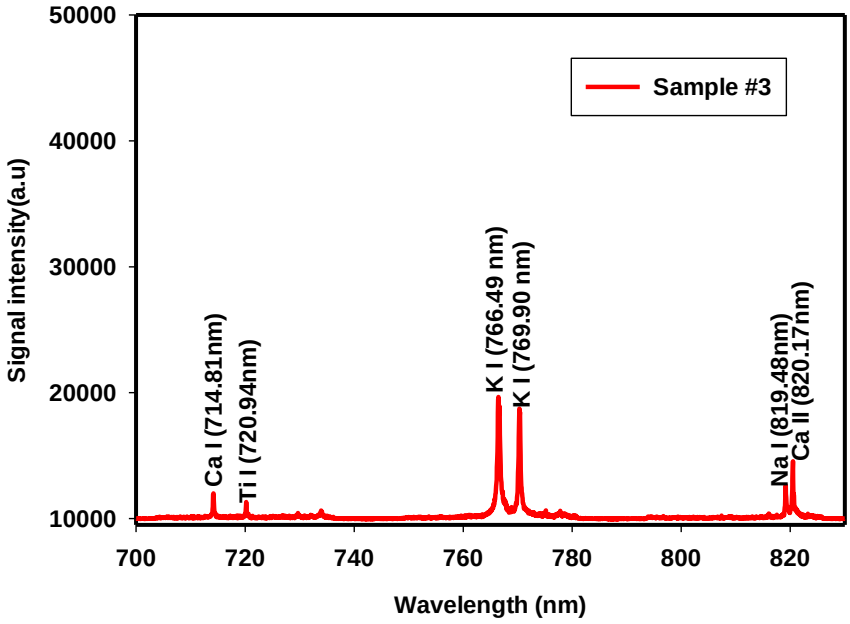

Figure 6.11: A typical LIBS spectrum recorded for crayfish (sample #3) at wavelength range of 700 nm to 830 nm

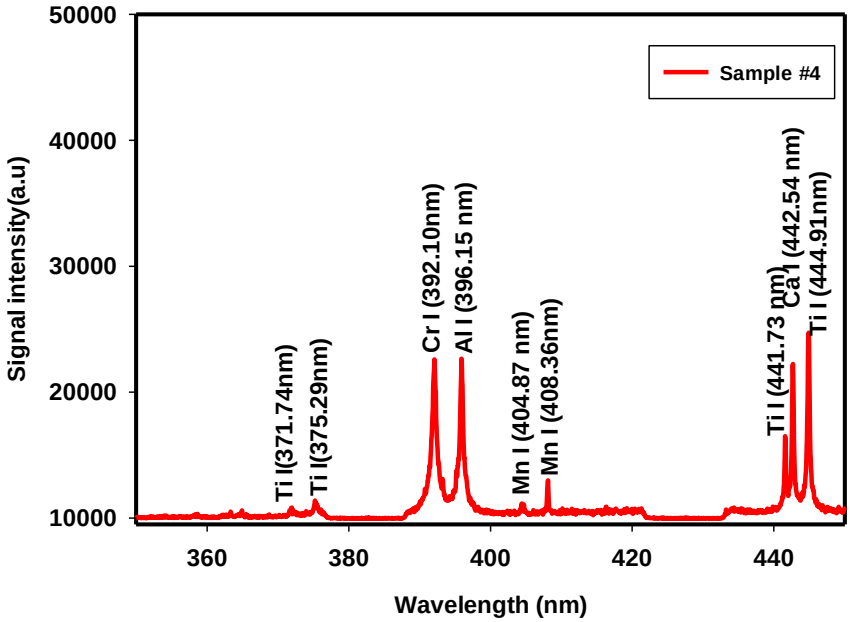

Figure 6.12 : A typical LIBS spectrum recorded for crayfish (sample #4) at wavelength range of 350 nm to 450 nm

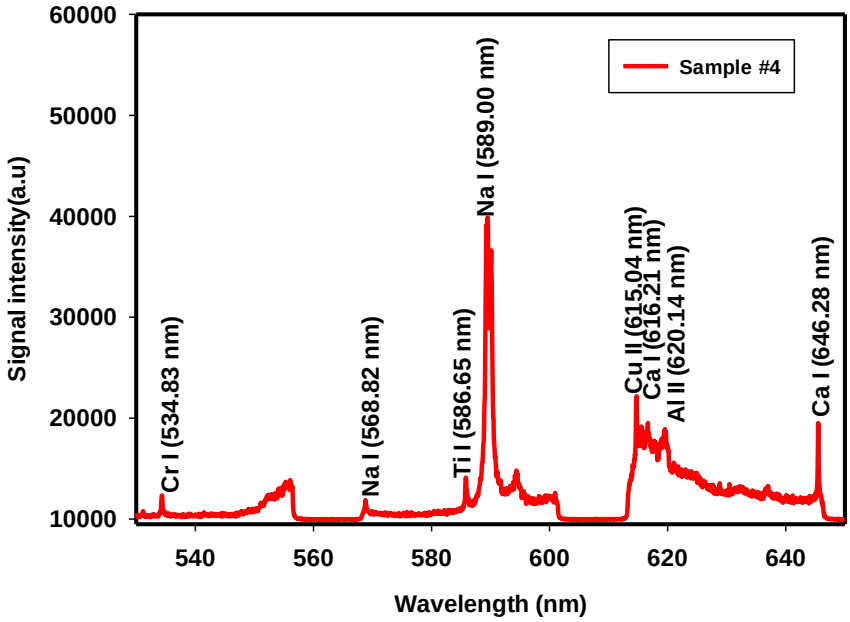

Figure 6.13: A typical LIBS spectrum recorded for crayfish (sample #4) at wavelength range of 530 nm to 650 nm

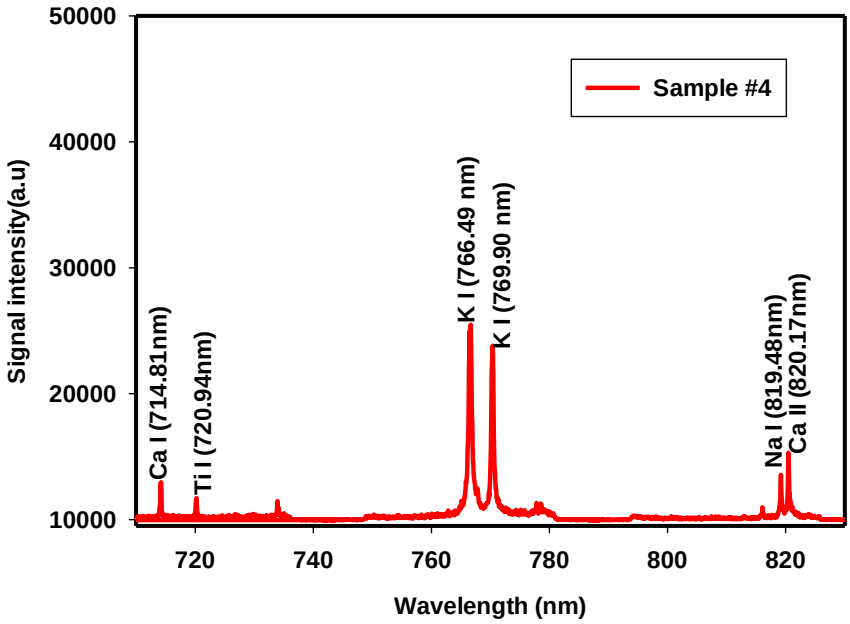

Figure 6.14 : A typical LIBS spectrum recorded for crayfish (sample #4) at wavelength range of 710 nm to 830 nm

The constituents of green grape are presented in Fig. 6.15, Fig.6.16 and Fig.6.17. The elements present in the investigated green grape include manganese, iron, calcium, titanium, potassium as presented in Fig.6.15. Sodium fingerprints are also identified in the spectrum presented in Fig.6.16 while strong lines of potassium are shown in Fig.6.17.

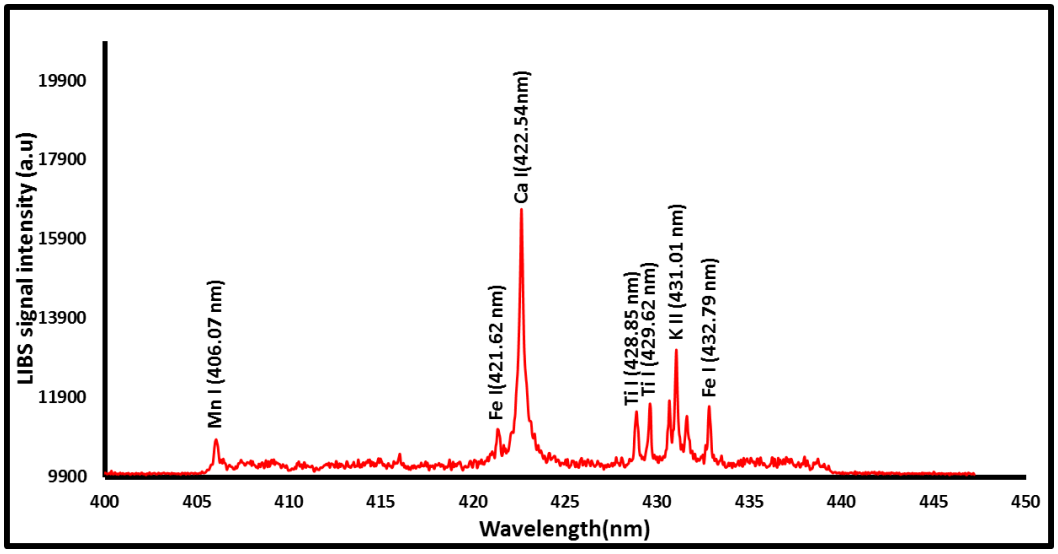

Figure 6.15: A typical LIBS spectrum recorded for green grape sample at wavelength range of 400 nm to 450 nm

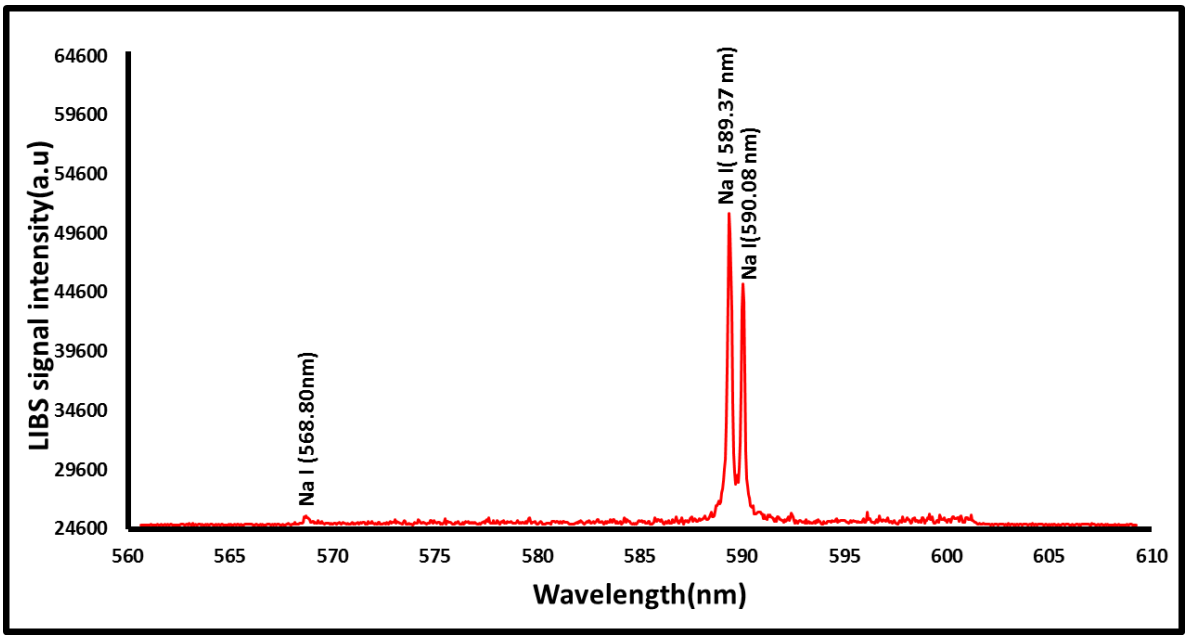

Figure 6.16: A typical LIBS spectrum recorded for green grape sample at wavelength range of 560 nm to 610 nm

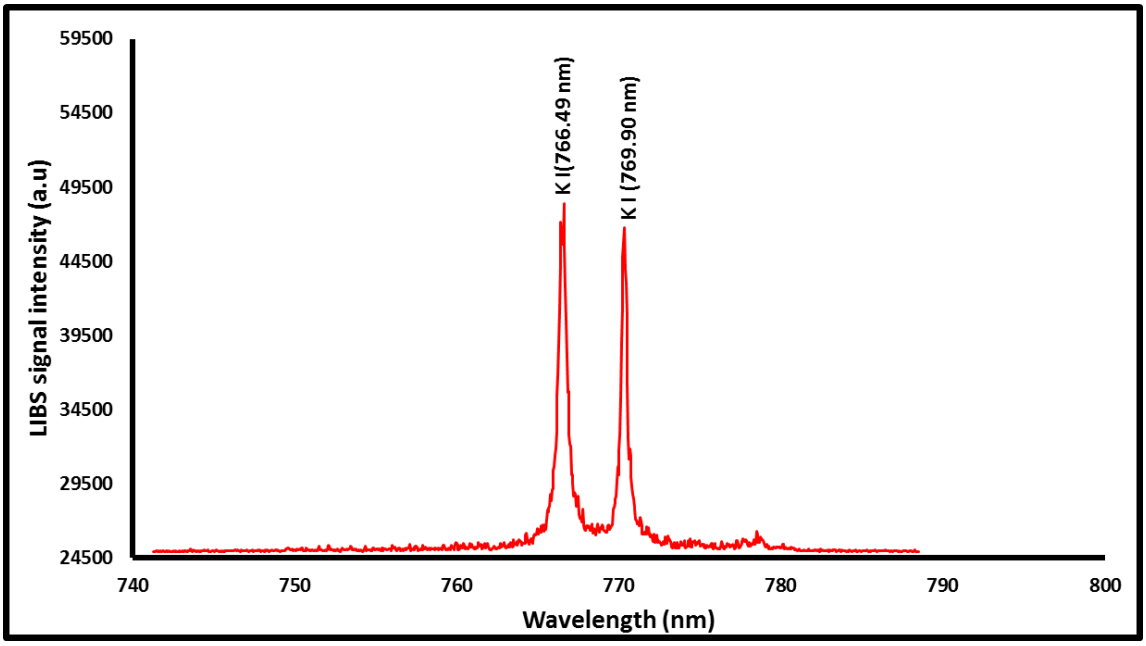

Figure 6.17: A typical LIBS spectrum recorded for green grape sample at wavelength range of 740 nm to 800 nm

Similarly, the constituents of the investigated black grape are presented in Fig.6.18 which includes manganese and titanium. Calcium, potassium, magnesium, titanium and manganese are shown in Fig. 6.19 as among the constituents of the black grape. Strong lines of sodium are identified and presented in Fg.6.20. Also, strong lines of potassium are shown in the spectrum presented in Fig.6.21.

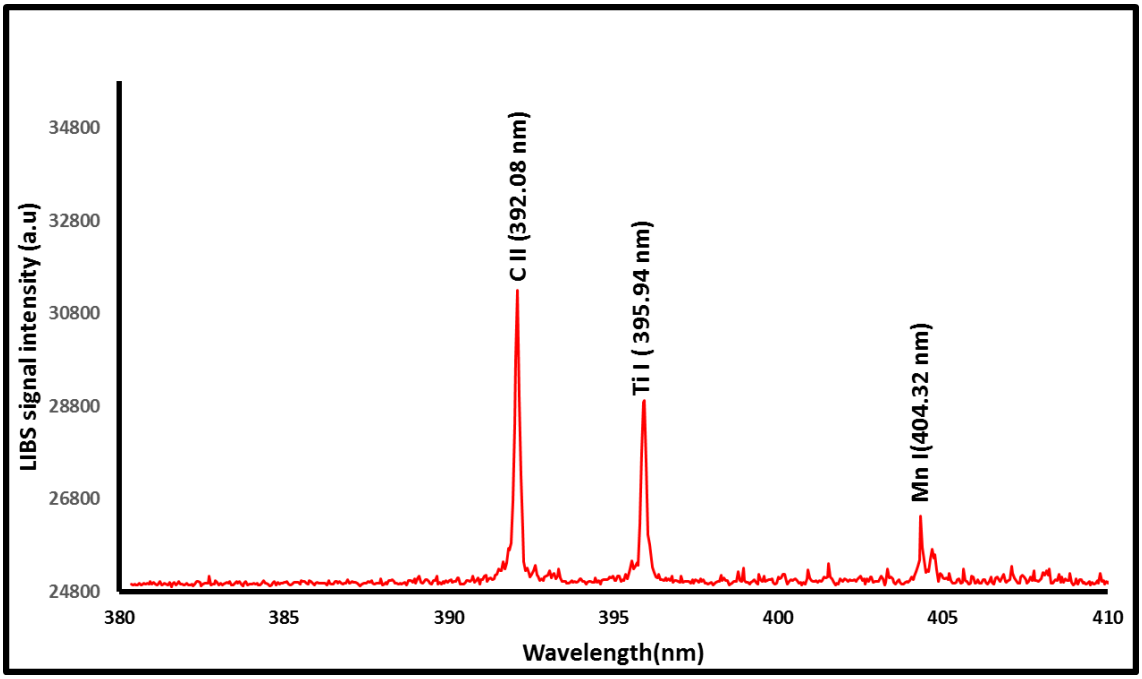

Figure 6.18: A typical LIBS spectrum recorded for black grape sample at wavelength range of 380 nm to 410 nm

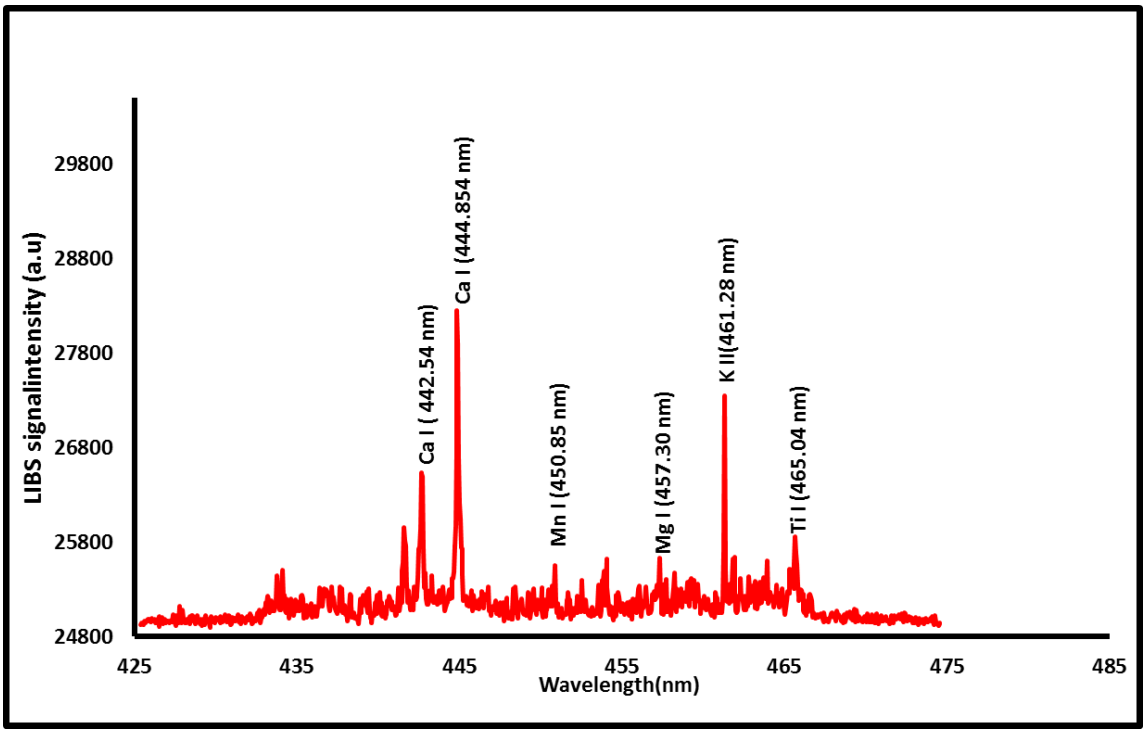

Figure 6.19 : A typical LIBS spectrum recorded for black grape sample at wavelength range of 425 nm to 485 nm

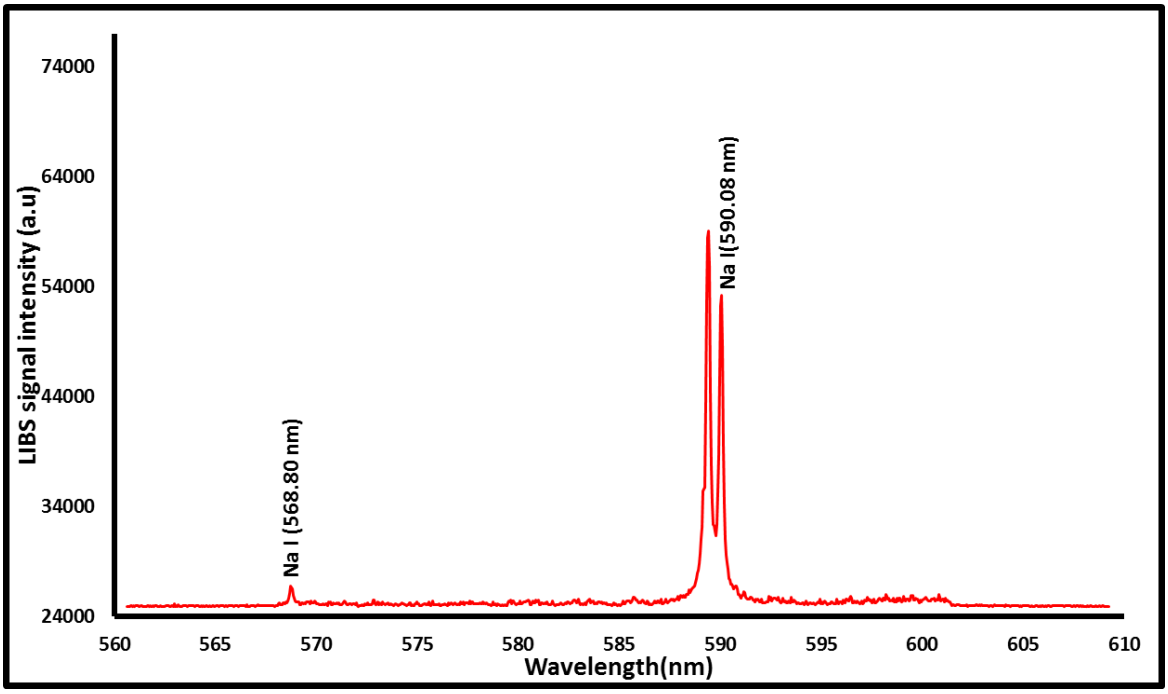

Figure 6.20: A typical LIBS spectrum recorded for black grape sample at wavelength range of 560nm to 610nm

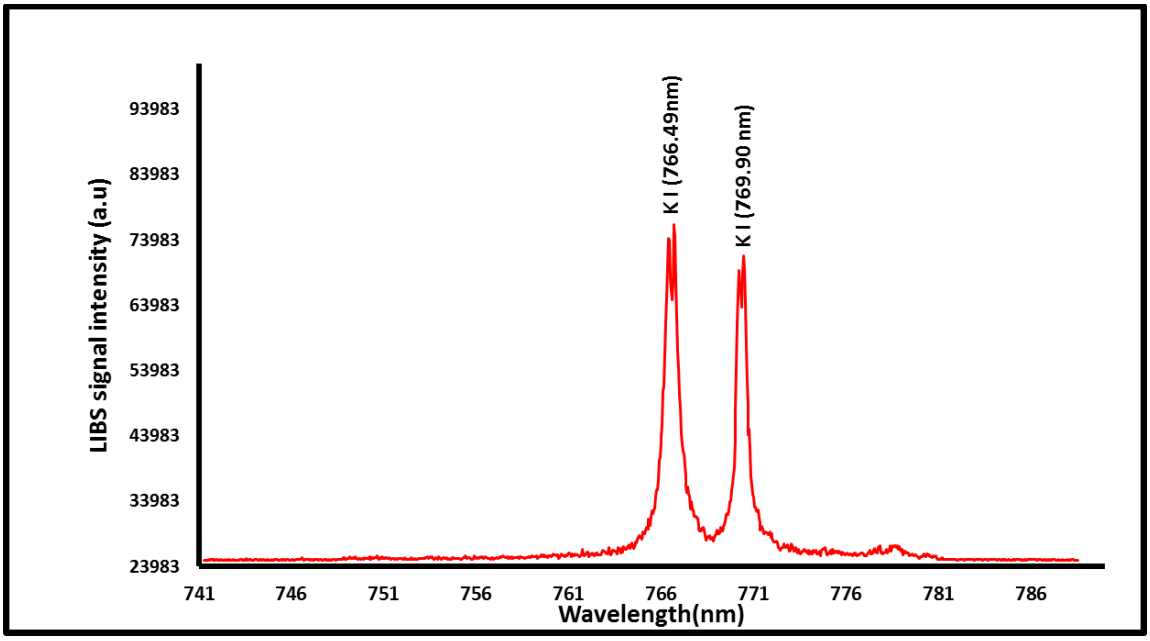

Figure 6.21: A typical LIBS spectrum recorded for black grape sample at wavelength range of 741 nm to 786 nm

6.1.1 Verification of thermodynamic equilibrium status of the plasma

The Complex interactions which occur during the formation and evolution of laser induced plasma include photo-ionization, ionization through collisions, three-body recombination, radiative recombination, collisional excitation and de-excitation, photo-excitation, radiative decay and Bremsstrahlung process. Photo-ionization is a process whereby photons from the laser ionize atoms of the ablated material. Ionization by collisions is a term used to describe the process through which the ionized electrons result into subsequent ionization due to atomic collisions. When electron combine with ion and thereby losses its energy and momentum to the electrons in the vicinity of the ion, the process is referred to as three-body recombination. The kinematic of all these interactions and processes are to be incorporated while holistically describing the laser

induced plasma. The validity of the conventional calibration free LIBS relies heavily on assumption that the laser induced plasma is in local thermodynamic equilibrium and other assumptions which include stoichiometric ablation and optical thinness of the plasma [130], [131]. This implies that the scheme is only valid when the laser induced plasma is isothermal, static and homogenous. Truly speaking, laser induced plasma is neither static nor homogenous or isothermal; it is characterized with a temperature gradient that changes during plasma evolution. Although, McWhirter LTE validity condition is necessary for laser-induced plasma but rather insufficient since the plasmas are inhomogeneous and evolve in time [133]. Another condition that compliments McWhirter criterion for the validity of LTE is the assumption that the attainment of ionization –excitation equilibrium requires a large time scale as compared to the rate of variation of thermodynamic parameters such as electron density and plasma temperature. In order to estimate the plasma temperature, Boltzmann plot was constructed using calcium emission lines of sample #3 at wavelengths 442.54nm, 616.21nm and 646.26nm as shown in Fig.6:22. Other parameters used in constructing the Boltzmann plot are extracted from NIST database.

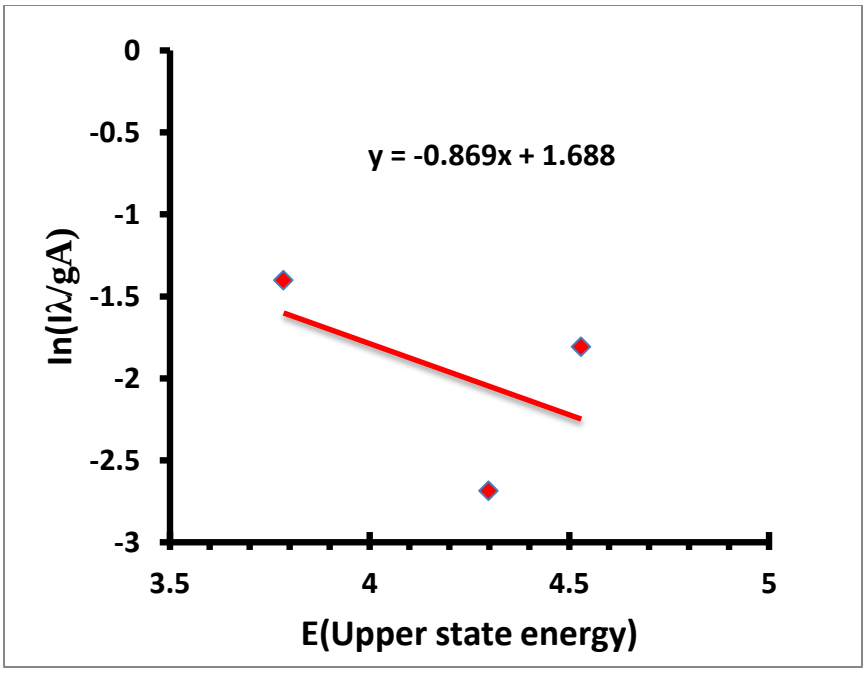

Figure 6.22: Boltzmann plot using calcium emission lines

The plasma temperature as determined form the slope of Fig.6.22 was obtained as 13,354.4K. This is within the limit (10,000K to 18,000K) of plasma temperature that ensures local thermodynamic equilibrium [4], [130]–[132], [134].

6.2 Quantitative analysis of the constituents of crayfish and grape samples

The chemometric tools developed and implemented for quantitative analysis of these samples include hybrid SVR and hybrid ELM chemometrics. These chemometric tools were developed using similar approach implemented for standard bronze samples but with test set cross validation in this case. The details of the chemometrics with inclusion of the results of GSA for optimizing the hyper-parameters of the models are presented in this section. The results of the chemometrics are also compared with that of ICP-OES while standard deviations as well as other error analysis are presented. The elements quantified include calcium, potassium and sodium in each of the samples.

6.2.1 Convergence of chemometric models for crayfish and grape samples using GSA

The convergence of the developed GSA-SVR hybrid chemometric for the quantitative analysis of crayfish and grape samples is presented in Fig.6.23. Similar graph for GSA-ELM chemometric is presented in Fig. 6.24. The significance of gravitational search algorithm in hybrid GSA-SVR chemometric is to determine optimum values of model parameters which include the regularization factor, kernel option and epsilon while the parameters optimized in the case hybrid GSA-ELM chemometric include the number of hidden neurons of the selected activation function.

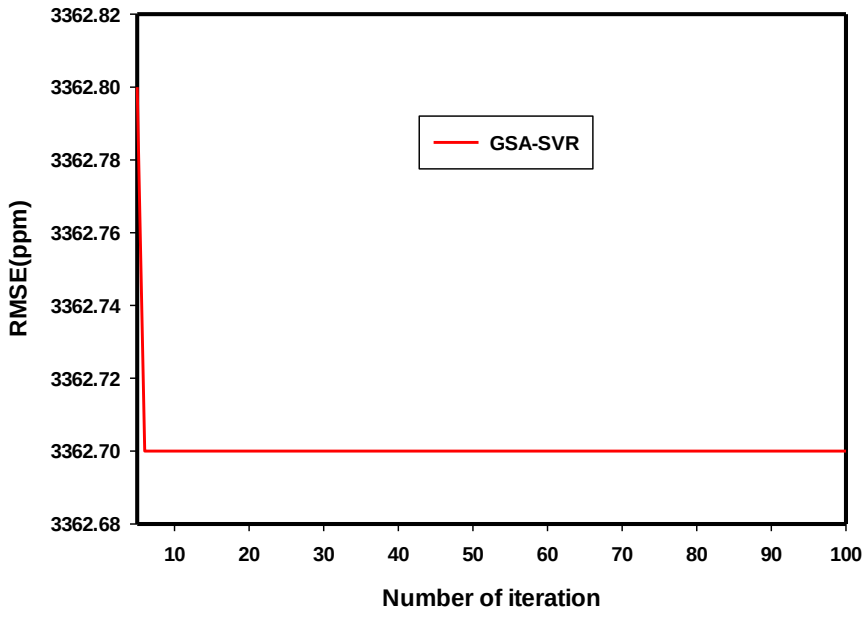

Figure 6.23 : A graph of RMSE against the number of iteration for performance sensitivity of GSA –SVR model to the number of agents

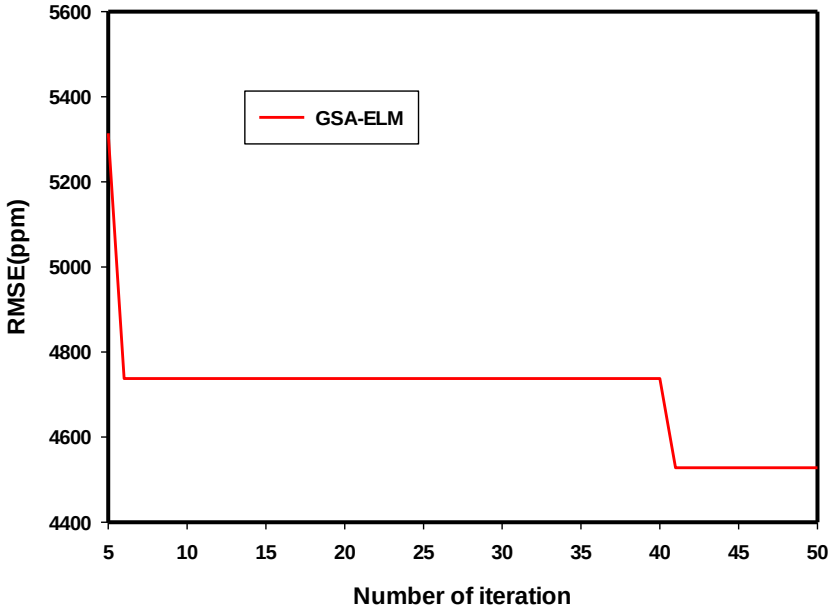

Figure 6.24: A graph of RMSE against the number of iteration for performance sensitivity of GSA –ELM model to the number of agents

The optimum values of the hyper-parameters for each of the hybrid chemometric models are presented in table 6.1.

Table 6.1: Optimum values of chemometrics parameters used for quantitative analysis of crayfish and grape samples

Hyper-parameters	GSA-SVR	GSA-ELM
Regularization factor	632.4383	Not applicable
Epsilon	0.3695	Not applicable
Kernel option	0.508	Not applicable
Lambda	4*10^5e-7	Not applicable
Kernel Function	Poly	Not applicable
Hidden neuron	Not applicable	39
Activation function	Not applicable	Sig

6.3 Comparison of the results of the developed hybrid chemometrics for quantitative analysis of crayfish and grape samples with that of ICP results

Table 6.2 compares the results of the developed hybrid chemometric models with ICP results for the investigated samples. The elements quantified in each of the samples as shown in the table includes calcium, sodium and potassium. The calcium concentrations obtained using chemometrics GSA-SVR and GSA-ELM for sample #1 are 5475ppm and 5947ppm, respectively while the results of the ICP is 5474.88ppm. These concentrations are very close. Similarly, the results of the developed hybrid chemometrics for calcium concentration in sample #2, sample #3(Only GSA-SVR shows a closer value), sample #4 and green grape are close to the results of ICP. Similar comparable results are obtained for other elements except few elements that show wider disparity such as sodium concentration of black grape for GSA-ELM chemometric.

Table 6.2: Comparison of the results of ICP with the hybrid GSA-SVR and GSA-ELM chemometrics

Sample	Sample constituent	ICP (ppm)	GSA-ELM (ppm)	GSA-SVR (ppm)
Sample #1	Ca	5475	----	5947
	Na	898	1518	2556
	K	12637	8863	10155
Sample #2	Ca	7409	-----	5993
	Na	1001	1518	2536
	K	9377	8863	10240
Sample #3	Ca	10459	5997	9649
	Na	3056	1518	2541

	K	9297	------	10259
Sample #4	Ca	6697	5997	5937
	Na	805	1518	2541
	K	12123	9297	6898
Black grape	Ca	834	5997	5940
	Na	593	9080	2491
	K	10941	8863	9812
Green grape	Ca	1119	1518	2731
	Na	876	8863	1743
	K	10481	8863	5937

6.4 Error analysis of the results of the developed hybrid chemometrics for crayfish and grape samples

The difference between the results of the developed hybrid chemometrics and ICP results are analyzed using the frequently used performance measuring parameters in chemometrics model which include root mean square error (RMSE), mean absolute error (MAE), mean relative error (MRE) and normalized root mean square error(NRMSE) [1], [47], [79]. Each of these parameters are formulated using the relations presented in Equation 6.1 to 6.4. The values of each of the performance measuring parameters for the investigated crayfish and grape samples are presented in table 6.1

$$RMSE = \sqrt{\frac{1}{M}\sum_{j=1}^{M} e_j^2} \quad (6.1)$$

$$MAE = \frac{1}{M}\sum_{j=1}^{M} e_j \qquad (6.2)$$

Where $e = \left| C_{ICP} - C_{chemometric} \right|$

$$MRE = \frac{1}{M}\sum_{j=1}^{M} \mathrm{Re}_j \qquad (6.3)$$

where $\mathrm{Re} = \left| \frac{C_{ICP} - C_{chemometric}}{C_{ICP}} \right| \text{ X } 100$

$$NRMSE = \frac{\sqrt{\frac{1}{M}\sum_{j=1}^{M} e_j^2}}{C_{ICP}^{Max} - C_{ICP}^{Min}} \qquad (6.4)$$

Where C_{ICP} and $C_{estimated}$ are the elemental concentration obtained from ICP and the developed hybrid chemometrics, respectively.

Table 6.3 : Performance measuring parameters and their values of the developed hybrid chemometrics for crayfish and grape samples

Performance measuring parameters	GSA-ELM	GSA-SVR
MRE	189.06	107.15
MAE	2299.86	1866.15
NRMSE	0.45	1.66
RMSE	3464.02	2379.63

CHAPTER 7

Conclusions

This research work proposes three methods of enhancing the performance of chemometric techniques. The proposed performance enhancement methods include internal reference preprocessing method (IRP), homogenous hybridization and hybrid fusion. These methods are implemented on support vector regression (SVR) and extreme learning machine (ELM) chemometrics, hybridized with gravitational search algorithm (GSA). While applying the proposed homogenous hybridization to support vector regression (SVR) chemometric, On the basis of RMSE, GSA-A-HSVR-WIRP performs better than GSA-SVR-WIRP model with 75.17% performance improvement and 65.40% performance improvement was obtained on the basis of MAE. Similarly, GSA-A-HSVR-IRP performs better than GSA-A-SVR-IRP with performance enhancement of 50.53%, 95.41% and 94.92% on the basis of CC, RMSE and MAE, respectively. Comparison of the proposed hybrid ELM chemometric with hybrid SVR shows that A-ELM performs better than A-SVR with performance improvement of 60.24%, 62.28% and 89.06% on the basis of RMSE, MAE and CC, respectively. For the proposed hybrid fusion method of performance enhancement, A-SVR-ELM model performs better than A-SVR model with performance improvement of 101.36%, 91.03% and 94.97% on the basis of CC, RMSE and MAE, respectively. In the same vein, A-SVR-ELM performs better than ordinary A-ELM with performance improvement of 77.43%, 86.65% and 6.50% on the basis of RMSE, MAE and CC as respectively. A-ELM-SVR model performs better than

ordinary A-SVR with a performance improvement of 101.96%, 95.76% and 95.34% on the basis of CC, RMSE and MAE, respectively while it performs better than ordinary A-ELM with a performance improvement of 6.83%, 89.32% and 87.64%, respectively. A-ELM-SVR model also performs better than A-SVR-ELM model with a performance improvement of 0.3%, 52.71% and 7.4% on the basis of CC, RMSE and MAE, respectively. For the hybrid chemometrics developed using integrated peak intensities, I-HSVR-GSA-WIRP outperforms I-SVR-GSA-WIRP with performance improvement of 50.53%. HELM-GSA-WIRP outperforms ELM-GSA-WIRP with performance improvement of 58.33%, 58.41% and 0.6183% on the basis of RMSE, MAE and CC, respectively. I-HSVR-GSA-WIRP outperforms I-SVR-GSA-WIRP with performance improvement of 59.61% while performance improvement of 11.06% was obtained when the models are compared on the basis of correlation coefficient. The results of the developed hybrid chemometrics for the investigated crayfish and grape samples are comparable with that of ICP results. The performance enhancement demonstrated by the proposed methods would definitely widen the applicability of chemometrics techniques and ultimately promote precise quantitative analysis of LIBS spectra.

Recommendations

The following are the recommendations for future work

- The proposed IRP might be implemented in other chemometrics for performance enhancement.
- Fuzzy logic based chemometrics have not been developed and applied for quantitative analysis of LIBS spectra. This can be a future work
- The proposed chemometrics in this work and methods of performance enhancement can be incorporated to LIBS tool box for easy assessment of the techniques.

References

[1] T. Zhang *et al.*, "A novel approach for quantitative analysis of multi-elements in steels based on laser-induced breakdown spectroscopy(LIBS) and random forest regression(RFR)," *J. Anal. At. Spectrom.*, vol. 29, pp. 2323–2329, 2014.

[2] C. Chen, Q. Shi, S. Wang, Q. Lin, and Y. Duan, "A novel method for metallic element analysis in particle samples using a laser-induced breakdown spectroscopy technique," *J. Anal. At. Spectrom.*, vol. 31, pp. 1527–1533, 2016.

[3] T. X. Phuoc, P. Wang, and D. McIntyre, "Detection of rare earth elements in Powder River Basin sub-bituminous coal ash using laser-induced breakdown spectroscopy (LIBS)," *Fuel*, vol. 163, pp. 129–132, 2016.

[4] M. A. Gondal, Y. B. Habibullah, U. Baig, and L. E. Oloore, "Direct spectral analysis of tea samples using 266 nm UV pulsed laser-induced breakdown spectroscopy and cross validation of LIBS results with ICP-MS," *Talanta*, vol. 152, pp. 341–352, 2016.

[5] G. S. Senesi, "Laser-Induced Breakdown Spectroscopy (LIBS) applied to terrestrial and extraterrestrial analogue geomaterials with emphasis to minerals and rocks," *Earth-Science Rev.*, vol. 139, pp. 231–267, 2014.

[6] N. Khajehzadeh, O. Haavisto, and L. Koresaar, "On-stream and quantitative mineral identification of tailing slurries using LIBS technique," *Miner. Eng.*, vol. 98, pp. 101–109, 2016.

[7] S. Natarajan and H. C. Bajaj, "Recovered materials from spent lithium-ion batteries (LIBs) as adsorbents for dye removal: Equilibrium, kinetics and mechanism," *J. Environ. Chem. Eng.*, vol. 4, no. 4, pp. 4631–4643, 2016.

[8] E. Tognoni, G. Cristoforetti, S. Legnaioli, and V. Palleschi, "Calibration-Free Laser-Induced Breakdown Spectroscopy: State of the art," *Spectrochim. Acta - Part B At. Spectrosc.*, vol. 65, no. 1, pp. 1–14, 2010.

[9] I. B. Gornushkin, S. V Shabanov, S. Merk, E. Tognoni, and U. Panne, "Effects of non-uniformity of laser induced plasma on plasma temperature and concentrations determined by the Boltzmann plot method: implications from plasma modeling," *J. Anal. At. Spectrom.*, vol. 25, no. 10, pp. 1643–1653, 2010.

[10] K. K. Herrera, E. Tognoni, I. B. Gornushkin, N. Omenetto, B. W. Smith, and J. D. Winefordner, "Comparative study of two standard-free approaches in laser-induced breakdown spectroscopy as applied to the quantitative analysis of aluminum alloy standards under vacuum conditions," *J. Anal. At. Spectrom.*, vol. 24, no. 4, p. 426, 2009.

[11] Q. Shi, G. Niu, Q. Lin, T. Xu, F. Li, and Y. Duan, "Quantitative analysis of

sedimentary rocks using laser-induced breakdown spectroscopy: comparison of support vector regression and partial least squares regression chemometric methods," *J. Anal. At. Spectrom.*, vol. 30, no. 12, pp. 2384–2393, 2015.

[12] U. Thissen, M. Pepers, B. Üstün, W. J. Melssen, and L. M. C. Buydens, "Comparing support vector machines to PLS for spectral regression applications," *Chemom. Intell. Lab. Syst.*, vol. 73, no. 2, pp. 169–179, Oct. 2004.

[13] J. . Dong *et al.*, "A method for improving the accuracy of calibration-free laser-induced breakdown spectroscopy (CF-LIBS) using determined plasma temperature by genetic algorithm (GA)," *J. Anal. At. Spectrom.*, vol. 30, no. 6, pp. 1336–1344, 2015.

[14] M. . b Xu *et al.*, "A single-beam-splitting technique combined with a calibration-free method for field-deployable applications using laser-induced breakdown spectroscopy," *RSC Adv.*, vol. 5, no. 6, pp. 4537–4546, 2015.

[15] E. Axente *et al.*, "Accurate analysis of indium–zinc oxide thin films via laser-induced breakdown spectroscopy based on plasma modeling," *J. Anal. At. Spectrom.*, vol. 29, no. 3, p. 553, 2014.

[16] Z. Wang, C. Yan, J. Dong, T. Zhang, J. Wei, and H. Li, "Acidity analysis of iron ore based on calibration-free laser-induced breakdown spectroscopy (CF-LIBS) combined with a binary search algorithm (BSA)," *RSC Adv.*, vol. 6, no. 80, pp. 76813–76823, 2016.

[17] E. Hywel Evans, C. D. Palmer, and C. M. M. Smith, "Atomic spectrometry update. Advances in atomic spectrometry and related techniques," *J. Anal. At. Spectrom.*, vol. 27, no. 6, p. 909, 2012.

[18] N. Kumar, A. Bansal, G. S. Sarma, and R. K. Rawal, "Chemometrics tools used in analytical chemistry: An overview," *Talanta*, vol. 123, pp. 186–199, 2014.

[19] E. Hywel Evans, J. Pisonero, C. M. M. Smith, and R. N. Taylor, "Atomic spectrometry update:review of advances in atomic spectrometry and related techniques," *J. Anal. At. Spectrom.*, vol. 30, pp. 1017–1037, 2015.

[20] B. Malik, K. Chaitanya, and M. Benaissa, "Support vector regression with digital band pass filtering for the quantitative analysis of near-infrared spectra," *J. Chemom.*, vol. 28, no. 2, pp. 116–122, 2014.

[21] N. Xin, X. Gu, H. Wu, Y. Hu, and Z. Yang, "Application of genetic algorithm-support vector regression (GA-SVR) for quantitative analysis of herbal medicines," *J. Chemom.*, vol. 26, no. 7, pp. 353–360, 2012.

[22] U. Thissen, B. Ustün, W. J. Melssen, and L. M. C. Buydens, "Multivariate calibration with least-squares support vector machines.," *Anal. Chem.*, vol. 76, no. 11, pp. 3099–3105, 2004.

[23] G. Bin Huang, Q. Y. Zhu, and C. K. Siew, "Extreme learning machine: Theory and

applications," *Neurocomputing*, vol. 70, no. 1–3, pp. 489–501, 2006.

[24] Q.-Y. Zhu, A. K. Qin, P. N. Suganthan, and G.-B. Huang, "Evolutionary extreme learning machine," *Pattern Recognit.*, vol. 38, no. 10, pp. 1759–1763, 2005.

[25] G. Bin Huang and L. Chen, "Convex incremental extreme learning machine," *Neurocomputing*, vol. 70, no. 16–18, pp. 3056–3062, 2007.

[26] E. Rashedi, H. Nezamabadi-pour, and S. Saryazdi, "GSA: A Gravitational Search Algorithm," *Inf. Sci. (Ny).*, vol. 179, no. 13, pp. 2232–2248, 2009.

[27] L. Sun and H. Yu, "Correction of self-absorption effect in calibration-free laser-induced breakdown spectroscopy by an internal reference method," *Talanta*, vol. 79, no. 2, pp. 388–395, 2009.

[28] S. Musazzi, *Springer Series in Optical Sciences 182 Laser-Induced Breakdown Spectroscopy*. Springer New York, 2014.

[29] M. Hemmerlin and J. M. Mermet, "Effect of the chemical form of the additives in poly(vinyl chloride) and poly(ethylene) materials on laser ablation efficiency using inductively coupled plasma atomic emission spectrometry," *Spectrochim. Acta Part B At. Spectrosc.*, vol. 52, no. 11, pp. 1687–1694, 1997.

[30] F. He, J. H. Price, K. T. Vu, a Malinowski, J. K. Sahu, and D. J. Richardson, "Optimisation of cascaded Yb fiber amplifier chains using numerical-modelling.," *Opt. Express*, vol. 14, no. 26, pp. 12846–58, 2006.

[31] T. Brabec and F. Krausz, "Intense few-cycle laser fields: Frontiers of nonlinear optics," *Rev. Mod. Phys.*, vol. 72, no. 2, pp. 545–591, 2000.

[32] I. V. Cravetchi, M. T. Taschuk, Y. Y. Tsui, and R. Fedosejevs, "Evaluation of femtosecond LIBS for spectrochemical microanalysis of aluminium alloys," *Anal. Bioanal. Chem.*, vol. 385, no. 2, pp. 287–294, 2006.

[33] A. Sarkar, S. K. Aggarwal, and D. Alamelu, "Laser induced breakdownspectroscopy for rapid identification of different types of paper for forensic application," *Anal. Methods*, vol. 2, no. 1, pp. 32–36, Jan. 2010.

[34] A. Sarkar, R. V. Shah, D. Alamelu, and S. K. Aggarwal, "Studies on the ns-IR-Laser-Induced Plasma Parameters in the Vanadium Oxide," *J. At. Mol. Opt. Phys.*, vol. 2011, pp. 1–7, 2011.

[35] U. Keller, "Recent developments in compact ultrafast lasers," *Nature*, vol. 424, no. 6950, pp. 831–838, 2003.

[36] D. Strickland and G. Mourou, "Compression of amplified chirped optical pulses," *Opt. Commun.*, vol. 56, no. 3, pp. 219–221, 1985.

[37] L. B. Guo *et al.*, "Enhancement of optical emission from laser-induced plasmas by combined spatial and magnetic confinement," *Opt. Express*, vol. 19, no. 15, p.

14067, 2011.

[38] M. R. Leahy-Hoppa *et al.*, “Ultrafast laser-based spectroscopy and sensing: Applications in LIBS, CARS, and THz spectroscopy,” *Sensors*, vol. 10, no. 5, pp. 4342–4372, 2010.

[39] O. Svelto, *Principles of lasers*. 2010.

[40] T. Lippert *et al.*, “Novel applications for laser ablation of photopolymers,” *Appl. Surf. Sci.*, vol. 186, pp. 14–23, 2002.

[41] R. Menzel, *Photonics*. 2007.

[42] L. Fornarini, V. Spizzichino, F. Colao, R. Fantoni, and V. Lazic, “Influence of laser wavelength on LIBS diagnostics applied to the analysis of ancient bronzes,” *Anal. Bioanal. Chem.*, vol. 385, no. 2, pp. 272–280, 2006.

[43] R. Fantoni, L. Caneve, F. Colao, L. Fornarini, V. Lazic, and V. Spizzichino, “Methodologies for laboratory Laser Induced Breakdown Spectroscopy semi-quantitative and quantitative analysis—A review,” *Spectrochim. Acta Part B At. Spectrosc.*, vol. 63, no. 10, pp. 1097–1108, Oct. 2008.

[44] D. von der Linde, K. Sokolowski-Tinten, and J. Bialkowski, “Laser–solid interaction in the femtosecond time regime,” *Appl. Surf. Sci.*, vol. 109–110, no. March 2016, pp. 1–10, 1997.

[45] C. Gómez, A. Costela, I. García-Moreno, and R. Sastre, “Comparative study between IR and UV laser radiation applied to the removal of graffitis on urban buildings,” *Appl. Surf. Sci.*, vol. 252, no. 8, pp. 2782–2793, 2006.

[46] E. C. Ferreira, E. A. Menezes, W. O. Matos, D. M. B. P. Milori, A. R. A. Nogueira, and L. Martin-Neto, “Determination of Ca in breakfast cereals by laser induced breakdown spectroscopy,” *Food Control*, vol. 21, no. 10, pp. 1327–1330, 2010.

[47] T. Takahashi and B. Thornton, “Quantitative methods for compensation of matrix effects and self-absorption in LIBS signals of solids,” *Spectrochim. Acta - Part B At. Spectrosc.*, vol. 138, pp. 31–42, 2017.

[48] F. Anabitarte and A. Cobo, “Laser-Induced Breakdown Spectroscopy : Fundamentals , Applications , and Challenges,” vol. 2012, 2012.

[49] M. Markiewicz-Keszycka *et al.*, “Laser-induced breakdown spectroscopy (LIBS) for food analysis: A review,” *Trends Food Sci. Technol.*, vol. 65, pp. 80–93, 2017.

[50] L. Barrette and S. Turmel, “On-line iron-ore slurry monitoring for real-time process control of pellet making processes using laser-induced breakdown spectroscopy: Graphitic vs. Total carbon detection,” *Spectrochim. Acta - Part B At. Spectrosc.*, vol. 56, no. 6, pp. 715–723, 2001.

[51] K. H. Lepore *et al.*, “Matrix Effects in Quantitative Analysis of Laser-Induced Breakdown Spectroscopy (LIBS) of Rock Powders Doped with Cr, Mn, Ni, Zn, and Co,” *Appl. Spectrosc.*, vol. 71, no. 4, pp. 600–626, 2017.

[52] S. M. Clegg, E. Sklute, M. D. Dyar, J. E. Barefield, and R. C. Wiens, “Multivariate analysis of remote laser-induced breakdown spectroscopy spectra using partial least squares, principal component analysis, and related techniques,” *Spectrochim. Acta - Part B At. Spectrosc.*, vol. 64, no. 1, pp. 79–88, 2009.

[53] H. Drucker, C. J. C. Burges, L. Kaufman, A. J. Smola, and V. N. Vapnik, “Support Vector Regression Machines,” *Adv. Neural Inf. Process. Syst.*, vol. 9, 1996.

[54] P. R. Filgueiras, J. C. L. Alves, and R. J. Poppi, “Quantification of animal fat biodiesel in soybean biodiesel and B20 diesel blends using near infrared spectroscopy and synergy interval support vector regression,” *Talanta*, vol. 119, pp. 582–589, 2014.

[55] I. Barman, C.-R. Kong, N. C. Dingari, R. R. Dasari, and M. S. Feld, “Development of Robust Calibration Models Using Support Vector Machines for Spectroscopic Monitoring of Blood Glucose,” *Anal. Chem.*, vol. 82, no. 23, pp. 9719–9726, 2010.

[56] A. Ciucci, M. Corsi, V. Palleschi, S. Rastelli, A. Salvetti, and E. Tognoni, “New Procedure for Quantitative Elemental Analysis by Laser-Induced Plasma Spectroscopy,” *Appl. Spectrosc.*, vol. 53, no. 8, pp. 960–964, 1999.

[57] B. Praher, V. Palleschi, R. Viskup, J. Heitz, and J. D. Pedarnig, “Calibration free laser-induced breakdown spectroscopy of oxide materials,” *Spectrochim. Acta - Part B At. Spectrosc.*, vol. 65, no. 8, pp. 671–679, 2010.

[58] P. J. Kolmhofer, S. Eschlböck-Fuchs, N. Huber, R. Rössler, J. Heitz, and J. D. Pedarnig, “Calibration-free analysis of steel slag by laser-induced breakdown spectroscopy with combined UV and VIS spectra,” *Spectrochim. Acta Part B At. Spectrosc.*, vol. 106, pp. 67–74, 2015.

[59] A. Matsumoto *et al.*, “A calibration-free approach for on-site multi-element analysis of metal ions in aqueous solutions by electrodeposition-assisted underwater laser-induced breakdown spectroscopy,” *Spectrochim. Acta - Part B At. Spectrosc.*, vol. 118, pp. 45–55, 2016.

[60] D. Bulajic *et al.*, “A procedure for correcting self-absorption in calibration free-laser induced breakdown spectroscopy,” *Spectrochim. Acta - Part B At. Spectrosc.*, vol. 57, no. 2, pp. 339–353, 2002.

[61] R. Gaudiuso, M. D. Aglio, O. De Pascale, S. Loperfido, A. Mangone, and A. De Giacomo, “Laser-induced breakdown spectroscopy of archaeological findings with calibration-free inverse method : Comparison with classical laser-induced breakdown spectroscopy and conventional techniques,” *Anal. Chim. Acta*, vol. 813, pp. 15–24, 2014.

[62] S. M. Pershin, F. Colao, and V. Spizzichino, “Quantitative Analysis of Bronze Samples by Laser-Induced Breakdown Spectroscopy (LIBS): A New Approach , Model , and Experiment,” *Laser Phys.*, vol. 16, no. 3, pp. 455–467, 2006.

[63] A. De Giacomo *et al.*, “ns- and fs-LIBS of copper-based-alloys : A different approach,” *Appl. Surf. Sci.*, vol. 253, pp. 7677–7681, 2007.

[64] J. A. Aguilera, C. Aragón, G. Cristoforetti, and E. Tognoni, “Application of calibration-free laser-induced breakdown spectroscopy to radially resolved spectra from a copper-based alloy laser-induced plasma,” *Spectrochim. Acta Part B At. Spectrosc.*, vol. 64, no. 7, pp. 685–689, 2009.

[65] V. S. Burakov, V. V Kiris, and P. A. Naumenkov, “CALIBRATION-FREE LASER SPECTRAL ANALYSIS OF GLASSES AND COPPER ALLOYS,” vol. 71, no. 5, pp. 676–682, 2004.

[66] G. Yang *et al.*, “The basicity analysis of sintered ore using laser-induced breakdown spectroscopy (LIBS) combined with random forest regression (RFR),” *Anal. Methods*, vol. 9, no. 36, pp. 5365–5370, 2017.

[67] T. Zhang *et al.*, “Quantitative and classification analysis of slag samples by laser induced breakdown spectroscopy (LIBS) coupled with support vector machine (SVM) and partial least square (PLS) methods,” *J. Anal. At. Spectrom.*, vol. 30, no. 2, pp. 368–374, 2015.

[68] J. . Wei, J. . Dong, T. . Zhang, Z. . Wang, and H. . b Li, “Quantitative analysis of the major components of coal ash using laser induced breakdown spectroscopy coupled with a wavelet neural network (WNN),” *Anal. Methods*, vol. 8, no. 7, pp. 1674–1680, 2016.

[69] J. Yang, C. Yi, J. Xu, and X. Ma, “Laser-induced breakdown spectroscopy quantitative analysis method via adaptive analytical line selection and relevance vector machine regression model,” *Spectrochim. Acta - Part B At. Spectrosc.*, vol. 107, pp. 45–55, 2015.

[70] N. C. Dingari, I. Barman, A. K. Myakalwar, S. P. Tewari, and M. Kumar Gundawar, “Incorporation of support vector machines in the LIBS toolbox for sensitive and robust classification amidst unexpected sample and system variability,” *Anal. Chem.*, vol. 84, no. 6, pp. 2686–2694, 2012.

[71] C. Yan, J. Qi, J. Ma, H. Tang, T. Zhang, and H. Li, “Determination of carbon and sulfur content in coal by laser induced breakdown spectroscopy combined with kernel-based extreme learning machine,” *Chemom. Intell. Lab. Syst.*, vol. 167, no. May, pp. 226–231, 2017.

[72] X. Chen, X. Li, S. Yang, X. Yu, and A. Liu, “Discrimination of lymphoma using laserinduced breakdown spectroscopy conducted on whole blood samples,” *Biomed. Opt. Express*, vol. 9, no. 3, pp. 1057–1068, 2018.

[73] G. Kim, J. Kwak, J. Choi, and K. Park, “Detection of nutrient elements and contamination by pesticides in spinach and rice samples using laser-induced breakdown spectroscopy (LIBS),” *J. Agric. Food Chem.*, vol. 60, no. 3, pp. 718–724, 2012.

[74] Y. Tian, Z. Wang, X. Han, H. Hou, and R. Zheng, “Comparative investigation of partial least squares discriminant analysis and support vector machines for geological cuttings identification using laser-induced breakdown spectroscopy,” *Spectrochim. Acta - Part B At. Spectrosc.*, vol. 102, pp. 52–57, 2014.

[75] T. F. Boucher *et al.*, “A study of machine learning regression methods for major elemental analysis of rocks using laser-induced breakdown spectroscopy,” *Spectrochim. Acta - Part B At. Spectrosc.*, vol. 107, pp. 1–10, 2015.

[76] X. Li, Z. Wang, Y. Fu, Z. Li, and W. Ni, “A model combining spectrum standardization and dominant factor based partial least square method for carbon analysis in coal using laser-induced breakdown spectroscopy,” *Spectrochim. Acta - Part B At. Spectrosc.*, vol. 99, pp. 82–86, 2014.

[77] M. D. Dyar *et al.*, “Comparison of univariate and multivariate models for prediction of major and minor elements from laser-induced breakdown spectra with and without masking,” *Spectrochim. Acta - Part B At. Spectrosc.*, vol. 123, pp. 93–104, 2016.

[78] J. Sirven, B. Bousquet, L. Canioni, and L. Sarger, “Laser-Induced Breakdown Spectroscopy of Composite Samples : Comparison of Advanced Chemometrics Methods Laser-Induced Breakdown Spectroscopy of Composite Samples : Comparison of Advanced Chemometrics Methods,” *Anal. Chem.*, vol. 78, no. 5, pp. 1462–1469, 2006.

[79] K. Li *et al.*, “Analytical-performance improvement of laser-induced breakdown spectroscopy for steel using multi-spectral-line calibration with an artificial neural network,” *J. Anal. At. Spectrom.*, vol. 30, no. 7, pp. 1623–1628, 2015.

[80] J. Yang, C. Yi, J. Xu, and X. Ma, “A laser induced breakdown spectroscopy quantitative analysis method based on the robust least squares support vector machine regression model,” *J. Anal. At. Spectrom.*, vol. 30, no. 7, pp. 1541–1551, 2015.

[81] D. Pokrajac *et al.*, “Automatic Classification of Laser-Induced Breakdown Spectroscopy (LIBS) Data of Protein Biomarker Solutions.,” *Appl. Spectrosc.*, vol. 68, no. 9, pp. 1067–75, 2014.

[82] Z. Hou, Z. Wang, T. Yuan, J. Liu, Z. Li, and W. Ni, “A hybrid quantification model and its application for coal analysis using laser induced breakdown spectroscopy,” *J. Anal. At. Spectrom.*, vol. 31, no. 3, pp. 722–736, 2016.

[83] L. Sheng *et al.*, “Classification of iron ores by laser-induced breakdown spectroscopy (LIBS) combined with random forest (RF),” *J. Anal. At. Spectrom.*,

vol. 30, no. 2, pp. 453–458, 2015.

[84] T. Zhang *et al.*, "A novel approach for the quantitative analysis of multiple elements in steel based on laser-induced breakdown spectroscopy (LIBS) and random forest regression (RFR)," *J. Anal. At. Spectrom.*, vol. 29, no. 12, pp. 2323–2329, 2014.

[85] A. J. Smola, B. Sch, and B. Schölkopf, "A Tutorial on Support Vector Regression," *Stat. Comput.*, vol. 14, no. 3, pp. 199–222, 2004.

[86] T. O. Owolabi, K. O. Akande, and S. O. Olatunji, "Estimation of surface energies of hexagonal close packed metals using computational intelligence technique," *Appl. Soft Comput.*, vol. 31, pp. 360–368, 2015.

[87] A. Majid, A. Khan, G. Javed, and A. M. Mirza, "Lattice constant prediction of cubic and monoclinic perovskites using neural networks and support vector regression," *Comput. Mater. Sci.*, vol. 50, no. 2, pp. 363–372, 2010.

[88] Y. Wang, F. Cao, and Y. Yuan, "A study on effectiveness of extreme learning machine," *Neurocomputing*, vol. 74, no. 16, pp. 2483–2490, 2011.

[89] T. O. Owolabi, Y. F. Zakariya, K. O. Akande, and S. O. Olatunji, "Estimation of melting points of fatty acids using homogeneously 3 hybridized support vector regression," *Neural Comput. Appl.*, 2016.

[90] E. Castillo and B. Guijarro-berdi, "A Very Fast Learning Method for Neural Networks Based on Sensitivity Analysis," *J. Mach. Learn. Res.*, vol. 7, pp. 1159–1182, 2006.

[91] S. O. Olatunji, A. Selamat, and A. A. A. Raheem, "An hybrid model through the fusion of sensitivity based linear learning method and type-2 fuzzy logic systems for modeling PVT properties of crude oil systems," *2011 Malaysian Conf. Softw. Eng.*, pp. 354–360, Dec. 2011.

[92] T. O. Owolabi, K. O. Akande, S. O. Olatunji, A. Alqahtani, and N. Aldhafferi, "Estimation of Curie temperature of manganite-based materials for magnetic refrigeration application using hybrid gravitational based support vector regression," *AIP Adv.*, vol. 6, no. 10, p. 105009, 2016.

[93] F.-Y. Ju and W.-C. Hong, "Application of seasonal SVR with chaotic gravitational search algorithm in electricity forecasting," *Appl. Math. Model.*, vol. 37, no. 23, pp. 9643–9651, 2013.

[94] D. Goswami and S. Chakraborty, "Parametric optimization of ultrasonic machining process using gravitational search and fireworks algorithms," *Ain Shams Eng. J.*, vol. 6, no. 1, pp. 315–331, 2015.

[95] Y. Mohamed Shuaib, M. Surya Kalavathi, and C. Christober Asir Rajan, "Optimal capacitor placement in radial distribution system using Gravitational Search Algorithm," *Int. J. Electr. Power Energy Syst.*, vol. 64, no. 2015, pp. 384–397,

2015.

[96] J. Xiang *et al.*, “A novel hybrid system for feature selection based on an improved gravitational search algorithm and k-NN method,” *Appl. Soft Comput.*, vol. 31, no. 2015, pp. 293–307, 2015.

[97] F. Y. Ju and W. C. Hong, “Application of seasonal SVR with chaotic gravitational search algorithm in electricity forecasting,” *Appl. Math. Model.*, vol. 37, no. 23, pp. 9643–9651, 2013.

[98] X. Han *et al.*, “Feature subset selection by gravitational search algorithm optimization,” *Inf. Sci. (Ny).*, vol. 281, pp. 128–146, 2014.

[99] V. N. Vapnik, “The Nature of Statistical Learning Theory,” *Springer-Verlag New York, Inc*, Jun. 1995.

[100] I. a. Naguib and H. W. Darwish, “Support vector regression and artificial neural network models for stability indicating analysis of mebeverine hydrochloride and sulpiride mixtures in pharmaceutical preparation: A comparative study,” *Spectrochim. Acta - Part A Mol. Biomol. Spectrosc.*, vol. 86, pp. 515–526, 2012.

[101] J. Peng and L. Li, “Support vector regression in sum space for multivariate calibration,” *Chemom. Intell. Lab. Syst.*, vol. 130, pp. 14–19, 2014.

[102] D. Zheng, J. Wang, and Y. Zhao, “Non-flat function estimation with a multi-scale support vector regression,” *Neurocomputing*, vol. 70, no. 1–3, pp. 420–429, 2006.

[103] S. O. Olatunji, “Comparison of Extreme Learning Machines and Support Vector Machines on Premium and Regular Gasoline Classification for Arson and Oil Spill Investigation,” *ASIAN J. Eng. Sci. Technol.*, vol. 1, no. 1, 2010.

[104] S. O. Olatunji, A. Selamat, and A. Abdulraheem, “A hybrid model through the fusion of type-2 fuzzy logic systems and extreme learning machines for modelling permeability prediction,” *Inf. Fusion*, vol. 16, pp. 29–45, Mar. 2014.

[105] P. Hannaford, *Excitations of Atoms and Broadening of Spectral Lines*, vol. 28, no. 10. 1981.

[106] “[W._Demtroder]_Laser_Spectroscopy_-_Basic_Concepts(b-ok.xyz).pdf.” .

[107] M. Cirisan, M. Cvejić, M. R. Gavrilović, S. Jovićević, N. Konjević, and J. Hermann, “Stark broadening measurement of Al II lines in a laser-induced plasma,” *J. Quant. Spectrosc. Radiat. Transf.*, vol. 133, pp. 652–662, 2014.

[108] M. Cvejić, M. R. Gavrilović, S. Jovićević, and N. Konjević, “Stark broadening of Mg i and Mg II spectral lines and Debye shielding effect in laser induced plasma,” *Spectrochim. Acta - Part B At. Spectrosc.*, vol. 85, pp. 20–33, 2013.

[109] A. Díaz-Soriano, J. M. Alcaraz-Pelegrina, A. Sarsa, M. S. Dimitrijević, and C. Yubero, “A simple and accurate analytical model of the Stark profile and its

application to plasma characterization," *J. Quant. Spectrosc. Radiat. Transf.*, vol. 207, pp. 89–94, 2018.

[110] N. Ben Nessib, "Ab initio calculations of Stark broadening parameters," *New Astron. Rev.*, vol. 53, no. 7–10, pp. 255–258, 2009.

[111] J. Bengoechea, J. A. Aguilera, and C. Aragón, "Application of laser-induced plasma spectroscopy to the measurement of Stark broadening parameters," *Spectrochim. Acta - Part B At. Spectrosc.*, vol. 61, no. 1, pp. 69–80, 2006.

[112] F. Bredice *et al.*, "Measurement of Stark broadening of Mn I and Mn II spectral lines in plasmas used for Laser-Induced Breakdown Spectroscopy," *Spectrochim. Acta - Part B At. Spectrosc.*, vol. 62, no. 11, pp. 1237–1245, 2007.

[113] C. Aragón, J. A. Aguilera, and J. Manrique, "Measurement of Stark broadening parameters of Fe II and Ni II spectral lines by laser induced breakdown spectroscopy using fused glass samples," *J. Quant. Spectrosc. Radiat. Transf.*, vol. 134, pp. 39–45, 2014.

[114] M. Burger and J. Hermann, "Stark broadening measurements in plasmas produced by laser ablation of hydrogen containing compounds," *Spectrochim. Acta - Part B At. Spectrosc.*, vol. 122, pp. 118–126, 2016.

[115] N. M. S. Sahal-Bréchot, M.S. Dimitrijević, "Stark-B database, (online). Available http://stark-b.obspm.fr," no. (accessed May 2018).

[116] H. R. Griem, "Spectral Line Broadening by Plasmas," *Pure Appl. Phys.*, vol. Volume 39, p. Pages 1-410, 1974.

[117] D. Zhang *et al.*, "Enhancement mechanism of femtosecond double-pulse laser-induced Cu plasma spectroscopy," *Opt. Laser Technol.*, vol. 96, pp. 117–122, 2017.

[118] A. Rodero and M. C. García, "Gas temperature determination of non-thermal atmospheric plasmas from the collisional broadening of argon atomic emission lines," *J. Quant. Spectrosc. Radiat. Transf.*, vol. 198, pp. 93–103, 2017.

[119] M. Ivković and N. Konjević, "Stark width and shift for electron number density diagnostics of low temperature plasma: Application to silicon LIBS," *Spectrochim. Acta - Part B At. Spectrosc.*, vol. 131, pp. 79–92, 2017.

[120] M. Suchoňová, J. Krištof, M. Pribula, M. Veis, F. L. Tabarés, and P. Veis, "Analysis of LiSn alloy at several depths using LIBS," *Fusion Eng. Des.*, vol. 117, pp. 175–179, 2017.

[121] K. Elsayed *et al.*, "Design and construction of Q-switched Nd:YAG laser system for LIBS measurements," *Opt. Laser Technol.*, vol. 44, no. 1, pp. 130–135, 2012.

[122] A. Alonso-Medina, "Experimental determination of the Stark widths of Pb I spectral lines in a laser-induced plasma," *Spectrochim. Acta - Part B At.*

Spectrosc., vol. 63, no. 5, pp. 598–602, 2008.

[123] Http://www.onlinemetals.com/, *online metalstore*. .

[124] D. A. Cremers and L. J. Radziemski, *Handbook of Laser-Induced Breakdown Spectroscopy*. John Wiley & Sons, 2013.

[125] B. Di Bartolo and O. Forte, *Advances in Spectroscopy for Lasers and Sensing*, vol. 231. 2006.

[126] V. O. Borisov, X. Mao, and E. R. Russo, "Effects of crater development on fractionation and signal intensity during laser ablation inductively coupled plasma mass spectrometry," *Spectrochim. Acta Part B At. Spectrosc.*, vol. 55, pp. 1693–1704, 2000.

[127] K. O. Akande, T. O. Owolabi, S. O. Olatunji, and A. Abdulraheem, "A Novel Homogenous Hybridization Scheme for Performance Improvement of Support Vector Machines Regression in Reservoir Characterization," *Appl. Comput. Intell. Soft Comput.*, vol. 2016, pp. 1–10, 2016.

[128] K. O. Akande, S. O. Olatunji, T. O. Owolabi, and A. AbdulRaheem, "Feature Selection-Based ANN for Improved Characterization of Carbonate Reservoir," in *society of petroleum egineers*, 2015.

[129] "Atomic Spectra Database, The National Institute of Standards and Technology (NIST)," *https://www.nist.gov/pml/atomic-spectra-database*, 2010.

[130] M. A. Gondal, Y. B. Habibullah, L. E. Oloore, and M. A. Iqbal, "Determination of carcinogenic fluorine in cigarettes using pulsed UV laser-induced breakdown spectroscopy," *Appl. Opt.*, vol. 54, no. 17, p. 5560, 2015.

[131] M. A. Gondal, M. A. Dastageer, F. F. Al-Adel, A. A. Naqvi, and Y. B. Habibullah, "Detection of highly toxic elements (lead and chromium) in commercially available eyeliner (kohl) using laser induced break down spectroscopy," *Opt. Laser Technol.*, vol. 75, pp. 99–104, 2015.

[132] A. M. Alhasmi, M. A. Gondal, M. M. Nasr, S. Shafik, and Y. B. Habibullah, "Detection of toxic elements using laser-induced breakdown spectroscopy in smokers' and nonsmokers' teeth and investigation of periodontal parameters.," *Appl. Opt.*, vol. 54, no. 24, pp. 7342–9, 2015.

[133] G. Cristoforetti *et al.*, "Local Thermodynamic Equilibrium in Laser-Induced Breakdown Spectroscopy: Beyond the McWhirter criterion," *Spectrochim. Acta - Part B At. Spectrosc.*, vol. 65, no. 1, pp. 86–95, 2010.

[134] M. A. Gondal, Y. B. Habibullah, U. Baig, and L. E. Oloore, "Direct spectral analysis of tea samples using 266 nm UV pulsed laser-induced breakdown spectroscopy and cross validation of LIBS results with ICP-MS," *Talanta*, vol. 152, pp. 341–352, 2016.

[135] N. KonjeviÄ‡ and W. L. Wiese, “Experimental Stark widths and shifts for spectral lines of neutral and ionized atoms,” *J. Phys. Chem. Ref. Data*, vol. 19, no. 6, pp. 1307–1385, 1990.

[136] T. O. Owolabi and M. A. Gondal, “A hybrid intelligent scheme for estimating band gap of doped titanium dioxide semiconductor using crystal lattice distortion,” *Comput. Mater. Sci.*, vol. 137, pp. 249–256, 2017.

Vitae

Name :Taoreed Owolabi Olakunle

Nationality :Nigerian

Date of Birth :12/15/1985

Email :owolabitaoreedolakunle@gmail.com

Address :Physics department, Adekunle Ajasin University , Akungba Akoko, Nigeria

Postal Address: PMB 001, Adekunle Ajasin University, Akungba Akoko. Nigeria

Academic Background :•MS in Physics(3.63/4), Magnetic and superconducting properties of FeSe (AS) iron-based superconductor, 2015, King Fahd University of Petroleum and Minerals, Saudi Arabia. •BSC in Physics and Electronics (First Class Honors, 4.53/5.00), 2010, Adekunle Ajasin University, Ondo-State, Nigeria

Outcomes of this work

Published work

1. Taoreed. O. Owolabi and M. A. Gondal, "Estimation of surface tension of methyl esters biodiesels using computational intelligence technique," *Appl. Soft Comput. J.*, vol. 37, pp. 227–233, 2015.
2. Taoreed. O. Owolabi, and M. A. Gondal. Novel techniques for enhancing the performance of support vector regression chemometric in quantitative analysis of LIBS spectra *Journal of Analytical Atomic Spectrometry 2017.*
3. Taoreed. O. Owolabi, and M. A. Gondal. '*A hybrid intelligent scheme for estimating band gap of doped titanium dioxide semiconductor using crystal lattice distortion'* Comput Mater Sci 2017;137:249–56
4. Taoreed. O. Owolabi, and M. A. Gondal, "Development of hybrid extreme learning machine based chemo-metrics for precise quantitative analysis of LIBS spectra using internal reference pre-processing method," *Anal. Chim. Acta,* 2018.

Submitted work

Taoreed. O. Owolabi and M. A. Gondal, Quantitative analysis of LIBS spectra using hybrid chemomertic models through fusion of extreme learning machines and support vector regression. *Journal of intelligent and fuzzy system (under review)*

Appendix 1

Constituents of the standard bronze samples as supplied by the supplier

CONCAST METAL PRODUCTS CO.

PO BOX 816 - MARS, PA 16046

October 27 , 2016

OnlineMetals
8001 ThyssenKrupp Parkway

Northwood, OH 43619
Attn: Quality Control Department

CERTIFICATE OF ANALYSIS

THE FOLLOWING MATERIAL IS CERTIFIED TO:

COUNTRY OF MELT U.S.A.
COUNTRY OF MANUFACTURE U.S.A.
REACH CURRENT REV. 12-16-2013
NO WELD REPAIR PERFORMED ON MATERIAL
DFARS CURRENT (DFARS 225.872) 12/31/2012
CATSCA 2010 COMPLIANT
CERTIFICATION OF CONFORMANCE
M07 AS CONTINUOUS CAST TEMPER
OnlineMetals
Accounts Payable, P.O. Box 5116
Southfield, MI 48086-5116
ASTM B505/B505M-14

GENERAL PRODUCT INFORMATION

Heat#: 1612595
Manufacture Date: 07/22/16
Alloy: 932
Shape: SOLID
Size#: 0 X 1
Internal Standards: ASTM B505

Customer PO#: 65610
Customer Job#: 10453
Customer Part#: 10453
Control#:
Date Shipped: 10/27/16
Quantity Shipped: 4
Weight Shipped: 119.00
Packslip#: 252306
Invoice#: 0
Country of Origin: UNITED STATES

CHEMICAL ANALYSIS

		DEFINED BY SPECIFICATION Minimum		Maximum	MEASURED IN LABORATORY
**	Cu	81.0000	-	85.0000	81.2192
	Sn	6.3000	-	7.5000	6.4670
	Pb	6.0000	-	8.0000	7.6680
	Zn	2.0000	-	4.0000	3.7800
	Fe		-	.2000	0.1250
	Ni		-	1.0000	0.4030
	SB		-	.3500	0.2530
	P		-	1.5000	0.0410
	S		-	.0800	0.0390
	Al		-	.0050	0.0024
	Si		-	.0050	0.0024

** In determining copper minimum, copper may be calculated as copper plus nickel

Physical Analysis *	Yield .5% UNDER LOAD (PSI)	N/mm²	Tensile (PSI)	N/mm²	Elongation in 2 in. min %	Brinell Hardness BRINELL 500
Defined By Specification	20000	137.9	35000	241.3	10	0 - 0

This is to certify that all material listed is free from mercury contamination and no mercury bearing equipment was used in any of our manufacturing, fabricating, assembly or testing operations. No materials containing Class I or Class II ODC's; CFC's; Halons or HCFC's are used in our manufacturing process. None of the EPA's listed ODC's are used in our testing, assembly or fabricating procedures. Additionally we do not purchase, from our suppliers, any of the EPA's listed ODC's. * Minimum tensile and yield strength shall be reduced 10% for cast bars having a thickness, diameter, cross section or wall of 4" or more. All Nickel measurements are inclusive of Cobalt concentrations.

ISO 9001 REGISTERED FIRM

GRI CERTIFICATE NO.'S
25513/A/0001/AN/En
32119/A/0001/UK/En

CONCAST METAL PRODUCTS

Dominic P. Lemaire
Lab Manager

CONCAST METAL PRODUCTS, PO BOX 816, MARS Pennsylvania 16046 (800-626-7071)

NATIONAL BRONZE & METALS, INC.
WWW.NBMMETALS.COM

HOUSTON, TEXAS
2929 W 12TH ST. - HOUSTON, TX 77008
PO BOX 800818 - HOUSTON, TX 77280

P: 713-869-9600
F: 713-869-9124
sales@nbmmetals.com

MILL TEST REPORT "MTR"

MATERIAL DESCRIPTION

ALLOY:	CDA 863
SPECIFICATION:	ASTM B505-12
TEMPER:	Continuous Cast
HEAT NUMBER:	R6218
SIZE:	1" Solid
PRODUCTION ORDER NO:	6562
CAST DATE:	July 1, 2013

SPECIFIED CHEMICAL PROPERTIES

	Cu	Sn	Pb	Zn	Ni + Co
Minimum/Maximum (in %)	60 - 66	0.2 max	0.2 max	22 - 28	1.0 max
Actual Analysis (in %)	**62.90**	**0.02**	**0.01**	**26.41**	**0.02**

	Fe	Al	Mn	Other Elements
Minimum/Maximum (in %)	2.0 - 4.0	5.0 - 7.5	2.5 - 5.0	1.0 max
Actual Analysis (in %)	**2.43**	**5.210**	**2.909**	**0.091**

SPECIFIED MECHANICAL PROPERTIES

	TENSILE	YIELD (at 0.5% EUL)	ELONGATION (in 2 in.)	HARDNESS
Minimum	110 ksi*	62 ksi*	14%	
Actual Analysis 1	**119.4 ksi**	**70.9 ksi**	**18%**	

* Minimum tensile and yield strengths are reduced by 10% for materials that are 4" and over in the cross section.

This is to certify that all material is free from mercury contamination and no mercury bearing equipment was used in any of our manufacturing, fabrication, assembly or testing operations. No materials containing Class I or Class II ODC's, CFC's, halons or HCFC's are used in our manufacturing process. None of the EPA's listed ODC's are used in our testing, assembly or fabricating procedures. Additionally, we do not purchase from our suppliers any of the EPA's listed ODC's.

Method of chemical analysis: Optical Emission Spectrometer

Method of mechanical testing: per ASTM E8/8M

This material has not undergone any type of welding or weld repair during or after production.

The recording of false, fictitious or fraudulent statements on this document may be punishable as a felony under federal statutes.

This material was manufactured in the United States of America and complies with DFARS 252.225.7014 Alt 1 requirements.

Signature on file. Please contact the undersigned if official signature is required.

Stephanie DaDante
ISO Coordinator
National Bronze & Metals, Inc.
Lorain, Ohio 44055
sdadante@nbmmetals.com

F08.02

CONCAST METAL PRODUCTS CO.

CERTIFICATE OF ANALYSIS

THE FOLLOWING MATERIAL IS CERTIFIED TO:

PO BOX 816 - MARS, PA 16046

October 27 , 2016

OnlineMetals
8001 ThyssenKrupp Parkway

Northwood, OH 43619
Attn: Quality Control Department

GENERAL PRODUCT INFORMATION

Heat#: 1414340

Manufacture Date: 10/14/14
Alloy: C67300
Shape: SOLID
Size#: 0.0 X 1.0
Internal Standards: 0" To 1" Inclusive

Customer PO#: 65610
Customer Job#: 23320
Customer Part#: 23320
Control#:
Date Shipped: 10/27/16
Quantity Shipped: 1
Weight Shipped: 34.00
Packslip#: 252306
Invoice#: 0
Country of Origin: INDIA

CHEMICAL ANALYSIS

	DEFINED BY SPECIFICATION Minimum		Maximum	MEASURED IN LABORATORY
Cu	58.0000	-	63.0000	59.4000
Sn		-	.3000	0.0500
Pb	.4000	-	3.0000	1.7600
Zn	27.7000	-	39.1000	35.1700
Fe		-	.5000	0.0600
Ni		-	.2500	0.0600
Al		-	.2500	0.0300
Mn	2.0000	-	3.5000	2.5000
Si	.5000	-	1.5000	0.9700

PRODUCTION MILL HEAT # 15-RA1703

Physical Analysis *	Yield .5% UNDER LOAD (PSI)	N/mm²	Tensile (PSI)	N/mm²	Elongation in 2 in. min %	Brinell Hardness ROCKWELL B
Defined By Specification	**40000**	**275.8**	**65000**	**448.2**	**12**	**70 - 100**
1414340-1	53660	370.0	70630	487.0	24	77

This is to certify that all material listed is free from mercury contamination and no mercury bearing equipment was used in any of our manufacturing, fabricating, assembly or testing operations. No materials containing Class I or Class II ODC's; CFC's; Halons or HCFC's are used in our manufacturing process. None of the EPA's listed ODC's are used in our testing, assembly or fabricating procedures. Additionally we do not purchase, from our suppliers, any of the EPA's listed ODC's. * Minimum tensile and yield strength shall be reduced 10% for cast bars having a thickness, diameter, cross section or wall of 4" or more. All Nickel measurements are inclusive of Cobalt concentrations.

ISO 9001 REGISTERED FIRM

GRI CERTIFICATE NO.'S
25513/A/0001/AN/En
32119/A/0001/UK/En

CONCAST METAL PRODUCTS

Dominic P. Lemaire
Lab Manager

CONCAST METAL PRODUCTS, PO BOX 816, MARS Pennsylvania 16046 (800-626-7071)

CERTIFICATE OF TEST

Customer **COPPER AND BRASS SALES INC.**
Invoice No **330720K16**
P.O. No **5400305651**
MILL **BOO YOUNG IND.**
Country of Melting & Manufacturing **SOUTH KOREA**

No **2016BY0712A1-1**
Date **07/12/16**
Commodity **NAVAL BRASS C464 ,ROUND (AST AND TURNED)**
Spec **PER ASTM B-21/B-21M, REV. 2014, ROHS COMPLIANT**

Job No.		DESCRIPTION			Quantity		Temper	Remarks	B/D No.	Mat No.	Inspection Result	
Line No.	Lot No.	SIZE			Pieces	Wt., Lbs	-	-	BY-	-	Dimension	Surface
~~0130~~	~~15R 00077~~	~~6" DIA, ROUND, CAST/TURNED, 4.26 FT L~~				~~904~~	~~CAST AND TURNED~~			CURD00268	GOOD	GOOD
Chemical/Physical	Element	Cu	Pb	Fe	Sn	-	Zn	S/C	T.S., Ksi	Y.S., Ksi	E/L (%)	HRB
Composition, %	Spec	59 ~62	0.20 MAX	0.10 MAX	0.5 ~1.0	-	Rem.	Ammonia	-	-	-	-
0130	15R 00077	60.3030	0.0133	0.0159	0.8145	-	Rem.	GOOD	N/A	N/A	N/A	N/A
MERCURY FREE												

WE CERTIFY THAT ABOVE INFORMATION IS TRUE AND OUR MATERIAL MEETS THE ABOVE ASTM SPECIFICATIONS.

SIGNED FOR BOO YOUNG IND.

Lloyds Pacific International, Inc.

From: ThyssenKrupp Materials NA
Cust. ONLINE METALS LAX WILL CALL
CstAr 7824
Wgt.: 64.400 LB
Del.: 2404872061
CstOr 66318
Date 11/09/2016

CONCAST METAL PRODUCTS CO.

CERTIFICATE OF ANALYSIS

PO BOX 816 - MARS, PA 16046

November 21 , 2016

OnlineMetals
8001 ThyssenKrupp Parkway

Northwood, OH 43619
Attn: Quality Control Department

THE FOLLOWING MATERIAL IS CERTIFIED TO:

COUNTRY OF MELT U.S.A.
COUNTRY OF MANUFACTURE U.S.A.
REACH CURRENT REV. 12-16-2013
RoHS-2 CURRENT REV. (2011/65/EU)
NO WELD REPAIR PERFORMED ON MATERIAL
DFARS CURRENT (DFARS 225.872) 12/31/2012
CATSCA 2010 COMPLIANT
CERTIFICATION OF CONFORMANCE
M07 AS CONTINUOUS CAST TEMPER
OnlineMetals
Attn: Accounts Payable P.O. Box 5116
Southfield, MI 48086-5116
ASTM B505/B505M-14

GENERAL PRODUCT INFORMATION

Heat#: 1612947

Manufacture Date: 08/15/16
Alloy: 954
Shape: SOLID
Size#: 0 X 1
Internal Standards: ASTM B505

Customer PO#: 66776
Customer Job#: 14386
Customer Part#: 14386
Control#:
Date Shipped: 11/21/16
Quantity Shipped: 6
Weight Shipped: 210.00
Packslip#: 253406
Invoice#: 0
Country of Origin: UNITED STATES

CHEMICAL ANALYSIS

	DEFINED BY SPECIFICATION Minimum		Maximum	MEASURED IN LABORATORY
Cu	83.0000	-	87.0000	85.8150
Fe	3.0000	-	5.0000	3.4640
Ni		-	1.5000	0.0520
Al	10.0000	-	11.5000	10.4330
Mn		-	.5000	0.2360

Physical Analysis *	Yield .5% UNDER LOAD (PSI)	N/mm²	Tensile (PSI)	N/mm²	Elongation in 2 in. min %	Brinell Hardness BRINELL 3000
Defined By Specification	32000	220.6	85000	586.1	12	0 - 0
1612947-1						187

This is to certify that all material listed is free from mercury contamination and no mercury bearing equipment was used in any of our manufacturing, fabricating, assembly or testing operations. No materials containing Class I or Class II ODC's; CFC's; Halons or HCFC's are used in our manufacturing process. None of the EPA's listed ODC's are used in our testing, assembly or fabricating procedures. Additionally we do not purchase, from our suppliers, any of the EPA's listed ODC's. * Minimum tensile and yield strength shall be reduced 10% for cast bars having a thickness, diameter, cross section or wall of 4" or more. All Nickel measurements are inclusive of Cobalt concentrations.

ISO 9001 REGISTERED FIRM

GRI CERTIFICATE NO.'S
25513/A/0001/AN/En
32119/A/0001/UK/En

CONCAST METAL PRODUCTS

Dominic P. Lemaire
Lab Manager

CONCAST METAL PRODUCTS, PO BOX 816, MARS Pennsylvania 16046 (800-626-7071)

ISO 9001 2008
AS 9100 Rev.C
LRQ. 0902066

BOLTON AEROSPACE LIMITED

AEROSPACE

TEST CERTIFICATE

EN 10204:2004 3.1

CUSTOMER SHIPPED TO: THYSSENKRUPP MATERIAL NA INC COPPER AND BRASS SALES PO BOX 5116 SOUTHFIELD MI 48086-5116	**TEST CERTIFICATE NO.**	L20454 Rev 0
	BATCH NO. (LOT NO.)	L20454
	CERT. OF CONFORMITY	
	WORKS ORDER NO.	N26096
	ALLOY	CA10
	QUANTITY ORDERED	454 kg
SPECIFICATION ASTM B150-12 C64200 HR50 AMS 4634B 2009 HR50 QQ-C-465B AMD1 C64200	**WEIGHT DESPATCHED**	492 kg
	CUSTOMER ORDER NO.	5400191092-R05
	DESCRIPTION SILICON ALUMINIUM BRONZE ROUND ROD 1.000" X 144.000" LENGTH	

MECHANICAL/PHYSICAL PROPERTIES

Tensile Specification	Dia	Area	0.5 % Yield	U.T.S.	Elongation 4D	Hardness	
	mm	mm²	ksi	ksi	%	$HB_{10/1000}$	HRB
ASTM E8	12.51	122	74.6	100.3	29	200	97
	12.50	122	76.1	100.0	29	200	97

CHEMICAL COMPOSITION %

Cu+ Ag	Zn	Fe	Mn	Al	Ni	Sn	Pb	Si	Ni+Co	As
BAL	0.04	0.18	0.02	6.82	0.15	0.01	<0.01	1.78	0.15	<0.01

"The products to which this declaration relates conform to the conditions and requirements of the purchaser and to the description, quantity and specification stated".
"These products have been produced under a certified quality system. The test results have been determined by an assessed or accredited laboratory"

REMARKS
MERCUROUS NITRATE TEST SATISFACTORY
PART # CURD01120
COUNTRY OF MELT & MANUFACTURE IS U.K.
NO WELD REPAIRS

We certify that material is free from mercury contamination

Signed for and on behalf of
BOLTON AEROSPACE LIMITED

Chief Inspector M HUDSON

Date Tuesday, 24 September 2013

Bolton Aerospace Limited
PO Box 22, Hadleigh Road, Ipswich, Suffolk, IP2 0EG
Tel: +44 (0) 1473 252127 Fax: +44 (0) 1473 218229
Email: mail@boltonmetals.com www.boltonmetals.com

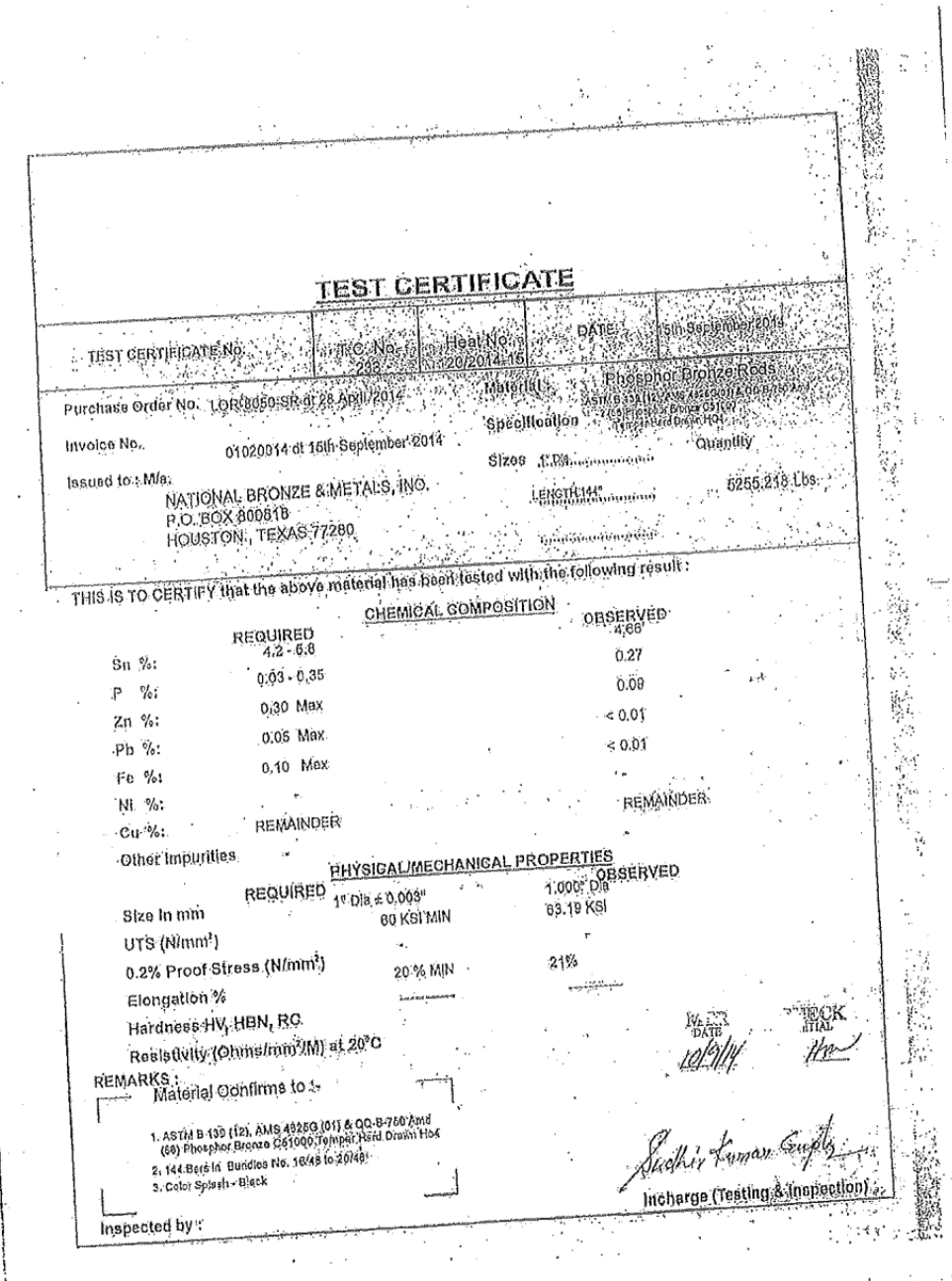

TEST CERTIFICATE

TEST CERTIFICATE No.	T.C. No.	Heat No.	DATE
	233	120/2014-15	5th September 2014

Purchase Order No. LOR/8050-SR dt 28 April 2014

Material : Phosphor Bronze Rods

Invoice No. 01020014 dt 16th September 2014

Specification : ASTM B 139/B 139M-12, AMS 4625G(01) & QQ-B-750 Alloy C51000 Temper H04

Issued to : M/s. NATIONAL BRONZE & METALS, INC. P.O. BOX 800818 HOUSTON, TEXAS 77280

Sizes : 1" Dia LENGTH 144"

Quantity : 5255.218 Lbs.

THIS IS TO CERTIFY that the above material has been tested with the following result :

CHEMICAL COMPOSITION

	REQUIRED	OBSERVED
Sn %:	4.2 - 6.8	4.66
P %:	0.03 - 0.35	0.27
Zn %:	0.30 Max	0.09
Pb %:	0.05 Max	< 0.01
Fe %:	0.10 Max	< 0.01
Ni %:	-	-
Cu %:	REMAINDER	REMAINDER
Other Impurities	-	-

PHYSICAL/MECHANICAL PROPERTIES

	REQUIRED	OBSERVED
Size in mm	1" Dia ± 0.003"	1.000" Dia
UTS (N/mm²)	60 KSI MIN	63.19 KSI
0.2% Proof Stress (N/mm²)	-	-
Elongation %	20 % MIN	21%
Hardness HV, HBN, RC	----	----
Resistivity (Ohms/mm²/M) at 20°C	-	-

QA DATE 10/9/14

TECK INITIAL

REMARKS :

Material Confirms to :-

1. ASTM B 139 (12), AMS 4625G (01) & QQ-B-750 Alloy (58) Phosphor Bronze C51000 Temper H04 Rod Drawn Hex
2. 144 Bars In Bundles No. 16/48 to 20/48
3. Color Splash - Black

Inspected by :

Sudhir Kumar Gupta

Incharge (Testing & Inspection)

From: ThyssenKrupp Materials NA
Cust. ONLINE METALS - WALLINGFORD
CstAr 18267
Wgt.: 37 LB

Del.: 2403915742
CstOr 41926
Date 06/09/2015

John R. Zambetti

Appendix 2

The developed hybrid chemometrics codes

```
%%%this iteratively read data 4rm excel, train it with SVr and display the
%%%result
clear;clc;
%load('SVRfuncData.xlsx');%.xlsx;
C=160.8091;lambda=1e-7;epsilon=0.6653;kerneloption=0.3951;kernel='gaussian';
shtNo = {'C510','C673','C932','C954','C863','C642','C655'};%%samples sheet no in excel
doc
samplNo = length(shtNo);
dataCon = cell(1,samplNo);%%create a container for the data
%%%iterate to take all the samples
for ss = 1 : samplNo
dataCon{ss} = xlsread('D:/deta/Desktop/proposed PHD thesis/proposed PHD thesis/CF-
LIBS/chemometric manuscript/extreem learning
machine/PhD_codes/AutSVRprog/SVRfuncData',shtNo{ss});
end

idx = 1:samplNo;%%indx for each modelling

for ss = 1 : samplNo
    idxcnrt = idx; idxcnrt(ss)=[];
    dat.tr = [];%%initialize  data collection

    %%extract training data
    for sl = 1 : samplNo-1
        idxn = idxcnrt(sl);
        dat.tr =[dat.tr;dataCon{idxn}];
    end
    dat.ts = dataCon{ss};%%extract testing data

    %%divide data into output/input training/testing
    dat.xtr = dat.tr (:,2:end);%%training input data
    dat.ytr = dat.tr (:,1);%%training output data
    dat.xts = dat.ts (:,2:end);%%testing input data
    dat.yts = dat.ts (:,1);%%testing output data

   [cc(ss),rmse(ss),predDat{ss},trgtDat{ss}]=
SVRfunc(dat.xtr,dat.ytr,dat.xts,dat.yts,C,lambda,epsilon,kerneloption,kernel);%%obtain
perf of SVR

%    predDat{ss} = pred;
%    TargDat{ss} = trgt;
tro=predDat{1};
```

```
tro.ts;
end
```

```
Undefined function 'svmreg' for input arguments of type 'double'.

Error in SVRfunc (line 8)
[xsup,ysup,w,w0] = svmreg(x,y,C,epsilon,kernel,kerneloption,lambda,verbose);%% this
generate support vectors xsup, weights w, bias w0

Error in mainProg (line 33)
   [cc(ss),rmse(ss),predDat{ss},trgtDat{ss}]=
SVRfunc(dat.xtr,dat.ytr,dat.xts,dat.yts,C,lambda,epsilon,kerneloption,kernel);%%obtain
perf of SVR
```

Published with MATLAB® R2015a

```
function [cc,rmse,pred,trgt]=
SVRfunc(x_tr,output_tr,x_ts,output_ts,C,lambda,epsilon,kerneloption,kernel)

for runs = 1:1
```

```
verbose=1;% display the output of the
x=x_tr;y=output_tr;

[xsup,ysup,w,w0] = svmreg(x,y,C,epsilon,kernel,kerneloption,lambda,verbose);%% this
generate support vectors xsup, weights w, bias w0
                                                                    %%xsup is
used to generate redicted output for training data

% to predict for the training set

xtest=x_tr; %[xtest1;xtest2]';

% size(xsup),size(xtest),size(w),size(w0),
y0 = svmval(xtest,xsup,w,w0,kernel,kerneloption);%%%predict the output for input training
data

y2 = output_tr; %yk';%%target of the training data/output training data
[r] = corrcoef([y2,y0 ]);%%5 finding correlation between predicted training data and its
target

actual_tr=output_tr;pred_tr=y0;cc_tr=r(2);
%x=depth_tr;
target=actual_tr;
ypred=pred_tr;
pred.tr =pred_tr;
trgt.tr = target;
[cc.tr,rmse.tr,Er.tr,Ea.tr,Emin.tr,Emax.tr,SD.tr] = err_comp(target,ypred);
```

```
%%%%all the performance indicators for training data
cc_tr(runs)=cc.tr;
rmse_tr(runs)=rmse.tr;
Ea_tr(runs)=Ea.tr;
SD_tr(runs)=SD.tr;
```

```
Error using SVRfunc (line 6)
Not enough input arguments.
```

testing

```
xtest=x_ts; %[xtest1;xtest2]';%%tesing input data
ys = svmval(xtest,xsup,w,w0,kernel,kerneloption);%%%validating xsup with testin input
data

actual_ts=output_ts;pred_ts=ys;cc_ts=r(2);
%x=depth_ts;
target=actual_ts;%%%%actual testing output data
ypred=pred_ts;%%%predicted tesing output data
pred.ts = pred_ts;
trgt.ts = target;
[cc.ts,rmse.ts,Er.ts,Ea.ts,Emin.ts,Emax.ts,SD.ts]=err_comp(target,ypred);

cc_ts(runs)=cc.ts;rmse_ts(runs)=rmse.ts;Ea_ts(runs)=Ea.ts;SD_ts(runs)=SD.ts;
```

```
end

%%%%the .tr and .ts makes it possible to use jsut one variable for display of both tr&ts
SD_rmse.tr=std(rmse_tr);SD_cc.tr=std(cc_tr);
SD_rmse.ts=std(rmse_ts);SD_cc.ts=std(cc_ts);
SD_Ea.tr=std(Ea_tr);SD_Ea.ts=std(Ea_ts);
cc.ts=mean(cc_ts);%%%corr coef of testing
cc.tr=mean(cc_tr);%%%corr coeff of trainin
Ea.tr=mean(Ea_tr);%%%avg absolute error4 trainin
Ea.ts=mean(Ea_ts);%%avg absolute err 4 testing
rmse.tr=mean(rmse_tr);%%%% root mean square
rmse.ts=mean(rmse_ts);%%%%root mean square testing


disp('End of svm Networks')
```

Published with MATLAB® R2015a

```
function[cc2,rmse,Er,Ea,Emin,Emax,SD]=err_comp(yoriginal, ypredict)
%cc is the correlation coefficient
%rmse is the root mean square error
%Er is the mean/average percent relative error
%Ea is the mean/average absolute percent error
%Emax is the
```

```
if size(ypredict,1)>size(ypredict,2)%%% ensuring the data is a column vector
    ypredict=ypredict;%%leave if is column
else ypredict=ypredict';%change if it is row
end

n_tr=length(ypredict);
% varx=sum(ypredict.^2)/n_tr - (sum(ypredict)^2)/(n_tr^2);
% vary=sum(yoriginal.^2)/n_tr - (sum(yoriginal)^2)/(n_tr^2);
% covxy=sum(ypredict.*yoriginal)/n_tr  - (sum(ypredict)*sum(yoriginal))/(n_tr^2);
% cc=covxy/(sqrt(varx * vary));
%


cc=corrcoef(ypredict,yoriginal);%%corrcoeficient of predicted and actual trainin
data(cpmes as 2by 2 matrix, auto on main diag&cross on the other)
% size(ypredict),size(yoriginal),
% pause,
%

cc2=cc(2);

diff=yoriginal-ypredict;
diff2=double(diff);
diffsq=diff2.^2;
%mse=mean(diffsq);
%rmsed=mse^.5

rmse=errperf(yoriginal,ypredict,'rmse');%matlab fucntion for calculatin various
errors,cal rmse in this instance

% size(yoriginal), size(ypredict),
% pause,
%
% rmse2=sqrt(mse(yoriginal-ypredict));
%Er=errperf(yoriginal,ypredict,'mpre');
%Ea=errperf(yoriginal,ypredict,'mapre');

L=length(yoriginal);
Eit=[]; %diff2=[],diff=0
for x=1:L;
    Ei=((yoriginal(x)-ypredict(x))/yoriginal(x))*100;%dif is Ei

               %diff2=[diff2,diff];
    Eit=[Eit,Ei];%for computing average percent relative error
end %%% Eit=((yoriginal-ypredict)./yoriginal)*100
Er=(sum(Eit))/L;%%%average percent relative error/Eit=((yoriginal-
ypredict)./(L*yoriginal))*100
diff=(Ei-Er).^2;%this is used for computing SD,standard deviation, square of the error
variance
sd=sum(diff);%%%standard deviation/std(Eit,L)
Ea=(sum(abs(Eit)))/L;%%%%average absolute value of the error
Emax=max(abs(Eit));%%max absolute value
Emin=min(abs(Eit));%%min absolute value
```

```
diffav=sd/(L-1);%%
SD=double(sqrt(diffav));%%diff implemenatation of sd
```

```
Error using err_comp (line 7)
Not enough input arguments.
```

Published with MATLAB® R2015a

development of ELM-GSA-WIRP model with optimum value of HN obtained from GSA

```
clear all
close all
% disp('');
% disp('------This is the begining of ELM ------');
% disp('');
% disp('EXTREME LEARNING MACHINES');
% disp('======================');
% disp('');
% dat=xlsread('datagsa2_vali.xlsx',2);
% datt=xlsread('datagsa2_vali.xlsx',3);
% x_tr=[dat(:,2),dat(:,3),dat(:,4),dat(:,5),dat(:,6)];
% output_tr=dat(:,1);
% x_ts=[datt(:,2),datt(:,3),datt(:,4),datt(:,5),datt(:,6)];
% output_ts=datt(:,1);
% depth_tr=dat(:,1);
% depth_ts=datt(:,1);
```

```
dat=xlsread('datagsa2_vali.xlsx',2);
datt=xlsread('datagsa2_vali.xlsx',3);
x_tr=dat(:,2);
output_tr=dat(:,1);
x_ts=datt(:,2);
output_ts=datt(:,1);
depth_tr=dat(:,1);
depth_ts=datt(:,1);
```

```
% load('datat');
%  x_tr= [x_tr; x_ts];
%  output_tr =[output_tr; output_ts];


%fxn = {'sig','tansig','sin','tribas','radbas'};%'tansig';
```

```
 nodes= 53;
act_fxn = 'sin' ;
%act_fxn = 'sig' ;
%act_fxn = 'hardlim' ;

%training
 [InputWeight, BiasofHiddenNeurons, OutputWeight, yO_tr, TrainingTime] =
new_elm_train(x_tr, output_tr, nodes, act_fxn); %'sig'

%save('ElmNetede','InputWeight', 'BiasofHiddenNeurons', 'OutputWeight');
```

run the best model

```
 %load('ElmNet4');
 %load ElmNetHWIRP1;  %
 %load ElmNetHWIRP2a; %
 %load ElmNetHWIRP3;%load ElmNetHWIRP4a
  %load('ElmNet5');  %ElmNetHWIRP5aaa; %ElmNetHWIRP6aaa;%load ElmNetHWIRP7aa
  %load ElmNetWIRP1;%load ElmNetIRP1;%load ElmNetIRP2a;%ElmNetIRP3aa;%load ElmNetIRP4
  load ElmNetWIRP1a;%load ElmNetIRP5a;%load ElmNetIRP6;%load ElmNetIRP7
 % load ElmNetWIRP2a
 %load ElmNetIRP3aa
 %load ElmNetWIRP3
%load ElmNetWIRP4aaa
%load ElmNetWIRP6
%load ElmNetWIRP7b
%load ElmNetWIRP5

[trx_rmse,  ypredict_tr, reTrainingTime] = new_elm_predict(x_tr, output_tr, InputWeight,
BiasofHiddenNeurons, OutputWeight,  act_fxn);

[tsx_mse, ypredict_ts, TestingTime] = new_elm_predict(x_ts,output_ts,InputWeight,
BiasofHiddenNeurons, OutputWeight, act_fxn);

 [trcc,trrmse,Ertr,Eatr,Emaxtr,SDtr]=errors_compute(output_tr, ypredict_tr);

fprintf('Correlation Coefficient-- (training data): = %f \n',trcc),
%plotregression(output_tr,ypredict_tr)
 fprintf('Root Mean Square Errors (training data): = %5.5f \n',trrmse),%
[output_tr, ypredict_tr]
%
 [tscc,tsrmse,Er,Ea,Emax,SD]=errors_compute(output_ts,ypredict_ts);
%
%  fprintf('Correlation Coefficient-- (testing data): = %f \n',tscc),
%
  [output_ts,ypredict_ts]
  errorr=tsrmse
  errortr=trrmse
%  figure(2);
%  %plot(ypredict_ts,output_ts,'ob')
%  plotregression(output_ts,ypredict_ts)
```

```
%  %xlim([0, 1.1*max(ypredict_ts)]),ylim([0 ,1.1*max(output_ts)])
%  fprintf('Root Mean Square Errors (testing data): = %5.5f \n',tsrmse),%
%
%
```

```
Error using *
Inner matrix dimensions must agree.

Error in new_elm_predict (line 74)
 tempH_test=InputWeight*TV.P;

Error in RunMainELM2 (line 65)
[trx_rmse,  ypredict_tr, reTrainingTime] = new_elm_predict(x_tr, output_tr, InputWeight,
BiasofHiddenNeurons, OutputWeight,  act_fxn);
```

Published with MATLAB® R2015a

```
function [InputWeight, BiasofHiddenNeurons, OutputWeight, yO_tr, TrainingTime] =
new_elm_train(TrainingData, TrainingTarget,  NumberofHiddenNeurons, ActivationFunction)
Elm_Type=0;
REGRESSION=0;
CLASSIFIER=1;

%%%%%%%%%% Load training dataset
%train_data=load(TrainingData_File);
T=TrainingTarget';
P=TrainingData';
clear TrainingData;                                   %   Release raw training data array
clear TrainingTarget;
%%%%%%%%%% Load testing dataset
%test_data=load(TestingData);
% TV.T=TestingData(:,end)';
% TV.P=TestingData(:,1:end-1)';
% clear TestingData;                                    %   Release raw testing data
array

NumberofTrainingData=size(P,2);
%NumberofTestingData=size(TV.P,2);
NumberofInputNeurons=size(P,1);

if Elm_Type~=REGRESSION
    %%%%%%%%%% Preprocessing the data of classification
    sorted_target=sort(T,2);
    label=zeros(1,1);                                 %   Find and save in 'label' class
label from training and testing data sets
    label(1,1)=sorted_target(1,1);
    j=1;
    for i = 2:(NumberofTrainingData)
        if sorted_target(1,i) ~= label(1,j)
            j=j+1;
            label(1,j) = sorted_target(1,i);
```

```
        end
    end
    number_class=j;
    NumberofOutputNeurons=number_class;

    %%%%%%%%%% Processing the targets of training
    temp_T=zeros(NumberofOutputNeurons, NumberofTrainingData);
    for i = 1:NumberofTrainingData
        for j = 1:number_class
            if label(1,j) == T(1,i)
                break;
            end
        end
        temp_T(j,i)=1;
    end
    T=temp_T*2-1;

    %%%%%%%%%% Processing the targets of testing
%     temp_TV_T=zeros(NumberofOutputNeurons, NumberofTestingData);
%     for i = 1:NumberofTestingData
%         for j = 1:number_class
%             if label(1,j) == TV.T(1,i)
%                 break;
%             end
%         end
%         temp_TV_T(j,i)=1;
%     end
%     TV.T=temp_TV_T*2-1;

end                                                 %   end if of Elm_Type

%%%%%%%%%%% Calculate weights & biases
start_time_train=cputime;

%%%%%%%%%%% Random generate input weights InputWeight (w_i) and biases
BiasofHiddenNeurons (b_i) of hidden neurons
InputWeight=rand(NumberofHiddenNeurons,NumberofInputNeurons)*2-1;
BiasofHiddenNeurons=rand(NumberofHiddenNeurons,1);
tempH=InputWeight*P;
clear P;                                            %   Release input of training data
ind=ones(1,NumberofTrainingData);
BiasMatrix=BiasofHiddenNeurons(:,ind);              %   Extend the bias matrix
BiasofHiddenNeurons to match the demention of H
tempH=tempH+BiasMatrix;

%%%%%%%%%%% Calculate hidden neuron output matrix H
switch lower(ActivationFunction)
    case {'sig','sigmoid'}
        %%%%%%%% Sigmoid
        H = 1 ./ (1 + exp(-tempH));
    case {'tansig'}
        H = tansig(tempH);
    case {'sin','sine'}
```

```
        %%%%%%%% Sine
        H = sin(tempH);
    case {'hardlim'}
        %%%%%%%% Hard Limit
        H = double(hardlim(tempH));
    case {'tribas'}
        %%%%%%%% Triangular basis function
        H = tribas(tempH);
    case {'radbas'}
        %%%%%%%% Radial basis function
        H = radbas(tempH);
        %%%%%%%% More activation functions can be added here
end

clear tempH;                                    %   Release the temparary array for
calculation of hidden neuron output matrix H

%%%%%%%%%% Calculate output weights OutputWeight (beta_i)
OutputWeight=pinv(H') * T';                        % implementation without

end_time_train=cputime;
TrainingTime=end_time_train-start_time_train   ;     %   Calculate CPU time (seconds)
spent for training ELM

%%%%%%%%%% Calculate the training accuracy
Y=(H' * OutputWeight)';
yO_tr =Y';
%   Y: the actual output of the training data
% if Elm_Type == REGRESSION
%     TrainingAccuracy=sqrt(mse(T - Y))  ;             %   Calculate training accuracy
(RMSE) for regression case
% end
% clear H;

% %%%%%%%%%% Calculate the output of testing input
% start_time_test=cputime;
% tempH_test=InputWeight*TV.P;
% clear TV.P;             %   Release input of testing data
% ind=ones(1,NumberofTestingData);
% BiasMatrix=BiasofHiddenNeurons(:,ind);              %   Extend the bias matrix
BiasofHiddenNeurons to match the demention of H
% tempH_test=tempH_test + BiasMatrix;
% switch lower(ActivationFunction)
%     case {'sig','sigmoid'}
%         %%%%%%%% Sigmoid
%         H_test = 1 ./ (1 + exp(-tempH_test));
%     case {'sin','sine'}
%         %%%%%%%% Sine
%         H_test = sin(tempH_test);
%     case {'hardlim'}
%         %%%%%%%% Hard Limit
%         H_test = hardlim(tempH_test);
%     case {'tribas'}
```

```
%         %%%%%%%% Triangular basis function
%         H_test = tribas(tempH_test);
%     case {'radbas'}
%         %%%%%%%% Radial basis function
%         H_test = radbas(tempH_test);
%         %%%%%%%% More activation functions can be added here
% end
% TY=(H_test' * OutputWeight)';                       %   TY: the actual output of the
testing data
% end_time_test=cputime;
% TestingTime=end_time_test-start_time_test           %   Calculate CPU time (seconds)
spent by ELM predicting the whole testing data
%
% if Elm_Type == REGRESSION
%     TestingAccuracy=sqrt(mse(TV.T - TY))            %   Calculate testing accuracy
(RMSE) for regression case
% end
```

```
Error using new_elm_train (line 8)
Not enough input arguments.
```

Published with MATLAB® R2015a

```
function [TestingAccuracy, yO_ts, TestingTime] = new_elm_predict(TestingData,
TestingTarget, InputWeight, BiasofHiddenNeurons, OutputWeight, ActivationFunction)

%%%%%%%%%% Macro definition
Elm_Type=0;
REGRESSION=0;
CLASSIFIER=1;

%%%%%%%%%% Load testing dataset
%test_data=load(TestingData_File);

%Fatai
%y_ts=test_data(:,1) % Actual Target
y_ts=TestingTarget; % Actual Target
[n_ts,p]=size(y_ts);
%Fatai

%TV.T=test_data(:,1)';
TV.T=y_ts';
%TV.P=test_data(:,2:size(test_data,2))';
TV.P=TestingData';

%clear test_data;                                   %   Release raw testing data array
```

```
NumberofTestingData=size(TV.P,2);

%load elm_model.mat;

if Elm_Type~=REGRESSION

NumberofOutputNeurons = size(TV.P,1) ;

    %%%%%%%%%% Processing the targets of testing
    temp_TV_T=zeros(NumberofOutputNeurons, NumberofTestingData);
    for i = 1:NumberofTestingData
        for j = 1:size(label,2)
            if label(1,j) == TV.T(1,i)
                break;
            end
        end
        temp_TV_T(j,i)=1;
    end
    TV.T=temp_TV_T*2-1;

end                                                 %   end if of Elm_Type

%%%%%%%%%% Calculate the output of testing input
start_time_test=cputime;
 tempH_test=InputWeight*TV.P;
clear TV.P;             %   Release input of testing data
ind=ones(1,NumberofTestingData);
BiasMatrix=BiasofHiddenNeurons(:,ind);              %   Extend the bias matrix
BiasofHiddenNeurons to match the demention of H
tempH_test=tempH_test + BiasMatrix;
switch lower(ActivationFunction)
    case {'sig','sigmoid'}
        %%%%%%%% Sigmoid
        H_test = 1 ./ (1 + exp(-tempH_test));
    case {'tansig'}
        H_test = tansig(tempH_test);
    case {'sin','sine'}
        %%%%%%%% Sine
        H_test = sin(tempH_test);
    case {'hardlim'}
        %%%%%%%% Hard Limit
        H_test = hardlim(tempH_test);
    case {'tribas'}
        %%%%%%%% Triangular basis function
        H_test = tribas(tempH_test);
    case {'radbas'}
        %%%%%%%% Radial basis function
        H_test = radbas(tempH_test);
        %%%%%%%% More activation functions can be added here
end
TY=(H_test' * OutputWeight)'                       %   TY: the actual output of the
testing data
```

```
end_time_test=cputime;
yO_ts = TY';
%save('H_shown','H_test')
jj= H_test(:,1)'* OutputWeight;
TestingTime=end_time_test-start_time_test   ;        %   Calculate CPU time (seconds)
spent by ELM predicting the whole testing data

if Elm_Type == REGRESSION
    TestingAccuracy=sqrt(mse(TV.T - TY))  ;          %   Calculate testing accuracy
(RMSE) for regression case
end

if Elm_Type == CLASSIFIER
%%%%%%%%%% Calculate training & testing classification accuracy
    MissClassificationRate_Training=0;
    MissClassificationRate_Testing=0;

    for i = 1 : size(T, 2)
        [x, label_index_expected]=max(T(:,i));
        [x, label_index_actual]=max(Y(:,i));
        if label_index_actual~=label_index_expected
            MissClassificationRate_Training=MissClassificationRate_Training+1;
        end
    end
    TrainingAccuracy=1-MissClassificationRate_Training/size(T,2);
    for i = 1 : size(TV.T, 2)
        [x, label_index_expected]=max(TV.T(:,i));
        [x, label_index_actual]=max(TY(:,i));
        if label_index_actual~=label_index_expected
            MissClassificationRate_Testing=MissClassificationRate_Testing+1;
        end
    end
    TestingAccuracy=1-MissClassificationRate_Testing/size(TV.T,2)  ;
end
```

```
Error using new_elm_predict (line 13)
Not enough input arguments.
```

Published with MATLAB® R2015a